Time-resolved photoelectron spectroscopy at surfaces

Martin Aeschlimann [a], Jan Philipp Bange [b], Michael Bauer [c,d], Uwe Bovensiepen [e], Hans-Joachim Elmers [f], Thomas Fauster [g], Lukas Gierster [h], Ulrich Höfer [i,j], Rupert Huber [j], Andi Li [k], Xintong Li [l], Stefan Mathias [b], Karina Morgenstern [m], Hrvoje Petek [k], Marcel Reutzel [b], Kai Rossnagel [c,d,o], Gerd Schönhense [f], Markus Scholz [n], Benjamin Stadtmüller [p], Julia Stähler [h,q], Shijing Tan [l], Bing Wang [l], Zehua Wang [k], Martin Weinelt [r,*]

[a] Department of Physics and Research Center OPTIMAS, University of Kaiserslautern-Landau, Erwin-Schrödinger-Str. 46, 67663 Kaiserslautern, Germany
[b] Georg-August-Universität Göttingen, I. Physikalisches Institut, Friedrich-Hund-Platz 1, 37077 Göttingen, Germany
[c] Institut für Experimentelle und Angewandte Physik, Christian-Albrechts-Universität zu Kiel, Leibnizstr 19, 24118 Kiel, Germany
[d] Kiel Nano, Surface and Interface Science KiNSIS, Christian-Albrechts-Universität zu Kiel, Christian-Albrechts-Platz 4, 24118 Kiel, Germany
[e] Fakultät für Physik, Universität Duisburg–Essen, Lotharstrasse 1, 47057 Duisburg, Germany
[f] Institut für Physik, Johannes Gutenberg-Universität Mainz, Staudingerweg 7, 55128 Mainz, Germany
[g] Lehrstuhl für Festkörperphysik, Friedrich-Alexander-Universität Erlangen-Nürnberg, Staudtstr. 7, 91058 Erlangen, Germany
[h] Institut für Chemie, Humboldt-Universität zu Berlin, Brook-Taylor-Str. 2, 12489 Berlin, Germany
[i] Fachbereich Physik, Philipps-Universität Marburg, Renthof 5, 35032 Marburg, Germany
[j] Institut für Experimentelle und Angewandte Physik, Universität Regensburg, Universitätsstraße 31, 93053 Regensburg, Germany
[k] Department of Physics and Astronomy and the IQ Initiative, University of Pittsburgh, Pittsburgh, PA 15260, USA
[l] Hefei National Research Center for Physical Sciences at the Microscale and New Cornerstone Science Laboratory, University of Science and Technology of China, Hefei, Anhui 230026, China
[m] Lehrstuhl für Physikalische Chemie I, Ruhr-Universität Bochum, Universitätsstrasse 150, 44801 Bochum, Germany
[n] Deutsches Elektronen-Synchrotron DESY, Notkestr. 85, 22607 Hamburg, Germany
[o] Ruprecht Haensel Laboratory, Deutsches Elektronen-Synchrotron DESY, Notkestr. 85, 22607 Hamburg, Germany
[p] Experimentalphysik II, Institute of Physics, Augsburg University, Universitätsstraße 2, 86159 Augsburg, Germany
[q] Fritz-Haber-Institut der Max–Planck-Gesellschaft, Faradayweg 4-6, 14195 Berlin, Germany
[r] Fachbereich Physik, Freie Universität Berlin, Arnimallee 14, 14195 Berlin, Germany

ARTICLE INFO

ABSTRACT

Light is a preeminent spectroscopic tool for investigating the electronic structure of surfaces. Time-resolved photoelectron spectroscopy has mainly been developed in the last 30 years. It is therefore not surprising that the topic was hardly mentioned in the issue on "The first thirty years" of surface science. In the second thirty years, however, we have seen tremendous progress in the development of time-resolved photoelectron spectroscopy on surfaces. Femtosecond light pulses and advanced photoelectron detection schemes are increasingly being used to study the electronic structure and dynamics of occupied and unoccupied electronic states and dynamic processes such as the energy and momentum relaxation of electrons, charge transfer at interfaces and collective processes such as plasmonic excitation and optical field screening. Using spin- and time-resolved photoelectron spectroscopy, we were able to study ultrafast spin dynamics, electron–magnon scattering and spin structures in magnetic and topological materials. Light also provides photon energy as well as electric and magnetic fields that can influence molecular surface processes to steer surface photochemistry and hot-electron-driven catalysis. In addition, we can consider light as a chemical reagent that can alter the properties of matter by creating non-equilibrium states and ultrafast phase transitions in correlated materials through the coupling of electrons, phonons and spins. Electric fields have also been used to temporarily change the electronic structure. This opened up new methods and areas such as high harmonic generation, light wave electronics and attosecond physics. This overview certainly cannot cover all these interesting topics. But also as a testimony to the cohesion and constructive exchange in our ultrafast community, a number of colleagues have come together to share their expertise and views on the very vital field of dynamics at surfaces. Following the introduction, the interested reader will find a list of contributions and a brief summary in Section 1.3.

---

* Corresponding author.
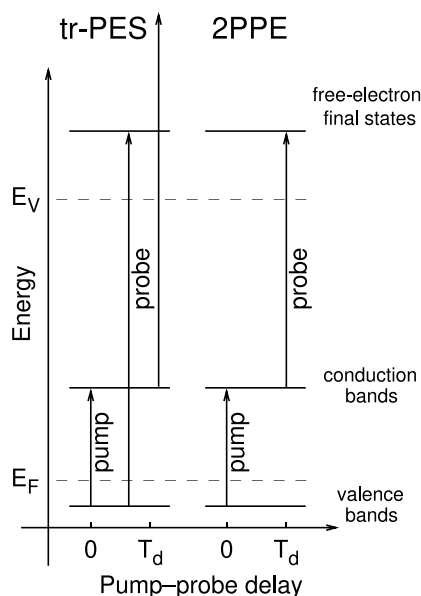 E-mail address: weinelt@physik.fu-berlin.de (M. Weinelt).

Fig. 1. Energy diagram of time-resolved photoemission.

1. Introduction

Angle-resolved photoemission allows to measure the dispersion of the occupied band structure (valence bands and core levels) at surfaces. Time-resolved photoemission probes the electronic structure as a function of the time after the excitation of the surface by a pump pulse. The pump pulse excites electrons from previously occupied states into unoccupied states (conduction bands). The probe pulse of the time-resolved photoemission experiment may sample the reduced population in the valence bands or the temporary population in the conduction bands. The latter signal detects electrons in an energy window without signal in the absence of the pump pulse. In contrast can the valence-band population only be reduced by a small proportion without destroying the sample which makes this effect more difficult to detect. However, changes of the valence-band structure following for example an optical-induced phase transition may be resolved.

1.1. Modes of time-resolved photoemission

Two different modes can be distinguished in time-resolved photoemission (Fig. 1):

- In time-resolved photoelectron spectroscopy (tr-PES) the probe photon energy exceeds the work function $\Phi = E_V - E_F$. This leads to a large signal from the occupied valence bands. The electrons pumped to the conduction bands appear in the spectra at higher energy, but for metals on top of the tail of the Fermi distribution of thermally and optically excited electrons. The higher kinetic energies of the emitted electrons, however, allow to sample the whole surface Brillouin zone in an angle-resolved photoemission experiment.
- Two-photon photoemission (2PPE) requires photons from pump and probe pulse to emit electrons from the sample, i. e. both photon energies are smaller than the work function of the sample. This mode provides spectra with low background limited to a rather narrow range of electron energies and of the surface Brillouin zone.

In both modes energy spectra at fixed pump–probe delay or time scans at a selected energy may be recorded.

The pump pulse is usually provided by a pulsed laser source. The photoemission probe also has to be pulsed and synchronized to the pump pulse with an adjustable time delay. The most convenient way is the generation of the probe pulse from the same laser source as the pump pulse. This may be achieved by frequency doubling, tripling or quadrupling of the laser pulse in nonlinear crystals. Higher photon energies can be generated as higher harmonics in gas cells. In a free-electron laser the photocathode may be triggered by the laser source. More elaborate is the exploitation of pulsed synchrotron radiation which requires considerable effort to synchronize the laser source with the electron bunches circulating in the storage ring. Any electron spectrometer may be used for electron detection. The pulsed nature of the laser source offers the possibility of time-of-flight spectroscopy for repetition rates <1 MHz. In this detection mode all the electrons emitted by a laser pulse can be registered regardless of their kinetic energy.

1.2. Development of time-resolved photoemission

The advances of time-resolved photoemission are closely related to the availability of pulsed laser sources. The first time-resolved photoelectron spectroscopy was reported from ZnTe in 1982 and employed 5 ps pulses at a repetition rate of 1 Hz [1]. Experimental progress was made towards angle-resolved tr-PES by using higher photon energies and time-of-flight detection on the InP(110) surface [2]. Excited electrons relax on metal surfaces on much shorter time scales than on semiconductors. In 1988 the first 2PPE experiment using 55 fs laser pulses at a repetition rate of 8 kHz from image-potential states on Ag(100) was reported [3]. The surface space-charge dynamics and surface recombination on Si(111) surfaces was the first study using combined laser and synchrotron radiation with 20 ns pulses at a repetition rate of 6 kHz [4]. The further development of laser sources has led to a steady advancement of the experimental possibilities which are in part reviewed in other contributions of this chapter. Today laser pulses achieve attosecond precision [5] with complete control of the electric field [6] (see also Chs. 9 and 10). Developments in effective electron detection will be described in Chs. 6 and 11.

1.3. List of contributions

This article reviews important aspects of electron dynamics at surfaces and their analysis by time-resolved photoelectron spectroscopy. The individual chapters listed below have been contributed by authors working in the field. We do not claim to cover the field but still hope to give a reasonable overview.

1. **Introduction**
2. **Image-potential states**
   Thomas Fauster
   Image-potential states on metal surfaces have lifetimes in the femtosecond range and serve as an ideal testbed for investigating various aspects of 2PPE in considerable detail. The knowledge acquired from these studies can be transferred to adsorbate or adlayer systems relevant in many areas of surface science.
3. **Carrier relaxation in graphene and graphite**
   Michael Bauer
   Over the past two decades, the relaxation and thermalization dynamics of photoexcited charge carriers in graphite and graphene have been thoroughly investigated using various types of ultrafast techniques. This chapter reviews our current understanding of the microscopic interactions and the relevant time scales involved in this process, focusing on the contributions of time- and angle-resolved photoemission to this topic.
4. **Femtosecond solvation dynamics of Cs$^+$ ions at solid interfaces**
   Uwe Bovensiepen and Karina Morgenstern
   Alkali ions coadsorbed with a solvent on metal surfaces represent a model system for metal–electrolyte interfaces. Their preparation under ultrahigh vacuum conditions allows to exploit the

quantitative insights available from well-established surface science methodology. Here, microscopic information on the atomic structural and femtosecond electron transfer driven dynamics is presented.

5. **Ultrafast dynamics of photostationary states in time-resolved photoemission**
   Julia Stähler and Lukas Gierster
   Excited states with lifetimes exceeding the inverse repetition rate of commonly used light sources in time-resolved photoemission studies can play a crucial role in data analysis and interpretation, but are easily overlooked despite their abundance. The resulting photostationary states may have very different physical and chemical properties than the ground state and, moreover, serve as the precursor for photoinduced phase transitions.

6. **Time-resolved momentum microscopy of 2D materials**
   Jan Philipp Bange, Marcel Reutzel, and Stefan Mathias
   The optoelectronic properties of two-dimensional van der Waals semiconductors and their heterostructures are dominated by tightly bound electron–hole pairs called excitons. The energy landscape of excitons is complex and not fully accessible with all-optical spectroscopies, because most excitons in two-dimensional materials are optically dark, including, *e.g.*, dark intralayer, hybrid, and interlayer excitons. Time-resolved momentum microscopy turned out to be a powerful tool to firstly identify such dark exciton states in momentum space and to secondly follow their ultrafast formation and thermalization dynamics.

7. **Time-resolved photoemission electron microscopy**
   Martin Aeschlimann and Benjamin Stadtmüller
   Time-resolved photoemission electron microscopy, or tr-PEEM, is one of the most widely used methods to study ultrafast charge and spin carrier dynamics on the nano- and mesoscopic scale. In this chapter, we will first summarize the main features of modern tr-PEEM experiments. Then, we will give an insight into pioneering work in the field of tr-PEEM, focusing on exemplary cases from the fields of plasmonics as well as semiconductor surfaces and interfaces.

8. **Ultrafast Spin Dynamics probed by tr-ARPES**
   Martin Weinelt
   I give a brief introduction to the field of ultrafast magnetization dynamics and highlight some of the contributions that time-resolved photoelectron spectroscopy has made to the microscopic understanding of femtosecond spin dynamics.

9. **The transition from perturbative to nonperturbative multiphoton photoemission**
   Hrvoje Petek, Andi Li, Zehua Wang, Marcel Reutzel, Xintong Li, Shijing Tan, and Bing Wang
   The transition region, where light interaction shifts from perturbative one driving of multiphoton excitation to nonperturbative one driving of electron currents at PHz frequencies, is particularly rich for the discovery of novel light–matter phenomena. Here we present research on novel coherent phenomena for the well-known surface states of Cu(111) and Ag(111) oriented single crystals, and perform coherent spectroscopy with suboptical cycle resolution to explore how these similar materials respond differently to intense optical fields. Our intent is to build on well-established topics in surface science to open new areas of research in surface and solid-state ultrafast quantum physics.

10. **Subcycle Photoemission**
    Ulrich Höfer and Rupert Huber
    Elementary processes underlying strong-field light–matter interaction, high-harmonic generation, and all-optical band-structure engineering are now becoming accessible in direct band-structure videography. Exemplifying the scope of these new possibilities, this chapter will illustrate subcycle photoemission of lightwave-driven Dirac currents and the birth of Floquet–Bloch bands in the surface of a topological insulator.

11. **Progress in momentum imaging**
    Gerd Schönhense and Hans-Joachim Elmers
    The key element of photoelectron emission microscopes and momentum microscopes is the cathode lens, with the sample being an integral part of the lens. A large electrostatic field between sample and first electrode, although prohibitive for non-flat samples, was considered mandatory to achieve high lateral resolution. A novel front lens configuration enables the reduction of the electrostatic field at the sample surface to zero and even to negative values. Experimental results confirm the functionality of this approach.

12. **Time-resolved FEL photoelectron spectroscopy**
    Markus Scholz and Kai Rossnagel
    Advances in high-repetition-rate free-electron lasers (FELs) are opening new possibilities for time-resolved photoelectron spectroscopy, enabling the dynamical investigation of quantum materials, soft matter systems, and interfacial reactions. The combination of valence- and core-electron spectroscopy allows the detailed tracking of coupled electronic dynamics and atomic motion on the femtosecond timescale with high momentum resolution and atomic site specificity. The ongoing development of FEL and photoelectron spectrometer technology promises unprecedented sensitivity and multimodality to dissect and correlate the electronic and structural response to optical or lower energy excitation, providing novel valuable insights into the many-body response of excited systems.

2. Image-potential states

Thomas Fauster

Image-potential states are loosely bound electronic states in front of metal surfaces (Fig. 2) [7]. They arise from the long-range image potential of an electron screened by the charge density in the metal. The image-potential states form a series of unoccupied states labeled by the quantum number *n* with energies $E_n = -0.85$ eV$/(n+a)^2$ relative to the vacuum level E_V and a free-electron-like dispersion parallel to the surface. The quantum defect *a* accounts for the relative position of the image-potential states in the projected bulk band gap [8]. The states have lifetimes in the femtosecond range [3] and served as an ideal testbed for investigating various aspects of 2PPE in considerable detail. Fig. 3(a) shows a series of spectra for image-potential states on Cu(001) for different time delays approximately normalized to the same maximum peak height. The relative intensities change with time delay indicating a lifetime increase with quantum number *n*. The maximum of the probability density of the wave functions of the more loosely bound image-potential states with higher quantum numbers is further away from the surface reducing the overlap with bulk states which is the dominating factor for decay. The decrease of the linewidth with time delay visible for the $n = 1$ image-potential state in Fig. 3(a) can be explained by modeling the 2PPE process using optical Bloch equations [9].

Fig. 3(b) presents time-resolved scans at the energies of the first three image-potential states on a semilogarithmic scale. From the linear slope the lifetime is readily obtained and increases with quantum number *n*. In the scan for the $n = 3$ state oscillations are visible which originate from quantum beats by the coherent excitation of the $n = 3$ and 4 states [10]. The beating frequency allows a precise determination of the energy difference between the two states. For higher quantum numbers several states are coherently excited and wave packets develop representing the transition to the classical picture of a particle bouncing back and forth between the bulk and vacuum barrier [10].

The high dynamic range in time-resolved 2PPE spectra allows to study scattering effects of electrons in image-potential states. The trace for the $n = 1$ image-potential state in Fig. 3(b) changes slope for delay times larger than 400 fs to a slope similar to the one for the $n = 2$ state. The explanation is scattering of electrons from the $n =$
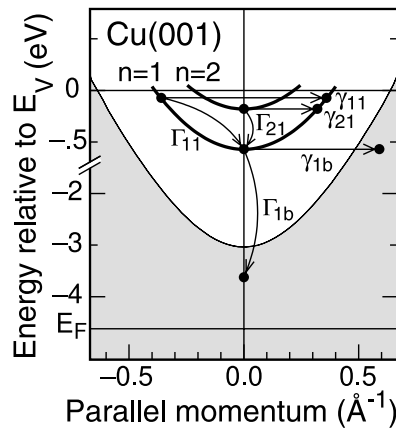
Fig. 2. Dispersion of the $n = 1$ and $n = 2$ image-potential states in the projected bulk band structure (shaded area) of the Cu(001) surface. The arrows indicate elastic (γ_{nm}) and inelastic (Γ_{nm}) scattering processes between image-potential states and bulk bands (subscript b).
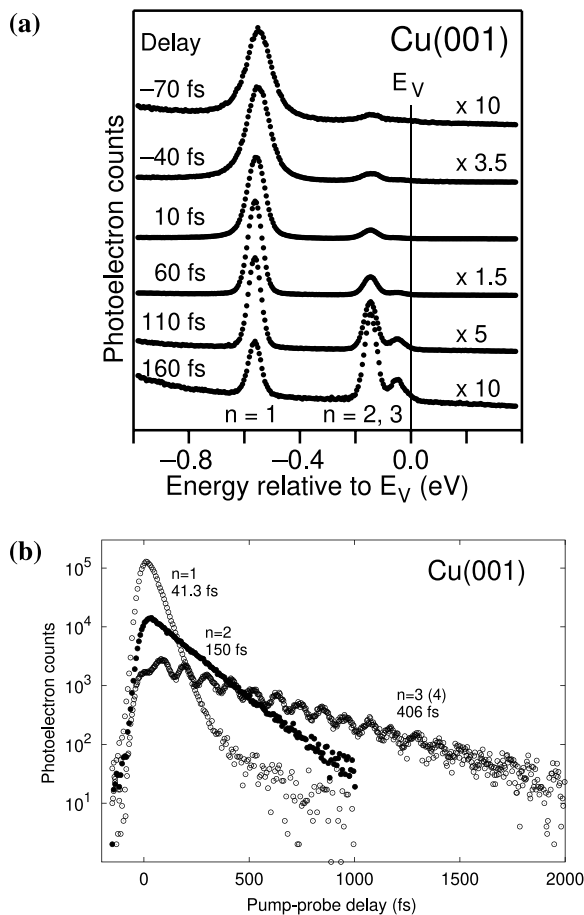
(a)

(b)

Fig. 3. Energy- and time-resolved 2PPE from image-potential states on Cu(001). (a) Series of spectra for various pump–probe delays. The spectra are approximately normalized to the same maximum peak height by the factors given at the right. (b) Traces as a function of pump–probe delay at the energies of the $n = 1, 2, 3$ image-potential states on a semilogarithmic scale. The linear slope indicates an exponential decay with lifetimes increasing with quantum number n.

elastic. Detailed studies showed that inelastic processes are attributed to electron–electron scattering [11] while the elastic processes occur in scattering by defects [12] or steps [13].

Image-potential states can be resolved on metal surfaces without band gaps in the projected bulk band structure [14] or on semiconductor surfaces [15]. The knowledge acquired from studies on clean metal surfaces can be transferred to adsorbate or adlayer systems relevant in many areas of surface science.

3. Hot carrier relaxation and thermalization in graphene and graphite studied with time- and angle-resolved photoemission

Michael Bauer

3.1. Introduction

Due to its layered structure and simple band structure, graphite can be considered as model system for the study of hot carrier relaxation in interaction with a two-dimensional electronic environment. With the first unambiguous production of graphene [16], which in simple terms can be described as a single, one-atom-thick layer of graphite, this topic became even more interesting: a thorough microscopic understanding of the dissipative electronic processes in graphene and its parent compound can provide important insights into the unique electronic and optical properties of this fascinating material. In particular, one is interested in the ultrafast carrier dynamics near the Fermi energy E_F at the K-points (H-points) of the Brillouin zone, where low-energy excitations in graphene (graphite) resemble relativistic Dirac fermions [17,18]. In this context, all-optical time-resolved spectroscopies have in recent years provided valuable insights into the involved mechanisms and their relevance [19–22]. However, these techniques are indirect as they often mix initial and final state contributions and, in particular, do not provide momentum resolution.

In contrast, the capabilities of time-resolved photoemission enable one to probe in an exceptionally direct way the ultrafast dynamics of electronic excitations with energy and momentum resolution. These techniques have 'the potential to directly provide the out-of equilibrium single-particle spectral function, the statistical distribution of the carriers, and its time evolution' [23]. It is therefore not surprising that time-resolved 2PPE was used to investigate the decay dynamics of photoexcited charge carrier in graphite already shortly after it had become an established technique in surface science [24,25]. However, the low photon energies available in these two pioneering studies limited the accessible momentum range to values close to the Γ-point: The time-resolved 2PPE signal only provided indirect access to the relevant electronic states near $\overline{K}$ most likely via quasi-elastic scattering into the accessible momentum range.

The development of high harmonic generation (HHG) sources, which deliver short photon pulses in the extreme ultraviolet spectral range [27,28], and their combination with state-of-the-art angle-resolved photoemission (ARPES) [29,30] considerably extended the photoelectron kinetic energy range available for time-resolved photoemission experiments. This finally made it possible to access electronic states at the boundary of a typical Brillouin zone or even beyond [31–34]. The first time-resolved ARPES (tr-ARPES) studies on graphene and graphite were published in 2013 [23,35,36] and numerous other tr-ARPES results on the dynamics of hot charge carriers in these materials have subsequently been published. In the following, the main experimental and theoretical findings on the different processes and mechanisms involved in the relaxation of hot charge carriers and their characteristic time scales are comprehensively summarized. The focus is on how this general picture has been formed or confirmed from the results of the various tr-ARPES studies.
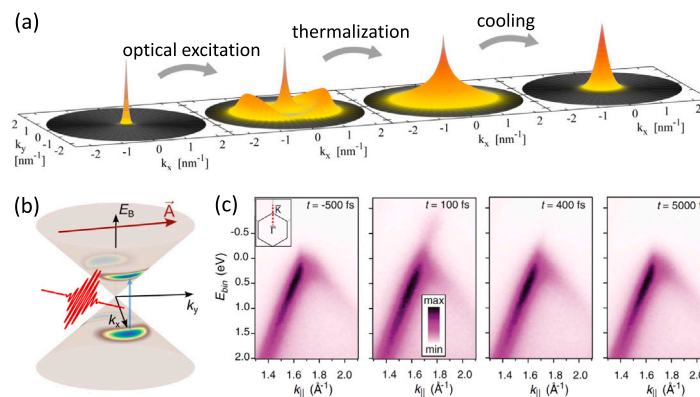
2 state with its longer lifetime to the $n = 1$ state at times when the initial population of the $n = 1$ state with a shorter lifetime has already decayed. Such interband scattering processes can be inelastic or

Fig. 4. Photoexcitation and carrier relaxation dynamics in graphene and graphite. (a) Illustration of the sequential steps: Optical excitation of the carrier system generates an anisotropic non-equilibrium distribution. Carrier–carrier and carrier–phonon interactions drive the electron system towards an FD-distributed electron system (internal thermalization). The cooling of the electron gas is due to thermalization with the phonon bath. (b) Illustration of the photoexcitation process within the Dirac cone with linearly polarized light. The red arrow indicates the direction of polarization. The absorption of the polarized laser pulse leads to an non-equilibrium energy distribution and to an anisotropic moment distribution due to pseudospin selection rules. (c) Carrier relaxation within the Dirac cone of graphene as probed using tr-ARPES. (a) adapted from [26], copyright IOP Publishing. Reproduced with permission. All rights reserved, (b) courtesy of H. Beyer, (c) reprinted figure with permission from [23]. Copyright (2013) by the American Physical Society.

3.2. Results

Fig. 4(a) schematically illustrates the sequential steps of excited carrier relaxation within the Dirac cone of graphene (and graphite) after the absorption of a linearly polarized ultrashort light pulse in the near-infrared to visible spectral region. The optical excitation initially generates a non-equilibrium carrier distribution characterized by a distinct deviation from the Fermi–Dirac (FD) distribution and an angular population anisotropy in momentum space [see Fig. 4(b)]. The latter is due to sub-lattice pseudospin selection rules for vertical interband transitions within the Dirac cone and can, therefore, be associated with an (optically induced) pseudospin polarization [37]. The recovery of a complete thermal equilibrium state within the graphene layer involves in a first step the (internal) thermalization of the photoexcited carrier distribution and in a further step its cooling by interaction with the lattice until finally electronic and lattice subsystems have reached the same temperature. Over the last two decades various experimental and theoretical studies could provide a comprehensive and quantitatively consistent picture on the details of the individual steps, the relevant interactions, and the characteristic time scales. The tr-ARPES data of graphene shown in Fig. 4(c) give an idea of how this technique could contribute to answering these questions: It is capable of directly mapping the changes in the distribution of hot carriers and their relaxation pathways within the Dirac cone in energy–momentum space.

3.2.1. Internal thermalization

Energy relaxation. The internal thermalization of the nascent carrier distribution restores both a FD distribution and an isotropic momentum distribution. Interestingly, the two processes are driven by distinctly different interactions and therefore take place on experimentally distinguishable time scales [40,41]. The formation of the FD distribution is governed by carrier–carrier interactions via (nearly) collinear scattering processes along the Dirac cone, which hardly affect the momentum distribution of the hot carriers. This process is extremely efficient, so that non-thermal contributions in the energy distribution of the excited carriers disappear on exceptionally short time scales. Detailed investigations of this process therefore rely on experimental setups that offer a time resolution in the range of 10 fs or even below. Fig. 5(a) shows energy distribution curves as a function of time delay evaluated from tr-ARPES data of graphite recorded with a 10 fs-tr-ARPES setup [38]. The data clearly reveal the non-equilibrium character of the hot charge carrier distribution right at time zero and its complete disappearance within 50 fs after photo excitation. In another study (of graphene) conducted with a very similar experimental setup, further

details of the involved interaction processes could be uncovered [42]. By comparing the temporal evolution of the number of conduction band electrons and their average kinetic energy, the authors were able to show that the initial internal energy redistribution among the excited charge carriers is dominated by impact ionization processes rather than Auger heating, in qualitative agreement with results of an high-time resolution all-optical study [21].

Momentum relaxation. The isotropization of the nascent momentum distribution relies on interactions that redistribute the charge carriers over the Dirac cone, i.e. it relies on non-collinear interactions that are associated with a finite momentum transfer. The most important mechanism here is the scattering of the hot charge carriers with optical phonons at Γ and K yielding characteristic time scales for the decay of the momentum anisotropy (and the associated pseudospin polarization) of several 10 fs [41]. This view has been experimentally confirmed *e.g.* by polarization-dependent all-optical pump–probe studies [22]. However, the momentum resolution of tr-ARPES is required to directly map the momentum anisotropy within the Dirac cone and its decay: Fig. 5(b), taken from Ref. [39], shows two-dimensional momentum maps of the carrier population in the Dirac cone of graphene at the energy of the nascent carrier population in the conduction band at different time delays. Near time zero (−25 and +60 fs), a momentum anisotropy in the charge carrier distribution is clearly visible. It is caused by the excitation with a laser pulse that is linearly polarized along the x-direction. 175 fs after the excitation this anisotropy is not seen any more (the lack of photoemission intensity in and near the $-k_x$-direction does not reflect the momentum anisotropy, but is due to photoemission matrix element effects and is also referred to as 'dark corridor' [43]). Tracking the decay of the momentum anisotropy with sufficient time resolution, a characteristic momentum isotropization time (pseudospin decay time) of about 40 fs has been reported [44]. It should be noted, however, that also (non-collinear) carrier–carrier scattering can to some extent contribute to the loss of pseudospin polarization [26]: Experimentally, this has just recently been demonstrated in a fluence-dependent tr-ARPES study, which showed that the decay of the momentum anisotropy slows down, when the laser-pump excitation fluence is reduced [45].

Interestingly, the partial decoupling of energy and momentum relaxation on ultrashort time scales also results in a momentum anisotropy in the electron temperatures (as deduced from fits of FD functions to the charge carrier distributions at different momenta within the Dirac cone) [39,44]. This effect is quite pronounced and can lead to transient differences in the electron temperature within the Dirac cone of up to several 100 K.
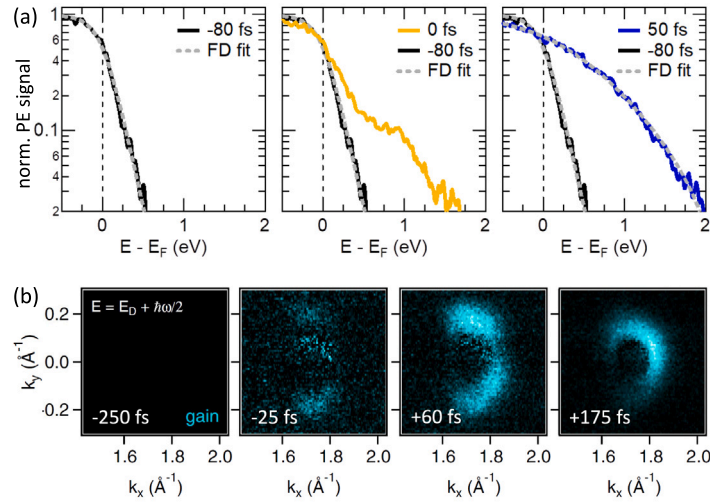
Fig. 5. Non-equilibrium distribution and momentum anisotropy in the Dirac cone, investigated with tr-ARPES. (a) Energy distribution curves at different delays near time zero. The dashed lines show the results of fitting a FD function to the experimental data before time zero and 50 fs after time zero. (b) Carrier momentum distribution at the energy of the nascent carrier distribution near time zero. The polarization of the excitation laser pulse is aligned along the k_x axis. The residual signal anisotropy at +175 fs is due to photoemission matrix elements. (a) Reprinted figure with permission from [38]. Copyright (2018) by the American Physical Society, (b) Reprinted figure with permission from [39]. Copyright (2017) by the American Physical Society.

Direct signatures of the interaction of the photoexcited carriers with the relevant optical phonons in graphite could be detected with a tr-ARPES setup designed with specific emphasis on energy resolution and using a high repetition cavity-based HHG source [46]. In the study, well-separated spectral side peaks accompanying the nascent non-thermal peak in the electron distribution were observed. The former appear at an energy of about 165 meV below the nascent electron peak. This value corresponds exceptionally well to the energy of the optical phonon mode at K relevant for the decay of the momentum anisotropy. The side peaks are therefore indicative for intervalley scattering processes from K to K'. In a combined tr-ARPES/time-resolved Raman scattering study, it was furthermore shown that the hot charge carriers indeed couple predominantly to the optical phonons at K. The optical phonon branches at Γ are mainly populated indirectly (delayed by about 65 fs) via phonon–phonon coupling [47].

3.2.2. Electron–lattice thermalization

Even though momentum isotropization involves electron–phonon interactions, yet, the electronic and lattice systems are still out of equilibrium. The further energy and momentum exchange between these two subsystems can in principle occur via direct coupling of carriers to the optical phonon bath and direct coupling to the acoustic phonon bath. Pioneering THz time-domain spectroscopy experiments on graphite implied very early that coupling to selected optical phonons is particularly strong as long as the hot carrier temperature exceeds the temperature of the optical phonons [19]. This was later supported by the findings on the decay of the pseudospin polarization discussed above. It is this process that is expected to dominate the heat exchange between carrier and lattice system after excitation with near-infrared or visible wavelength: The coupling to the acoustic phonon bath is in the first instance considerably suppressed due to momentum mismatch [48]. However, as first proposed in a theory work by Song et al. [49] and confirmed experimentally in transport measurements [50] and an all-optical pump–probe study of graphene [51], the situation can be more complex in the presence of defects: Defect centers can act as an additional source of momentum, weakening the constraints of momentum conservation for direct heating of the acoustic phonon bath through interaction with the excited charge carriers. At sufficient high defect densities, this channel can even equally contribute to the electron–lattice heat exchange speeding up the rate at which both subsystems equilibrate. We are therefore faced with two limiting cases describing electron–lattice thermalization in graphite and graphene,
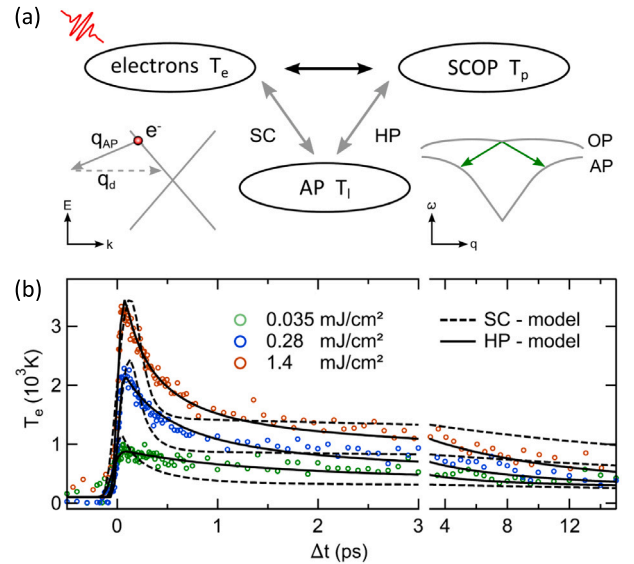

Fig. 6. Cooling of the electron gas: thermalization with the lattice. (a) Schematic representation of possible electron–phonon coupling channels for the cooling of hot charge carriers. Supercollision (SC) scattering processes (left) allow overcoming the intrinsic momentum imbalance q_d in the direct coupling between hot carriers and acoustic phonons (AP), where q_{AP} is the acoustic phonon momentum. In the hot-phonon (HP) scenario (right), coupling to the lattice involves optical phonons (OP) that decay into low-energy APs through anharmonic coupling (green arrows) (b) Experimental electron temperature transients for different fluences compared to fits to the data based on a three-temperature model (dashed line: SC model; solid line: HP model). *Source:* (a) and (b) reprinted figures from [35] with permission.
© 2015 by the American Physical Society.

which are schematically illustrated in Fig. 6(a): For low-defect samples carrier–lattice interaction is almost exclusively mediated by carrier-optical phonon interaction. The heating of the acoustic phonon bath is finally achieved by anharmonic coupling to the optical phonon bath. This scenario is also referred to as hot phonon assisted (HP) process. For high defect densities the carriers couple via both channels efficiently to the lattice. This scenario is referred to as supercollision (SC) model to account for the promotion of heat exchange by the defects. Through targeted manipulation of the defect density it is indeed

possible to gradually tune between these two limiting cases [51]. Both, HP- and SC-type behavior could also be observed in tr-ARPES studies. In a study of hydrogen-intercalated quasi-free-standing graphene a fit of a three-temperature model to electron temperature transients [52] evaluated from tr-ARPES data clearly showed that the carrier–lattice thermalization occurs in a SC-mediated process [23]. In a study of graphite (highly ordered pyrolitic graphite), a corresponding analysis of the data showed that the heating of the lattice can only be described consistently with an HP process [see Fig. 6(b)] [53].

3.3. Summary and outlook

Thanks to comprehensive theoretical and experimental efforts, we have now achieved a detailed and quantitative understanding of the microscopic processes involved in the relaxation of the nascent carrier distribution in graphene and graphite initially generated by ultrafast optical excitation. As probably the most direct probe to study electronic excitations in energy–momentum space, tr-ARPES has contributed substantially to this impressive achievement. However, this in no way means that this material class has lost its appeal as a fertile playground for ultrafast spectroscopies. On the contrary, the many fascinating properties of graphene in combination with flexible tuning capabilities, *e.g.* in stacking 2D quantum materials on demand [54], open up a wide range of possibilities for addressing fundamental questions in the context of light-driven and non-equilibrium processes in low-dimensional systems. Recent examples clearly show that tr-ARPES could and will be an indispensable tool and a key player in this concert. These include phenomena such as the renormalization of quasiparticle self-energies under nonequilibrium conditions [55,56], electronic structure manipulation via Floquet engineering [57–59], carrier and charge transfer dynamics in 2D homo- and heterostructures [60–62], and light-field-driven Landau–Zehner–Stückelberg interferences [63].

4. Femtosecond solvation dynamics of Cs^+ ions at solid interfaces

Uwe Bovensiepen and Karina Morgenstern

4.1. Electron transfer and solvation dynamics at interfaces

The interface of a solid electrode with a liquid electrolyte is a fundamental problem in physical chemistry. It is characterized by the formation of two layers of opposite polarity leading to an electrical double layer addressed early on in the 19th century by Helmholtz [64] by an electrostatic model of a dielectric interface. Nowadays, the complexity of the problem, including microscopic interactions of the solvent molecules, the ions, and electrode interface, is well established. In the liquid electrolyte, diffusion of the ions is very important in addition. It forms the foundation of various energy conversion applications which are widely used in daily life. For an overview see Refs. [65,66].

Dedicated developments like photoelectron emission spectroscopy operating under near ambient conditions made remarkable contributions towards a comprehensive understanding of the electrical double layer [67]. Complementary efforts following a bottom up approach using well established surface science techniques under ultrahigh vacuum conditions analyze the microscopic interactions at such interfaces in a rather selective manner. Recent results of studies based on low temperature scanning tunneling microscopy and non-linear photoelectron emission spectroscopy with femtosecond time resolution gave very detailed insight into the cooperation and/or competition of the local interactions. The interfaces investigated are essentially solid structures formed from ions and solvent molecules adsorbed at sufficiently low temperature on single crystal metal surfaces to form stable structures. Thereby, the surface represents the electrode and the ion-solvent adsorbates the electrolyte. The adsorbed structures that exemplify the electrolyte consist of ions and the solvent. In this contribution, we focus
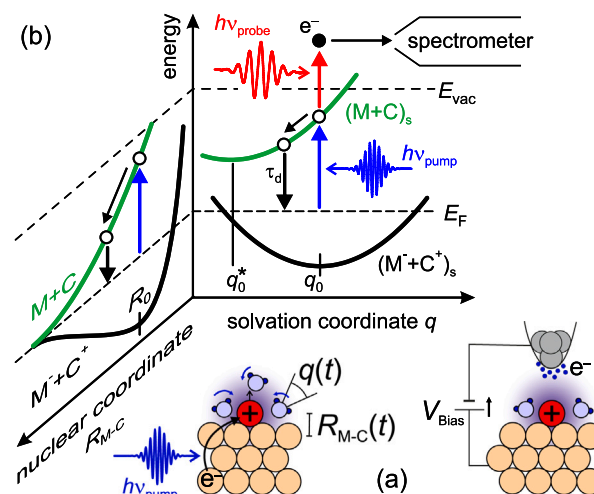

Fig. 7. (a) At the left, the solvated alkali cation on the metal surface is illustrated with R_{M-C} being the distance of the ion core to the metal surface and q the solvation coordinate. Optical excitation by $h\nu_{pump}$ induces electron transfer from the metal to the unoccupied valence resonance of the cation. At the right, this surface is sketched as part of a tunnel junction with an applied bias voltage in a scanning tunneling microscope. (b) Total energy of the neutral alkali C (alkali cation C^+) adsorbed on a surface of a metal M (M^- for an ionized alkali upon adsorption of a neutral alkali). The diagram depicts the projection of a schematic two-dimensional potential energy surface along two coordinates R_{M-C} and q, see (a), representing the ion substrate distance R_{M-C} and a solvation coordinate q. Femtosecond laser pulses $h\nu_{pump}$ and $h\nu_{probe}$ combined with photoelectron spectroscopy allow us the analysis of the population evolution on the multidimensional potential energy surface and of the time-dependent interaction with the electrode surface.

on Cs^+ cations on Cu(111) single crystal metal surfaces coadsorbed with Xe and D_2O as examples for non-polar and polar solvents, respectively.

Alkali ions on metal surfaces are widely investigated in surface science. Already in early investigations by Taylor and Langmuir the pronounced lowering of the work function of a tungsten substrate upon adsorption of Cs has been attributed to the transfer of the alkali valence electron to the metal substrate leaving a cation on the surface [68]. This understanding prevails for sufficiently low coverage of adsorbed alkalis at which the mutual interaction between the alkali on the metal surface is absent [69–73]. Upon adsorption of neutral Cs the 6s valence electron is transferred to the metal substrate inducing the bonding of the remaining Cs^+ cation to the metal surface. In detail, the charge transfer is considered to be slightly smaller than 1 e^- due to back-donation effects. In the experiments, the preparation of alkali cations proceeds by evaporating neutral atoms from commercial getter sources onto the metal surface on which the ionization forms spontaneously.

The charge transfer induces an unoccupied resonance in the electronic structure at the interface whose ultrashort lifetime has generated widespread interest in ultrafast surface dynamics. It appears in two-photon photoemission spectroscopy (2PPE) as a very pronounced spectral feature [71,74,75].

Fig. 7(a) depicts the adsorbed cation on the metal surface with the distance of the ion core to the metal R_{M-C}. Optical excitation by a photon energy $h\nu_{pump}$ in resonance with the Fermi energy E_F of the metal as an initial state and the unoccupied valence electron resonance as an intermediate state in 2PPE induces electron transfer across the interface: $M^- + C^+ \rightarrow M + C$. An electron can also be transferred to the ion in a tunnel junction which is part of scanning tunneling microscope as depicted at the right. The corresponding electronic excitation transiently neutralizes the ion within the lifetime of the resonance τ_d. Importantly, it also weakens the ion-metal bonding, inducing nuclear wave packet dynamics along R_{M-C} since the final state is an antibonding potential energy surface [76], as illustrated in Fig. 7(b) at the left along the nuclear coordinate R_{M-C}.

In a next step, we consider a solvent coadsorbed with the alkali ions on the surface to be similar to an electrolyte. The solvent polarizes the environment of the alkali cation on the surface which can be described by a rotation of the solvent dipole by an angle q in polar solvents like water or ammonia. In non-polar solvents the solvation coordinate q describes the local charge redistribution in the solvent. The charge transfer excitation in the solvated case $(M^- + C^+)_s \rightarrow (M + C)_s$ launches a dynamics also along q. The dynamics evolves therefore along two coordinates R and q. It is important to realize that the excitation starts from the stable ground state solvent coordinate q_0 representing an energy minimum of the potential energy surface $(M^- + C^+)_s$. It reaches the potential energy surface $(M + C)_s$ at an unfavored solvation coordinate in a vertical transition, leading to an energy gain with the evolution to q_0^* in this excited state potential. The dynamic response along the solvation coordinate prevails, while the electron transfer $(M^- + C^+)_s \rightarrow (M + C)_s$ weakens the solvation since an electron is attached to the cation, neutralizing it.

To probe the dynamics in the time domain, a second femtosecond laser pulse is spatially and temporally overlapped with the first one. The relative time delay of both pulses is varied to analyze the evolution as a function of time. Such a time-dependent 2PPE experiment employs the pump–probe concept with the advantage of a weak background in the 2PPE signal due to its non-linear character [77]. The probe pulse photon energy $h\nu_{probe}$ is chosen (i) to be below the surface work function Φ to avoid linear photoelectron emission contributions and (ii) to obtain a favorable photoemission matrix element at such final states only few eV above the vacuum level E_{vac}. The experimental data reported in this contribution was obtained by a non-collinear 2PPE autocorrelation measurement with $h\nu_{pump} = h\nu_{pump} = 3.1\,eV$ which is provided by the second harmonic of a Ti:sapphire amplifier.

From a surface science point of view, it is – more or less – obvious that the atomic/molecular structure of surfaces is linked to the dynamics. It is therefore essential to provide a comprehensive analysis of the surface structure [78]. Following earlier work [79–81], the authors continued their collaboration on the topic of ion solvation at surfaces presented here.

Here, we report on results obtained for one non-polar and one polar solvent coadsorbed with Cs on Cu(111) to focus on the effect of two qualitatively different solvents. Although non-polar solvents like benzene and alkanes are well established, we decided to study xenon as a non-polar solvent [82] because of its large atomic polarizability and the expected pronounced effects. As a polar solvent, we studied water as the most abundant one.

The experiments were performed in two different laboratories dedicated to low temperature scanning tunneling microscopy (STM) at the Ruhr University of Bochum and time-resolved photoelectron spectroscopy at the University of Duisburg–Essen. The sample preparation routines were coordinated between the two teams and the surfaces prepared in the two laboratories are comparable to each other. The Cu(111) surfaces were prepared by sputter-anneal cycles. The Cs atoms were deposited at $T = 200\,K$ from commercial Cs dispensers (SAES getters). STM images were recorded at 8 K; 2PPE spectra were taken at 25 K and/or 80 K. The alkali coverage was determined by counting the ions on the Cu(111) surface using STM and an analysis of the work function in 2PPE [69,70]. For further details on the sample preparation, we refer to the corresponding original publications [83–85].

4.2. $Cs^+/Cu(111)$ coadsorbed with Xe as a non-polar solvent

Xenon interacts with metal surfaces by van der Waals interaction. The first monolayer (ML) desorbs from Cu(111) at 82 K [83]. Adsorption of Xe at a coverage $\Theta_{[Xe]} \leq 1\,ML$ on a Cu(111) surface with pre-adsorbed Cs^+ ions results in a carpet-like growth of Xe wetting $Cs^+/Cu(111)$ and forming a regular hexagonal structure. As concluded from protrusions observed by STM within and at the perimeter of Xe aggregates on $Cs^+/Cu(111)$, see Fig. 8(a), the xenon aggregates provide
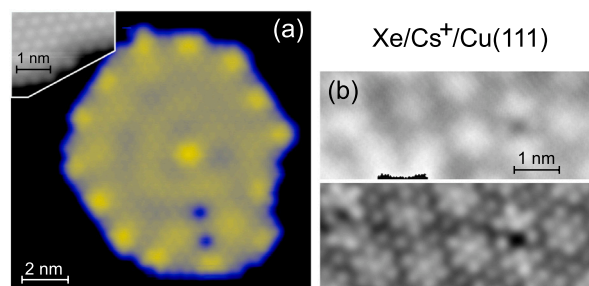

Fig. 8. STM images (a) of a Xe-Cs aggregate adsorbed on Cu(111) using a false-color scale, tunneling current $I = 10\,pA$ and voltage $V = -25\,mV$. The inset shows an aggregate border at 1 ML Xe/Cu(111), $I = 44\,pA$ and $V = 7\,mV$. (b) Original (top) and Laplace filtered STM image (bottom) of 1 ML Xe on top of 0.16 ML $Cs^+/Cu(111)$, $I = 89\,pA$ and voltage $V = 250\,mV$.
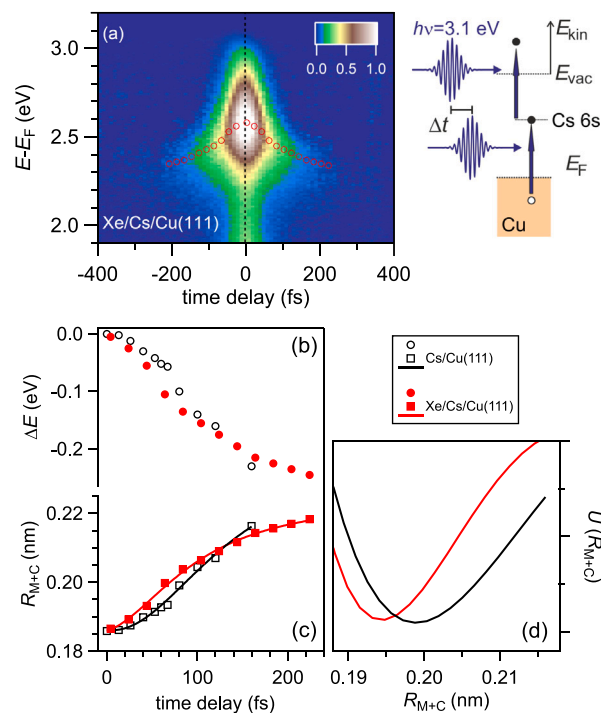*Source:* Original figure published in Ref. [86].

Fig. 9. (a) 2PPE intensity of 1 ML Xe/0.16 ML Cs^+ / Cu(111) at $T = 30\,K$ in a false color representation as a function of $E - E_F$ and time delay. The time-dependent energy of the Cs $6s$ feature is indicated by red circles. (b) Time-dependent change of intermediate state energy ΔE plotted for Xe/Cs^+/Cu(111) from panel (a) and for bare Cs^+/Cu(111) using data from Ref. [87]. The respective distances R_{M+C} and the excited state potential energy surface $U(R_{M+C})$ are determined with (red) and without (black) coadsorbed Xe.
Source: Original figure published in Ref. [86].

favorable, localized sites for the alkali ions which are as individual ions mobile on the bare Cu(111) surface. As recognized from the center protrusion in Fig. 8(a), a Xe heptamer is formed when the Xe aggregate covers an adsorbed Cs^+. By adsorbing a full ML of Xe on a larger Cs^+ coverage $\Theta_{Cs} = 0.16\,ML$, a higher density of such heptamers were generated forming a regular homogeneous superstructure which is depicted in Fig. 8(b).

Such surfaces were analyzed by femtosecond time-resolved 2PPE experiments. Fig. 9(a) shows the intensity of a 2PPE intensity autocorrelation measurement using a photon energy $h\nu_{pump} = h\nu_{probe} = 3.1\,eV$ in a false color representation. The 2PPE spectrum is characterized by a pronounced resonance which originates from the above-mentioned electron transfer to the Cs $6s$ resonance on Cu(111) occurring 2.5 eV

above the Fermi energy E_F of the Cu(111) surface. From these measurements two observables are extracted. First, the relaxation time of the electron transfer resonance accounts for the electron transfer back to Cu(111) [71]. To determine these relaxation times, we integrate the spectrum within 200 to 150 meV. As a function of time, these integrated intensities are characterized by a single exponential decay [68], yielding relaxation times of (13 ± 3) fs and (80 ± 10) fs for $Cs^+/Cu(111)$ and for 1 ML $Xe/Cs^+/Cu(111)$, respectively. See Ref. [86] for details. Xe adsorption increases the relaxation time six-fold which implies that Xe reduces the interaction strength of the Cs $6s$ resonance with Cu(111) strongly. The second observable is the time-dependent energy of the electron transfer resonance, which is depicted by open red circles in Fig. 9(a). For bare Cs^+ on Cu(111), a very similar time-dependent energy was reported earlier [87] which is replotted in Fig. 9(b) by open black circles. This effect was explained by an energy transfer to the nuclear motion of Cs^+ along the normal coordinate R_{M+C} [76,87] as depicted in Fig. 7. Following Ref. [87], the time-dependent energy was used as an input to quantify R_{M+C}, to infer the excited state potential $U(R_{M+C})$, and how it is changed by the adsorption of Xe, see Fig. 9(c) and (d), respectively. Upon Xe adsorption, the potential minimum shifts (4.0 ± 1.5) pm closer to the Cu(111) surface.

These experimental findings establish that upon Xe coadsorption the electronic interaction of the wavefunction Ψ_{6s} of the electron transfer resonance with Cu(111) is reduced while the ionic interaction of the Cs^+ ion core with Cu(111) is increased. These effects are explained as follows. The Xe layer has a repelling effect to Ψ_{6s} away from the metal surface, a phenomenon known from lifetime studies of image potential states [88–90]. The presence of Xe between two Cs^+ ion cores on Cu(111) induces an effective attraction of the two ions, see Ref. [86] for details. Similarly, it is concluded that Xe mediates an attraction between the Cs^+ ion core and the Cu(111) surface. Essentially, this study showcases the importance of the Coulomb interaction in the context of Xe coadsorption where the electron cloud of the Xe atoms has an attractive interaction with the positive ion core of the cation while it repels the electronic wavefunction of its excited state. It is important to emphasize that this behavior is specific for the metallic surface. In the gas phase, the Cs^+-Cs^+ repulsion is much larger than the energy gain induced by the presence of Xe. On the metallic surface, the Cs^+-Cs^+ repulsion is reduced an order of magnitude and, then, the attractive interaction mediated by Xe becomes dominant [86].

4.3. $Cs^+/Cu(111)$ coadsorbed with D_2O as a polar solvent

As an example for a polar molecular solvent, we analyzed water D_2O coadsorbed with Cs^+ on Cu(111). Water is very important in life in general. Metal–water interfaces are key in electrochemistry and a challenging model system for liquid–solid interfaces, as introduced above in the context of the electrical double layer. The key questions we target in this work is how water modifies the interactions at the alkali–metal interface. We follow the same scientific approach presented in Section 4.2. To analyze the structure on a molecular and atomic level, we use low temperature STM; to study the dynamics of electronic phenomena, we use femtosecond time-resolved 2PPE. Here, we show that it is very important to have access to such complementary insights in order to develop a comprehensive understanding.

Fig. 10 shows in panels (a) and (b) STM images for lower and higher numbers of water molecules per Cs^+ on Cu(111). Panel (a) is characteristic for the initial hydration of the surface exhibiting inhomogeneous structures. At the left side unperturbed, regularly ordered Cs^+ ions are found as for bare $Cs^+/Cu(111)$, shown in the inset. In other parts, considerably larger protrusions are present as indicated, e.g., by the black circle. Increasing the water coverage to approximately 10 water molecules per Cs^+ ion, see panel (b), the surface appears more homogeneous although the lateral particle size varies considerably. We assign it to a variation of the number water molecules attached to an ion. Upon increasing the temperature to 50 K the particles become
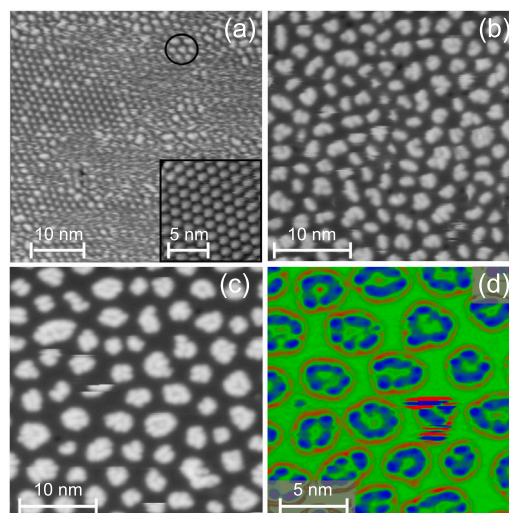

Fig. 10. Scanning tunneling microscopy of Cs^+ ions coadsorbed on Cu(111) with D_2O. (a) Initial hydration; circle surrounds some of the larger clusters. Inset: bare $Cs^+/Cu(111)$. (b) STM image of hydration at approximately ten D_2O molecules per Cs^+ ion. (c) Ten D_2O molecules per Cs^+ ion annealed at 50 K for 15 min. (d) STM image of a coverage similar to (c), Laplace filtered on a false-color scale. Tunneling parameters: (a) $V = -250$ mV, $I = 10$ pA; (b) 53 mV, 7.5 pA; (c) 40 mV, 7.5 pA; (d) 100 mV, 10 pA.
Source: Original figure published in Ref. [84].

more mobile and forms larger clusters, see Fig. 10(c). Panel (d) depicts similar data on a false color scale and spatially enhanced. Based on calculations of the interaction energies among different water molecules, between the ion and water, and the metal and the ion, we conclude that hydrogen bonds between water and water–ion interaction compete on the metal surface for the rather large Cs^+ ion. As a result, typical bulk solvation structures, in which the solvent molecules arrange around the solute, differ on the Cu(111) surface. Since the water–water interaction is dominant, the ion cores are surrounding the water constituents, a situation which we term "inside-out" solvation of Cs^+ on Cu(111) [84].

In order to analyze the electron dynamics at these interfaces, we prepared such surfaces at $T = 80$ K and investigate the static, unoccupied electronic states as a function of the number of water molecules per Cs^+ which we term ρ. The water coverage was determined by thermally programmed desorption experiments and the alkali coverage was concluded from the change in work function. The ratio of these two quantities determines ρ, see Ref. [84]. Since these two methods provide spatially averaged information, ρ is a spatially averaged quantity as well. In 2PPE spectroscopy, we distinguish two spectral signatures which coexist for $2 < \rho < 4$. The one signature at higher energy, i.e., further from the Fermi energy of Cu(111) E_F, is attributed to bare $Cs^+/Cu(111)$ sites, c.f., Fig. 10(a). The second signature is 300 meV lower in energy and originates from sites with D_2O attached to $Cs^+/Cu(111)$; see Ref. [84] for details. These spectral features represent an electron transfer across the interface to the Cs $6s$ resonance in a different environment. Following the methodology presented for the Xe coadsorbed to $Cs^+/Cu(111)$, see above, time-resolved 2PPE was used to determine the electronic relaxation time and the energy transfer rate. For D_2O coadsorption, time-resolved 2PPE experiments were performed as a function of ρ.

Fig. 11 depicts in panel (a) the 2PPE intensity autocorrelation integrated within 1 eV energy width in order to include the electronic states at all energies which are transiently populated in the electron transfer process. See Ref. [85] for details. The autocorrelation traces for different ρ group into three different coverage regimes. The fastest relaxation is observed for $\rho = 0$; $0 < \rho < 2$ exhibit identical dynamics with slower relaxation, and the data for $3 < \rho < 7$ show the same
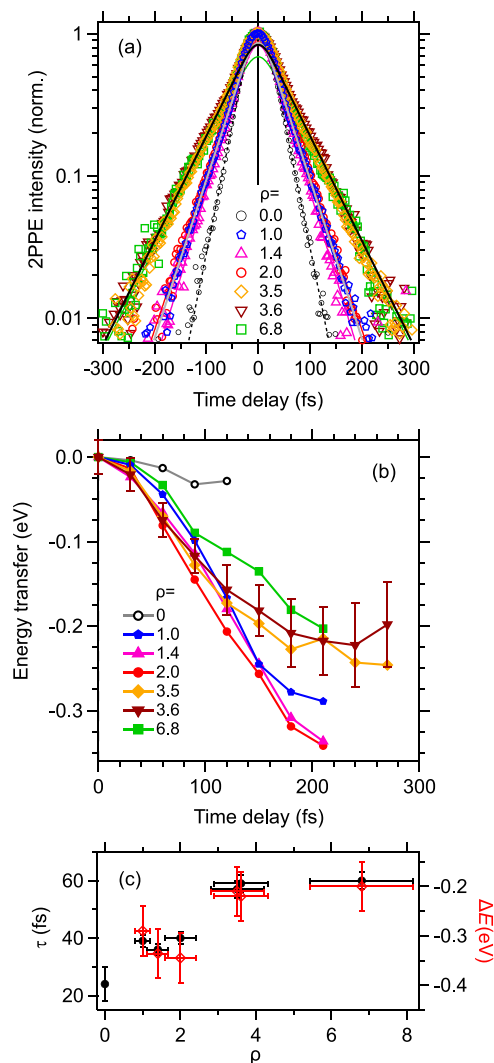
Fig. 11. The energy-integrated and time-dependent intensity of the 2PPE autocorrelation for different coverage ratio ρ is indicated by different symbols. $\rho = 0$ is a reference measurement for bare Cs^+/Cu(111) without coadsorbed water. Lines are the results of modeling the single-exponential decay with relaxation time τ convoluted with a Gaussian to describe the autocorrelation of the UV laser pulses. The gray line describes the data for $\rho = 1.0$, and the black line for $\rho = 3.5$. The color of further lines indicates ρ according to the legend. (b) Time-dependent energy transfer from the electronic to the nuclear degree of freedom determined from the energy shift of Cs 6s resonance in the time-resolved 2PPE spectra for different coverage ratios ρ. Data for negative and positive t are averaged. The vertical error bars indicated for $\rho = 3.6$ are representative for all ρ. (c) Filled black circles represent the relaxation times (left axis) as a function of ρ determined by the single-exponential decay fit to the data in (a). The value at $\rho = 0$ is a reference value representing the chosen data analysis by exponential decay times. Open symbols in red depict the energy transfer (right axis) of the Cs 6s resonance to nuclear motion taken from the data shown in (b) at a time delay of 210 fs .
Source: Original figure published in Ref. [85].

decay which is the slowest among the three intervals. All these autocorrelation traces indicate single exponential relaxation dynamics which broadens the autocorrelation traces at normalized intensities below 0.6. The corresponding exponential relaxation times were determined by fitting the autocorrelation traces using a Gaussian as the laser pulse autocorrelation function convoluted with a single exponential decay. The 2PPE autocorrelation traces indicate that the relaxation times characterizing the electron transfer process from the ion on top of the surface back to the metal substrate group into three different relaxation regimes with characteristic times τ for the three different intervals of ρ: $\tau \simeq 60$ fs for $3 < \rho < 7$; $\tau \simeq 40$ fs for $0 < \rho < 3$, and $\tau \leq 24$ fs for $\rho = 0$. The exact values are given in Fig. 11.

This observation indicates that the dynamics of energy transfer depends on the number of solvent molecules such that a larger ρ results in a weaker and slower energy transfer. Considering that we observe for $0 < \rho < 3$ a larger and faster energy transfer to the solvent than for $3 < \rho < 7$, we conclude that the larger ρ, which implies more water–water interaction known already to be decisive for the static solvatomer structure, hampers the dynamic energy transfer to the solvent. The hydrogen bonding water–water interaction has been found in calculations of the actual solvatomer structures on Cu(111) to set in at $\rho = 4$, see Ref. [85] for details. Therefore, we explain the delayed and reduced energy transfer to the solvent observed in Fig. 11(c) for $3 < \rho < 7$ by hydrogen bonding among the water molecules. It limits the molecular rearrangement along the solvation coordinate q and delays the solvent response to charge transfer, *c.f.*, Fig. 7.

Clearly, the three coverage regimes in the energy transfer dynamics occur in both dynamic observables, the relaxation time and the energy transfer, as shown on both ordinates in Fig. 11(c). This finding raises the question of the microscopic origin of the identified step-like coverage dependence between $\rho = 2$ and 4. A detailed analysis of the probability that clusters of a particular size are formed was done in a STM experiment under Cs^+ excess. The most abundant clusters, occurring with 89% probability, are assigned to one water molecule attached to Cs^+. The second most abundant species, 11% of the clusters, consist out of three water molecules per Cs^+. Clusters with two water molecules were not identified [85]. The step in the dynamics as a function of coverage ratio is therefore originating microscopically from the fast response assigned to clusters which consist of one water molecule attached to a Cs^+. The slower response is associated with clusters containing three water molecules attached to one Cs^+.

This overview has presented recent results of the correlation of structure and dynamics in the solvation dynamics of Cs^+ coadsorbed on Cu(111) with polar and non-polar solvents. In the following, we discuss concepts to generalize these studies to further ions and solvents, including metal–liquid interfaces.

4.4. Perspective

These studies showcase the close correlation of microscopic structure and ultrafast dynamics that is characteristic for such ion-solvent structures on surfaces. For a more comprehensive study, an analysis of the solvation dynamics of anions adsorbed on metallic surfaces in the presence of a solvent is desired. Such adsorbed anions are formed by the adsorption of halogen atoms on metal surfaces, conceptually very similar to the work reported in this contribution. However, the corresponding charge transfer resonances represent hole transfer and occur, therefore, several eV below the Fermi energy of the metal surface [91]. For the STM studies the analysis of hole transfer is straight forward by a change of the sign in the bias voltage, see Fig. 7. For the time-resolved photoelectron emission spectroscopy the analysis of hole transfer is, on the contrary, a fundamental challenge. The hole excitation has to be distinguished from the large number of photo-electrons emitted in linear photoemission stemming from the metallic substrate which is an experimental challenge. Recent developments, which exploit high harmonic generation in noble gases in time-resolved photoemission experiments [30], might facilitate such experiments in combination with sophisticated spectrometers that detect small pump-induced changes on a large background [92]. A further expansion of the experimental approach to molecular ions, differing from the elemental ions in their symmetry, charge state, and charge distribution might aid the fundamental understanding of a broader range of electrolytes.

In our study, we established that solvation and electron transfer dynamics of polar and non-polar solvents occur on very similar time and energy scales. The example of Xe as a non-polar solvent was chosen specifically due to its large atomic polarizability as a heavy noble gas atom with $Z = 54$. It is therefore a fundamentally interesting question

whether more typical non-polar solvents like benzene with $Z = 42$ exhibit similar electron transfer and solvation dynamics.

Under ambient conditions, which are highly relevant for energy conversion applications, the investigated structures are thermodynamically instable. Nevertheless, we expect that similar structural [72] motifs occur in electrolytes as thermal fluctuations on time scales which are orders of magnitude slower than the ultrafast electron transfer times. In this context, our fundamental investigations demonstrate that under ambient conditions no single and well-defined electron transfer time is existent that no single and well-defined electron transfer time exists under ambient conditions. Rather a manifold of transfer times which are determined by the transient fluctuating structural motifs at metal–electrolyte interfaces are to be expected.

Acknowledgments

5. Ultrafast dynamics of photostationary states in time-resolved photoemission

Julia Stähler and Lukas Gierster

5.1. Motivation: Steady state = ground state?

A great advantage of time-resolved photoelectron spectroscopy (PES) compared to optical techniques is the measurement of absolute binding energies and sensitivity to excited state populations that are not connected to optically allowed transitions from the ground state, as *e.g.* triplet states. PES is also surface sensitive, which is not the case for linear optical probes. In both spectroscopic techniques, large backgrounds resulting from stationary responses often complicate the detection of photoinduced spectral changes or modulations. To circumvent these issues, optical spectroscopists commonly measure differential time-resolved signals [93–95], *e.g.* using lock-in amplifiers. In the case of time-resolved PES, the photoelectron yield at a given energy (and momentum) is detected for a certain time delay. If the time-dependent modulation of the signal is too low compared to the steady state background to be recognized in a reasonable data representation, a common approach is to subtract the "negative delay spectrum" from the whole data set [96–100]. This procedure is based on the assumption that the signal at negative delays shows no correlation between pump and probe laser pulses[1], i.e. reflects the ground state response of the sample. For typical laser repetition rates in time-resolved PES in the kHz to MHz ranges, this translates to the assumption of excited state lifetimes significantly shorter than μs or ns. As, historically, time-resolved PES was initially primarily applied to metal surfaces or to alkali/metal or rare gas/metal systems [77,96,101–106], this assumption was absolutely justified. In the last decades, however, the investigated systems became more complex: molecular adlayers [98, 107–109], semiconductors [110–119], topological insulators and many more system types (see [120] and references therein) were investigated, demanding to revisit the assumption of excited state lifetimes shorter

than ns or μs if the "negative delay spectrum" is supposed to be subtracted as a background.

In this contribution, we show that – to our experience – the presence of long-lived states with lifetimes exceeding the inverse repetition rate of our 200 kHz laser system (i.e. 5 μs) is rather the rule than the exception. Among other phenomena, we observed trapped electrons [121–124], defect [125–127] and charge transfer excitons [128] as well as polarons in previous studies. The long lifetimes of these quasiparticles range from μs to several minutes and lead to photostationary signals in the steady state spectra. In other words, the time-dependent signal observed is actually often related to dynamics created by photoexcitation of an excited rather than the ground state, which needs to be considered when interpreting correlated signals on ultrafast timescales. We demonstrate simple tests for long-lived states and encourage critical examination of past and future works, as a startlingly large number of 80 % of the samples investigated in our group in the past 15 years exhibited photostationary states.

The following collection of very different examples for long-lived excited states is picked, on the one hand, to illustrate the breadth of material systems exhibiting such feature and, on the other hand, to highlight the scientific relevance of stationary states that do not equal the ground state of the system: photostationary states of matter have significant impact on various physical and chemical properties, ranging from the reactivity of water clusters to photoinduced insulator-to-metal-transitions.

5.2. Frozen hot electrons

The first observation of, at the time, "extraordinarily" long-lived states using time-resolved 2PPE spectroscopy is part of the PhD work of Cornelius Gahl, who investigated the transfer and solvation dynamics at D_2O/metal interfaces [129] under the guidance of Uwe Bovensiepen in the group of Martin Wolf. They initially found that after electron injection into the conduction band of *amorphous* ice, electrons localize dynamically in the aqueous environment and are stabilized by polarization of the surrounding molecular environment [130]. Being localized right in front of a metal surface, the non-equilibrium electron population decays on sub-ps timescales with decay constants initially dominated by the electronic structure of the metal substrate and later strongly influenced by the screening of the amorphous ice environment [131]. The dynamics, however, change dramatically upon crystallization of the amorphous ice: while electron injection still occurs via a delocalized state in the molecular adlayer, electrons are trapped at pre-existing orientational defect sites accompanied with an abrupt energy loss of more than 1 eV and a lifetime on minute timescales (*cf.* scheme in Fig. 12a). While, retrospectively, understanding of the 2PPE spectra may be straightforward now, the observation of a very dominant spectral signature (e_T) that vanished when the probe pulses hit the sample (*cf.* Ref. [129]) was very puzzling at the time. Gahl verified the astoundingly long lifetime of the excited state e_T by laser pulse duration-dependent measurements and developed the *pump-wait-probe* scheme (details below) to quantify the decay on macroscopic timescales. Among other findings, he discovered that the energetic stabilization of the trapped electron signal has not yet reached equilibrium, even minutes after the initial excitation (*cf.* Fig. 12b) and can be accelerated at higher temperatures (*cf.* Fig. 12c).

In later years, it turned out that, what appeared to be a peculiarity of crystalline ice, is a general phenomenon for frozen layers of common polar solvents: also thick *amorphous* ice layers [122], as well as ammonia (NH_3) [121,132] and dimethyl sulfoxide (DMSO) [123,124] adsorbed on Cu(111) show not only electron solvation dynamics on ultrafast timescales, but also electron trapping. The trapped electron state e_T shows, for all these systems, lifetimes on the order of several seconds to minutes. In all cases, it was determined using the *pump-wait-probe* scheme depicted in Fig. 13: initially, a train of laser pulses (*pump*) creates a photostationary population of the trapped electron
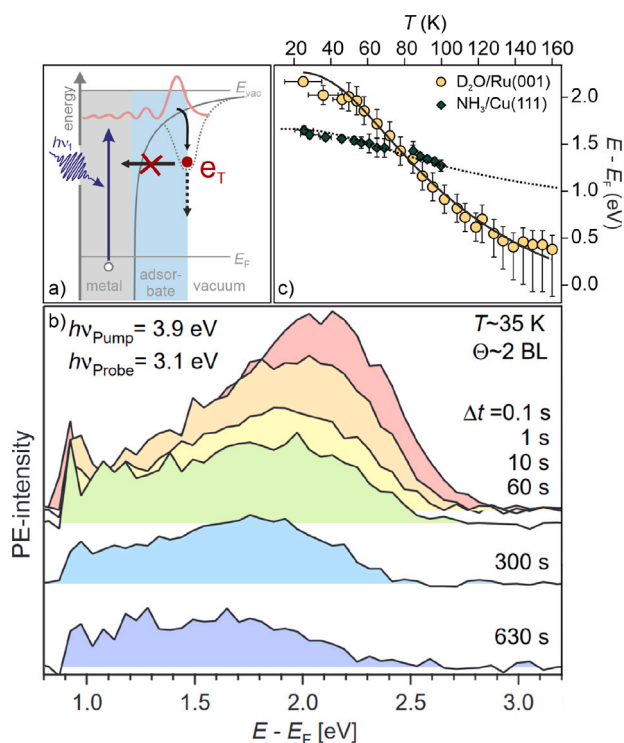

Fig. 12. Electron trapping in polar solvents on metal surfaces. (a) Illustration of the elementary steps: photoexcitation leads to charge injection into the adsorbate layer, followed by ultrafast electron trapping at pre-existing potential minima. As electron back transfer is suppressed, the trapped electrons e_T can undergo further stabilization on macroscopic timescales. (b) Stabilization dynamics and population decay on minute timescales of trapped electrons in $D_2O/Cu(111)$, adapted and modified from [129]. (c) Temperature-dependent stabilization of trapped electrons in D_2O and NH_3 crystallites. *Source:* Adapted and modified from [121].
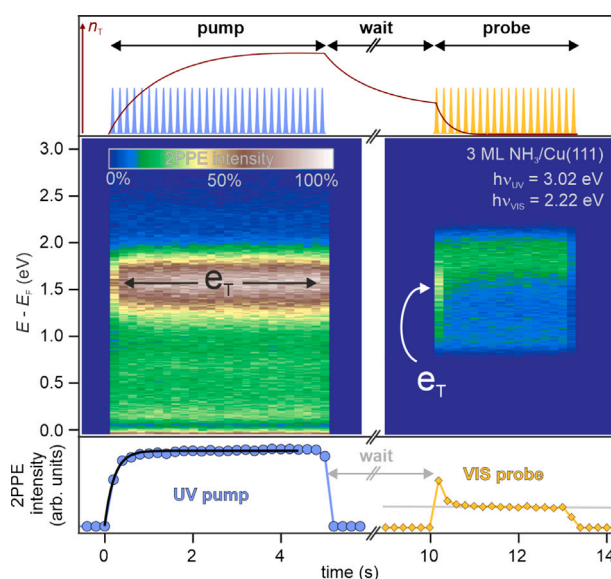

Fig. 13. Pump-wait-probe scheme for the detection of dynamics on macroscopic timescales. Pump: a train of pump laser pulses (blue) builds up a photostationary state. Wait: The sample remains in darkness and the electron population (red, top panel) decays. Probe: a train of probe laser pulses (orange) emits the remaining electron population. Center and bottom panel adapted from [121].

state that results from the population and depopulation probabilities of the pump photons. Subsequently, the sample is left in darkness (*wait*) for the desired, macroscopic time delay, and, finally, another laser pulse train with a different photon energy (*probe*) samples the remainder of the e_T population.

While some features of the trapped electrons differ for the three solvents, as for instance the exact lifetime (few to hundreds of seconds) or exact intermediate state energy above the Fermi level, the electron traps are localized at the solvent molecule–vacuum interface in all cases, and the long lifetime is rationalized by a strong suppression of its wave function overlap with the (unoccupied) states in the metal substrate by molecular screening and solvation that lead to a polaron-like state. The long lifetime and localization at solvent crystallite surfaces make these trapped electrons ideal precursors for catalytic reactions that drive processes like dissociative electron attachment [132], the di-electron hydrogen evolution reaction [122], or the oxygen reduction reaction [124].

5.3. Metastability, photodoping, and hidden phases

Beyond electron capture at pre-existing trapping sites, also other quasiparticles exhibit lifetimes of µs or longer. The reasons for the long lifetime can be manifold: for instance, electron–hole recombination may be spin- or optically forbidden and energy or momentum release may be hindered due to a lack of appropriate scattering partners and suppressed coupling. Exciton lifetimes, for example, are significantly enhanced when they relax to the triplet state or localize due to defects or dopants [133]. In the case of ZnO, defect excitons (DX) result from the photoexcitation of deep donor levels, likely oxygen vacancies, just above the valence band maximum (*cf.* Fig. 14a) [126].

Electrons populate a bound exciton state in the Coulomb potential of the localized photohole and, as expected from previous 2PPE work on semiconductors [111], exhibit the flat dispersion of their initial state (*cf.* Fig. 14b). In this particular case of *n*-type ZnO, the DX binding energy is sufficiently large to shift this non-equilibrium electron state below the Fermi level. As a consequence, the electrons do not have any relaxation channel except for recombination, as all adjacent electronic levels are occupied. The result is a µs lifetime that is reflected in a DX intensity that varies as a function of laser repetition rate R as shown in Fig. 14c. Note that, as shown in the inset, ca. 50 % of the photostationary DX population is affected by the repetition rate variation and, thus, the remaining 50 % exhibit an even longer lifetime.

Photostationary spectral signatures like the DX are easily missed in time-resolved PES, as they appear at energies *below* the Fermi energy and can be mistaken with states that are occupied in equilibrium. For the particular case presented above, the peak could for example be interpreted as an occupied shallow donor-type defect level that can be ignored when interpreting the ultrafast dynamics at higher energies above E_F. However, depending on their density, photostationary states can have significant impact on the sample's properties, both, (i) in the metastable state long after photoexcitation and (ii) on ultrafast timescales as discussed in the following.

Per definition, photostationary states only occur out of equilibrium. If they alter the material properties as, *e.g.* the sample conductivity, their density can, in addition, become the relevant state quantity for a phase transition. Any phase transition driven by photostationary states, thus creates a phase that has no equivalent in the equilibrium phase diagram or, in trendy terms, is a "hidden phase" or a "new state of matter".

For the particular case of ZnO, we could show that the photoinduced enhancement of the DX density can lead to the transition to a metallic phase, both in the (i) metastable, photostationary state *and* on (ii) ultrafast timescales [125,126]. Due to the similarity of DX and shallow donors, enhancement of their density leads to the formation of a metallic state by the same mechanism originally introduced by Mott [134] for chemical doping and illustrated in Fig. 14e: at sufficient (photo−)doping density, the electron wave functions start overlapping, and a delocalized, metallic "impurity" band is formed.
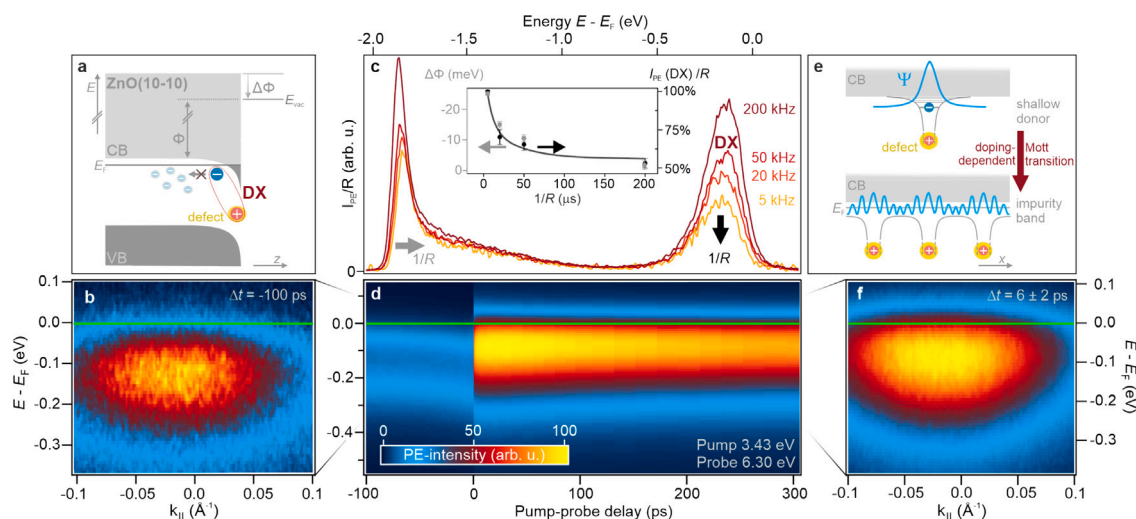
Fig. 14. Long-lived defect excitons (DX) drive an insulator-to-metal Mott transition. (a) Energy level alignment at the ZnO surface. (b) Angle-resolved PES of localized DX shows a flat dispersion. (c) The DX intensity depends on laser repetition rate due to population dynamics on μs timescales, which is also reflected in work function variations (inset). (d) Photoexcitation leads to the ultrafast generation of a surface metal that shows (f) a nearly free electron dispersion. The mechanism is the photoinduced analogue of the chemical Mott transition illustrated in (e). Panel (c), (e) adapted and modified from [126]. (b), (d), (f) adapted and modified from [125].

The ultrafast Mott transition in ZnO (*cf.* Fig. 14d and f) occurs for excitation densities above a remarkably low critical fluence of $F_C = 13.6$ μJ cm^{-2} [125] compared to photoinduced phase transitions in correlated materials [135–138] and decays on a 100 ps timescale to a semiconducting phase of ZnO with a photostationary DX density below threshold.

This example highlights the severe impact of long-lived states on not only studies using time-resolved photoelectron spectroscopy, but ultrafast techniques using highly repetitive light sources in general: as soon as densities of photostationary electronic states become sufficiently large, their localization will collapse and has the potential to change the electronic structure near E_F significantly.

5.4. Predictions and surprises

As mentioned above, various sources for long-lived excited states are imaginable and, beyond trapped electrons in polaron-like states (*cf.* Section 5.2) and DX in intrinsically defect-rich metal oxides (*cf.* Section 5.3) discussed above, it is straight-forward to predict long lifetimes for exciton triplet states in organic compounds. Their decay dynamics are naturally difficult to observe, as the direct transition to the ground state is optically forbidden and phosphorescence photon counts low [139]. Time-resolved photoelectron spectroscopy of triplet states is possible [100], however if the triplet lifetime exceeds the inverse repetition rate of the laser system, its determination requires procedures beyond ordinary pump–probe experiments as described above.

In the case of the spirobifluorence derivative SP6 (2,7-bis(biphenyl-4-yl)-2',7'-ditertbutyl-9,9'-spirobifluorene, inset in Fig. 15a), the electronic level of the triplet state is not directly probed in 2PPE [140]. Instead, a spectral signature A is observed that does not show any spectral shift as a function of photon energy, but exhibits dynamics on μs-timescales as a function of repetition rate (*cf.* Fig. 15b). We could demonstrate that these peculiar properties originate from autoionization in the SP6 film that is driven by triplet–triplet annihilation (TTA) as illustrated by the scheme in Fig. 15a: after photoexcitation, the SP6 molecules undergo intersystem crossing (ISC) to the triplet with a time constant of 240 ps [141]. The remarkably long intrinsic triplet lifetime of 100 ms allows for energy transfer between triplets within a Dexter radius of 1.3 nm. As the excited state energy of the triplet is larger than its binding energy, this Dexter energy transfer results in electron emission, which is independent of the photon energy used.
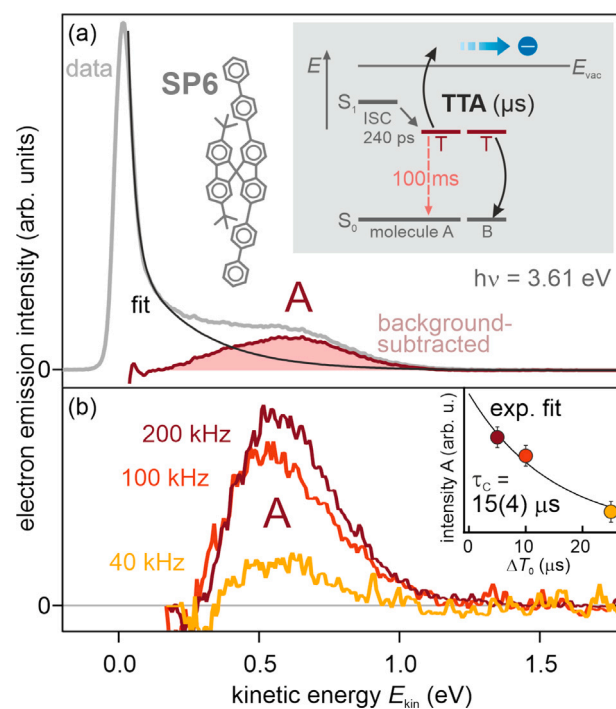

Fig. 15. Autoionization of organic SP6 molecules by TTA. a) Background subtraction procedure and SP6 molecule. Inset: TTA scheme. b) Repetition rate-dependent spectra unveil dynamics on μs timescales related to TTA.
Source: All panels adapted and modified from [140].

The quantum yield of this process shows a clear excitation density dependence that cannot be rationalized by traditional pump–probe photoelectron emission [140].

It is important to note that the spectral signature A could have, due to the absence of dynamics on ultrafast timescales, easily been accidentally erased from the data set by subtraction of the negative delay spectrum. Even if it had been identified as an excited state of the system, the lack of ultrafast dynamics and absent photon energy dependence could have led to an assignment to a *final* state as well. Lastly, this example shows that the μs decay dynamics observed in

repetition rate-dependent experiments do not *have to* reflect the actual excited state lifetime (here 100 ms).

All examples of long-lived excited states given above show dynamics on timescales clearly exceeding the ultrafast regime. Their lifetime was, if sufficiently long, either determined by pump-wait-probe experiments [121–124,129] or by examination of the repetition rate dependence of the photostationary state intensity [126,140] in combination with fluence dependent experiments and modeling. The underlying assumption is that the probabilities of photoinduced excited state *population* and *depopulations* by photoemission and population decay determine a stationary, average population of the excited state (for a detailed discussion see, *e.g.* Refs. [122,129]).

It is quite tempting to assume that a photo*stationary* signal, which shows a superposition of the μs- to minute-dynamics probed by up to millions of laser pulses does not show any dependence on the pump–probe time delay. In this case, subtraction of the negative delay spectrum unveils, as in the absence of long-lived excited states, the correlated signal of a pump–probe laser pulse pair on ultrafast timescales, which may [123] or may not [140] show the formation dynamics of the long-lived species. However, recently, we could demonstrate that the assumption of a pump–probe delay-*independent* photostationary state is not always valid [128]. If the probe laser pulse has a sufficiently large impact on the limiting value of the photostationary, excited state population as illustrated by the inset of Fig. 16, the photostationary state of each particular, ultrafast pump–probe time delay may differ. The surprising and counter-intuitive result is the observation of ultrafast dynamics of photostationary signals as is the case for the 100 ps formation of μs-lifetime hybrid excitons at the organic/inorganic hybrid interface of p-quinquephenyl-pyridine (5P-Py) molecules on ZnO(10-10) (*cf.* Fig. 16, [128]). In this particular case, the long-lived excited state is populated via a precursor state with a hybrid exciton formation time of 100 ps. When the probe laser pulse interacts with the sample during this lifetime of the precursor state (gray, Fig. 16), it reduces the population that can eventually transfer into the hybrid exciton state. This creates a ps-delay-dependence of the photostationary state intensity.

The above described observations show that not all time delay-dependent spectral changes have to result from pump-induced dynamics monitored by the succeeding laser probe pulse. It is, therefore, very important to examine ultrafast dynamics observed in time-resolved photoemission studies carefully: ultrafast dynamics that are monitored traditionally using pump–probe laser pulse pairs separated by an ultrashort time delay must be disentangled from delay-dependent changes of a photostationary state. The latter *always* are a product of a sequence of events occurring on multiple timescales that needs to be understood before interpretation. This is even more relevant for time-resolved experiments in the few-eV photon energy range, as it is here *a priori* not clear, which photons (pump or probe) are responsible for the photoemission step [128].

5.5. Discussion and conclusions

The above collection of time-resolved PES experiments illustrates that various different types of excited states may exhibit lifetimes exceeding the inverse of typical light source repetition rates. Depending on the type of long-lived quasiparticle, their presence can cause very different properties of the photostationary state in terms of, for instance, reactivity, conductivity, and spectral properties. Actually, in some cases it is only the long lifetime and build-up of a photostationary population that enables the investigation of minority species that could not be studied otherwise. Their impact on the properties of the investigated system can still be major as is the case for electron-driven chemistry [122,132], highly efficient carrier production in TTA [140], and photoinduced transitions to so-called hidden phases [125,126].

Unfortunately, such long-lived excited states are easily missed or misinterpreted when examining time-resolved PES data as discussed
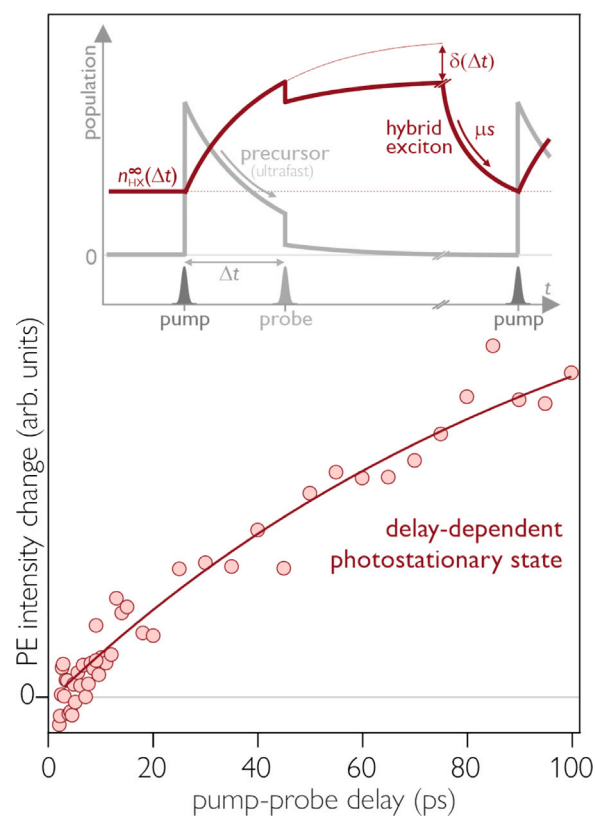

Fig. 16. Ultrafast dynamics of photostationary states: the steady state population n^∞ of a photostationary state can depend on the pump–probe time delay (inset), as is the case for the ps-build-up of hybrid excitons at the 5P-Py/ZnO interface (main).

above. As far as our experience goes, however, they are quite abundant, and easily identified by the enquiring eye. Although the sample selection of our group clearly is not statistically relevant, we emphasize that more than 80 % of the investigated systems in the group showed some form of photostationary signal. This astounding abundance makes it advisable to always test for long-lived states with lifetimes exceeding the inverse repetition rate of the laser system, in particular in time-resolved PES experiments performed at high kHz to MHz repetition rates.

The first and easiest test for photostationary states is the comparison of the "negative delay spectrum" to a probe-only spectrum. If a long-lived state is created, the pump beam will modify the probe-only spectrum at negative pump–probe delays, i.e. when the pump arrives after the probe beam in the repetitive laser excitation. Beyond the photostationary population itself, accompanying, unusual dynamics near the secondary cut-off that are resulting from the change of surface dipole due to charged or dipolar long-lived states near the surface may be observed [126]. More sophisticated analyses as repetition rate dependencies (for states with lifetime on the order of the inverse laser repetition rate), pump-wait-probe experiments (for very long-lived states), but also fluence- and photon energy dependencies can follow in order to understand the stationary state that sets the stage for the ultrafast spectroscopy.

In conclusion, long-lived excited states may occur in very different settings: in the absence of decay and/or energy loss channels, the presence of defect or dopant sites as well as strong polaronic responses that stabilize excited states. Due to their lifetime, the stationary state during time-resolved experiments does not equal the ground state. This may have grave consequences for the non-equilibrium dynamics occurring

on ultrafast timescales and should be considered when interpreting time-resolved experiments.

6. Time-resolved momentum microscopy of 2D materials: Ultrafast dynamics of bright and dark excitons

Jan Philipp Bange, Marcel Reutzel, and Stefan Mathias

6.1. Introduction

An exciton is a charge neutral compound-particle made out of a Coulomb-bound pair of a negatively charged electron and a positively charged hole. Excitons are characterized by their quantum number, binding energy and Bohr radius, they are observed in semiconductors, and can, in the simplest case, be described in a two-band model without momentum offset: Here, the single-particle electron- and hole-components are positioned in the conduction band minimum and the valence band maximum, respectively [Fig. 17(a)], building up the two-particle exciton wavefunction. Such excitons are termed to be optically bright because of their high oscillator strength, making them directly accessible in photoluminescence experiments, as has been shown in groundbreaking experiments on exfoliated monolayer transition metal dichalcogenides (TMDs) [142–146]. However, the single-particle electronic structure of two-dimensional (2d) TMDs is much more complicated than can be captured in a simple two-band model, and exhibits various high symmetry points with band maxima and minima in the hexagonal Brillouin zone, as illustrated in Fig. 17(b). These band extrema in the electronic structure of the TMDs lead to a more complex exciton landscape beyond the picture of momentum-direct transitions in a two-band model. For example, in monolayer WSe_2, an electron in the conduction band at the Q (also called Σ) valley and an electron in the valence band at the K valley can form a momentum-indirect exciton [147–153]. A direct excitation with light as well as a direct electron–hole recombination with emission of a photon is then, due to the momentum off-set of electron and hole, prohibited. Hence, such a state is called a dark exciton state.

For a complete understanding of the semiconductor's optoelectronic properties, it is thus crucial to capture the formation and thermalization dynamics of not only the bright, but also the dark exciton states. In the following, we will summarize how time-resolved momentum microscopy [154,155] – a new variant of time- and angle-resolved photoelectron spectroscopy [30,103,120,156] – has evolved into a key experimental tool that is capable of providing such information, using mono- and heterobilayer TMDs as an example.

6.2. Femtosecond momentum microscopy from exfoliated van-der-Waals materials

Time-resolved momentum microscopy experiments can be performed at free-electron-lasers [157] and in table-top laboratory experiments [55,92,158–164]. Here, we will focus on the latter setup, which combines a multidimensional photoelectron detector with a laser-driven high-harmonic-generation (HHG) beamline operating at repetition rates larger than 100 kHz. The HHG beamline routinely provides photons with energies between 20 eV and 70 eV, which is sufficient to probe the K-points in 2d van-der-Waals materials [30,34, 165,166].
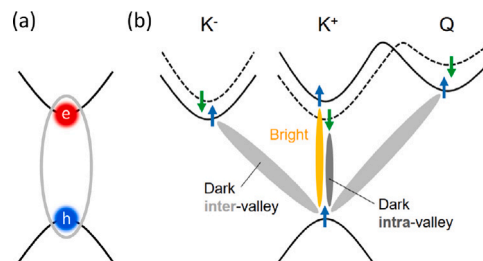

Fig. 17. Exciton landscape in TMDs. (a) Two-band model of excitons with electron in conduction band and hole in valence band. (b) Bright and dark exciton landscape in TMDs.
Source: Figure adapted from [152].
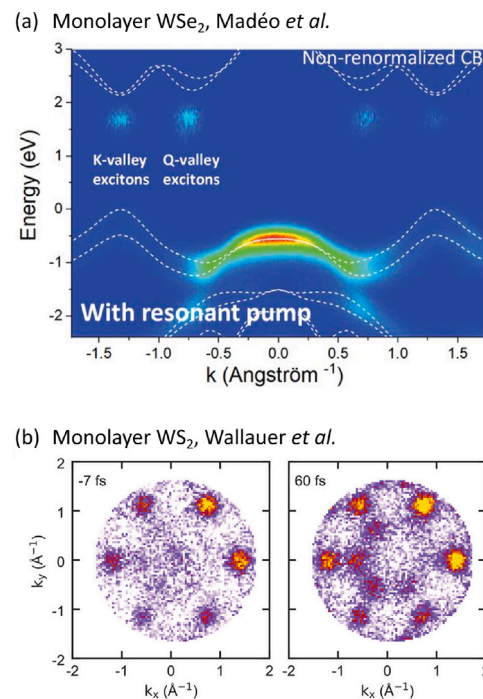© 2018 by the American Physical Society.

Fig. 18. Excitons in time-resolved momentum microscopy. (a) Photoelectron spectrum of monolayer WSe_2. Image reprinted from [160] with permission from AAAS. (b) Momentum–momentum cut of the exciton landscape of monolayer WS_2.
Source: Image reprinted with permission from [162].
© 2021 American Chemical Society.

The working principle of the momentum microscope is detailed in Refs. [167,168] and also in the present collection in the article by Elmers and Schönhense. Here, we emphasize that, because of its microscope-type working principle, it allows to perform photoemission experiments on exfoliated 2d materials in a region-of-interest of <100 μm^2 [160,162,169]. Moreover, it is possible to perform time-resolved photoemission spectroscopy experiments with simultaneous sub-micron-scale spatial resolution by combining the experimental scheme with dark-field imaging techniques [170].

6.3. Photoemission fingerprints of excitons

Fig. 18(a) depicts a cut through a 3d data set $[I(E, k_x, k_y)]$ along the high-symmetry direction Γ-Q-K for a monolayer of WSe_2. This data was measured in a seminal work by Madéo et al. at a pump–probe delay of 0.5 ps [160], and nicely illustrates the appearance of excitonic signals in the photoemission spectrum. By plotting the photoemission intensity in colorscale, the occupied valence bandstructure is visualized

for energies of $E - E_{\text{VBM}} < 0$ eV. Very noticeable is a single band with high spectral weight at the Γ-point, and, with much lower spectral weight, the higher-lying valence band maxima at the K-points, being indicative for the presence of a monolayer WSe$_2$ [171]. The splitting of the band at the K-points due to spin–orbit coupling is also visible and is highlighted by the dashed theory lines. To study excitons, a pump pulse of $h\nu = 1.72$ eV has been applied, which is resonant to the bright A1s exciton located at the K-point in the WSe$_2$ monolayer. During the photoemission process, excitons break up and the electron part of the exciton is detected above the valence band maximum inside the single-particle band gap (dashed theory lines) [111,155,172–174]. Therefore, the photoemission spectral weight at the K-point stems from the break-up of optically bright A1s excitons and the detection of the respective electrons in the photoelectron analyzer. We note that such bright A1s excitons can straightforwardly be detected in all-optical spectroscopy, too. However, the full potential of the momentum microscopy scheme becomes clear when monitoring the spectral weight at the Q (also called Σ) valley. This photoemission signal originates from the break-up of momentum-indirect Q excitons.

To further illustrate this, we select a work by Wallauer et al., now for a monolayer of WS$_2$ [Fig. 18(b)], that shows the appearance of excitonic signals at the respective energy in a k_x-k_y cut through the $I(E, k_x, k_y)$ momentum microscopy data set [162]. In the left panel, the data is shown for -7 fs pump–probe delay, i.e. during the excitation with the sub-50-fs pump pulse, where spectral weight is only visible at the K-points. By changing pump–probe-delay to 60 fs, i.e. after the direct optical excitation, it becomes apparent that spectral weight is transferred to all three Q- and Q'-points. In the following, we will have a closer look at these formation and thermalization processes of excitons and review the recent efforts on exciton dynamics in mono- and heterobilayer TMDs.

6.4. Ultrafast exciton formation dynamics in monolayer TMDs

Having identified bright and dark excitons in momentum space using photoelectron momentum microscopy, in this section, the ultrafast dynamics of bright and dark excitons of monolayer TMDs are discussed. We note that the exciton band-alignment for monolayer WSe$_2$ and monolayer WS$_2$ is similar, so that the same bright and dark exciton species is excited via optical excitation and scattering, however, with slightly different femtosecond dynamics.

As mentioned above, after resonant excitation, spectral weight resulting from the A1s exciton appears in the K valley of the momentum microscopy data set. This is illustrated again in Fig. 19(a) for the monolayer WSe$_2$, but now the energy distribution curves at the K-point are plotted as function of pump–probe time delay [160]. The energy scale is referred to the energy of the valence band maximum E_{VBM} at the K-point and corresponds to the exciton energy E_{exc} [111,155,172–174]. In monolayer WSe$_2$, E_{exc} determined with photoelectron spectroscopy was measured to be 1.73 ± 0.03 eV [160] and 1.67 ± 0.05 eV [175], consistent with previous photoluminescence experiments [176,177].

From this time-resolved data plot, one clearly sees that the intensity of the signal at the K-points decreases for larger delay times [top panel of Fig. 19(a)] and concomitantly signal of the dark intralayer excitons at the Q-points appears (bottom panel). Note that Tungsten-based TMDs are expected to host also momentum-indirect excitons with electron and holes components separated in K and K' valleys [151,178,179]. In photoemission spectroscopy it cannot be straightforwardly distinguished between signal from these excitons and the bright A1s excitons at the K valley [163,164], thus both are referred to as K excitons here.

By integrating the intensity of the excitons in the corresponding regions in energy and momentum space, which we illustrate with the work by Bange et al. in Fig. 19(b) [175], it is possible to monitor the dynamics of the individual exciton species in detail. The integration areas are shown as black circles in the momentum maps at the bottom of Fig. 19(b). In the top panel of Fig. 19(b), the orange data points
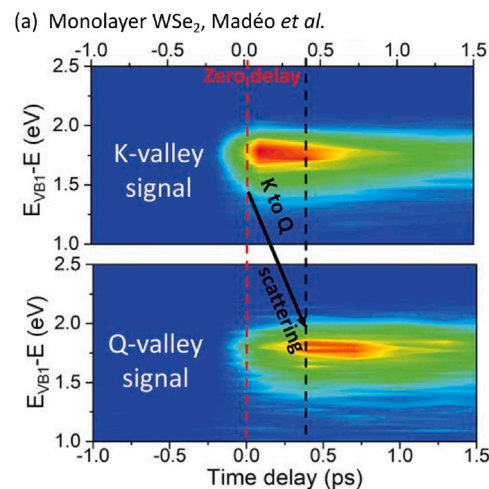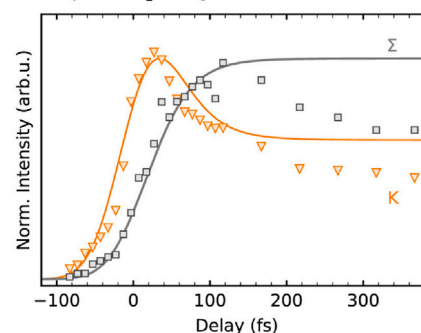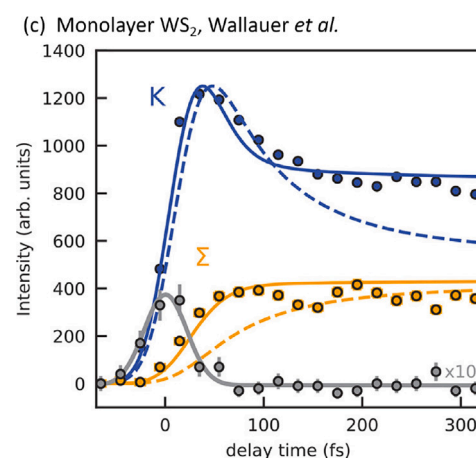
Fig. 19. Bright and dark exciton dynamics: (a) Energy versus time plot for monolayer WSe$_2$. Reprinted from [160] with permission from AAAS. (b) Dynamics of the signal at the K and the Σ-point in monolayer WSe$_2$. Image reproduced from [175] under Creative Commons Attribution License 4.0 (CC BY). (c) Same experiment on a monolayer of WS$_2$. Reprinted with permission from [162].
© 2021 American Chemical Society.

correspond to the extracted time-evolution of the photoemission signal at the K-point, i.e. K-excitons including A1s excitons, and the gray data points correspond to the signal at the Σ-point, i.e. the dark intralayer Σ excitons (the Q-point is called Σ-point in this work). Clearly, when approaching pump–probe overlap at 0 fs, the signal at the K-point shows a steep increase due to direct excitation with the optical pulse. To be more accurate, initially, the pump light creates a coherent polarization, which, after scattering, develops to an incoherent population of excitons [151,180,181]. The photoemission signal hence contains contributions from both the incoherent and coherent excitons [162]. We note that it has been shown that the rising behavior of the signal can be dependent on the chosen pump photon energy. Slightly off-resonant pumping can shift the maximum to earlier delay times [162].

Furthermore, it can be seen in Fig. 19(b) that the intensity of the dark Σ intralayer excitons [gray data points in Fig. 19(b)], in comparison to the A1s excitons at K, rises at later delay times. This provides direct evidence that the exciton population at Σ is not created by the optical excitation, but via scattering of the corresponding electron from the K to the Σ-point. This bright-to-dark exciton formation process is understood by exciton–phonon scattering, an interpretation that is fully supported by microscopic modeling [151,162,175,182]. For the data shown in Fig. 19(b) a K-Σ transfer time of $\tau_\Sigma = 36 \pm 3$ fs in WSe$_2$ was extracted at room temperature [175].

Fig. 19(c) shows in comparison the bright and dark exciton dynamics in monolayer WS$_2$ from the work of Wallauer et al. [162]. Also here, a fast rise of the signal at the K-point after resonant excitation of the A1s excitons ($h\nu_{\text{pump}} = 2.03$ eV, blue data points) is followed by the distinct and delayed rise of the signal at the Σ-point (yellow data points). While one sees for qualitatively identical exciton landscapes the same exciton species and scattering processes, the exciton energies and transfer times are slightly different, with $E_{\text{exc}}(\text{A1s}) \approx 2$ eV, and a K-Σ transfer time of $\tau_{\text{transfer}} = 16 \pm 5$ fs in WS$_2$ at room temperature.

Finally, on the longer timescale, one finds for both WSe$_2$ and WS$_2$ that the rise of the Σ exciton occupation occurs until a steady state situation between K excitons and Σ excitons is reached. This quasi-equilibrium is a result of backward and forward scattering between K and Σ states that are close in energy. In the decay of the K signal in Fig. 19(b,c) two characteristic decay times are present. The first and faster decay corresponds to the build-up of the steady state between K and Σ excitons. The second and longer decay time, which can better be seen in Fig. 19(b) for WSe$_2$, can be attributed to exciton recombination (note that this process is not included in theory, straight lines). Intriguingly, the latter decay time is similar for both K and Σ states and measured in WSe$_2$ to be 1–2 ps at room temperature [175]. This experimental results hint that both the exciton population at K and at Σ decay by recombination of bright excitons at the K-point, which is in agreement with reports from time-resolved all-optical spectroscopies [151,183–188].

6.5. Formation of interlayer excitons in a type II band-aligned heterostructure

In addition to momentum microscopy experiments on monolayer TMDs, the technique has also been used to study ultrafast charge-transfer dynamics in atomically-thin TMD heterostructures [169,172, 175,189]. Here, we now focus on our works on ultrafast exciton formation and thermalization dynamics in a type II band-aligned TMD heterobilayer, namely, a $\approx 10°$ twisted WSe$_2$/MoS$_2$ structure [169,170, 172,175].

With van-der-Waals materials, it is also possible to stack different types of monolayers on top of each other to create new artificial crystals [c.f. illustration in Fig. 20(a)]. As a result, emergent properties of the heterostructure can be realized and controlled by using different monolayers, twist angles, and dielectric environments. One example for tuneability in heterostructures is the moiré potential, which is introduced by the twist angle or lattice mismatch between
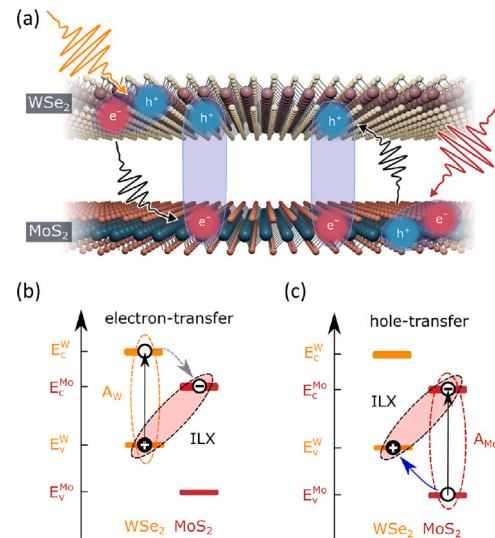

Fig. 20. Energy alignment in a WSe$_2$/MoS$_2$ heterostructure. (a) Light pulses exciting intralayer excitons in the WSe$_2$ layer (orange pulse) or MoS$_2$ (red pulse) lead to formation of interlayer excitons. (b) Resonant excitation of A1s excitons in WSe$_2$ induces electron-transfer process. (c) Hole-transfer is initiated by resonant excitation of A1s excitons in MoS$_2$.
Source: Panel (a), (b) and (c) are adapted from [172] under Creative Commons Attribution License 4.0 (CC BY).

the layers. Exciton properties can be influenced by this additional periodic potential leading to confinement and trapping of so-called moiré excitons [189–193].

In type II band-aligned heterostructures, the valence band maxima and conduction band minima form a staggered arrangement [Fig. 20(b)]. In this case, after excitation of an intralayer exciton, the electron component of the exciton can transfer across the interface to form an interlayer exciton (ILX). This electron transfer process is illustrated in Fig. 20(a, b). Remarkably, for the interlayer excitons, the hole component is located in one layer while the electron component is located in the other layer. While spectral evidence for the existence of such interlayer excitons has been obtained using optical spectroscopy [177,194], the exact formation mechanism has been the subject of debate [194–200].

6.5.1. Ultrafast electron-transfer mediated by dark Σ excitons

Time-resolved momentum microscopy serves here as the perfect tool to study the ILX formation mechanism, because the technique allows to identify the full exciton landscape in momentum space. Fig. 21(a) depicts momentum-integrated energy distribution curves as function of pump–probe delay upon resonant excitation of the A1s exciton in a WSe$_2$ layer of an $\approx 10°$ twisted WSe$_2$/MoS$_2$ heterostructure. Initially, high photoemission intensity is found at about 1.7 eV above the valence band maximum (orange dotted line), which shows that intralayer A1s-excitons are resonantly excited. As pump–probe delay proceeds, spectral weight shifts to a signal with lower energy (red dotted line). This is the photoemission signal of ILXs that can clearly be identified in energy when comparing it to the single WSe$_2$ monolayer. In addition, the ILX was shown to exhibit a unique momentum fingerprint that is related to the moiré superlattice (not shown here, see [155,169,170]). Note that, for the case of a single monolayer, no shift of spectral weight to lower energies is observed, because no interlayer excitons are formed [see Fig. 21(b)].

By filtering spectral features in energy–momentum space of the multidimensional data set, dynamics of the individual exciton species in this heterobilayer can be extracted: Intralayer A1s-excitons of WSe$_2$, hybridized excitons at the Σ-point, and interlayer excitons. The corresponding exciton formation and thermalization dynamics for all excitons is shown in Fig. 21(c) with orange, gray and red data points,
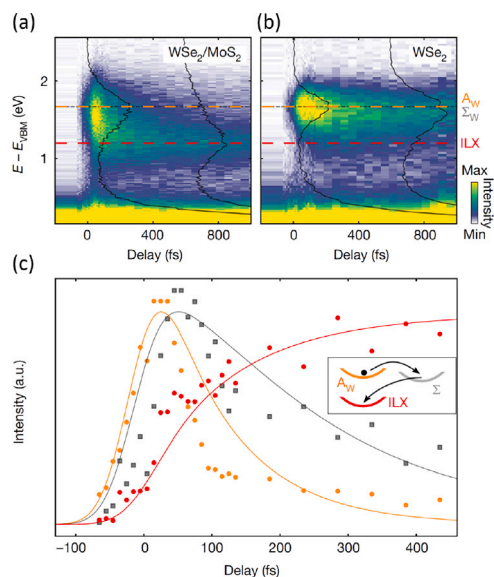
Fig. 21. Formation of interlayer excitons in a type II heterostructure WSe_2/MoS_2: (a) Energy distribution curves as a function of delay show the formation of ILX after resonant excitation of A1s excitons in the WSe_2 layer. (b) Energy distribution curves for the same excitation in single monolayer WSe_2. Only intralayer excitons are present. (b) Ultrafast formation dynamics of intralayer A1s excitons, hybrid Σ, and interlayer excitons (orange, gray and red data points, respectively). Solid lines are microscopic theory. (Copyright by Springer Nature).
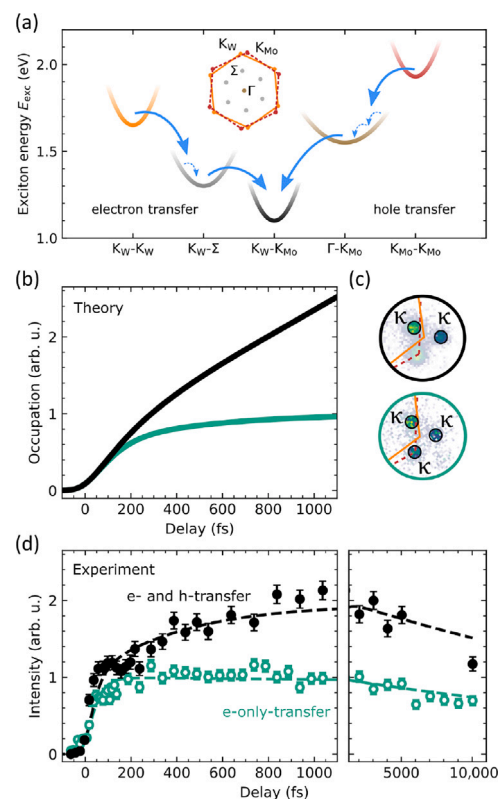*Source:* (a), (b) and (c) are reprinted from [169].

Fig. 22. Electron-and hole-transfer dynamics: (a) Calculated exciton landscape of intralayer, hybrid and interlayer excitons. Electron- and hole transfer are induced by pumping resonantly with 1.7 eV or 1.9 eV light, respectively. (b) Exciton dynamics simulation as predicted by microscopic theory. Formation of ILX due to electron-only (green line) and electron- and hole-transfer mechanism (black line). The hole transfer process takes an order of magnitude longer than the electron transfer process. (c) The momentum-filtered regions of interest are marked with black circles around the κ-points. (d) Evolution of photoemission intensity of ILXs due to electron-only (green points) and electron- and hole-transfer processes (black points). Hole-transfer occurs for delays longer than 1 ps.
Source: Panels (a), (b), (c) and (d) are adapted from [172] under Creative Commons Attribution License 4.0 (CC BY).

respectively. It is immediately noticeable that the contributions of intralayer, Σ, and interlayer excitons rise with certain delayed onsets. In addition, both the A1s-exciton signal as well as the Σ exciton signal show a fast decay after the initial rise. In contrast, the interlayer exciton signal decays comparably slower with a decay time of $\tau = 33.2 \pm 4.7$ ps [169]. The delayed onsets can be interpreted as a sequential electron transfer mechanism in which the hybridized Σ exciton is transiently involved.

Solid lines in Fig. 21(c) show an exciton dynamics simulation based on the microscopic calculation of the hybrid exciton landscape in the heterobilayer [169,175,201]. In the model, the formation pathway of interlayer excitons is verified as a cascade through exciton states. Exciton–phonon interaction leads to scattering from the K-point to the Σ-point. At the Σ-point, the electron contribution of the exciton is hybridized, which enables efficient tunneling of electrons between the layers. An additional scattering event with a phonon then transfers the electron from the hybridized Σ-point to the K-point of the MoS_2 layer, i.e. the ILXs are formed.

6.5.2. Hole-transfer dynamics

Looking at the energy alignment of the bands in Fig. 20(c) shows that in addition to the electron-transfer process to form the ILX, also a hole-transfer process is possible (see Fig. 20(a)). After resonant excitation of A1s excitons in the MoS_2 layer, the hole can transfer from the MoS_2 valence band maximum into the energetically favorable valence band maximum of the WSe_2 layer, and again, the ILX is formed.

The initial condition for such a hole transfer process in the exciton landscape, starting from the A1s exciton in MoS_2 (exciton energy of 1.9 eV), is, both in energy and momentum, very different to the electron transfer process that starts from the A1s exciton in the WSe_2 [exciton energy of 1.7 eV, see Fig. 22(a)]. Thus, different formation dynamics can be expected. Indeed, looking at the theory, the microscopic model predicts a comparably much longer transfer time for the hole transfer process, which is on the order of a few picoseconds (Fig. 22(b), black line). The reason for this behavior is a different formation pathway, which is not mediated by the electron going through the Σ-point, but

mediated by the hole that, according to theory, goes through the Γ-point. For this hole-mediated formation pathway, however, the phase space for exciton–phonon scattering is comparably reduced [151,178, 201–203]. In addition, more excess energy needs to be relaxed via additional intraband scattering processes to form the ILX, because the structure is now excited with 1.9 eV in the MoS_2 layer instead of the lower 1.7 eV in the WSe_2 [197,201]. The simulated dynamics are shown in Fig. 22(b), where the green line shows the very fast electron transfer discussed above, and where the black line illustrates the combined electron and hole transfer showing, accordingly, both the fast electron transfer and the comparably slower hole transfer components in the ILX formation process. We note that both transfer processes were taken into account, because resonant pumping of the A1s exciton in MoS_2 also leads to off-resonant pumping of the A1s exciton in the WSe_2 layer. The unambiguous signature of the hole transfer is, hence, the slower and persistent increase in ILX exciton population for time delays on the order of several picoseconds.

Experimental realization of the hole transfer is done by tuning the pump pulse energy to be resonant to the A1s exciton in MoS_2, i.e. $h\nu_{pump} = 1.9$ eV. The measured formation dynamics of the ILX is shown in Fig. 22(b). Black data points correspond to the resulting combined electron- and hole-transfer process. For comparison, green data points show the electron-only transfer from before, where only the A1s exciton in WSe_2 was excited ($h\nu_{pump} = 1.7$ eV). It is directly evident

that the hole-transfer process leads to a slow rise of the ILX signal beyond 1 ps. Hence, the experiment directly reproduces the predicted slower formation time for the hole-transfer process. For a quantitative analysis, the dotted lines show best fit results from a rate equation analysis. The rise time for the electron transfer is extracted to 40 ± 10 fs, while the rise time for the hole-transfer process is on the order of 2.2 ± 1 ps. Note that the experimental data also shows a decay due to recombination of bright excitons and decay over defect channels, which is not included in the microscopic modeling.

6.6. Outlook

This article summarizes the strength of time-resolved momentum microscopy for the study of ultrafast formation and thermalization dynamics of bright and dark excitons in 2d van-der-Waals heterostructures.

In particular, because of its momentum sensitivity and access to micrometer-sized samples, time-resolved momentum microscopy promises to be a key experimental technique to gain unprecedented insights into the correlated and out-of-equilibrium physics of quantum materials in the time domain. The method clearly enables further studies in major future research fields: *e.g.*, charge-transfer and hybridization dynamics at organic 2d semiconductor interfaces [204], advanced light–matter engineering as control of Floquet–Bloch states in two-dimensional materials [58,59,205–207], and the formation of (novel) correlated electronic quantum phases in van-der-Waals devices [208, 209].

Acknowledgments

7. Time-resolved photoemission electron microscopy

Martin Aeschlimann and Benjamin Stadtmüller

7.1. Introduction

Since the pioneering experimental observation of the thermalization dynamics of photoexcited non-equilibrium carriers in gold [210], time-resolved photoemission spectroscopy has emerged as a powerful tool for studying the ultrafast response of materials. This experiment relies on a dedicated pump–probe scheme, in which an ultrashort – femtosecond – light pulse excites carriers from the valence band into the excited states while a second time-delayed pulse (not necessary with the same photon energy) photoexcites the system thus probing the carrier population dynamics at a well-defined instance in time. The photoemission distribution is then typically recorded by a hemispherical electron spectrometer or a time-of-flight detector system. This

procedure provides crucial insights into the quasi-particle lifetimes of optically excited charge and spin carriers and thus into the fundamental energy and (angular-) momentum dissipation processes in materials. Larger optical excitation strength can also reveal non-equilibrium band structure renormalizations, melting of charge, and spin-ordered phases of condensed matter.

Despite numerous groundbreaking studies over the past two decades, time-resolved photoemission experiments typically suffer from a lack of high spatial resolution. Using spatially averaging detector systems, such as hemispherical electron spectrometers or time-of-flight analyzers, the spatial resolution is determined by the spot size of the probe beam, which can only be focused up to the diffraction limit. This has long limited the application of time-resolved photoemission to spatially extended model systems with largely homogeneous non-equilibrium dynamics.

This severe limitation of time-resolved photoemission can be overcome by replacing the conventional spatially averaging photoemission detector systems with a photoemission electron microscope. This combination, known as time-resolved photoemission electron microscopy (tr-PEEM), is nowadays a highly complementary tool for time-resolved photoemission with high spatial resolution down to a few tens of nanometers, as highlighted by in the second part of this article.

The rise of PEEM started in the mid-20th century when PEEM was predominantly used as a surface science technique to provide detailed surface maps of electronic and chemical properties [211]. The first efforts towards bringing PEEM to the time domain started with the availability of high-speed devices for image recording similar to modern streaking cameras, which allowed the investigation of fast, non-reversible processes on surfaces [212]. Modern tr-PEEM experiments based on pump–probe schemes and femtosecond lasers started around the year 2002 with the first attempts to resolve the electron dynamics in the femtosecond time range [213–215]. However, the lack of availability of energy analyzers at that time severely hampered obtaining a full picture of the ultrafast electron dynamics on the nanoscale. Nowadays, modern state-of-the-art tr-PEEM experiments with highly efficient energy analyzers and sub-50 nm spatial resolutions have opened the door for novel investigations of ultrafast electron dynamics on the nanoscale and has thus become a working horse method for fields such as plasmonics and nano-optics. In addition, such experiments allow the investigation of complex heterostructures that can typically only be fabricated with sufficient quality on the (sub) micrometer scale.

In the following, we will introduce the instrumentation and operation procedures of modern tr-PEEM experiments and highlight the corresponding capabilities of tr-PEEM with selected examples.

7.2. The instrumentation of Tr-PEEM

The basic outline of a time-resolved PEEM experiment is illustrated in Fig. 23. The two major parts are the optical setup for pump–probe spectroscopy and the photoemission electron microscopy detector. The pump and probe laser pulses are delivered by femtosecond laser oscillator or amplifier light sources with pulse durations smaller than 30 fs, see Fig. 23(a). These pulses are often frequency-converted to trigger a selected ultrafast response of the material (pump beam) or to employ specific resonant or off-resonant transition for the detection of the ultrafast dynamics (probe beam). Thereby, the photon energies of the ultrashort pulses are no longer limited to the visible spectral range generated by conventional non-linear frequency conversion schemes in non-centrosymmetric crystals (second, third, and fourth harmonics generation, sum and difference frequency generation). In particular, the realization of high flux fs-XUV light sources driven by high harmonics generation has pushed the available spectral range for tr-PEEM experiments towards the extreme ultraviolet (EUV) and soft X-ray range [216]. A Mach–Zehnder interferometer allows adjusting the difference in the optical pathway between the pump and probe pulse
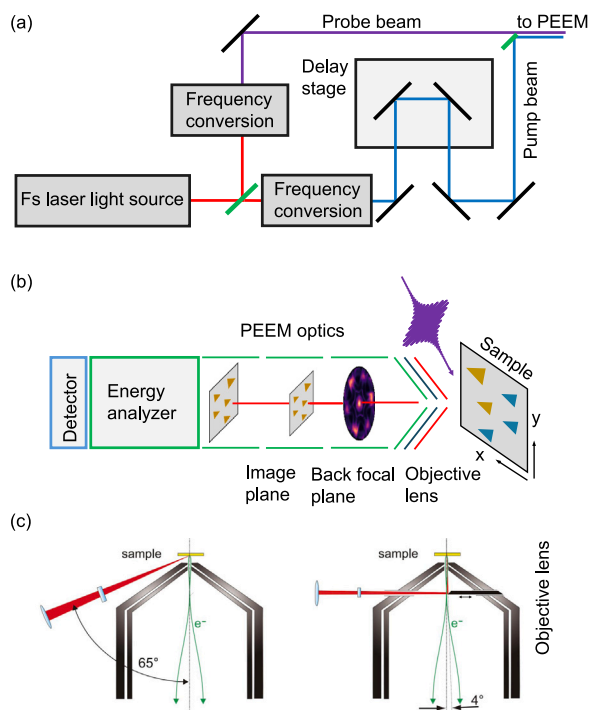
Fig. 23. Schematic representation of the two key components of the tr-PEEM experiment: the optical setup for the pump probe spectroscopy (a) and the PEEM detector system (b). (c) The two different excitation geometries of the PEEM system with a linear arrangement of the electron optics [218].

with an accuracy of better than $100\,$nm corresponding to a timing accuracy of $<0.3\,$fs. This precise control of the timing between the photon densities of the pump and probe pulses is the basis for imaging the ultrafast (incoherent) response of the sample with fs time resolution. In addition, active stabilized interferometers can be used for true interferometric studies of the ultrafast material response using pump and probe pulses with a fixed relative phase relationship [217]. Scanning the time delay between these waves in steps of about $100\,$as can provide unprecedented insights into coherent electron excitations at surfaces, such as coherent energy transfer processes between nanostructures in a resonator or the propagation of surface plasmon polaritons on metal surfaces. Finally, the (nearly) collinear pump and probe beams are focused and guided onto the sample surface. The emitted photoelectrons are then detected by the PEEM system with the two key components that are shown in Fig. 23(b).

First, the electron optics allows to image the distribution of the emitted photoelectrons onto the detector system. It starts with the objective lens that collects the photoemitted electrons from the sample surface. This lens is crucial for focusing the electrons and determining the initial magnification and resolution of the image. This image can either be a real space image of the sample surface, or a momentum image of the emitted electrons that is created in the back focal plane of the objective lens, in analogy to the focus plane of optical lenses. Second, the energy analyzer determines the kinetic energy of the photo-emitted electrons. This capability allows the differentiation of electrons originating from different electronic states or chemical environments within the sample. The two main concepts for energy analyzers are pass filters such as dispersive (double) hemispherical electron spectrometers [219] or time-of-flight analyzers combined with spatially dense delay line detectors [220]. In particular, time-of-flight (ToF) analysis systems are highly advantageous for time-resolved PEEM experiments because they count all electrons in the energy analysis process, in contrast to pass filter techniques that essentially discriminate a significant number of electrons in the detection process. In this regard, the combination

of high repetition rate laser light sources and ToF energy analyzer allows for a superior signal-to-noise ratio in tr-PEEM experiments (with moderate data acquisition time).

This basic design of PEEMs can be complemented by other components. The most important examples are electron mirrors, which reduce the spherical and chromatic aberrations of the electron optics [221] and thus improve the spatial resolution of the system [222,223]. In addition, imaging spin filters can be used to provide spin contrast in the PEEM images for a spin component parallel to the surfaces [224]. A key parameter for tr-PEEM is the spatial resolution. In the simplest case, the PEEM exhibits electrostatic lenses for imaging the emitted electrons which allows for a rather simple operation of the detector system as well as long-term stability of the imaging conditions. The spatial resolution of such PEEM systems is typically better than $50\,$nm, which is substantially below the diffraction limit of optical microscopy in the visible range. The spatial resolution of PEEM systems can be pushed to even smaller values below $10\,$nm when using electromagnetic lenses in combination with electron mirrors. However, maintaining this ultimate spatial resolution in tr-PEEM experiments with acquisition times of several hours is often challenging as even small fluctuations in the operation conditions can have a substantial impact on the imaging conditions and thus the resolution of the experiments.

The different types of electron optics (electrostatic vs. electromagnetic lenses) also have an important impact on the experimental geometry, in particular on the available angles of incidence in a tr-PEEM experiment. In particular, the normal incidence geometry is highly desirable for the tr-PEEM investigations in the field of plasmonics due to the interfaces of the plasmonic fields with the electric field of the light pulses [225]. PEEMs with electrostatic lens systems and linear, concentric geometry typically exhibit a gracing angle of incidence (of $65°$–$68°$ from the sample surface normal). Normal incidence can only be achieved by inserting a small optical mirror into the electrostatic optics column near the electron propagation axis, see Fig. 23(c). In contrast, both gracing and normal incidence can be easily achieved in PEEM systems using electromagnetic lens systems. These devices feature a nonlinear array of electromagnets with magnetic prisms in front of the sample surface, allowing direct access to the sample surface for both gracing and normal incidence of the light pulses without interfering with the lens system arrangement or the electron beam.

In the following, we will present selected examples that highly the unique impact of tr-PEEM for the field of ultrafast surface science.

7.3. Pioneering and ongoing work in the application of Tr-PEEM and Itr-PEEM

As mentioned above, tr-PEEM allows for the direct observation of the energy relaxation and spatial diffusion of photoexcited hot electrons, providing fundamental insights into the mechanisms governing their behavior. The development of time-resolved PEEM dates back to 2002, when O. Schmidt et al. [213] first demonstrated time-resolved imaging of hexagonal Ag patches during optical excitation by the fs pump pulse (see Fig. 24) few years later, A. Kubo et al. [214] first introduced the interferometric time-resolved-(itr-) PEEM technique by imaging the in-phase oscillations of four localized surface plasmon modes on a silver surface during optical excitation by the fs pump pulse (see Fig. 25). Since then, numerous tr-PEEM studies have been conducted across various research fields. Below, we highlight two primary research areas within tr-PEEM, though this overview is by no means exhaustive.

7.3.1. Tr-PEEM for surface plasmon dynamics

One of the most studied topics in ultrafast imaging with PEEM is the excitation of surface plasmons, which are collective oscillations of electrons at the interface between a metal and a dielectric. These excitations are confined to the surface or nanoparticles and can be excited by light, resulting in unique optical properties that are critical for
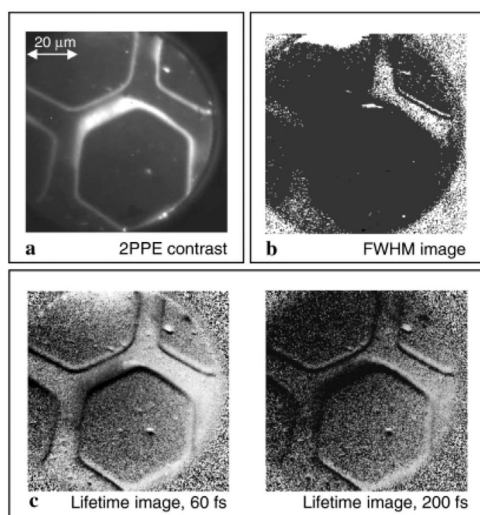
Fig. 24. Tr-2PPE microscopy of silver on gallium arsenide, taken from Ref. [213]. (a) PEEM image of the microstructured Ag layer (partly visible hexagonal patches) taken with 400 nm laser radiation. (b) FWHM image extracted from a pump–probe PEEM scan of the same area. The brightness value of each pixel corresponds to the FWHM of the respective autocorrelation trace. (c) Left: PEEM image taken at 60 fs delay (areas having shorter hot-electron lifetimes appear darker in the image); right: PEEM image taken at 200 fs delay.
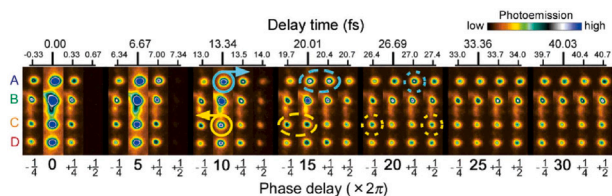

Fig. 25. Interferometric time-resolved photoelectron emission microscopy images (itr-PEEM) of the four different localized plasmons (A,B,C,D) on a silver grating. *Source:* Image taken from Ref. [214].

technological applications such as sensors, photovoltaics, and nanophotonics. Understanding the dynamics of surface plasmons is essential for optimizing these applications. For a review of all published tr-PEEM work in this area, see M. Dabrowski et al. [226]. The applications of tr-PEEM span several domains, including:

Localized surface plasmon (LSP) on noble metal nanoparticle and arrays. LSPs, also known as Mie plasmons, are the oscillations of free electrons in metallic nanoparticles relative to their positive lattice. The resonant frequencies of these oscillations are influenced by various factors, including free electron density, dielectric properties, nanoparticle size and shape, particle–particle interactions, coupling with other plasmonic or single-particle modes, and the surrounding dielectric environment. Time-resolved two-photon photoemission electron microscopy (tr-2PPE-PEEM) has been extensively used to investigate the dynamic properties of LSPs, see Fig. 26(a),(b) [227]. This technique is well-suited for studies on femtosecond or even attosecond timescales, and it is highly effective for examining coupling effects between nanoparticles, see Fig. 26(c) [228].

Surface plasmon polaritons (SPP). SPP waves are generated by the coupling of the electromagnetic field of a light pulse to the oscillations of free electrons at the metal's surface. These waves can be excited by various means, such as a grating or a simple slit. In tr-PEEM the generated signal is primarily influenced by the cross-interference between the pump-excited SPP and the probe light pulse, resulting in snapshots of the propagating SPP on a metal surface at different
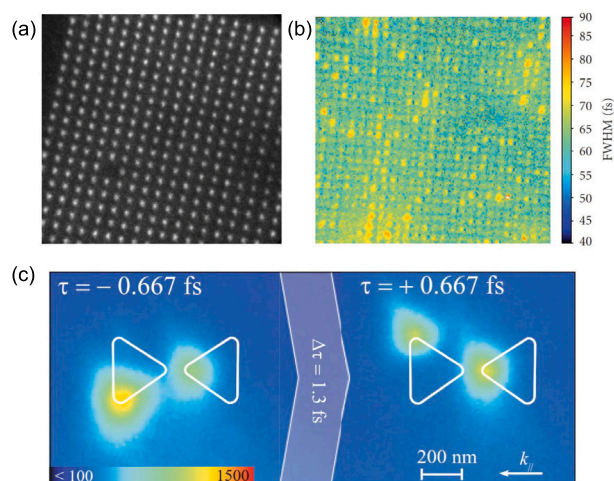

Fig. 26. PEEM images of a silver nanodot (diameter: 200 nm) array (a) the PEEM image is taken with the mercury vapor lamp (4.9 eV); (b) corresponding lifetime map (2PPE cross-correlation trace) [227]; (c) Temporal control of the photoemission peaks at the outer corners of the left nanoprisim within an optical circle using two cross-polarized laser pulses [228].
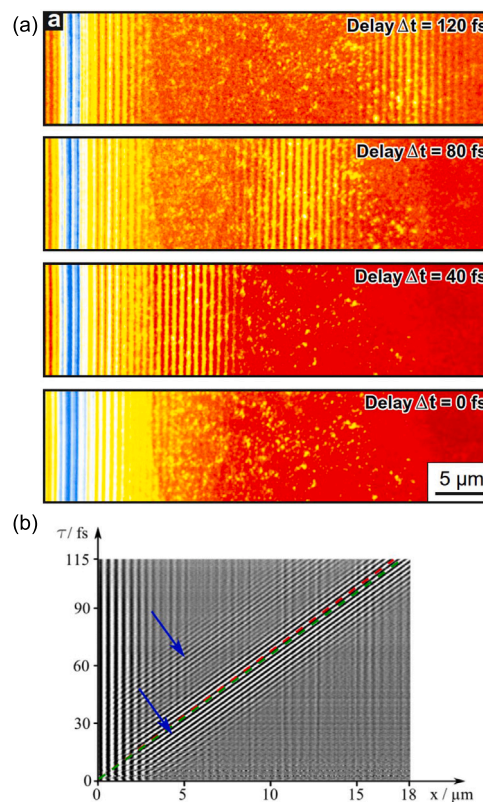
Fig. 27. (a) PEEM snapshots of a propagating SPP on a gold surface at different delay times [229];(b) Delay-path diagram of SPP propagating at the gold-vacuum interface deduced from a counter-propagating itr-PEEM measurement [230]. This illustration shows that the superposition signal contains two distinct contributions (see blue arrows), a dominating leading beating pattern, followed by a weaker second beating pattern. The two signals arise from different SPP excitation processes at the gold bar.

delay times, see Fig. 27(a). A counter-propagating PEEM detection mode provides an even more intuitive access to the SPP wave packet propagation. Particularly the group velocity and the phase velocity of the SPP can be deduced from these data in a very direct manner, see

Fig. 28. Experimental and simulated tr-PEEM images showing a plasmonic-vortex generation with a geometrical order $M = 10$ upon excitation with right hand circularly polarized light [232].
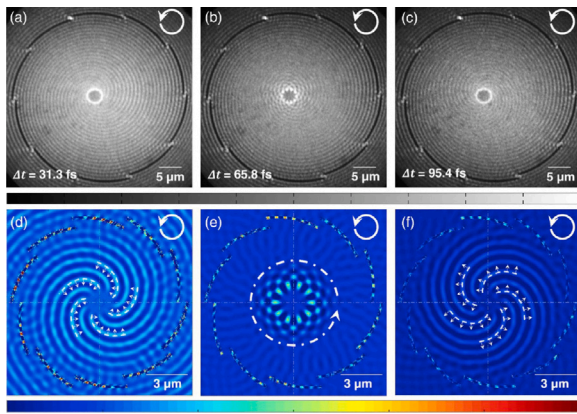*Source:* Image taken from Ref. [231].

Fig. 27(b). Furthermore, the coherent interaction between two fundamental plasmonic excitations — localized surface plasmons (LSPs) and surface plasmon polaritons (SPPs) — which is crucial for the operation of broadband nano-optical devices, is studied using itr-PEEM.

Plasmonic vortex structures. Plasmonic vortices, generated by illuminating Archimedean spiral coupling structures, create SPP phase fronts impregnated with orbital angular momentum (OAM) defined by the spiral geometry. Although many studies have documented the imaging of plasmonic vortices using continuous excitation or time-integrated measurements, their dynamics have only been captured through the advanced capabilities of itr-PEEM imaging. Fig. 28 illustrates the time evolution of a plasmonic vortex with a geometrical charge of $M = 10$, produced by a spiral with 10 equal segments, each inducing a π phase shift across the plasmonic wavefront. For a review of research in this field, see E. Prinz et al. [231].

7.3.2. Tr-PEEM for semiconductor surfaces and interfaces

The second highly investigated topic in ultrafast imaging with PEEM is charge carrier dynamics in semiconductor surfaces and low-dimensional materials. The advantage of tr-PEEM is that it resolves the dynamics of charges in space, time, and energy, which is especially beneficial when studying heterojunctions of materials. For a review of all published work in this area, see S. Kosar et al. [233]. Significant applications and key findings include:

Carrier dynamics in semiconductor surfaces. Tr-PEEM has been used to study the temporal and lateral behavior of photo-excited carriers at semiconductor surfaces, such as GaAs (pioneering work see Fig. 29 and Ref. [234]), Si, Cd_3As_2 nanoplates [235], and InSe/GaAs heterojunction [236]. These studies provide insights into carrier lifetimes, diffusion, recombination processes and the influence of surface states and defects.

Exciton dynamics in low-dimensional materials. Tr-PEEM has been applied to study exciton dynamics in low-dimensional materials, such as monolayers of transition metal dichalcogenides (TMDCs) like MoS_2 and WSe_2 (see Fig. 30). These materials exhibit strong excitonic effects due to reduced dimensionality and dielectric screening. Tr-PEEM studies have revealed the ultrafast lateral formation and dissociation of excitons, providing insights into the fundamental processes governing their photophysical properties. In addition, tr-PEEM has been used to study the charge transfer dynamics at the interfaces of heterostructures composed of different semiconductor materials or low-dimensional materials with unique electronic and optoelectronic properties. For instance, investigations on graphene/TMDC heterostructures have shown how photo-excited electrons transfer between the layers, influencing the overall electronic and optical behavior of the heterostructure.
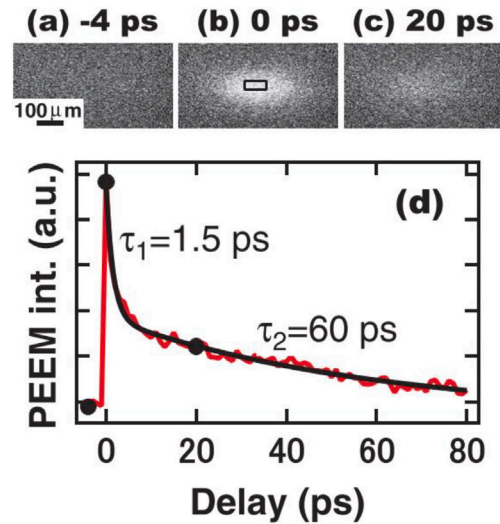

Fig. 29. Tr-PEEM images of GaAs sample for selected time delays between pump and probe. (b) Tr-PEEM decay dynamics averaged over rectangular region in (a).
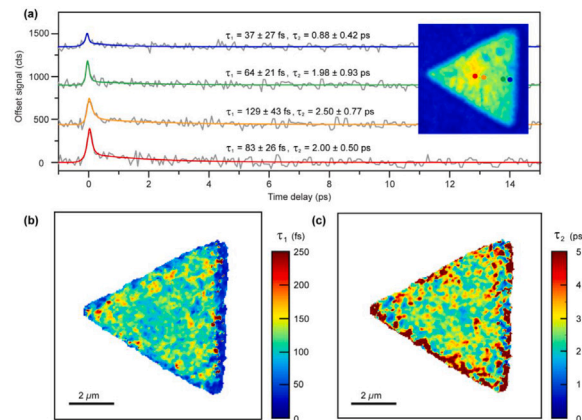*Source:* Taken from Ref. [234].

Fig. 30. Tr-PEEM study of a monolayer WSe_2. (a) Tr-PEEM traces for selected pixels (shown with colored circles) in the PEEM image of WSe_2 monolayer. (b) and (c) Time constant mapping of the fast and slow components to the fits of tr-PEEM traces [237].

Absorption in nanotextured thin films via Anderson-localized photon modes. The enhancement of light absorption in absorber layers is crucial in a number of applications, including photovoltaics. Combining coherent 2D nanoscopy with tr-PEEM, the existence of localized photonic states in nanotextured amorphous silicon layers as used in commercial thin-film solar cells has been demonstrated [238].

Quantum confinement effects. In quantum wells and other nanostructures, quantum confinement significantly alters the electronic states and carrier dynamics. Tr-PEEM has provided valuable insights into these effects by visualizing the spatial distribution and temporal evolution of confined carriers. Studies on InGaN/GaN quantum wells, for example, have demonstrated how quantum confinement affects carrier recombination and transport.

7.4. Future perspectives

The future of time-resolved PEEM in studying electron, plasmon, and exciton dynamics is highly promising, particularly for exploring novel materials. Extending these studies to emerging materials such as perovskites and novel 2D heterostructures will provide new insights

into their photo-excited states and carrier dynamics. Probing these advanced materials can uncover unique electronic and optical properties, potentially leading to breakthroughs in applications such as photovoltaics, optoelectronics, and quantum computing. This expansion of tr-PEEM research promises to significantly enhance our understanding of material behavior at the ultrafast timescale, paving the way for innovative technological advancements. In addition, one of the most exciting developments in this field is the extension of time-resolved PEEM to the attosecond regime, achieved through techniques such as streaking or reconstruction of attosecond beating by interference of two-photon transitions (RABBITT). Capturing the fastest electronic processes at the space–time limit provides deeper insights into the fundamental interactions that govern material properties.

8. Ultrafast spin dynamics probed by time-resolved photoelectron spectroscopy

Martin Weinelt

8.1. Introduction

Interest in ultrafast spin dynamics grew rapidly with the 1996 work of Beaurepaire and colleagues discovering sub-ps demagnetization of ferromagnetic (FM) nickel [239]. This raised the question of how and where spin angular momentum can be transferred within a few hundred femtoseconds (fs) [240]. Research in the field of ultrafast magnetism received a second boost in 2007 with the demonstration of "All Optical Switching" in the ferrimagnetic alloy FeCoGd by Stanciu et al., who revealed the application potential of ultrafast magnetism for the first time [241]. Since then, the field of "femtomagnetism" has been driven by the questions of how fast and by which microscopic processes spins and magnetic order can be manipulated by light and whether one can generally transfer established spintronic effects and applications into the fs range [242–247]. For further reading on the field, we refer to [245,248] and references therein.

In first order, light couples only to electronic excitations. Thus it is the interaction between electron, lattice, and spin subsystems [249] and/or spin transport [250] that drives ultrafast spin manipulation. The characteristic timescales of relevant interactions and the transport of spins by electrons and magnons are illustrated in Fig. 31.

Among the experimental probes of magnetization dynamics, photoelectron spectroscopy is a rather demanding, however, specific probe of the magnetic system [251]. As introduced in Ch. 1, two-photon
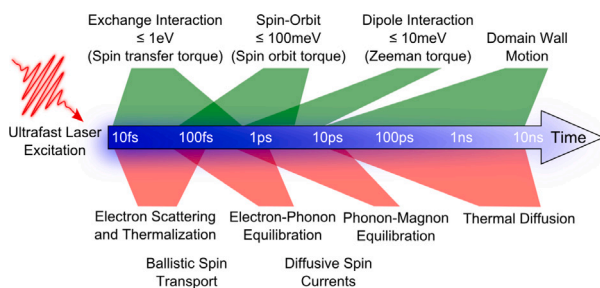

Fig. 31. Characteristic time- and energy-scales for spin interactions accessible via ultrafast laser excitation.
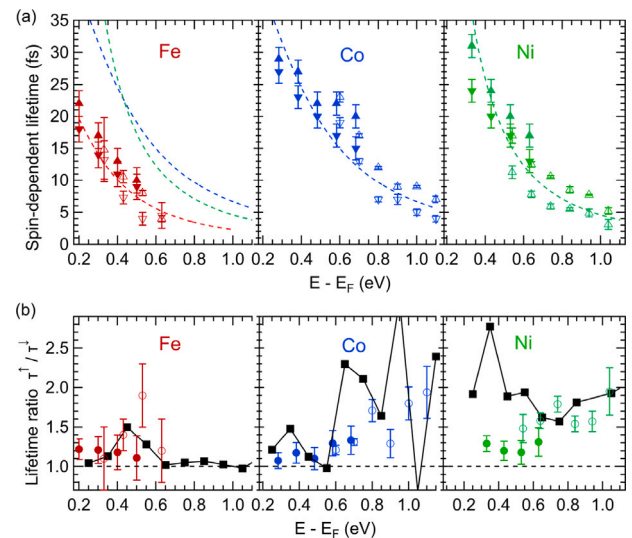

Fig. 32. (a) Spin-dependent hot electron lifetimes for majority (▲, △) and minority (▼, ▽) spin electrons for Fe, Co, and Ni. Open symbols are reproduced from [253]. (b) Respective lifetime ratios $\tau^{\uparrow}/\tau^{\downarrow}$. Filled black squares are calculated lifetime ratios from [270] including spin–orbit coupling and thus spin-flip scattering. All FM films were prepared by molecular beam epitaxy (MBE) on a Cu(001) substrate.

photoemission (2PPE) allows us to directly measure spin-dependent lifetimes of hot electrons [252–254] and unoccupied surface states, such as image-potential states (IPS) [255]. Time- and angle-resolved photoemission spectroscopy (tr-ARPES) gives access to hot electron population dynamics [103,256] and provides energy- and momentum-selective information on band shifts [256–260] and change of exchange splitting [261,262]. Overall, tr-ARPES enables us to unravel signatures of ultrafast spin dynamics in the electronic structure and, conversely, to disentangle fundamental magnetic couplings in the time domain. To measure in addition the spin polarization of photoelectrons [263–265], it requires spin-dependent scattering by means of spin–orbit or exchange interaction, which reduces the count rate per detected channel by 2–3 orders of magnitude and makes time- and spin-resolved experiments challenging [266] (*cf.* Ch. 11).

In this chapter, we will highlight some of the contributions that time-resolved photoelectron spectroscopy has made to the understanding of ultrafast spin and magnetization dynamics.

8.2. Electron lifetimes in 3d transition metals

There are two generally accepted models describing ultrafast demagnetization in FM metals, local spin-flip scattering of electrons at phonons via the Elliot–Yafet mechanism [249] and non-local (super-diffusive) spin transport from the ferromagnet into a "normal" metal (NM) [250]. Prerequisite for the latter are spin-dependent lifetimes or velocities of the photoexcited electrons (or holes), or spin-dependent transport across the FM|NM interface [267–269].

Spin-resolved 2PPE allows us to measure spin-dependent lifetimes of electrons excited to intermediate state energies $E_F < E < E_{vac}$ between Fermi energy E_F and vacuum level E_{vac}. First studies of the 3d ferromagnets were conducted by Aeschlimann et al. using monochromatic 2PPE ($h\nu = 3.1$ eV) and cesiated surfaces [252,253].

Figs. 32(a) and (b) compare spin-dependent lifetimes as a function of excitation energy for Fe (red), Co (blue), and Ni (green) and the liftime ratio $\tau^{\uparrow}/\tau^{\downarrow}$, respectively. Open symbols in Fig. 32(a) are from Refs. [252,253], filled triangles result from our studies [254,271] covering smaller excitation energies in bichromatic 2PPE with 1.55-eV pump and 4.65-eV probe pulses. The data from both experiments agree well. The (spin-integrated) lifetimes for Co and Ni are comparable
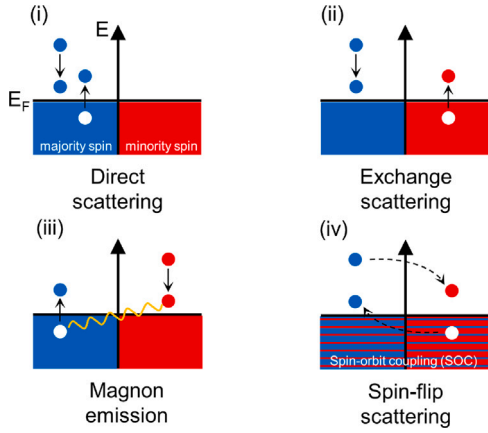
Fig. 33. Inelastic electron–electron scattering processes transferring energy and momentum of a photoexcited electron at energy E to an electron of the Fermi sea at $E < E_F$.

within the error bars, those for Fe are about half as long indicating an additional decay channel (*cf.* Section 8.3). The dashed lines in Fig. 32(a) model the spin-averaged data with $1/\tau = 2/(\tau^\uparrow + \tau^\downarrow) = \Gamma_D + \Gamma_{ee} \cdot (E - E_F)^2$, where $(E - E_F)^2$ approximates the increase of unoccupied final states (see Fig. 33) and the rate Γ_D accounts for electron scattering at defects. For the here probed bulk electrons with energy $E - E_F \geq 0.2$ eV electron–phonon scattering is usually neglected.

The lifetime of an optically excited electron in a metal is governed by inelastic electron–electron scattering via screened Coulomb interaction. As illustrated in Fig. 33 for FMs, this includes (i) direct scattering within the same spin channel [272], (ii) exchange scattering [273] and (iii) magnon emission. The wiggle line indicates multiple pairs of majority-spin holes and minority-spin electrons [255,274]. Please note that exchange scattering and magnon emission show only apparent spin flips, when considering the final state electrons. An essential prerequisite for spin-flip scattering (iv) is spin-mixing of the involved electronic states. This is caused by spin–orbit coupling, which leads to a reduction of the overall symmetry and k-dependent spin contributions $a(k)|\uparrow\rangle + b(k)|\downarrow\rangle$ near hybridization gaps in the electronic band structure [275,276]. Taking processes (i)–(iv) into account, we can qualitatively understand the lifetime ratios $\tau^\uparrow/\tau^\downarrow$ for the $3d$ FMs summarized in Fig. 32(b). Calculated values (filled black squares) are from Ref. [270]. At first glance, the experimental ratios of $\tau^\uparrow/\tau^\downarrow$ are surprisingly small.

For Ni and Co, the number of unoccupied final states for inelastic electron–electron scattering is significantly larger for minority than for majority spin electrons. Accordingly, first *ab initio* calculations for Ni predicted lifetime ratios of $\tau^\uparrow/\tau^\downarrow \geq 5$ near the Fermi level [272]. Significantly better agreement was found when including spin–orbit coupling in a relativistic band-structure calculation [270]. Theory and experimental results agree well for Co, but only moderately for Ni (Fig. 32(b)). Below we will show that the latter is most likely caused by electron transport.

For Fe, the larger exchange splitting leads to a suppression of majority spin states at E_F and theory predicts $\tau^\downarrow/\tau^\uparrow \simeq 1$ even without spin–orbit coupling [272]. However, due to the lower density of states at E_F, calculated lifetimes for Fe are significantly longer than for Ni and Co [270,272]. This discrepancy with the experimental results can be explained by (iii) magnon generation, which is strong for Fe but weak for Ni [274]. Note that conservation of angular momentum requires that inelastic scattering of electrons with minority (majority) spin is accompanied by emission (absorption) of spin waves. Magnon absorption occurs only at finite temperature and is thus not included in the calculations [274]. Data for Fe were recorded at 300 K, where low-energy magnons are excited.
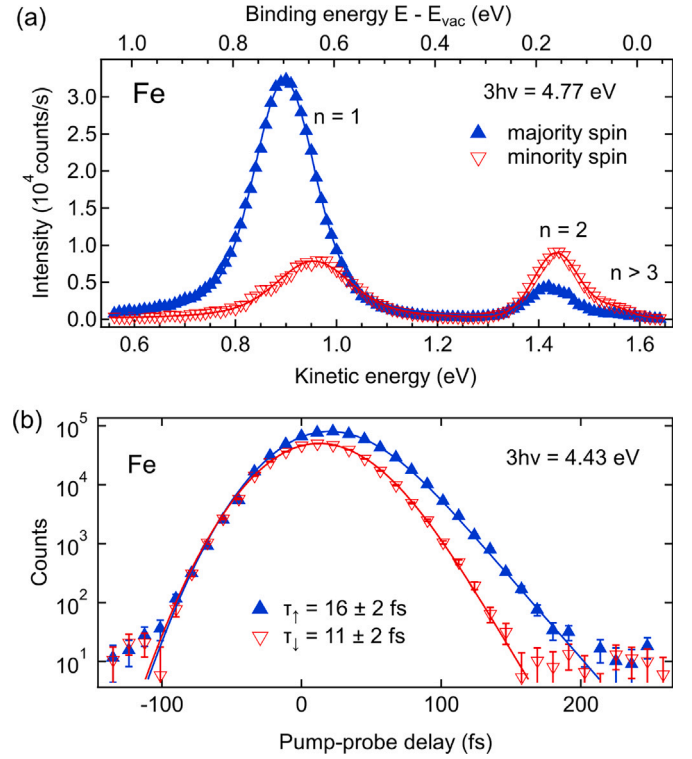

Fig. 34. (a) Spin- and energy-resolved 2PPE spectra of 3 ML Fe/Cu(100) at $k_\parallel = 0$ and (b) time-resolved traces of the exchange-split majority ($\triangle$) and minority ($\triangledown$) spin components of the $n = 1$ IPS. The Fe film has a tetragonal-distorted fcc structure. Measurements were performed at 90 K sample temperature.
Source: Figures (a) and (b) adapted from [278,279].

Obviously, processes (i)-(iv) lead to secondary electrons, *i.e.* to a multiplication of excited carriers. Note that the two final state electrons in (i) are indistinguishable, but not in (ii). Taking into account the spatial wave-function overlap, we expect that exchange scattering is stronger than direct scattering. We revealed the dominance of exchange scattering for Co in [254]. Exchange scattering favors an equalization of the number of excited minority and majority spin electrons (and holes) and hence $\tau^\uparrow/\tau^\downarrow \simeq 1$.

What is more, the 2PPE experiments allow us to independently estimate the inelastic mean free path in the $3d$ metals. Electrons photoexcited in the Cu substrate have a significantly longer lifetime than in the $3d$ FM [104]. As long as these Cu electrons can be transported through the FM adlayer, we observe a long-living tail in the 2PPE signal [271]. Varying the layer thickness, we determined λ to ≤ 7 ML (1.3 nm) for Fe, ≤ 20 ML (3.5 nm) for Co but 100 ML (17 nm) for Ni. These results corroborate studies investigating the role of spin transport in ultrafast magnetization dynamics of metallic bilayer systems [267,268,277]. *Vice versa* we expect that the 2PPE measurements of spin-dependent lifetimes in Ni [253,271] are affected by electron transport.

8.3. Image-potential states as sensors of spin dynamics

Image-potential states (IPS) were already introduced in Ch. 2. They are unoccupied electronic states in front of metal surfaces with quantized binding energy $E_n = E_{vac} - 0.85 \text{eV}/(n + a)^2$, where $n = 1, 2, \dots$ Since they are well accessible with $3h\nu$ pump and $1h\nu$ probe pulses, *i.e.* the 3rd harmonics and fundamental of a Ti:Sa(pphire) oscillator with 80 MHz repetition rate, they have long served as testbed to study ultrafast electron dynamics at metal surfaces [96,103]. Advancing spin-resolved 2PPE within the Priority Program 1133 "Ultrafast
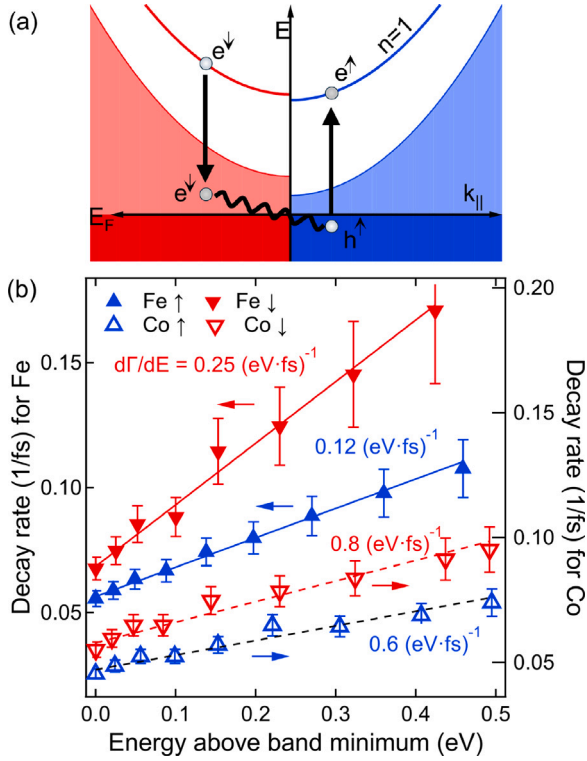
Fig. 35. (a) Sketch of an *intra-* and *inter-*band decay (dashed and solid arrows) mediated by magnon emission (wiggle line). (b) Decay rate of the $n = 1$ IPS on Fe (filled symbols, left axis) and Co (open symbols, right axis) in the majority spin ($\triangle$) and minority ($\triangledown$) spin band for increasing energy above the band minimum.
Source: Figure adapted from Refs. [255,279].

Fig. 36. (a) $E(k_\parallel)$-dispersion along ΓM and spin splitting of 5d bulk valence bands ($5d^\uparrow$ and $5d^\downarrow$) due to $5d - 4f$ exchange coupling. $5d_{z^2}^\uparrow$ is the majority spin component of the Gd surface state. (b) Magnetic linear dichroism in $4f$ photoemission at $k_\parallel = 0$.
Source: Figure adapted from [281].

magnetization processes" allowed us to study spin-dependent electron dynamics at FM surfaces. An overview can be found in [280].

Fig. 34(a) shows the Rydberg series of IPS of a 3ML Fe film on Cu(001). The IPS are exchange split with $E_{ex} = 56 \pm 5$ and 7 ± 3 meV for $n = 1$ and 2, respectively. $E_{ex} \sim (a^\downarrow - a^\uparrow)/n^3$ reflects the exchange splitting of the surface-projected bulk band-gap of Fe and scales with the penetration depth of the IPS $\sim n^{-3}$. The quantum defect a, which reflects the relative position of the image-potential states in the projected bulk band gap [8] (see Ch. 2), becomes spin dependent on FM surfaces. Recording the peak intensity of the $n = 1$ majority and minority spin components as a function of pump–probe delay, we obtained the time-resolved traces in Fig. 34(b). Displayed on a semi-logarithmic scale, the different slopes at positive delays (1.48-eV probe after 4.47-eV pump) reveal an exponential decay with spin-dependent lifetimes of $\tau_1^\uparrow = 16 \pm 2$ and $\tau_1^\downarrow = 11 \pm 2$ fs. The solid lines are fits to the data using optical Bloch equations [278]. The lifetime ratio $\tau_1^\uparrow/\tau_1^\downarrow$ of 1.45 ± 0.3 fits to the values for Fe bulk (*cf.* Fig. 32). For Co we obtained $\tau_1^\uparrow/\tau_1^\downarrow = 19/16 = 1.2 \pm 0.3$ [280].

As sketched in Fig. 35(a), the IPS shows a free-electron-like parabolic dispersion $E(k_\parallel)$ parallel to the surface. With increasing momentum $k_\parallel$, *i.e.* with increasing energy above the band minimum at $k_\parallel = 0$, the lifetime of the IPS decreases significantly since the number of *inter-* and *intra-*band decay channels (unoccupied bulk states and along the IPS parabola) increases. Fig. 35(b) shows the spin-dependent decay rates $1/\tau^\uparrow$ ($\blacktriangle$) and $1/\tau^\downarrow$ ($\blacktriangledown$) (left ordinate) as a function of energy above the band minimum. The slope of the decay rate $d\Gamma/dE$ is twice as large for the minority spin component $0.25\,(\text{eV fs})^{-1}$ as for its majority counterpart $0.12\,(\text{eV fs})^{-1}$. This can be easily explained if the emission of magnons is taken into account indicated by the wiggle line in Fig. 35(a). Minority spin electrons decaying within the image-potential band acquire twice the phase space of a majority-spin electron. *Intra-*band
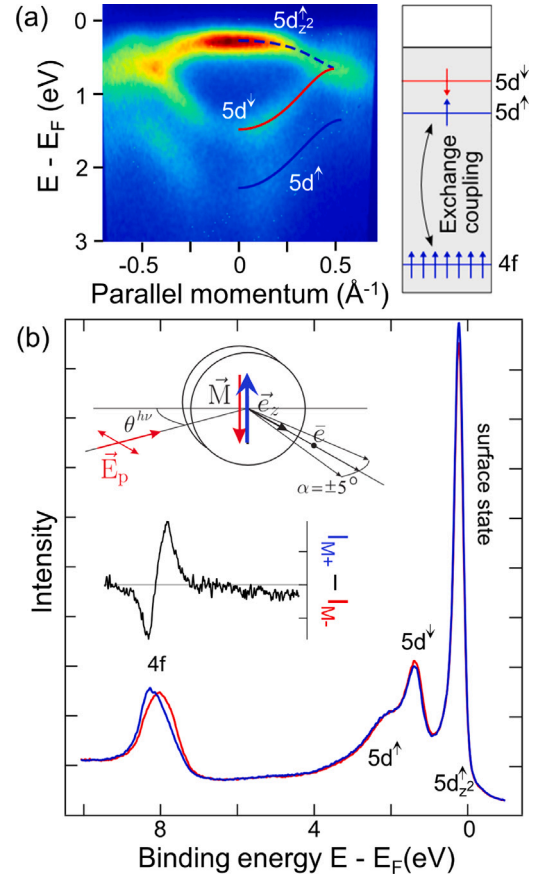
scattering occurs within the minority-spin IP band and via magnon emission into the majority spin IPS. Magnon absorption for majority-spin electrons is unlikely at 90 K sample temperature. Therefore, an electron in the majority-spin IPS can only decay along the majority spin band. The doubling of the phase space for the decay of minority-spin as compared to majority-spin IPS electrons upon magnon emission explains the doubling of the slope of the decay rate in Fe [255,274]. Obviously, magnon emission is highly efficient in Fe and occurs on the timescale of inelastic electron–electron scattering. For the IPS on cobalt we obtained a weaker spin dependence. The slope $d\Gamma/dE$ assumes values of 0.8 and $0.6\,(\text{eV fs})^{-1}$ (right ordinate in Fig. 35(b)) for the majority ($\triangle$) and minority spin ($\triangledown$) IPS. Hence for Co the effect of magnon emission and thus an apparent spin flip is significantly smaller.

8.4. tr-ARPES reveals disparate dynamics of 5d and 5f magnetic momenta in gadolinium

Despite its importance as a material component in all optical switching [241–243], the rare earth metal Gd is an ideal system to compare equilibrium *vs* non-equilibrium exchange interaction and spin dynamics. The $E(k)$-map in Fig. 36(a) illustrates the Gd valence electronic structure around the Γ-point for $k_\parallel$ along ΓM. ARPES data in Fig. 36 were recorded in the FM state at 90 K sample temperature. The localized Gd $4f^7$ electrons at ~ 8 eV binding energy contribute most to the atomic moment with $\mu_{4f} = 7\mu_B$ per atom. They spin-polarize the 5d valence electrons. The exchange splitting of the 5d bulk bands E_{ex} is proportional to the 5d magnetic moment ($\mu_{5d} = 0.55\mu_B \propto E_{ex} \simeq 0.9$ eV
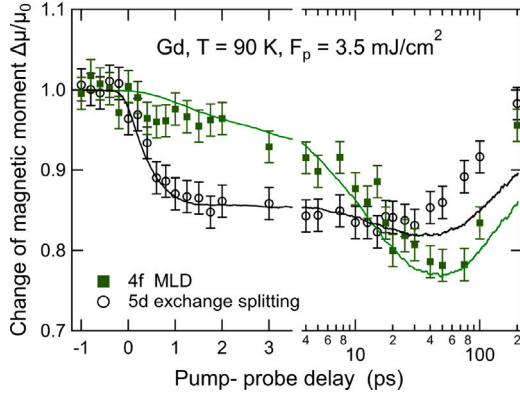
Fig. 37. Change of 5d exchange splitting and 4f magnetic linear dichroism as a function of pump–probe delay.
Source: Figure adapted from [262].

Fig. 38. Stoner-like behavior of the Gd surface state after laser excitation. (a) Spin-resolved spectra for selected pump–probe delays, (b) spin polarization and (c) binding energy. The spin polarization (filled circles) is derived from the peak areas in (a) and from time- and spin-resolved scans (open circles) at constant binding energies of 0.12 and 0.2 meV, indicated by the dashed vertical lines in (a).
Source: Figure adapted from Ref. [263].

in the ground state, $T \rightarrow 0\,K$) [260,262]. The 5d valence electrons mediate in turn magnetic ordering below the Curie temperature $T_C = 293\,K$ via indirect exchange interaction. Fig. 36(b) shows an energy distribution curve around normal emission ($\Delta k_\parallel = \pm 0.1\,\text{Å}^{-1}$). Reversal of the in-plane magnetization direction $\pm M$ leads to a small change in $4f$ intensity I^{4f}. This magnetic linear dichroism (in the angular distribution of the photoelectrons) MLD(AD) $= \int dE\, |I^{4f}_{M+} - I^{4f}_{M-}| \,/\, |I^{4f}_{M+} + I^{4f}_{M-}|$ is a measure of the $4f$ magnetic moment [282]. Thus tr-ARPES gives access to both μ_{5d} and μ_{4f} in a single experiment.

The time-resolved data in Fig. 37 were recorded using 1.61-eV pump pulses at 3.5 mJ/cm^2 pump fluence and 37.0-eV probe pulses, corresponding to the 23rd harmonic of our higher-order harmonic generation (HHG) setup. Thereby we reach a perpendicular momentum $k_\perp \simeq 6 \cdot \Gamma A$, i.e. close to the Γ point of the 4th Brillouin zone of Gd, where we probe the exchange-split Gd Δ_2-like Σ bulk valence bands. For further experimental details see [261,283]. It was very surprising that the magnetic moments of 5d and 4f have different dynamics, since the $5d - 4f$ intra-atomic exchange $J_{5d-4f} = 130\,meV$ suggests ultrafast exchange of angular momentum $\tau = \hbar/J_{5d-4f} \simeq 5\,fs$. However, despite including J_{5d-4f}, atomistic spin dynamics simulations (solid lines in Fig. 37) nicely reproduce the experimental result, if 5d spins are coupled to the electron temperature T_e, but 4f spins solely to the phonon temperature T_p. Since the 5d electrons reach temperatures of $T_e \sim 3000\,K$, their energy is sufficient to overcome the 4f exchange field. The transient breakdown of 5d-4f intra-atomic alignment only recovers on the $\sim$15-ps timescale of 4f-spin-lattice relaxation. The latter is slow, since rocking of the ions does hardly couple to the half filled $4f^7$ shell with spherical symmetric charge distribution ($L = 0$). The measurement of the spin polarization of the 5d bulk-bands is still an outstanding challenge. However, we studied the spin polarization of the 5d-derived $5d_{z^2}^\uparrow$ surface state, for which we expect comparable behavior.

8.5. Transient spin polarization of the $5d_{z^2}^\uparrow$ surface state in the ultrafast demagnetization of Gd

By combining an exchange-scattering spin detector [284] with a 300-kHz regenerative Ti:Sa amplifier, we were able to perform the first spin-, time-, and energy-resolved ultrafast demagnetization experiment [263]. In this experiment, we used the amplified fundamental as 1.55-eV pump and its 4th harmonic as 6.2-eV probe pulse to study the surface state of Gd (Figs. 36 and 38(a)). We found that the surface state shows an almost classical Stoner-like behavior in ultrafast demagnetization. Its exchange splitting decreases while its spin polarization
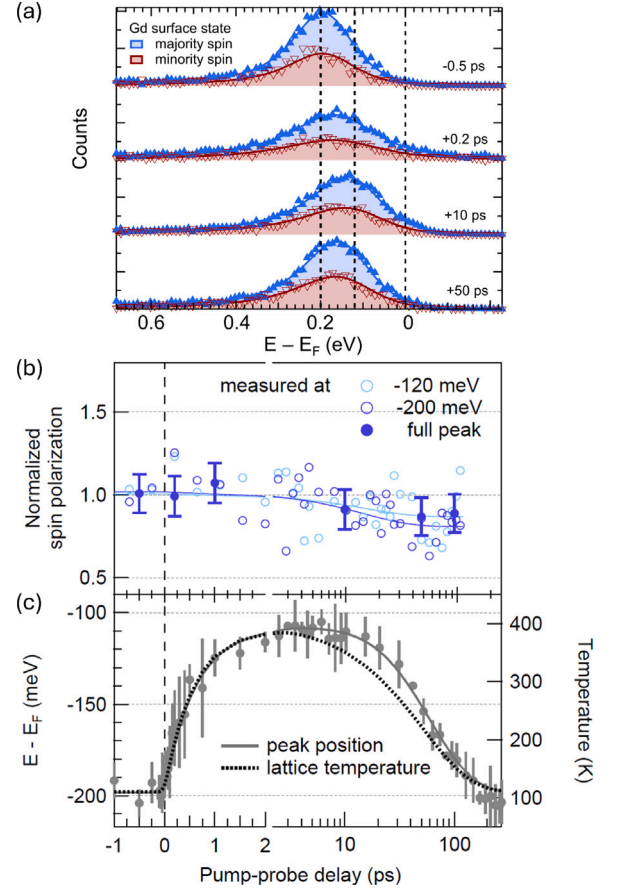
remains. In contrast, in the thermal phase transition complete spin mixing (also called band mirroring) but finite exchange splitting is observed at T_C [285]. Fig. 38(b) and (c) depict the spin polarization and the energetic shift of the majority-spin surface state. While the occupied surface state shifts within 1 ps towards its unoccupied minority spin partner (not shown), we do not observe a noticeable change in the spin polarization of this state. The electronic temperature is increased by the optical excitation (40 fs pump pulse) and subsequently drives the Stoner-like demagnetization by electron–phonon scattering (Fig. 38(c)). The spin polarization (Fig. 38(b)) decreases later with a time constant of $\sim$15 ps. We have modeled the lattice temperature T_p from the measured electron temperature T_e with the two temperature model (dotted line in Fig. 38(c)) [263]. At delays $<$2 ps the peak position follows T_p. Spin polarization and binding energy only depend on each other for longer delays. The deviation, which we find between the decay times of exchange splitting and spin polarization, parallels the demagnetization of 5d-valence and 4f-core levels. This suggests that the spins of the surface state and valence bulk bands stay aligned to that of the 4f shell, while all valence states (including the surface state) demagnetize Stoner-like. While the 5d valence electrons are directly affected by the 1.55-eV optical excitation leading to the decreasing exchange splitting, the 4f spin system remains cold for a long time, stabilizing the spin polarization. In contrast, in the equilibrium phase transition, these processes cannot be separated. Using ultrafast laser excitation, we are

able to disentangle exchange splitting and spin polarization, which opens a completely new view on the magnetic phase transition.

Finally, we would like to note that meanwhile two spin-resolved photoemission experiments have been performed using 10-kHz HHG sources to study spin dynamics in Co [264] and Fe [265]. In both experiments, demagnetization via band mirroring was observed without changing the exchange splitting. This implies that demagnetization takes place via magnons, which lead to spin mixing. For Fe we have seen strong evidence for inelastic electron scattering via magnon emission in Sections 8.2 and 8.3. For Co and Ni we would have rather predicted a Stoner-like behavior, *i.e.*, a change of the exchange splitting upon optical excitation [257]. But also for Ni it has been suggested that the spin system heats up on the time scale of inelastic electron–electron scattering [259]. Performing these experiments is still very tedious, but there is the prospect of advancing spin- and time-resolved ARPES in the future.

8.6. Summary and perspective

We have given a brief introduction to the field of ultrafast spin dynamics and explained what microscopic details can be revealed with spin- and time-resolved ARPES. This report is certainly not complete. For example, we were able to follow the spin transport in an antiferromagnetically coupled Gd/Fe bilayer by the ultrafast reverse change of spin polarization in the Gd and Fe layer [286]. Furthermore, we have shown that optically induced spin transfer [287] leads to a simultaneous ultrafast reaction of the exchange splitting [260].

What is on our wish list? We would like to combine a HHG source with high repetition rate (100–500 kHz), tunable and selectable photon energies (20–100 eV), and short pulse duration (20 fs) with efficient spin-resolved electron detection using, *e.g.*, the combination of a momentum microscope (Ch. 11) and a hemispherical analyzer [92]. Much of this equipment already exists, but the reliable combination of all components remains a challenge. It also requires an experimental environment of high standard in terms of air conditioning, temperature stability, and low interference due to vibrations. Under these conditions, spin- and time-resolved ARPES will most certainly provide unprecedented insights into ultrafast spin dynamics and femtomagnetism. Developing a microscopic understanding of ultrafast spin dynamics is on the one hand a building block to realize spintronic applications with THz speed and will on the other certainly train new scientists for future challenges in spin dynamics, surface science, and their application.

9. From perturbative to nonperturbative time-resolved photoemission

Hrvoje Petek, Andi Li, Zehua Wang, Marcel Reutzel, Xintong Li, Shijing Tan, and Bing Wang

9.1. Introduction

Light can act on solid or solid surface perturbatively by exciting multipole transitions between eigenstates [10,288–290], or nonperturbatively by external fields accelerating charges [291–293]. The acceleration of electron drift velocity by intense optical fields, as if it were a classical particle, has been invoked in high harmonic and attosecond pulse generation in gaseous matter [294,295]. When intense optical pulses are applied to solids, the interaction of driven electrons with periodic lattices undergo Bloch oscillations to generate Wannier–Stark ladders of states that have been implicated in high-harmonic emission from solids [296–300]. Indeed, driving of the electron motion in periodic lattices by intense optical fields as a means of actuating coherent THz or PHz processes, is of keen interest in the emerging field of lightwave electronics [301–305] and for achieving nonequilibrium phases of matter with novel functionality [306,307]. Intense nonlinear fields have also been applied to tracing of attosecond physics in field emission from nanometric metallic tips and related nanoparticles as sources of pulsed electron beams with potential applications in ultrafast electron microscopy and PHz electronics [291,292,308–311].

These methods for the probe and control of matter motivate the interrogation of electronic responses in crystalline solids with energy, momentum, and time resolution, which we describe here. From a surface science perspective, photoelectron emission from single crystalline surfaces provides a spectroscopic measure of the occupied solid and solid surface eigenstates with the orbital, magnetic, spin, and momentum quantum state specificity [312–315]. The application of tunable pulsed lasers has opened the possibility of also probing the transiently populated excited states of solids [316,317] with picosecond and even down to attosecond time resolution by methods of time-resolved multiphoton photoemission spectroscopy (TR-mPP) [77,104,156,302,318, 319]. Moreover, multiphoton transient spectroscopy has enabled phase and energy resolved study of nonequilibrium electron and nuclear dynamical phenomena in solids and solid surfaces [10,87,169,289, 320–324]. TR-mPP studies of the unoccupied electronic structure and dynamics involve either one or two-color excitation schemes. Time- and angle-resolved photoemission (TR-ARPES) typically employs two-color excitation, where one pulse populates unoccupied states by driving electronic transitions, and a second pulse further promotes the same electrons into the photoemission continuum typically above the photoemission horizon. This achieves full Brillouin zone spectroscopic imaging of excited electronic bands [30,120,169]; and evolution of electronic populations in energy, momentum, and time. The focus here, however, is on one-color multiphoton photoemission spectroscopy as a means of probing coherent responses of solids and surfaces with optical phase resolution, with a further goal of exploring the transition from perturbative to nonperturbative light–matter interactions. One-color methods, however, are challenged in exciting electrons above the photoemission horizon, limiting them to exploration of the electronic structure and electron dynamics near the Γ-point of the Brillouin zone [166,325]. Here we contrast the coherent responses of single crystal Cu(111) and Ag(111) surfaces in resonant or near-resonant one-color multiphoton excitation driving mPP from the occupied Shockley Surface state (SS), via the intermediate first ($n = 1$) image potential (IP) state into the final state (E_{fin}) photoemission continuum. We examine how intense optical fields alter (dress) the surface electronic structure [326] entering a transition from perturbative to nonperturbative interaction by projecting electrons from the field-dressed intermediate states into the photoemission continuum. While, the single particle electronic structures of Cu and Ag are very similar, their disparate screening responses
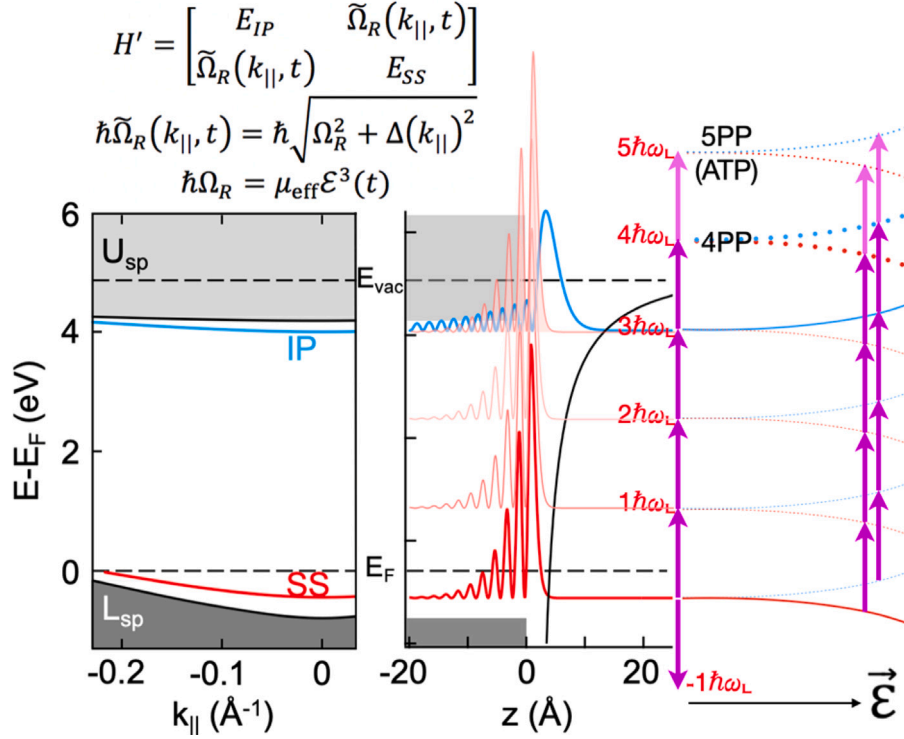
Fig. 39. The surface electronic structure of Cu(111) and its dressing in mPP process. The energy–momentum dispersion of SS and IP states within the projected band gap between the lower (Lsp) and upper sp-bands (Usp), as well as their surface/bulk probability densities. Excitation at $\hbar\omega_L = 1.54$ eV generates a Floquet ladder of states that brings the SS and IP states into three-photon resonance, leading to their field dressing, and ultimately elevates the coupled states above the vacuum level, E_{vac}, where 4PP and 5PP photoelectrons are emitted and detected. The dressing of the SS and IP states in the nonlinear excitation process is described by the perturbation Hamiltonian, H', where the off-diagonal elements consist of the generalized Rabi frequency, $4\hbar\Omega_R$, which includes the third-order electric dipole interaction, $\mu_{eff}\mathcal{E}^3(t)$, and detuning from the resonance by the surface band parallel dispersion, $\Delta(k_{||})^2$ [326]. As the optical field strength increases, the Stark effect, or more appropriately the A^2 vector potential interaction term in the Coulomb gauge, causes band repulsion within the Floquet ladder such that the photoemitted electrons carry the information on the Autler–Townes splitting of the optically coupled bands. Electrons excited to above the vacuum level can be promoted up and down in energy by Volkov process leading to above threshold photoemission (ATP).

produce distinct outcomes to application of intense optical fields [327]. The distinction of the low to high field physics is usually defined by quantifying the Keldysh parameter $\gamma = \omega(2mI_0)^{1/2}/(e\mathcal{E}_0)$ [328–330], where ω and $\mathcal{E}_0$ are the frequency and envelope amplitude of the driver field, I_0 is the ionization potential of the penultimate state, and e and m are the electron charge and mass. We perform experiments on Cu(111) and Ag(111) samples well within the perturbative limit $\gamma \gg 1$, yet as we follow the field interference amplitude crests and troughs, the response cycles between the perturbative and nonperturbative.

To further distinguish between perturbative and nonperturbative responses we consider how the complex ultrafast optical fields interact with matter. An optical field will interact with a solid by inducing linear and nonlinear polarization, which can be expressed as a power series of the applied field:

$$P^{tot}(E) = \epsilon_0 \ \Sigma_{i=1}^{\infty} c_i \ \chi^{(i)} E^i,$$

where c_i is a degeneracy factor, $\chi^{(i)}$ are terms of the complex linear and nonlinear susceptibility, and E^i are powers of the applied field. While odd i terms are found in nonlinear optics textbooks to describe the nonlinear optical refraction responses, such as harmonic generation [331], we emphasize the even terms, which are responsible for the linear and nonlinear photoemission [289,290,332,333]. We note that in nonlinear refraction, the detected photons communicate their origin in the nonlinear electronic response in matter that is integrated over energy and momentum eigenstates, while in photoemission this is communicated by photoemitted electrons that generally are eigenstate resolved. The expression for $P^{tot}(E)$ has two important implications. The first is that the condition that a nonlinear process is perturbative, is that the series converges, implying that for progressive terms, the condition $n_i/n_{i+1} < 1$ is satisfied. In a nonperturbative response, one

finds that, for example, the higher order ATP response exceeds the lower order mPP response, as can be seen in Fig. 4 of Ref. [334]. The second is that the applied field enters matter to transiently change its electronic properties in a coherent fashion that is communicated by photoelectrons with eigenstate resolution.

9.2. Optical dressing of the electronic band structure of Cu(111)

We examine the coherent optical responses in interferometric TR-mPP (ITR-mPP) from perspective of the Floquet theory [335–337]. In this experiment, mPP is measured in response to excitation by identical pump and probe pulses as their delay is scanned by a Mach–Zehnder interferometer with <100 as delay time resolution. The constructive and destructive interference crests and troughs modulate the electric field amplitude turning on and off high field dependent factors in mPP. In a perturbative regime, time-periodic optical potentials act in conjunction with space-periodic crystalline potentials to generate Floquet ladders where electronic bands are displaced in energy by integer photon quanta. Floquet physics has been vividly illustrated in TR-ARPES experiments, where intense IR fields generate virtual replicas of occupied bands of 2D materials, and VUV excitation projects them into the photoemission continuum to be detected [338]. Floquet bands are generated even on sub-optical cycle time-scales by single cycle THz field excitation [206]. Spectroscopy of Floquet ladders exposes avoided crossings of bands belonging to different photonic orders [58,59,206, 207,338]. We first consider the mPP excitation of Cu(111) where the Floquet ladder extends into the photoemission continuum to reveal dressing of the surface state bands in a resonant three-photon IP←SS excitation [326,334].

Fig. 39 shows the relevant band structure of Cu(111) for the discussion of mPP process that is induced by excitation with ~20 fs pulses
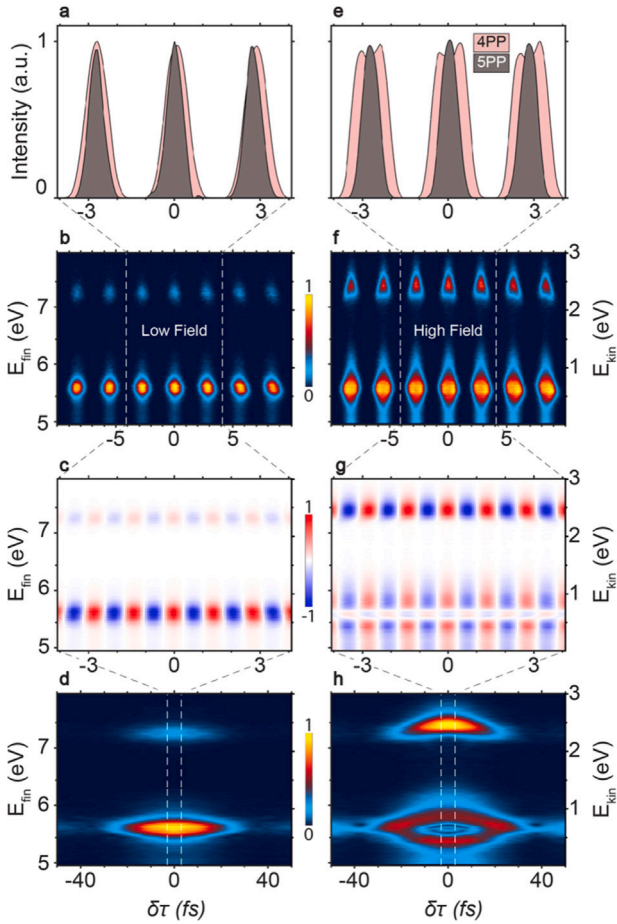
Fig. 40. ITR-2PP measurements of the field dressing of the SS and IP bands in perturbative mPP process. The measurements are performed at low, 0.13 V/nm (a–d), and high 0.32 V/nm (e–h), field strengths. (b) and (f) show the high and low field strength interference fringe signals from ITR-mPP measurements in three-photon resonant IP←SS excitation with $\hbar\omega_L = 1.53$ eV pulses of ~ 20 fs duration. The low field 5PP signals appear as replicas of 4PP, while at high field the fringes are distorted in energy and have different appearance in the two orders. (a) and (e) Show the line profiles of 4PP and 5 PP signals at low and high fields. Low field fringes are narrower in 5PP, because it is a higher order nonlinear process. (f) The high field fringes show splitting of 4PP fringes in crest maxima, because 5PP process depletes the population from 4PP. This can be attributed to Volkov ATP process. (c and g) Energy dependent phase signal from the $2\omega_L$ Fourier component of the ITR-mPP interferogram near $\delta\tau = 0$ fs that at low field the 4PP and 5PP signals have the same phase, while at high field the elongated 4PP fringes have the same phase as the 5PP fringes are associated with the field crests, while at the IP←SS resonance energy, the signal appears with the opposite phase, signifying that it is coming from the troughs. (d–h) The inverse transforms of the $2\omega_L$ Fourier component at low field shows a replication of the resonant IP←SS excitation signal from 4PP to 5PP, without distortion. The same signal at high field shows the dressing of the IP and SS bands by the Rabi frequency. The 5PP signal is pushed to higher energy than in low field and it appears more intense than 4PP, because it is more localized in energy and time.

at $\hbar\omega_L = 1.53$ eV, which drive the three-photon resonant IP←SS transition [323,326]. The intense optical field of ~ 0.32 V/nm generates a Floquet ladder raising the SS three-photon Floquet state into resonance with the IP state. This interaction is recorded in 4PP by projecting the electrons with the encoded interaction into the photoemission continuum. The multiphoton interaction is further captured in 5PP by above threshold photoemission (ATP). The three-photon resonant interaction causes formation of new eigenstates that are separated in energy by the instantaneous Rabi frequency [339] (see the perturbation Hamiltonian in Fig. 39) where the AC Stark effect acting on the Floquet ladders causes the Autler–Townes splitting of the electronic bands. The Stark effect driven by the applied field can both modulate the IP and SS band energies, as in Cu(111), as well as opening their

coupling to free electron vacuum states by lifting their energies by the $\mathcal{E}^2$ dependent ponderomotive energy, as happens in Ag(111). Here, the ponderomotive acceleration refers to electron quiver in an intense oscillating electric field, which increases its energy according to the A^2 term in light–matter interaction term (A is the vector potential of the internal optical field), for example in the Coulomb or velocity gauge [340].

Fig. 40 illustrates the onset of SS and IP state dressing in 4PP and 5PP at "low" and "high" optical excitation fields. The interferometric scanning of the delay, $\delta\tau$, between identical pump–probe excitation pulses at the low field strength shows the 4PP and 5PP signals enhanced by the IP←SS resonance [Fig. 40(a-b)] coming to the maximum intensity for constructive interference at $\delta\tau \sim 0$ fs. As expected for a perturbative process, the 5PP signal is approximately an order-of-magnitude weaker than 4PP, and has narrower fringe width [Fig. 40(a)], as expected for a higher order process. Fig. 40(c) shows a decomposition of the interferometric signal in Fig. 40(b) into its Fourier component that oscillates at twice the ω_L driving frequency ($2\omega_L$ phase). Notably, the $2\omega_L$ phase is the same for both the mPP orders [Fig. 2(b)], with their inverse Fourier transform of the $2\omega_L$ component appears as a single resonance peak in 4PP and 5PP [Fig. 40(c-d)]. At high field, however, the interference fringes for the 4PP signal split having a local minimum at the field crests. This suggests that the 5PP process depletes the 4PP signal [Fig. 40(e)]. Moreover, the 4PP and 5PP fringes become differently elongated in the energy dimension [Fig. 40(f)]. The Fourier filtered signal at the $2\omega_L$ phase [Fig. 40(g)] at the IP←SS resonance has a phase shift in 4PP, meaning that the undressed resonance condition occurs in the 4PP signal for the field troughs, while the dressed 4PP and 5PP signals occur for the field crests. The field dressing of the Cu(111) band structure is most vividly seen in Fig. 40(h), where the single peak at resonance in Fig. 40(d) becomes partitioned into two maxima separated by the Rabi frequency due to the Floquet state repulsion at $\delta\tau \sim 0$ fs [326]. Driving the IP←SS three-photon resonance dresses the Floquet bands causing Autler–Townes splitting at the Rabi frequency [341]. Note, that the elongation of the fringes in the energy dimension [Fig. 40(f)] and the different appearance of the 4PP and 5PP fringes already convey the band dressing and likely field driven Volkov type ATP population transfers [205,342]. Thus, mPP photoelectron distributions via the IP←SS resonant excitation evidence the electronic band dressing and how multi-order Floquet and Volkov processes modify the Cu(111) electronic band structure, presaging nonperturbative electron dynamics in the solid state [326,342,343].

9.3. Competition between the perturbative and nonperturbative electron emission from Ag(111)

Next we consider the transition from perturbative to nonperturbative photoemission in ITR-2PP spectroscopy of Ag(111). While DC field emission is a venerable topic in surface science [344,345], and Stark effect in STM spectroscopy of surface states is well understood [346,347], a theory describing the onset of high field emission from solid surfaces is a work in progress, where Ag(111) surface provides an intriguing example [343]. While the single-particle electronic structures of Ag(111) and Cu(111) are very similar [348], the onset of nonperturbative photoemission appears very differently on account of their collective plasmonic responses [327,349,350]. Specifically, Ag(111) has a sharp bulk plasmon resonance at $\omega_p = 3.8$ eV corresponding to a zero in its macroscopic dielectric function. At low excitation field strengths, the 2PP spectrum of low index Ag(111) surfaces has a plasmonic photoemission component at an energy $2\omega_p$ above the Fermi energy, E_F [319,351–353]. The excitation in Fig. 41 is performed below ω_p, where one can expect that the incident (vacuum) optical field at 0.29 V/nm to generate enhanced surface fields on account of the screening response, as well as retardation of its group velocity as its dielectric function approaches zero at the bulk plasmon frequency [327,349,354].
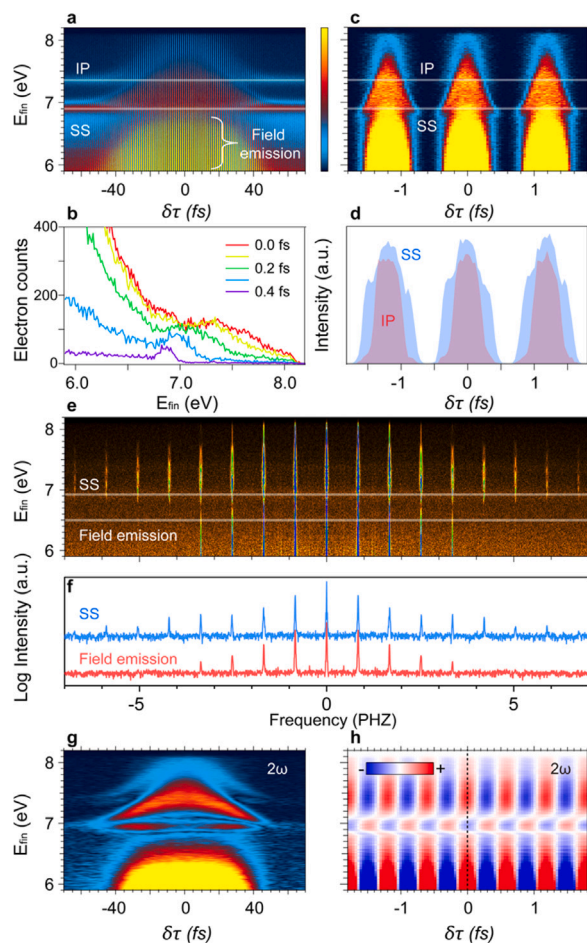
Fig. 41. ITR-2PP measurements of field emission from on Ag (111) surface. (a) 2D interferogram of the photoelectron counts vs E_{fin} and time delay ($\delta\tau$) for excitation at $k_\parallel = 0\,\text{Å}^{-1}$ for excitation with $\hbar\omega_L = 3.44\,\text{eV}$ pulses of $\sim$30 fs duration. The white lines indicate the E_{fin}'s of SS and IP states in low field 2PP process. The brace indicates the field emission signal that is driven at the pump–probe field crests reaching the maximum field strength of 0.29 V/nm. (b) Line profiles of photoelectron counts vs E_{fin} taken in 100 as intervals in the $\delta\tau = 0 - 0.4$ fs range from the 2D interferogram in (a). The line profiles show the shift of the SS state peak and growth of the field emission as the excitation field crests. (c) Enlarged region of the 2D interferogram in (a) showing the structure of individual fringes in response to the field interference modulation near $\delta\tau = 0$ fs. (d) Line profiles extracted from (c) at the energies of the SS and IP states showing transitions from mPP to field emission as the field crests. (e) 2D Fourier-transform spectra of the interferogram in (a) showing the Fourier components of dominant SS and field emission signals, which oscillate, respectively, at frequencies up to $8\omega_L$ and $4\omega_L$. (f) Line profiles extracted from (e) at the SS and field emission energies (indicated by white lines) showing their disparate Fourier spectra. (g) Inverse Fourier transform of the $2\omega_L$ component in (a) showing the field effects on the SS and IP states, as well as the field emission signal. (h) Energy dependent phase signal from the $2\omega_L$ Fourier component, showing the phase inversion between mPP signal from the SS state, which dominates in the field throughs, and field dependent signal which dominates at the crests.

Fig. 41(a) shows an interferogram of the normal emission signal taken from an ITR-2PP movie of energy, momentum, and time dependence of 2PP from Ag(111) (excitation with $\sim$ 30 fs pulses at $\hbar\omega_L = 3.44$ eV). The interferogram shows sharp 2PP signals from the SS and IP states that are excited non-resonantly at delays where the pump–probe pulse overlap is insignificant ($|\delta\tau| \geq 40$ fs). The dominant signal, however, appears below the SS peak $|\delta\tau| \leq 40$ fs, which we attribute to *intra*-band current driven photoemission. The interferogram shows evolution from 2PP to emission in presence of internal field, which we refer to as field emission and unravel. Fig. 41(b) shows several energy line profiles taken in $\delta\tau = 0 - 0.4$ fs range, where the pump–probe field approaches the crest at 0 fs. At 0.4 fs the signal is dominated by the SS peak (and the much weaker IP state peak) expected from

the perturbative 2PP spectra of Ag(111) [323,351]. When the delay $\delta\tau \to 0$ fs, the field cresting causes an upshift of the SS and IP peaks and a dominant signal below the SS peak to appear; we attribute these changes to ponderomotive energy of electrons and field driven intraband current photoemission. Ultimately, the AC Stark and the ponderomotive force are related interactions exacted by high fields on photoelectron distributions [340]. Thus, Fig. 41(b) shows, that a 0.4 fs advance of the field switches from the perturbative to nonperturbative light–matter interaction. Next, we examine this transition in images of individual interference fringes in the energy–time domain. The fringes in Fig. 41(c) have arrow-like shapes that repeat in $\sim$1.2 fs optical cycle intervals of the 3.44 eV field. The arrow points start at the 2PP energy of SS and shift up as the ponderomotive force grows when the field crests, as already observed in Fig. 41(b). Forming the arrow shaft at lower energy is the field emission signal, which also grows as the field crests. In Fig. 41(d) we show line profiles at the SS and IP energies. The SS line profile has a head-and-shoulders appearance: the shoulders correspond to the weak field SS signal in 2PP, and the head is the high field emission signal. At the IP state energy, the shoulders are much weaker and field processes dominate as the field crests. Furthermore, we examine the mPP and field responses by performing the Fourier transform (FT) of the data in Fig. 41(a). The FT in Fig. 41(e) shows distinct differences in the mPP and field emission responses. The line profiles in Fig. 41(f) show the SS signal has FT components up to $8\omega_L$, or 6.8 THz, while the stronger field emission signal has components only up to $4\omega_L$. In a second-order interferometric autocorrelation that has $\mathcal{E}^4$ dependence we would expect FT components up to $2\omega_L$. The fact that it is much higher for the data in Fig. 41(a) implies that higher order processes must be involved to generate the complex fringes in Fig. 41(c). The FT components of the field emission signal are considerably more truncated as it is expected to follow the $\mathcal{E}^2$ dependence of the AC stark effect. The high FT orders must result from commingling of the perturbative 2PP and nonperturbative field emission responses of Ag(111) on a single optical cycle time scales. To see the how these interactions define the measured photoelectron distributions, in Fig. 41(g) we present the inverse transform of the $2\omega_L$ Fourier component. The SS and IP features evolve from their 2PP energies at long $\delta\tau$ and undergo a ponderomotive shift as $\delta\tau$ decreases, just as seen in Fig. 41(b and c). Finally, in Fig. 41(h) the fringe phase signal from the $2\omega_L$ Fourier analysis shows that the 2PP signal at the SS energy is oscillating out-of-phase with the dominant field emission signal. This can be interpreted both as the mPP signal belonging to the interference troughs, as well as the SS state population being depleted by the field emission at the crests.

9.4. Conclusions

While Steinmann, Fauster, Echenique, Höfer, and their coworkers have pioneered the studies of the surface states of noble metals as the drosophilae for defining the surface electronic structure, dynamics, and adsorbate interactions [103,317,348,355–357], the same states offer a forum for exploring the transition from perturbative mPP to nonperturbative field emission coherent optical responses of solid state materials in the attosecond time and PHz frequency domains. While such visions may seem futuristic, we need to look back at the original application of noble metal surfaces as optical mirrors [358]. The reflection that we see every day comes from the attosecond collective response of free electrons in a metal that transfers the information coherently. Our experimental tools are approaching the capability to coherently probe [320] and control [321] the collective electronic screening responses of noble metal on a single optical cycle time scale at frequencies that target specific electronic responses. The two examples on interferometric probing of coherent responses of surface states of Cu(111) and Ag(111) surfaces show how light can interact perturbatively to engineer the electronic structure of matter through multiphoton interactions. We can also tailor optical fields to drive nonperturbative field interactions

to drive lightwave electronic and quantum plasmonic phenomena at PHz frequencies [305,359]. By tailoring optical fields to drive collective electronic responses, metal surfaces may no longer act only as passive mirrors of information, but we may design them to control the electronic and optical responses for applications in probing and controlling matter at the space–time limit [170,226,360–365].

10. Subcycle photoemission

Ulrich Höfer and Rupert Huber

10.1. Concept of subcycle photoemission

In the usual pump–probe scheme of time-resolved ARPES a photon in the near-infrared (NIR), visible (VIS) or ultraviolet (UV) spectral range excites an electron into a previously unoccupied state. Photoemission induced by a UV or extreme ultraviolet (XUV) pulse with variable time delay then probes the redistribution of the excited electrons and their lifetime in momentum space. Recent examples of this powerful pump–probe scheme from our group include the formation dynamics of dark excitons in monolayer semiconductors [162], time-resolved orbital tomography of adsorbed organic molecules [366] or the dynamics of photocurrents in the Dirac cone of topological insulators [367]. Many other examples are discussed in other chapters of this review.

A new development of time-resolved APRES makes use of the carrier electric field of intense terahertz (THz) and mid-infrared (MIR) pulses to accelerate the electrons and detects the dynamics with sub-optical-cycle time resolution (Fig. 42). The lightwave also interacts with the photoemitted electrons, and photoelectron streaking allows for *in situ* extraction of the electric field waveform directly at the surface [368]. With streaking compensation, subcycle APRES then provides unique insights into light–matter interaction through band-structure movies with a time resolution better than the oscillation period of the driving lightwave [206,368]. A convenient estimate whether an experiment accesses the strong field regime or not, is provided by the ponderomotive potential $U_p = e^2 E^2 / 4 m_e \omega^2$, i.e. the cycle-averaged quiver energy of a free electron in an electromagnetic field. If it exceeds the photon energy $\hbar\omega$, i.e. $U_p \gg \hbar\omega$, the classical electric field $E(t)$ of the lightwave dominates light–matter interaction over the quantized transitions with energy $\hbar\omega$ or multiples of $\hbar\omega$ of the usual perturbative regime.

Table 1 lists parameter sets for representative subcycle photoemission conditions. The first two rows correspond to the recent experiments performed at center frequencies of the driving field of 1 THz [368] and 25 THz [206]. In both cases, U_p exceeds $\hbar\omega$, so that the lightwave character dominates. This is even more so, when one considers that quasi-relativistic Dirac electrons with a linear dispersion were accelerated in both cases and thus the appropriate expression for the quiver energy in the material becomes $eE\upsilon_F / \sqrt{2\omega}$. The 60 THz case shows a realistic goal for the next-generation subcycle photoemission
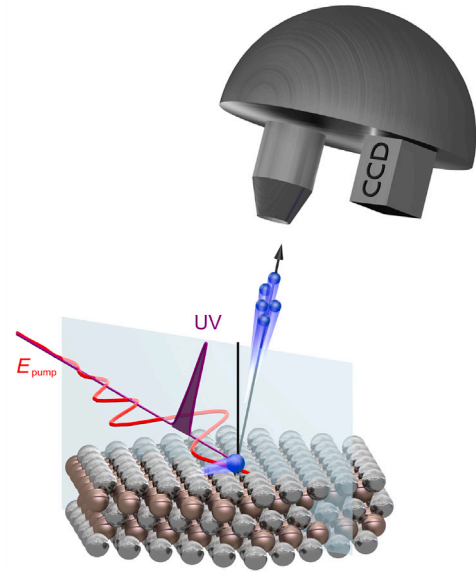

Fig. 42. Concept of subcycle ARPES. Electrons are accelerated by the pump electric field E_{THz} and photoemitted by UV probe pulses that are shorter than an optical half cycle of E_{THz}. They are probed by an hemispherical electron analyzer in the direction normal to the plane of incidence indicated by a transparent rectangle.
Source: Adapted from Ref. [368].

experiment, where the large field strength raise high hopes to observe extreme strong-field phenomena in momentum space. In contrast, the 500 THz case implying, *e.g.*, a VIS pump pulse with a fluence of 3 mJ/cm^2 in a 30-fs pulse sufficient to induce a phase transition [369], clearly remains in the photon excitation regime. Typical UV probe pulses are many orders of magnitude away from the strong-field regime.

10.2. Lightwave-driven Dirac currents

In the first experiment, this novel pump–probe scheme was used to measure ballistic electron currents in the Dirac surface state of the three-dimensional topological insulator Bi_2Te_3. Reimann et al. observed how an intense 1-THz lightwave accelerates Dirac fermions within the quasi-relativistic band structure of the topological surface state (TSS) of Bi_2Te_3 [368]. As for the probe pulse, a 100-fs, 6.2-eV UV light source was used. This is the best choice for the 1-THz waveform with an optical period of 1 ps, allowing for subcycle time resolution and high energy resolution simultaneously.

Fig. 43 displays three snapshots of ARPES spectra. The left and the right branches of the Dirac cone are initially occupied up to the same Fermi energy and Fermi wave vector. When the THz field is applied, the occupation becomes notably asymmetric. The opposite shift of the population for opposite THz field polarity hallmarks an ultrafast displacement of the Fermi surface in momentum space. The dynamical shift of the Fermi wave vector Δk_F can be immediately converted to a current density, whose peak intensity reached 2 A/cm [368]. Moreover, the dynamical modulation of the Fermi–Dirac distribution was modeled by a semiclassical Boltzmann equation including an elastic and an inelastic scattering term. As the solid lines in Fig. 43(d)–(f) show, the model excellently reproduced the experiment when the scattering times were set to 1 ps. Thus, the experiment demonstrates the first direct, contact-free probe of the inertia-free surface currents carried by the topologically-protected Dirac Fermions. The long scattering time and the large Fermi velocity of $\upsilon_F = 4.1$ Å/fs imply ballistic mean free paths of several 100 nm, opening a realistic parameter space for dissipation-free lightwave electronic devices.

Table 1
Representative parameter sets for subcycle photoemission.

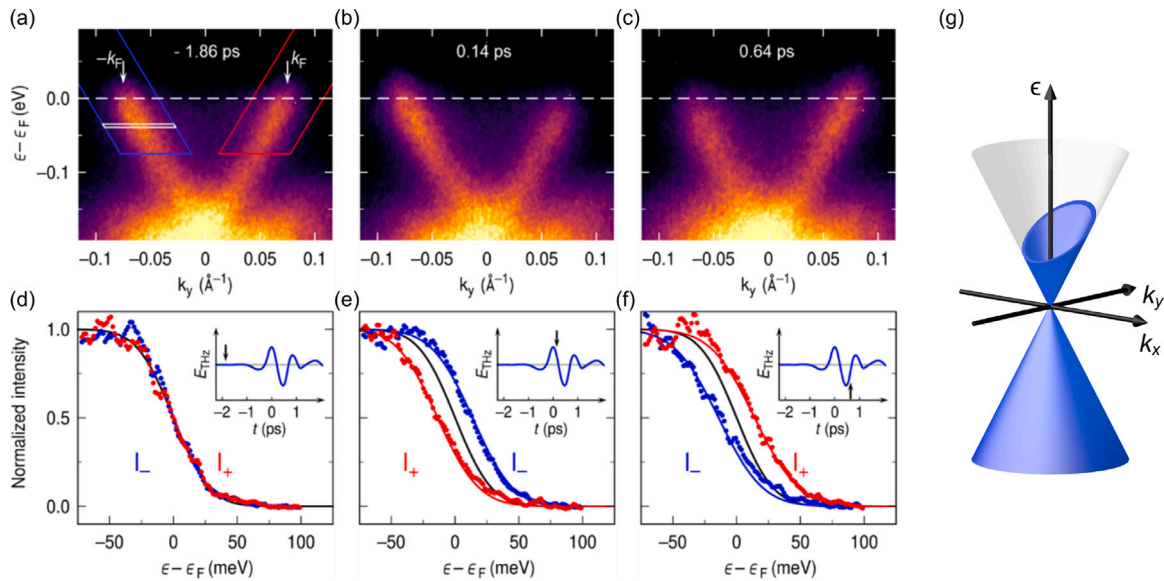|	λ (μm)	$\hbar\omega$ (eV)	Intensity (GW/cm^2)	E-field (MV/cm)	U_p (eV)
1 THz	300	4.1×10^{-3}	0.01	0.1	0.1
25 THz	12	0.10	10	3	0.15
60 THz	5	0.25	1000	30	2.5
500 THz	0.6	2.07	100	10	0.004
UV probe	0.2	6.20	0.1	0.3	5×10^{-7}

Fig. 43. Subcycle dynamics of Dirac currents. (a)–(c), ARPES maps before the arrival of the 1-THz field (−1.86 ps), just after the first positive maximum of the electric field (0.14 ps), and immediately after the negative crest of the electric field (0.64 ps). (d)–(f), Intensity distributions I_- and I_+ of the photoemission maps shown in (a)–(c) along the left (blue circles) and right (red circles) branches of the Dirac cone, respectively. The solid curves show the results of simulations based on the Boltzmann equation. The black curves depict the equilibrium situation and correspond to a Fermi–Dirac distribution at 80 K convoluted with the experimental energy resolution. The insets in (d)–(f) show the electric field reconstructed from photoelectron streaking, with the black arrows indicating the delay times of the corresponding snapshots. (g) Schematic of the Fermi surface shift and the acceleration of Dirac electrons by an electric field.
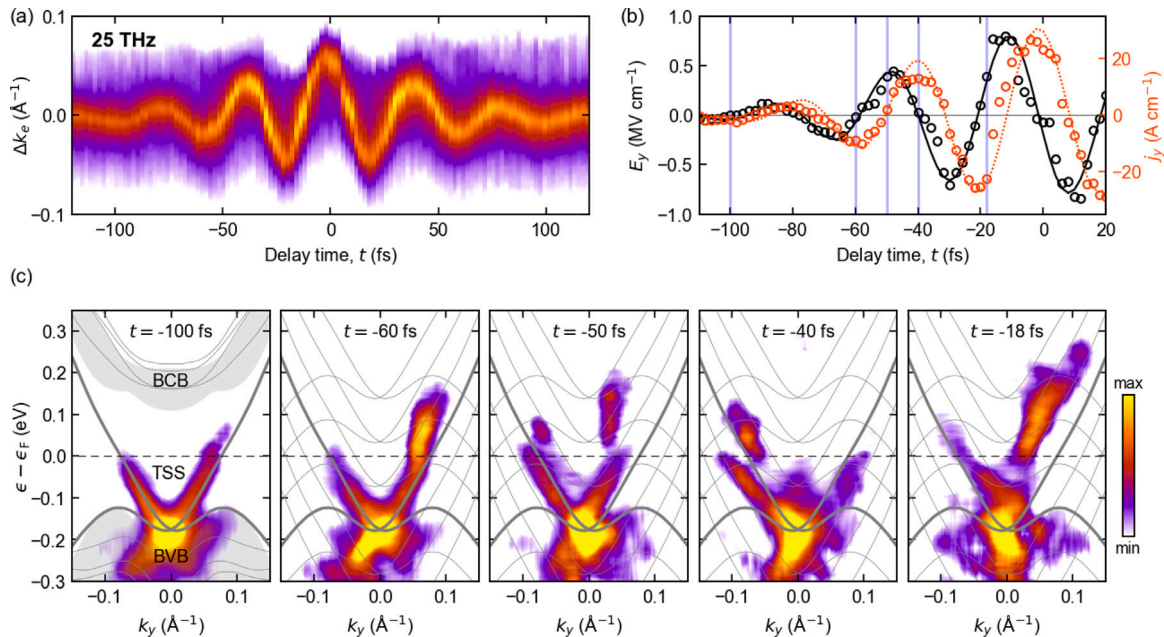*Source:* Adapted from Ref. [368].

Fig. 44. (a) Curvature-filtered photoelectron momentum-streaking trace of the 25 THz driving field. (b) First half of the electric-field waveform reconstructed from (a) (black circles) and current density extracted from the measured asymmetry in the population of the surface bands (red circles). The black solid curve is a fitted sinusoidal function with a peak amplitude of 0.8 MV/cm, and the dotted red line is the electric current induced by this waveform according to the semiclassical Boltzmann model. (c) Curvature-filtered ARPES maps recorded at the temporal positions indicated by the vertical lines in (b). The images are compensated for the streaking shifts in (a). The DFT band structure of Bi_2Te_3 is superimposed in the leftmost panel, and thin gray curves illustrate Floquet replicas as the TSS band structure shifted by integer multiples of the driving frequency.
Source: Adapted from Ref. [206].

10.3. Birth of Floquet–Bloch states

The second experiment extended subcycle ARPES to peak electric fields of MV/cm, where exotic strong-field phenomena can be induced by lightwaves. Ito et al. irradiated the TSS of Bi_2Te_3 with an intense MIR driving field with a center frequency of 25 THz and observed that dynamically engineered electronic states, Floquet–Bloch states, emerged within two optical cycles. Two-photon photoemission (2PPE) probe of 3 eV + 3 eV was used to achieve subcycle resolution for the

25-THz pump (duration of one optical cycle: 40 fs). The high temporal resolution inevitably broadens photoemission spectra, which was overcome by curvature-based second-derivative image processing [206]. Figs. 44(a,b) show a photoelectron streaking trace induced by the 25 THz lightwave, and the converted electric-field waveform at the surface, respectively. The amplitude of the surface electric field reached a peak value of 0.8 MV/cm, which corresponds to an incident amplitude of 7 MV/cm in vacuum, entering a range where nonperturbative high-harmonic generation is triggered from TSS [370].

The leftmost panel of Fig. 44(c) shows the 2PPE map of Bi_2Te_3 before the pump waveform. The curvature image processing sharply extracted the TSS band structure together with the bulk valence band (BVB). 40 fs later ($t = -60$ fs), the electric field has induced a pronounced asymmetry as the hallmark of lightwave-driven currents. A clear separation of electronic populations into multiple sidebands becomes apparent only one quarter of an oscillation cycle later ($t = -50$ fs), and the electron population oscillates back and forth along the momentum axis ($t = -40$ fs). Moving towards the maximum of the pulse envelope, the increasing carrier field shifts the electron population entirely to the upper branch near the field crest ($t = -18$ fs).

The newly emerging bands follow the ground-state band structure offset by integer multiples of $\hbar\omega = 0.1$ eV (thin gray curves) in consistency with the formation of Floquet replicas of Bloch electronic bands formed by a time-periodic electric field of light with frequency ω [205, 207]. The surprising finding that Floquet–Bloch sidebands build up already in the second optical cycle can be explained by the dynamical phase modulation of electronic wavefunctions caused by the driving field. Already after one optical cycle this causes constructive and destructive interference [206]. Furthermore, the experiment observed a transient population of the bulk conduction band (BCB) mediated by Floquet–Bloch bands at times exceeding $t = 0$ fs (not shown) [206].

10.4. Perspectives

The demonstration of subcycle ARPES and the two examples discussed in this section employed a conventional hemispherical electron analyser for electron spectroscopy and photoemission was restricted to the central region of the Brillouin zone. In the future, subcycle lightwave APRES can naturally be combined with recent developments reviewed in other sections of this article. Especially, the use of XUV probe light and momentum microscopy to map the full two-dimensional Brillouin zone will make the method considerably more versatile. Moreover, the rapid development of powerful THz and MIR light sources will make it possible to apply even higher field strengths and to work at considerably higher repetition rates. This development is expected to open the path for the investigation of a variety of strong-field phenomena in solids such as dynamical Bloch oscillation or Floquet-topological phases of matter at the level of the band structure. Combined with photoemission orbital tomography [366], lightwave ARPES has the potential to create cinematographic movies of molecular orbitals while they are shaped by light or during surface bond formation. While for technical reasons the highest field strengths are available only at frequencies that exceed 20 THz, the excitation of low frequency modes in the 1–10 THz range can induce phase transitions in materials and is generally considered most promising for materials engineering by light [371]. For this reason we expect that also setups like the one used by Reimann et al. in the first demonstration experiment will continue to play an important role in future applications of subcycle ARPES.

11. Progress in momentum imaging — lower electric field, smaller aberrations and reduced space charge effects

Gerd Schönhense and Hans-Joachim Elmers

11.1. Motivation for a new lens design

As discussed in previous chapters, the family of momentum microscopes (MM) includes instruments with either dispersive analyzers or time-of-flight (ToF) analyzers. The first instruments used two hemispherical analyzers in a tandem configuration [167,372–374], later followed by single hemispherical analyzers [375–378]. The ToF approach [168] requires pulsed excitation and is thus consistent with the pump–probe scheme of ultrafast photoemission experiments [157]. Experiments with HHG-based sources are discussed in Chapters 6 and 7, and experiments at FLASH in Chapter 12. More recently, a hybrid mode has been established that combines bandwidth selection by a dispersive analyzer with subsequent ToF analysis. The latter *slices* the selected band into a stack of momentum patterns with different kinetic energies. This hybrid approach has been achieved with large single hemispherical analyzers using laser radiation at 80 MHz pulse rate [379] and soft X-ray synchrotron radiation at 500 MHz pulse rate at the Diamond Light Source (Didcot, UK) [380]. A similar approach is used at the hard X-ray beamline P22 at PETRA III (DESY, Hamburg, Germany), where a compact dodecapole bandpass filter [381] is integrated into the standard linear column of a ToF-MM.

The lens system of a momentum microscope is similar to that of a photoemission electron microscope (PEEM). However, the principal planes (real-space and reciprocal-space images) are reversed. PEEMs are optimized for real-space imaging with best lateral resolution [382, 383], while MMs are optimized for reciprocal-space imaging, recording k_x-k_y patterns. For ARPES studies, the k-resolution is the crucial parameter with best values in the range of 0.005 Å^{-1} [372]. For photoelectron diffraction (PED) studies, the size of the k-field is crucial, as it determines the information content in the diffraction patterns. Large k-fields up to 12 Å^{-1} in diameter have been recorded with hard X-ray excitation [384,385].

The key element of PEEMs and MMs is the cathode lens, with the sample being an integral part of the lens. Early theoretical work [386–388] suggested that a large electrostatic field between the sample and the first electrode (extractor) is important for achieving high lateral resolution. Typical fields in the current generation of instruments are in the range of 3–8 kV/mm. Bauer, Rempfer and Tromp et al. refined the resolution equations and derived aberration coefficients for cathode lenses [389–393].

This high electric field can be prohibitive for certain experiments. The first obvious reason is that ARPES experiments require clean surfaces, often requiring cleaving in UHV. This can result in sharp corners or loose lamellae (for layered materials). Corners or protrusions increase the risk of field emission or even sparking. Second, the extractor field pulls slow background electrons into the lens column, where they exert Coulomb forces on the photoelectrons of interest. Especially in pump–probe experiments, large amounts of slow electrons released by the pump laser are often the main contributor to space charge effects (shifts and broadening of the signals). Third, cathode lens imaging relies on a homogeneous field between the sample and the extractor, which conflicts with 3-dimensional structures in the sample plane. Field distortions can occur at small microcrystals or electrodes of operando devices. Even worse, flat samples sometimes need to be tilted with respect to the optical axis to observe large off-normal emission angles at higher kinetic energies. The prevailing view that high extractor fields are essential for optimal performance of classical cathode objectives is frequently challenged by practical limitations, which impede their application. This chapter presents a solution to this conundrum.

11.2. Gap lens mode

A novel front lens configuration enables the reduction of the field at the sample surface to zero and even to negative (i.e., retarding) values. Prototypes of this lens have been utilized in a number of experiments. The homogeneous field of the extractor mode is supplanted by an additional lens field located within the gap between the sample and the extractor. The essential component responsible for generating this lens field is an annular electrode (R1), which is oriented concentric with respect to the extractor [see Fig. 45(a)]. By varying the potential
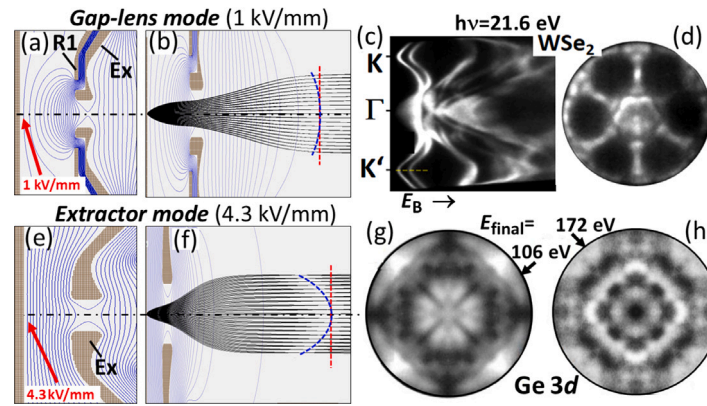
Fig. 45. Calculated equipotential contours and electron rays for the new front lens geometry (a,b) and for a classical extractor-type front lens (e,f). Ex and R1 denote the extractor and the ring electrode, respectively. In (a) the application of 18 kV at Ex and 2 kV at R1 results in a field strength as low as 1 kV/mm at the sample surface. In contrast, the application of 18 kV at Ex in (e) leads to a field strength of 4.3 kV/mm. (c,d) Valence band measurement of WSe_2 in the gap lens mode using a HHG-based photon source at CELIA, Bordeaux. (g,h) Photoelectron diffraction patterns of Ge $3d$ recorded in extractor mode with a hemisphere MM using Synchrotron radiation at the Diamond Light Source (Didcot UK). Simulations were conducted for $E_{kin} = 330$ eV and a polar-angle range of 30°. Data (c,d) and (g,h) from Ref. [380,395], respectively.

applied to this ring electrode, it is possible to vary the refractive power of the additional lens field and, in turn, to further adjust the field at the sample surface and its gradient. As illustrated in Fig. 45(a), the equipotential contours demonstrate a reduction in the field at the sample surface by a factor of more than four in comparison to the classical extractor mode depicted in Fig. 45(e). All simulations were conducted using the SIMION code [394].

Despite the much smaller field, the imaging properties of the so-called gap lens mode are better than those of the extractor mode, as can be seen from the ray patterns shown in Figs. 45(b,f). These patterns were simulated for a photoelectron kinetic energy of 330 eV and a polar angle range of 0–30°, corresponding to a k-field of 9 Å^{-1} diameter. The k-images are formed in the backfocal plane of the front lens (dashed red lines in b,f). With the new lens, the k-image is sharp up to the outer rim, while in extractor mode a significant spherical aberration (image curvature) is visible, see dashed blue curve. Its typical signature is the overfocus of the outer rays, which appears on the planar detector as image blur at the rim. This blur scales with the size of the source spot, which we assumed to be 80 μm diameter. Reducing the extractor voltage to below 18 kV would further increase this image blur.

The ray-tracing results are confirmed by first experiments. A typical example obtained in the gap-lens mode at a low kinetic energy of about 16 eV is shown in Figs. 45(c,d). These data were recorded for a WSe_2 sample with a ToF-MM using fs pulsed excitation from the HHG-based source at the CEntre Lasers Intenses et Applications (CELIA) in Bordeaux, France. The strong field reduction is very favorable for work with cleaved transition metal dichalcogenides (TMDC) samples (for details, see Ref. [395]). An example for higher kinetic energy is shown in Fig. 46. As an example for the extractor mode, two photoelectron diffraction patterns of Ge are shown in Figs. 45(g,h). These data were recorded with a hemisphere MM using Synchrotron radiation at the Diamond Light Source (Didcot UK). Large flat samples such as this Ge crystal do not normally carry the risk of field emission. Thanks to the small photon spot of about 30 μm diameter, the images show a good quality up to the outer rim. The richness of detail is surprising for these low kinetic energies; for more information, see Ref. [380].

As an interesting example of the new front lens geometry, we present soft X-ray photoemission results on the kagome metal CsV_3Sb_5. The (135)-kagome metals are interesting materials because they exhibit a combination of superconductivity, charge density wave (CDW) order, and nontrivial band topology (for details see the review article by Y. Hu et al. [396]). Fig. 46 shows the Fermi surface and the band dispersion of CsV_3Sb_5 measured with an energy resolution of 34 meV at a sample temperature of 30 K. A higher energy resolution (30 meV) could be achieved at lower drift energy on the expense of intensity [Fig. 46(g)].
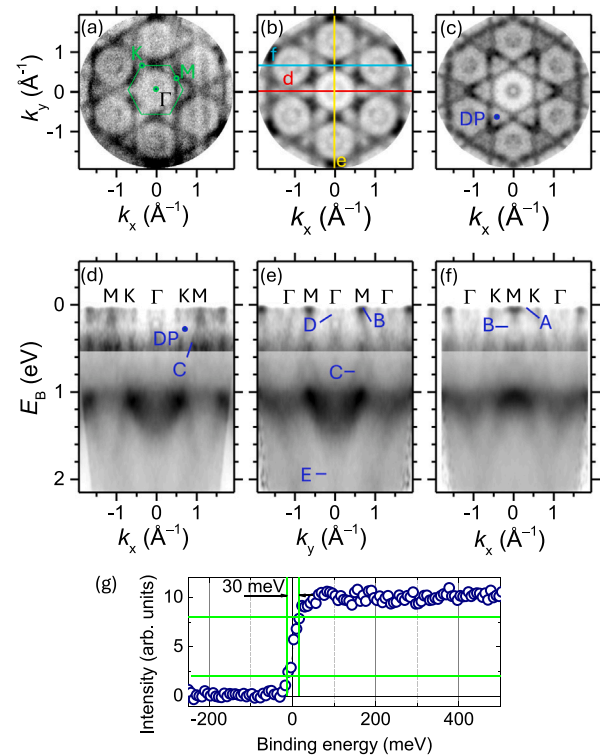
Fig. 46. ARPES measurements on the kagome metal CsV_3Sb_5, recorded in gap lens mode with R1 at 0 V with soft X-rays at $hv = 330$ eV from beamline P04 of PETRA III. (a) k_x - k_y section at the Fermi level as measured. (b) Same data as in (a) but sixfold symmetrized. (c) k_x - k_y section at a binding energy of 275 meV. (d–f) E_B vs $k_{||}$ sections along the lines marked in (b). The intensity brightness/contrast has been changed at $E_B = 500$ meV to better visualize states near the Fermi level. (g) Fermi edge profile showing that the resolution is given by the bandwidth of the exciting radiation.

In agreement with theory and previous ARPES measurements [396], we can identify the main band features. The sections over the Γ-K-M directions [Fig. 46(d,f)] show the van Hove singularities (VHS) at the M-point near the Fermi energy, which have a saddle-point nature. VHS-1 is indicated by the flat band (A) at the M-point in Fig. 46(d,f). Along the perpendicular direction across the M-point Fig. 46(e), it is connected to an electron-like parabola that is unoccupied at the M-point. VHS-2 is formed at a binding energy near 100 meV at the M-point with larger dispersion (B). In the perpendicular direction Γ-M [Fig. 46(e)] it forms an electron-like parabola (C) with a maximum

binding energy of 600 meV. VHS-3 at the M-point is connected to the lower Dirac point (DP) at the K-point. Along Γ-M [Fig. 46(e)] the band C forms a hole-like band.

Electron-like and hole-like behavior in perpendicular parallel momentum directions are the characteristics of a VHS. VHS-1 and VHS-2 show an electron-like state along the M-K direction and a hole-like state along the orthogonal M-Γ direction, and vice versa in the case of VHS-3. The flat dispersion of VHS-1 (A) extends over more than half of the K-M path, indicating a higher order nature of this van Hove singularity. The charge density wave (CDW)-induced hole-like band (D) that is backfolded from the M-point [Fig. 46(e)] appears in the empty space near the Fermi level at the Γ-point. The backfolded intensity is weak, which is typical of CDW-induced backfolding.

The dispersionless photoemission intensity at a binding energy between 1 and 1.2 eV corresponds to a flat band, suggesting electron correlation effects [397]. We confirm that the binding energy of the flat band is inconsistent with density function theory. As pointed out in Ref. [397], the energy position of a flat band in the kagome lattice is very sensitive to the hopping parameters. The electron-like band (E) [Fig. 46(e)] with a maximum binding energy of 2.2 eV is an uncorrelated electron band and its minimum is close to the inner potential.

These photoemission results confirm that the gap lens modes allow seven Brillouin zones of the Kagome metal CsV_3Sb_5 to be imaged simultaneously. The photoemission intensity varies from the central to the adjacent Brillouin zones. We attribute this effect to a variation of the photoemission matrix elements.

11.3. Repeller mode

Next to the weakly accelerating gap lens mode, used in Fig. 46, the field at the sample surface can be compensated or even reversed by putting R1 on a negative voltage. The zero-field mode is well suited for measurements under large off-normal angles or for operando devices with protruding electrodes on the surface. The repeller mode significantly reduces the space charge effect by eliminating all slow electrons from the beam within a short distance from the sample surface. Fig. 47 shows calculated trajectories of photoelectrons with $E_{kin} = 150$ eV in a weak repeller field of -23 V/mm. The 150 eV photoelectrons are accompanied by slow background electrons, which can outnumber the true photoelectrons by orders of magnitude. Here we show electrons with energies of 1 eV (green), 3 eV (blue) and 5 eV (red). The slow electron signal comprises secondary electrons (from cascade-like scattering processes), whose amount increases with increasing photoelectron energy. In pump–probe experiments another species of slow electrons can originate from the pump pulses (nPPE transitions). This contribution is strongly dependent on the pump fluence as well as on the presence of emission hot spots in the illuminated sample area. For a given sample, the Coulomb forces exerted by these electrons often set a limit to the maximum possible pump fluence.

Time markers in Fig. 47 illustrate the action of the repeller mode. The slow electrons are returned back to the surface within 240 ps, 400 ps and 600 ps for 1 eV, 3 eV and 5 eV electrons, respectively. In contrast, the 150 eV electrons are not visibly affected by the repeller field. This elimination of the slow electrons from the beam within the first few hundred μm above the sample surface terminates the Coulomb repulsion between the large amount of slow electrons and the photoelectrons. We note that in this early phase the mirror charge of the slow electrons diminishes the effective Coulomb field, which acts on the photoelectrons. This regime can readily be termed dipole regime (for details, see Ref. [398]).

The prediction of a substantial reduction of space-charge interaction has been validated in an experiment using the ToF-MM at FLASH. The central results are shown in Fig. 48. In the repeller mode (a), the signature of space charge interaction is absent and we just observe the laser assisted photoemission (LAPE) signal at pump–probe delay
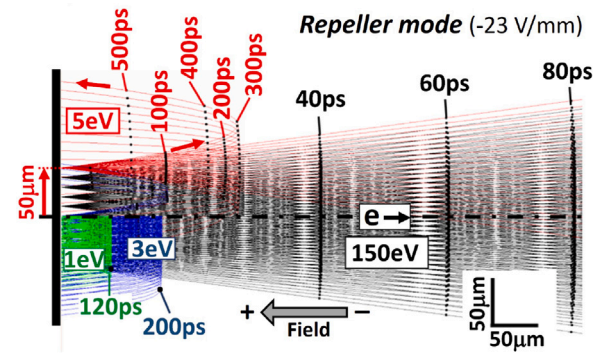

Fig. 47. Electron rays with time markers calculated for photoelectrons with a kinetic energy of 150 eV (black trajectories) in a weak repeller field of 23 V/mm. The slow electrons of 1 eV, 3 eV and 5 eV are emitted at the same instant as the photoelectrons and turn around after 120 ps, 200 ps and 300 ps, respectively. This leads to a substantial reduction of the Coulomb interaction between photoelectrons and slow electrons.
Source: From Ref. [398].
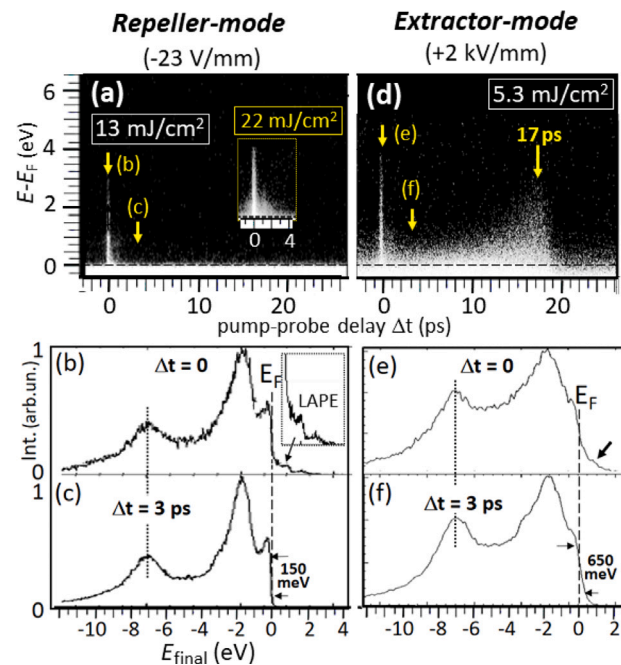
Fig. 48. Final-state energy distributions vs pump–probe delay Δt. (a–c) for the repeller mode at a pump fluence of 13 mJ/cm^2 and (d–f) for the extractor mode at a pump fluence of 5.3 mJ/cm^2. Measurements at the HEXTOF endstation of FLASH with $h\nu_{probe} = 111.6$ eV and $h\nu_{pump} = 1.2$ eV. (a) Intensity pattern for the repeller mode, plotted on a logarithmic intensity scale in the E_{final}-vs-Δt landscape. Main figure and inset for pump fluences of 13 mJ/cm^2 and 22 mJ/cm^2, respectively. (d) Same for the extractor mode and fluence 5.3 mJ/cm^2. (b,c,e,f) Corresponding spectra taken at pump–probe delays of 0 and 3 ps as stated in the panels.
Source: Data from Ref. [398].

$\Delta t = 0$. However, in extractor mode (d) we observe a dramatic long-range space charge artefact with its maximum at $\Delta t = 17$ ps, although the pump fluence is even lower. This artefact can be understood on the basis of a semi-analytical model [399], suggesting that the space charge interaction happens along the macroscopic flight path of the photoelectrons. Corresponding spectra at $\Delta t = 0$ and 3 ps are shown in Figs. 48(b,c) and (e,f) for the repeller and extractor mode, respectively. In repeller mode, we see the LAPE signals above E_F (b) and the Fermi edge has a width of 150 meV full width at half maximum (FWHM) (c). In extractor mode, the LAPE features are smeared out (e) and the width has increased to 650 meV FWHM due to the space charge interaction

Fig. 49. Valence band mapping for the W(110) surface at FLASH ($h\nu = 111.6$ eV) in repeller mode. (a) k_x-k_y momentum distribution. (b–e) $k_\parallel$-vs-E_B sections along the lines marked in (a). (b) and (c) represent the case without pump beam; (d) and (e) show the results with pump fluences of 13 and 25 mJ/cm^2, respectively, for a pump–probe delay of $\Delta t = 1$ ps.
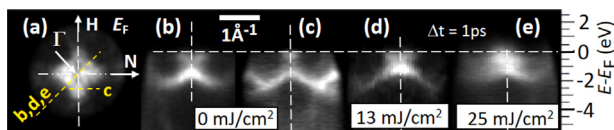*Source:* Data from Ref. [398].

(f). This weak repeller mode has been used in an experiment probing the metamagnetic phase transition in FeRh (details in Ref. [400]).

The limit of the pump fluence in repeller mode was elucidated by mapping the valence bands of tungsten with and without the pump pulse. The results for two high pump fluences are shown in Fig. 49. To avoid the LAPE signals, the time delay was set to 1 ps. At a pump fluence of 13 mJ/cm^2, the momentum pattern remained largely unchanged, as can be seen by comparing (b) and (d). At a fluence of 25 mJ/cm^2, the pattern appears significantly blurred, with some intensity above the Fermi level appearing in the center (e). This is consistent with the inset of Fig. 48(a), where at a fluence of 22 mJ/cm^2 an additional intensity appears near the LAPE signal at $\Delta t = 0$. In repeller mode the visible k-field is reduced by approximately a factor of 2.

11.4. Summary and conclusions

A novel front lens geometry has been developed, with an additional lens positioned in the gap between the sample and the extractor. This lens allows a significant reduction in the electric field at the sample surface (typically by a factor of 2–4 in the gap lens mode). This reduces the risk of field emission or flashover from microscopic protrusions, which can be a serious problem for cleaved samples. Simulations indicate that the imaging quality of the new front lens is superior to that of classical extractor lenses [see Figs. 45(b) and (f)]. We attribute this to two factors: First, the distance of the principal lens plane from the sample is about a factor of two smaller for the gap lens compared to the first converging lens in a classical objective (between extractor and focus electrode). Second, the gap lens is followed by an "aperture lens", with negative aberration coefficients [401]. The gap lens configuration is analogous to that of an optical microscope, where the objective lens is positioned in close proximity to the object. It is important to note, however, that Scherzer and Rose [402,403] demonstrated that, unlike in optical microscopy, spherical aberration cannot be eliminated in an electron-optical system with round lenses. This is known as the Scherzer theorem.

By adjusting the potential of the additional ring electrode [see Fig. 45(a,b)], the field at the sample can be set to either zero or even negative values, i.e. retarding. The zero field setting is particularly advantageous for the investigation of three-dimensionally structured samples, such as operando devices with electrodes or actuators on top. Negative fields establish the repeller mode, which directs all slow electrons back to the surface, thereby reducing the space charge interaction between the photoelectrons of interest and the large amount of slow background electrons (secondaries and pump-released electrons). The first experiments at FLASH are in agreement with theoretical predictions.

The reduced spherical aberration (visible in a smaller field curvature) allows the gap lens mode to record k-fields up to diameters of about 12 Å^{-1}, which is advantageous for photoelectron diffraction experiments. In real-space imaging (PEEM), fields of up to 4 mm in diameter can be recorded, which is a crucial aspect of the upcoming full-field imaging technique of PAXRIXS [404]. The situation is different with respect to chromatic aberration. Hemisphere-based MMs

record k-patterns with a narrow bandpass, so chromatic aberration is negligible. For ToF-based MMs, the chromatic aberration of the gap lens can be significant, which may result in a reduction of the simultaneously recorded energy band. Consequently, it may be necessary to use sequential recording of several smaller bands with subsequent concatenation of the stacks. Due to the time-resolved recording, the "chromatic aberration of magnification" can be numerically corrected a posteriori [405]. The details of this phenomenon are currently under investigation.

12. Time-resolved FEL photoelectron spectroscopy

Markus Scholz and Kai Rossnagel

12.1. Introduction

Free-electron lasers (FELs) generate highly coherent photon pulses with temporal widths ranging from femtoseconds to attoseconds in both the soft and hard X-ray ranges [406,407]. This remarkable capability enables the exploration of fundamental dynamical phenomena in materials and at interfaces, which can provide a deeper understanding of the interplay between electronic and structural degrees of freedom. Time-resolved photoelectron spectroscopy benefits greatly from high-repetition-rate FEL sources, as maintaining low count rates per pulse is critical to minimize space-charge effects and to manage the count rate limitations of delay-line detectors. To efficiently capture excited photoelectrons over the full half-space (2π solid angle) above the sample, advanced multidimensional spectrometers, such as the momentum microscope, are being used [157,168,408]. Another challenge is that the statistical intensity fluctuations of pulses from self-amplified spontaneous emission (SASE) FELs can reach up to 100%. This has necessitated the development of a single event-based data format for efficient filtering and sorting during post-processing [409]. Despite these limitations, high-repetition-rate FELs can outperform high-harmonic-generation (HHG) laser sources, especially when photon energies exceed 300 eV and pulse durations are below 100 fs. Since the pioneering time-resolved photoelectron experiments and studies of space-charge effects [410–413] at FLASH [406], the first FEL for extreme ultraviolet (XUV) and soft X-ray radiation, a vibrant user-driven science program has provided many important insights into the ultrafast dynamics of materials and interfaces. This short review focuses on selected experiments of the user community on interfacial reactions [414–416], soft matter systems [417,418], and quantum materials [419–425]. It concludes with a forward-looking discussion of ongoing advances in FEL light sources and photoelectron spectrometers.

12.2. Selected case studies

12.2.1. Surface reaction

The photochemical oxidation of carbon monoxide (CO) to carbon dioxide (CO$_2$) catalyzed by TiO$_2$ is essential for air purification, as CO is a major cause of fatal air poisoning in industrialized countries.

Wagstaffe *et al.* [415] used time-resolved X-ray photoelectron spectroscopy (tr-XPS) to study the ultrafast early reaction dynamics of the photoinduced oxidation of CO to CO$_2$ on the anatase TiO$_2$(101) surface (see Fig. 50). They revealed a reaction pathway involving the excitation of valence band electrons into *intra*-band gap states upon
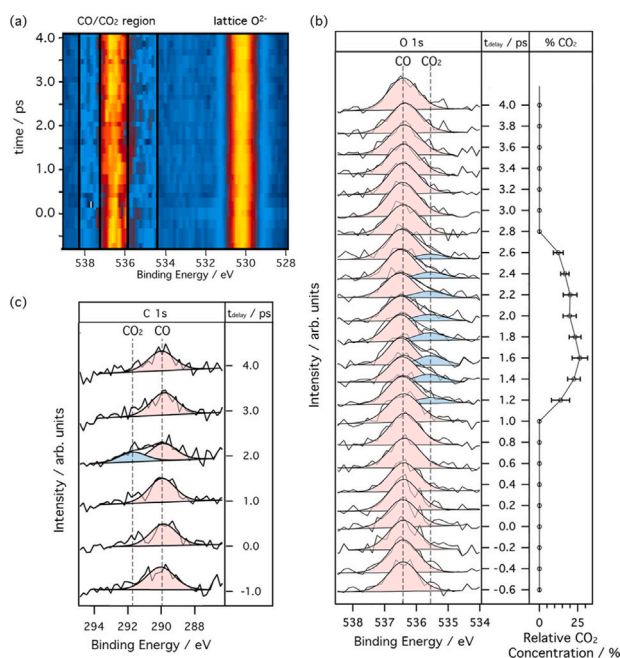
Fig. 50. Time-resolved XPS during the photooxidation of CO to CO_2 on anatase TiO_2(101). (a) Time-resolved O 1s intensity evolution and time-dependent (b) O 1s and (c) C 1s core-level spectra.
Source: Adapted from [415].

oxygen adsorption, forming an O_2–TiO_2 charge-transfer complex that activates oxygen below the TiO_2 band gap. The sample was pumped at a photon energy of 1.6 eV with a fluence of 4.4 mJ/cm^2 and probed at 647.9 eV. The effective time resolution was about 200 fs. The time evolution of the O 1s core-level emission shows an intensity shift to a lower binding energy and an additional peak at 536.6 eV, which the authors identified with the formation of CO_2 at about (1.2 ± 0.2) ps after optical excitation [Figs. 50(a) and 50(b)]. No other intermediates, such as CO_3^{2-}, COOH, or other oxygen-containing hydrocarbon species that would appear at lower binding energies, were detected, suggesting that the reaction occurred without the formation of long-lived carbon-containing intermediates. The C 1s core-level emission shows similar dynamics, with a peak corresponding to CO_2 at a binding energy of 291.8 eV observed at (2.0 ± 0.5) ps [Fig. 50(c)]. The authors concluded that with the capabilities of FEL-based tr-XPS, they were able to identify the relevant photogenerated charge carriers and the mechanisms driving oxygen activation that were previously inaccessible. This study provides crucial insight concerning reaction mechanisms and dynamics of the short-lived intermediates forming in the early stages of a chemical reaction. Furthermore, it is the first insight into the light-induced oxidation of CO to CO_2 on the surface of TiO_2 in real time.

12.2.2. Soft matter systems

Photoinduced charge generation is critical for natural and engineered photocatalytic and photovoltaic systems. Organic donor–acceptor systems, with their tunable properties, are promising for light harvesting. Improving efficiency requires detailed knowledge of the steps from light-induced excitation to charge separation.

Roth et al. [417] tracked the formation of free charge carriers in a model organic donor–acceptor system, CuPc:C_{60}, with tr-XPS at FLASH (see Fig. 51). The sample was pumped at 1.6 eV with a fluence of ~ 1 mJ/cm^2 and probed with a photon energy of 495.8 eV [Fig. 51(a)]. The effective time resolution was about 290 fs. In the spectral evolution of the C 1s XPS signal of the organic heterojunction, they observed that the signature of the C_{60} molecules shows a general shape change and shifts to a higher kinetic energy [Fig. 51(c)]. They interpret this

as the signature of additional electronic charge in the vicinity of the ionized C_{60} atoms, which could be directly correlated to the population of interfacial charge-transfer (ICT) states. They particularly found that the lifetime of ICT states results from competition between electron–hole recombination and ICT dissociation into delocalized charges [Fig. 51(b)]. About 20% of the photogenerated ICT states are converted into extractable charge carriers, while the remaining 80% recombine within about 1 ps [Fig. 51(d)]. These results suggest that charge separation from excitonic states plays an important role in light harvesting and opens new avenues for organic heterojunctions. The precise determination of the energetics, temporal dynamics, and channel efficiencies in such systems could lead to a better understanding and optimization of complex photovoltaic and photocatalytic systems.

Over the past decade, orbital tomography has emerged as an exciting modality of the photoemission technique, allowing the imaging of localized electronic wave functions in thin molecular films. The extension of the orbital tomography technique into the time domain requires XUV or X-ray photon energies and ultrashort pulses, which are currently only provided by SASE FELs or HHG sources.

Baumgärtner et al. [418] investigated the ultrafast charge transfer dynamics between a bilayer of pentacene deposited on Ag(110) (Fig. 52). The organic film was pumped at 3.1 eV with a fluence of 1 mJ/cm^2 and probed at 35 eV. The effective time resolution was about 215 fs. Imagine a molecule interacting with a surface, where charge transfer serves as the fundamental process and initial step of a molecule-surface reaction. Upon receiving a charge from the substrate, the atomic positions, electronic orbitals, and energy levels of the adsorbed molecule can undergo significant energetic rearrangement, while the local charge buildup in turn initiates the movement of mobile charge carriers in the substrate. This can lead to a modification of the local atomic structure at the adsorption site and a modification of the electronic structure by shifting, distorting, or splitting of bands. The measured time-resolved momentum distributions show an increase in intensity around the center after excitation, which decreases after 200 fs [Figs. 52(a)–(d)]. The dynamics and transient changes in the molecular orbitals can be explained by charge transfer between the molecule and the substrate and a charge redistribution from the $HOMO_{1st}$ to the partially filled $LUMO_{1st}$. Due to the strong interaction with the substrate, the molecule can also move relative to the surface, as supported by the computational results [Figs. 52(e)–(g)]. The results demonstrate the potential of sub-picosecond time-resolved orbital tomography of molecular thin films at SASE FELs. Future advances in temporal resolution, polarization control, and easy tunability of FEL light sources, together with progress in the theoretical framework, will make time-resolved tomography of molecular wave functions during chemical reactions feasible.

12.2.3. Quantum materials

Understanding ultrafast phenomena in quantum materials requires identifying the microscopic mechanisms of non-equilibrium energy transfer between electronic, spin, and lattice degrees of freedom.

A recent study by Shokeen et al. [423] on ferromagnetic Ni using time-resolved momentum microscopy has shown that the non-equilibrium electron and spin dynamics vary significantly with electron momentum, while the magnetic exchange interaction remains isotropic (Fig. 53). The Ni film was pumped at 1.2 eV with fluences of about 2.2 and 3.7 mJ/cm^2 and probed at 74 eV and 134 eV. The effective time resolution was about 230 fs. The momentum-integrated ultrafast dynamics in ferromagnetic Ni follow the generally accepted dynamics [239]. Laser excitation increases the electronic temperature in the Ni films, leading to demagnetization by energy and angular momentum transfer to the lattice and excitation of magnons [Fig. 53(a)]. Changes in the majority-spin band energy suggest the collapse of magnetic exchange splitting and reoccupation of majority/minority spin states, resulting in ultrafast demagnetization. In their time-resolved momentum microscopy data, the authors report momentum-dependent band-filling
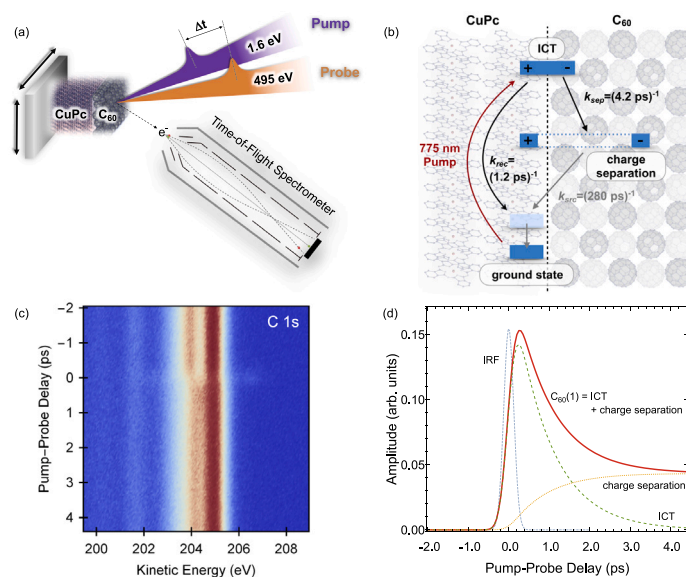
Fig. 51. Time-resolved XPS of CuPc:C_{60}. (a) Sketch of the experiment and (b) kinetic modeling of the C_{60} peak intensity. (c) C$1s$ intensity evolution of the C_{60} signal and (d) temporal evolution of the fraction of the C_{60} signal that shifted to lower binding energies.
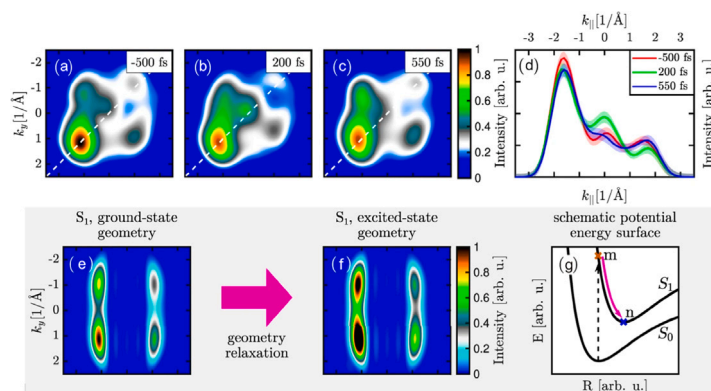*Source:* Adapted from [417].

Fig. 52. Charge transfer dynamics in bilayer pentacene on Ag(110). (a)–(c) Time-dependent photoemission intensity momentum maps of the pentacene HOMO$_{1st}$ at $E_B = 1.2$ eV. (d) Corresponding momentum distribution curves for HOMO$_{1st}$ along the indicated direction. Calculated photoemission intensity momentum maps for a pentacene molecule excited to the first singlet state (e) in the ground-state geometry and (f) excited-state geometry. (g) Schematic representation of the proposed molecular dynamics in the second layer after excitation: the shape of a molecule changes after the electronic excitation.
Source: Adapted from [418].

changes, which they describe as the buildup of a momentum-dependent quasi-chemical potential. They observe that this buildup is slightly delayed relative to the increasing electronic temperature and energy shift of the majority-spin 3d bands, and persists longer than the remagnetization and electronic temperature decay, suggesting a different underlying mechanism. Nonuniform k-dependent magnetization dynamics are detected, in contrast to uniform changes in the magnetic exchange splitting, indicating a spin-dependent energy transfer between the lattice and the electronic system. Momentum-dependent magnetic moments showed spin-dependent energy transfer with different dynamics at high and low fluences. This revealed transient electronic population changes following ultrafast demagnetization in Ni, identifying energy transfer from Brillouin-zone boundary phonons to the electronic system as spin-dependent and competing with electronic scattering, crucial for achieving thermal equilibrium [Figs. 53(b)–(d)]. These results highlight the impact of lattice-mediated scattering processes and open a pathway to uncover the elusive microscopic mechanisms of spin-lattice angular momentum transfer.

The shape of the energy distribution of emitted photoelectrons reflects many-body interactions such as Auger scattering and electron–phonon coupling. XPS line shapes are typically asymmetric in metals

due to core-hole screening, but symmetric in semiconductors. Optical excitation in semiconductors creates excited carriers that can change the lineshape of the core-level emission, allowing the study of non-equilibrium many-body effects with tr-XPS.

Dendzik *et al.* [420] have performed correlative core-*cum*-conduction tr-XPS experiments at FLASH (Fig. 54). The measurements were performed with 110 eV p-polarized XUV light. The photon energy spectrum of the pump laser was centered at 1.6 eV at a fluence of ~ 1.7 mJ/cm^2. The time and energy resolution were about 160 fs and 130 meV, respectively. Electron–hole excitations in the layered semiconductor WSe$_2$ were resonantly generated with femtosecond laser pulses to form excitons, and a momentum microscope was used to probe a broad spectral range simultaneously, capturing the excited states, the valence band, and the low-lying core levels of W and Se [Figs. 54(a) and 54(b)]. The resulting tr-XPS spectra of W$4f_{5/2}$ emissions exhibited distinct dynamics upon optical excitation, including changes in the energy position, spectral width, and lineshape of the core-level photoemission signal, along with a transient population of excited carriers. A theoretical model based on the Green's function formalism was developed to explain these core-level spectral changes, including dynamic screening
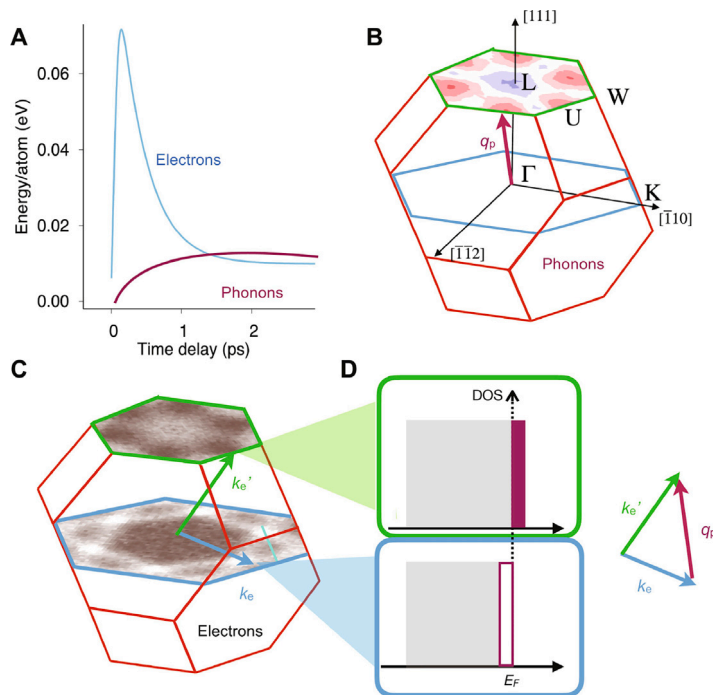
Fig. 53. Phonon–electron energy transfer in laser-excited Ni. (a) Schematic two-temperature model scenario: Laser-excited electrons transfer energy to phonons at the Brillouin zone boundary via electron–phonon coupling. Energy can also be transferred back from phonons to electrons when the electronic energy falls below a certain phonon mode energy. (b) Non-equilibrium energy distribution of phonons at the Brillouin zone boundary compared to the equilibrium distribution. (c) Photoemission intensity maps showing the electron distribution near the Fermi level in specific high-symmetry planes of the Brillouin zone. (d) Schematic illustration of the change in the electron occupation of states due to phonon absorption and electron scattering, with momentum conservation shown in the diagram.
Source: Adapted from [423].
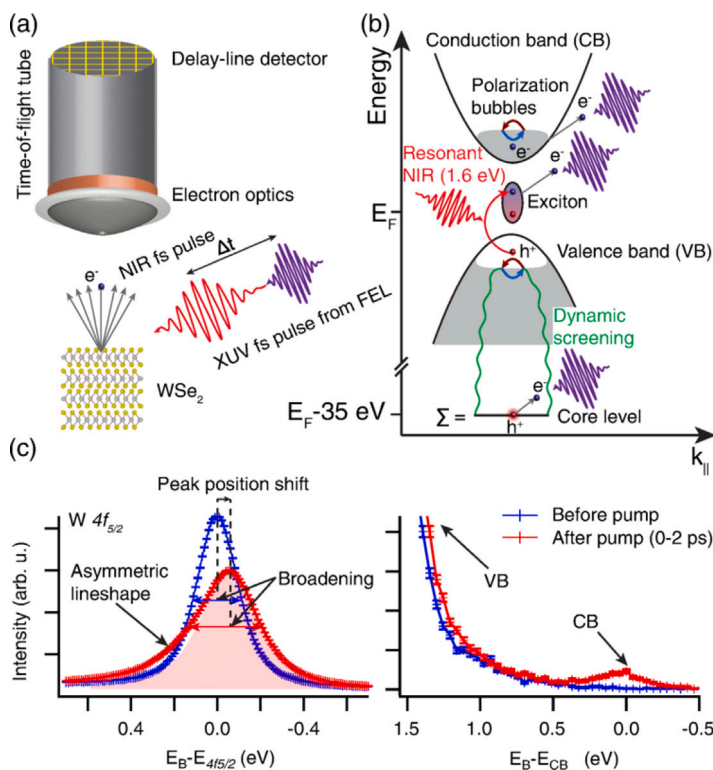
Fig. 54. Core-*cum*-conduction tr-XPS of WSe$_2$. (a) Illustration of the experimental setup. (b) Energy band diagram of photoexcited WSe$_2$: resonant generation of excited carrier populations in the valence and conduction bands. (c) Core and conduction photoelectron spectra showing emissions from the W $4f_{5/2}$ level (left) and the momentum-integrated conduction band (right) before (blue) and after optical excitation (red).
Source: Adapted from [420].
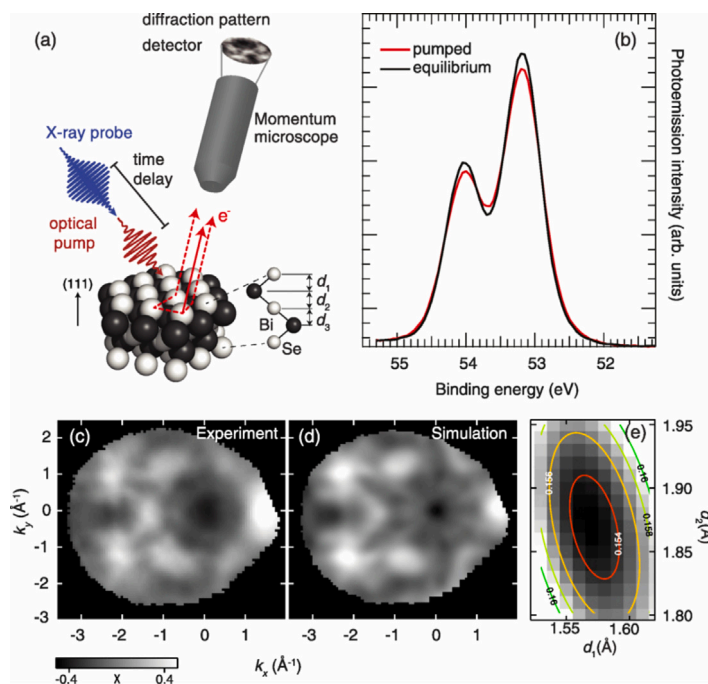
Fig. 55. trXPD of Bi_2Se_3. (a) Sketch of the experimental setup. (b) Se $3d$ core-level spectrum before and after optical excitation. (c) Se $3d$ modulation function, obtained before optical excitation. (d) Calculated modulation function for the best-fit structure. (e) Reliability factor for the comparison between experimental and theoretical modulation functions as a function of the first two interlayer distances d_1 and d_2.
Source: Adapted from [425].

of the core hole by excited carriers [Fig. 54(c)]. This model reproduces the experimental results and allows to disentangle the contributions of excitons and quasi-free carriers (QFCs). The ability to distinguish between excitons and QFCs using tr-XPS is remarkable because of their small energy difference of about 50 meV compared to the core-electron energy scales of tens of eV. Initially, excitons dominate the dynamics and transition to QFCs within the first picosecond. The different screening behavior of excitons and QFCs during photoemission facilitated this distinction. These results support the continuous phase-transition scenario of the excitonic Mott transition in transition-metal dichalcogenides.

Optical pump and ultraviolet (UV), vacuum ultraviolet, or XUV probe photoemission spectroscopy experiments have revealed the dynamic electronic properties of various materials. However, ultrafast spectroscopy-based methods for structure determination, such as time-resolved X-ray photoelectron diffraction (tr-XPD), are less developed due to the scarcity of ultrafast soft X-ray sources. While time-resolved momentum microscopy of the valence band structure provides insight into electron–phonon coupling, but relies on precise knowledge of phonon-induced structural changes at the surface, tr-XPD combines local structure information with chemical resolution and surface sensitivity, making it ideal for direct measurement of atomic displacements at the surface and thus a crucial complement to time- and angle-resolved photoelectron spectroscopy (tr-ARPES) data.

Curcio *et al.* [425] used tr-XPD to study the structural dynamics of the topological insulator Bi_2Se_3 by tracking the momentum distribution of the Se $3d$ core-level emissions after optical excitation (Fig. 55). The pump photon energy was 1.55 eV at a fluence of ~ 4.2 mJ/cm^2, while the probe photon energy was 113 eV. The high detection efficiency of the momentum microscope allowed them to collect sufficient time- and momentum-resolved data from the Se $3d$ emissions [Fig. 55(b)] within 19 hours. The effective time resolution was about 140 fs. The measured tr-XPD data were compared with the results of multiple scattering simulations [Figs. 55(c)–55(e)]. In particular, the authors focused on the first three interlayer distances d_1, d_2, and d_3 as defined in Fig. 55(a). The difference between the equilibrium and time-dependent distances,

e.g., Δd_1 and Δd_2, show clear oscillations with an amplitude around 0.01 Å after optical excitation. The oscillation period of about 500 fs is consistent with the expected excitation of an A_{1g} optical phonon mode. This phonon mode involves simultaneous motion of the outer Bi and Se layers in a quintuple layer relative to the central static Se layer. Changes in d_1 and d_2 should correlate, either in phase or out of phase, depending on the relative motion of the first and second layer atoms.

12.3. Perspective

Over the last decade, FEL-based time-resolved solid-state photoelectron spectroscopy has been successfully established at FLASH in the XUV and soft X-ray regime. As the case studies presented above show, the technique has proven its broad applicability and performance, in particular its unique position in time-resolved core-level spectroscopy. Currently, the technique is in the process of broadening its base and further developing its performance with the expected implementation at the high-repetition-rate FELs LCLS-II and European XFEL. At FLASH, the ongoing upgrade program aims at external seeding at photon energies up to the carbon K edge in the fundamental and third harmonic radiation beyond the $3d$ transition metal L-edge resonances, allowing the exploitation of core-level resonances. Expected temporal pulse lengths are less than 10 fs with spectral bandwidths close to the Fourier transform limit. At LCLS-II and the European XFEL, the available soft X-ray photon energy range extends from about 250 eV to 1.6 keV and 3 keV, respectively. For both of these SASE FELs, the temporal pulse length is expected to be less than 10 fs. These advances in probing photon sources will greatly benefit photoelectron spectroscopy experiments by providing increased temporal and spectral stability, full polarization control, and easy tunability of photon energy. In particular, the 1 MHz repetition rate at LCLS-II will significantly improve the efficiency of time-consuming tr-XPD measurements. To increase the efficiency of the momentum microscope, the integration of a space-charge suppression optics is predicted to be advantageous as discussed in the previous chapter [395,398]. This involves the use of a repeller electrode to generate a retarding and diverging field at the sample surface, thereby

decelerating and redirecting slow electrons within a short distance from the sample. This approach is expected to result in a significant reduction in space-charge interaction effects. Additionally, there are ongoing developments in multi-line delay-line detectors and time-resolving large area pixel detectors [426,427]. These advances promise improved multi-hit detection capabilities. We foresee that all these technical developments will make FEL-based time-resolved photoelectron spectroscopy a viable, efficient, sensitive, multimodal technique for studying ultrafast electronic-structural dynamics in materials and at interfaces, complementing and extending the capabilities of HHG-based tr-ARPES.

CRediT authorship contribution statement

Martin Aeschlimann: Conceptualization, Funding acquisition, Resources, Supervision, Writing – original draft, Writing – review & editing. **Jan Philipp Bange:** Writing – original draft, Writing – review & editing. **Michael Bauer:** Conceptualization, Funding acquisition, Project administration, Supervision, Writing – original draft, Writing – review & editing. **Uwe Bovensiepen:** Conceptualization, Data curation, Funding acquisition, Resources, Supervision, Writing – original draft, Writing – review & editing. **Hans-Joachim Elmers:** Conceptualization, Data curation, Funding acquisition, Investigation, Resources, Writing – original draft, Writing – review & editing. **Thomas Fauster:** Conceptualization, Data curation, Funding acquisition, Project administration, Supervision, Writing – original draft, Writing – review & editing. **Lukas Gierster:** Investigation, Writing – original draft, Writing – review & editing. **Ulrich Höfer:** Conceptualization, Data curation, Funding acquisition, Resources, Supervision, Writing – original draft, Writing – review & editing. **Rupert Huber:** Conceptualization, Data curation, Funding acquisition, Resources, Supervision, Writing – original draft, Writing – review & editing. **Andi Li:** Investigation. **Xintong Li:** Investigation. **Stefan Mathias:** Conceptualization, Data curation, Funding acquisition, Supervision, Writing – original draft, Writing – review & editing. **Karina Morgenstern:** Conceptualization, Data curation, Funding acquisition, Resources, Supervision, Writing – original draft, Writing – review & editing. **Hrvoje Petek:** Conceptualization, Funding acquisition, Supervision, Writing – original draft, Writing – review & editing. **Marcel Reutzel:** Conceptualization, Supervision, Writing – original draft, Writing – review & editing. **Kai Rossnagel:** Conceptualization, Data curation, Funding acquisition, Supervision, Writing – original draft, Writing – review & editing. **Gerd Schönhense:** Conceptualization, Data curation, Resources, Supervision, Writing – original draft, Writing – review & editing. **Markus Scholz:** Conceptualization, Funding acquisition, Project administration, Supervision, Writing – original draft, Writing – review & editing. **Benjamin Stadtmüller:** Funding acquisition, Project administration, Supervision, Writing – original draft, Writing – review & editing. **Julia Stähler:** Conceptualization, Data curation, Funding acquisition, Resources, Supervision, Writing – original draft, Writing – review & editing. **Shijing Tan:** Investigation, Writing – review & editing. **Bing Wang:** Funding acquisition. **Zehua Wang:** Investigation, Writing – review & editing. **Martin Weinelt:** Writing – original draft, Validation, Supervision, Resources, Project administration, Investigation, Funding acquisition, Conceptualization, Compilation and editing of the article.

Declaration of competing interest

The authors declare that they have no known competing financial interests or personal relationships that could have appeared to influence the work reported in this paper.

Data availability

Data will be made available on request.

References

[1] R.T. Williams, T.R. Royt, J.C. Rife, J.P. Long, M.N. Kabler, Picosecond time-resolved photoelectron spectroscopy of ZnTe, J. Vac. Sci. Technol. 21 (2) (1982) 509, http://dx.doi.org/10.1116/1.571748.

[2] R. Haight, J. Bokor, J. Stark, R.H. Storz, R.R. Freeman, P.H. Bucksbaum, Picosecond time-resolved photoemission study of the InP(110) surface, Phys. Rev. Lett. 54 (1985) 1302, http://dx.doi.org/10.1103/physrevlett.54.1302.

[3] R.W. Schoenlein, J.G. Fujimoto, G.L. Eesley, T.W. Capehart, Femtosecond studies of image-potential dynamics in metals, Phys. Rev. Lett. 61 (1988) 2596, http://dx.doi.org/10.1103/physrevlett.61.2596.

[4] J.P. Long, H.R. Sadeghi, J.C. Rife, M.N. Kabler, Surface space-charge dynamics and surface recombination on silicon (111) surfaces measured with combined laser and synchrotron radiation, Phys. Rev. Lett. 64 (1990) 1158, http://dx.doi.org/10.1103/PhysRevLett.64.1158.

[5] A.L. Cavalieri, N. Müller, T. Uphues, V.S. Yakovlev, A. Baltuška, B. Horvath, B. Schmidt, L. Blümel, R. Holzwarth, S. Hendel, M. Drescher, U. Kleineberg, P.M. Echenique, R. Kienberger, F. Krausz, U. Heinzmann, Attosecond spectroscopy in condensed matter, Nature 449 (7165) (2007) 1029, http://dx.doi.org/10.1038/nature06229.

[6] M. Krüger, M. Schenk, P. Hommelhoff, Attosecond control of electrons emitted from a nanoscale metal tip, Nature 475 (7354) (2011) 78, http://dx.doi.org/10.1038/nature10196.

[7] P.M. Echenique, J.B. Pendry, The existence and detection of Rydberg states at surfaces, J. Phys. C 11 (1978) 2065, http://dx.doi.org/10.1088/0022-3719/11/10/017.

[8] N.V. Smith, Phase analysis of image states and surface states associated with nearly-free-electron band gaps, Phys. Rev. B 32 (1985) 3549, http://dx.doi.org/10.1103/PhysRevB.32.3549.

[9] K. Boger, M. Roth, M. Weinelt, T. Fauster, P.-G. Reinhard, Linewidths in energy-resolved two-photon photoemission spectroscopy, Phys. Rev. B 65 (2002) 075104, http://dx.doi.org/10.1103/PhysRevB.65.075104.

[10] U. Höfer, I.L. Shumay, C. Reuß, U. Thomann, W. Wallauer, T. Fauster, Time-resolved coherent photoelectron spectroscopy of quantized electronic states on metal surfaces, Science 277 (1997) 1480, http://dx.doi.org/10.1126/science.277.5331.1480.

[11] W. Berthold, U. Höfer, P. Feulner, E.V. Chulkov, V.M. Silkin, P.M. Echenique, Momentum-resolved lifetimes of image-potential states on Cu(100), Phys. Rev. Lett. 88 (2002) 056805, http://dx.doi.org/10.1103/physrevlett.88.056805.

[12] K. Boger, M. Weinelt, T. Fauster, Scattering of hot electrons by adatoms at metal surfaces, Phys. Rev. Lett. 92 (2004) 126803, http://dx.doi.org/10.1103/PhysRevLett.92.126803.

[13] M. Roth, M. Pickel, J. Wang, M. Weinelt, T. Fauster, Electron scattering at steps: Image-potential states on Cu(119), Phys. Rev. Lett. 88 (2002) 096802, http://dx.doi.org/10.1103/PhysRevLett.88.096802.

[14] U. Höfer, P.M. Echenique, Resolubility of image-potential resonances, Surf. Sci. 643 (2016) 203, http://dx.doi.org/10.1016/j.susc.2015.07.019.

[15] M. Kutschera, M. Weinelt, M. Rohlfing, T. Fauster, Image-potential-induced surface state at Si(100), Appl. Phys. A 88 (2007) 519, http://dx.doi.org/10.1007/s00339-007-4074-x.

[16] K.S. Novoselov, A.K. Geim, S.V. Morozov, D. Jiang, Y. Zhang, S.V. Dubonos, I.V. Grigorieva, A.A. Firsov, Electric field effect in atomically thin carbon films, Science 306 (2004) 666, http://dx.doi.org/10.1126/science.110289.

[17] K.S. Novoselov, A.K. Geim, S.V. Morozov, D. Jiang, M.I. Katsnelson, I.V. Grigorieva, S.V. Dubonos, A.A. Firsov, Two-dimensional gas of massless Dirac fermions in graphene, Nature 438 (2005) 197, http://dx.doi.org/10.1038/nature04233.

[18] S.Y. Zhou, G.H. Gweon, J. Graf, A.V. Fedorov, C.D. Spataru, R.D. Diehl, Y. Kopelevich, D.H. Lee, S.G. Louie, A. Lanzara, First direct observation of Dirac fermions in graphite, Nat. Phys. 2 (2006) 595, http://dx.doi.org/10.1038/nphys393.

[19] T. Kampfrath, L. Perfetti, F. Schapper, C. Frischkorn, M. Wolf, Strongly coupled optical phonons in the ultrafast dynamics of the electronic energy and current relaxation in graphite, Phys. Rev. Lett. 95 (18) (2005) 187403, http://dx.doi.org/10.1103/PhysRevLett.95.187403.

[20] M. Breusing, C. Ropers, T. Elsaesser, Ultrafast carrier dynamics in graphite, Phys. Rev. Lett. 102 (2009) 086809, http://dx.doi.org/10.1103/PhysRevLett.102.086809.

[21] D. Brida, A. Tomadin, C. Manzoni, Y.J. Kim, A. Lombardo, S. Milana, R.R. Nair, K.S. Novoselov, G. Ferrari, M. Polini, Ultrafast collinear scattering and carrier multiplication in graphene, Nature Commun. 4 (2013) 1987, http://dx.doi.org/10.1038/ncomms2987.

[22] M. Trushin, A. Grupp, G. Soavi, A. Budweg, D. De Fazio, U. Sassi, A. Lombardo, A.C. Ferrari, W. Belzig, A. Leitenstorfer, D. Brida, Ultrafast pseudospin dynamics in graphene, Phys. Rev. B 92 (2015) 165429, http://dx.doi.org/10.1103/PhysRevB.92.165429.

[23] J.C. Johannsen, S. Ulstrup, F. Cilento, A. Crepaldi, M. Zacchigna, C. Cacho, I.C.E. Turcu, E. Springate, F. Fromm, C. Raidel, T. Seyller, F. Parmigiani, M. Grioni, P. Hofmann, Direct view of hot carrier dynamics in graphene, Phys. Rev. Lett. 111 (2013) 027403, http://dx.doi.org/10.1103/PhysRevLett.111.027403.

[24] S. Xu, J. Cao, C.C. Miller, D.A. Mantell, R.J.D. Miller, Y. Gao, Energy dependence of electron lifetime in graphite observed with femtosecond photoemission spectroscopy, Phys. Rev. Lett. 76 (1996) 483, http://dx.doi.org/10.1103/PhysRevLett.76.483.

[25] G. Moos, C. Gahl, R. Fasel, M. Wolf, T. Hertel, Anisotropy of quasiparticle lifetimes and the role of disorder in graphite from ultrafast time-resolved photoemission spectroscopy, Phys. Rev. Lett. 87 (2001) 267402, http://dx.doi.org/10.1103/PhysRevLett.87.267402.

[26] T. Winzer, E. Malic, The impact of pump fluence on carrier relaxation dynamics in optically excited graphene, J. Phys.: Condens. Matter. 25 (2013) 054201, http://dx.doi.org/10.1088/0953-8984/25/5/054201.

[27] A. McPherson, G. Gibson, H. Jara, U. Johann, T.S. Luk, I.A. McIntyre, K. Boyer, C.K. Rhodes, Studies of multiphoton production of vacuum-ultraviolet radiation in the rare gases, J. Opt. Soc. Am. B 4 (1987) 595, http://dx.doi.org/10.1364/JOSAB.4.000595.

[28] X.F. Li, A. L'Huillier, L.A. Ferray, G. Mainfray, Multiple-harmonic generation in rare gases at high laser intensity, Phys. Rev. A 39 (1989) 5751, http://dx.doi.org/10.1103/PhysRevA.39.5751.

[29] M.X. Na, A.K. Mills, D.J. Jones, Advancing time- and angle-resolved photoemission spectroscopy: The role of ultrafast laser development, Phys. Rep. 1036 (2023) 1, http://dx.doi.org/10.1016/j.physrep.2023.09.005.

[30] F. Boschini, M. Zonno, A. Damascelli, Time-resolved ARPES studies of quantum materials, Rev. Modern Phys. 96 (2024) 15003, http://dx.doi.org/10.1103/RevModPhys.96.015003.

[31] R. Haight, J.A. Silberman, Surface intervalley scattering on GaAs(110): Direct observation with picosecond laser photoemission, Phys. Rev. Lett. 62 (1989) 815, http://dx.doi.org/10.1103/PhysRevLett.62.815.

[32] R. Haight, Electron dynamics at surfaces, Surf. Sci. Rep. 21 (8) (1995) 275, http://dx.doi.org/10.1016/0167-5729(95)00002-X.

[33] M. Bauer, C. Lei, K. Read, R. Tobey, J. Gland, M. Murnane, H. Kapteyn, Direct observation of surface chemistry using ultrafast soft-X-ray pulses, Phys. Rev. Lett. 87 (2001) 025501, http://dx.doi.org/10.1103/PhysRevLett.87.025501.

[34] T. Rohwer, S. Hellmann, M. Wiesenmayer, C. Sohrt, A. Stange, B. Slomski, A. Carr, Y. Liu, L.M. Avila, M. Kalläne, S. Mathias, L. Kipp, K. Rossnagel, M. Bauer, Collapse of long-range charge order tracked by time-resolved photoemission at high momenta, Nature 471 (2011) 490, http://dx.doi.org/10.1038/nature09829.

[35] A. Stange, C. Sohrt, T. Rohwer, S. Hellmann, G. Rohde, L. Kipp, K. Rossnagel, M. Bauer, A direct view onto the carrier dynamics in graphite at the H point, EPJ Web Conf. 41 (2013) 04022, http://dx.doi.org/10.1051/epjconf/20134104022.

[36] I. Gierz, J.C. Petersen, M. Mitrano, C. Cacho, I.C.E. Turcu, E. Springate, A. Stöhr, A. Köhler, U. Starke, A. Cavalleri, Snapshots of non-equilibrium Dirac carrier distributions in graphene, Nature Mater. 12 (2013) 1119, http://dx.doi.org/10.1038/nmat3757.

[37] M. Trushin, J. Schliemann, Anisotropic photoconductivity in graphene, Europhys. Lett. 96 (2011) 37006, http://dx.doi.org/10.1209/0295-5075/96/37006.

[38] G. Rohde, A. Stange, A. Müller, M. Behrendt, L.-P. Oloff, K. Hanff, T. Albert, P. Hein, K. Rossnagel, M. Bauer, Ultrafast formation of a Fermi-Dirac distributed electron gas, Phys. Rev. Lett. 121 (2018) 256401, http://dx.doi.org/10.1103/PhysRevLett.121.256401.

[39] S. Aeschlimann, R. Krause, M. Chávez-Cervantes, H. Bromberger, R. Jago, E. Malić, A. Al-Temimy, C. Coletti, A. Cavalleri, I. Gierz, Ultrafast momentum imaging of pseudospin-flip excitations in graphene, Phys. Rev. B 96 (2017) http://dx.doi.org/10.1103/PhysRevB.96.020301, 020301(R).

[40] E. Malic, T. Winzer, E. Bobkin, A. Knorr, Microscopic theory of absorption and ultrafast many-particle kinetics in graphene, Phys. Rev. B 84 (2011) 205406, http://dx.doi.org/10.1103/PhysRevB.84.205406.

[41] E. Malic, T. Winzer, A. Knorr, Efficient orientational carrier relaxation in optically excited graphene, Appl. Phys. Lett. 101 (2012) 21, http://dx.doi.org/10.1063/1.4767356.

[42] I. Gierz, F. Calegari, S. Aeschlimann, M. Chávez Cervantes, C. Cacho, R. Chapman, E. Springate, S. Link, U. Starke, C. Ast, A. Cavalleri, Tracking primary thermalization events in graphene with photoemission at extreme time scales, Phys. Rev. Lett. 115 (2015) 086803, http://dx.doi.org/10.1103/PhysRevLett.115.086803.

[43] E. Shirley, L. Terminello, A. Santoni, F. Himpsel, Brillouin-zone-selection effects in graphite photoelectron angular distributions, Phys. Rev. B 51 (1995) 13614, http://dx.doi.org/10.1103/PhysRevB.51.13614.

[44] H. Beyer, P. Hein, K. Rossnagel, M. Bauer, Ultrafast decay of carrier momentum anisotropy in graphite, Phys. Rev. B 107 (2023) 115136, http://dx.doi.org/10.1103/PhysRevB.107.115136.

[45] J. Bakalis, S. Chernov, Z. Li, A. Kunin, Z.H. Withers, S. Cheng, A. Adler, P. Zhao, C. Corder, M.G. White, G. Schönhense, X. Du, R. Kawkami, T.K. Allison, Momentum-space observation of optically excited non-thermal electrons in graphene with persistent pseudospin polarization, Nano Lett. 24 (2024) 9353, http://dx.doi.org/10.1021/acs.nanolett.4c02378.

[46] M.X. Na, A.K. Mills, F. Boschini, M. Michiardi, B. Nosarzewski, R.P. Day, E. Razzoli, A. Sheyerman, M. Schneider, G. Levy, S. Zhdanovich, T.P. Devereaux, A.F. Kemper, D.J. Jones, A. Damascelli, Direct determination of mode-projected electron-phonon coupling in the time domain, Science 366 (2019) 1231, http://dx.doi.org/10.1126/science.aaw1662.

[47] J.A. Yang, S. Parham, D. Dessau, D. Reznik, Novel electron-phonon relaxation pathway in graphite revealed by time-resolved raman scattering and angle-resolved photoemission spectroscopy, Sci. Rep. 7 (2017) 40876, http://dx.doi.org/10.1038/srep40876.

[48] R. Bistritzer, A.H. MacDonald, Electronic cooling in graphene, Phys. Rev. Lett. 102 (2009) 206410, http://dx.doi.org/10.1103/PhysRevLett.102.206410.

[49] J.C.W. Song, M.Y. Reizer, L.S. Levitov, Disorder-assisted electron-phonon scattering and cooling pathways in graphene, Phys. Rev. Lett. 109 (2012) 106602, http://dx.doi.org/10.1103/PhysRevLett.109.106602.

[50] A.C. Betz, S.H. Jhang, E. Pallecchi, R. Ferreira, G. Fève, J.-M. Berroir, B. Plaçais, Supercollision cooling in undoped graphene, Nat. Phys. 9 (2012) 109, http://dx.doi.org/10.1038/nphys2494.

[51] T.V. Alencar, M.G. Silva, L.M. Malard, A.M. de Paula, Defect-induced supercollision cooling of photoexcited carriers in graphene, Nano Lett. 14 (2014) 5621, http://dx.doi.org/10.1021/nl502163d.

[52] L. Perfetti, P.A. Loukakos, M. Lisowski, U. Bovensiepen, H. Eisaki, M. Wolf, Ultrafast electron relaxation in superconducting $Bi_2Sr_2CaCu_2O_{8+\delta}$ by time-resolved photoelectron spectroscopy, Phys. Rev. Lett. 99 (2007) 197001, http://dx.doi.org/10.1103/PhysRevLett.99.197001.

[53] A. Stange, C. Sohrt, L.X. Yang, G. Rohde, K. Janssen, P. Hein, L.-P. Oloff, K. Hanff, K. Rossnagel, M. Bauer, Hot electron cooling in graphite: Supercollision versus hot phonon decay, Phys. Rev. B 92 (2015) 184303, http://dx.doi.org/10.1103/PhysRevB.92.184303.

[54] A.K. Geim, I.V. Grigorieva, Van der Waals heterostructures, Nature 499 (2013) 419, http://dx.doi.org/10.1038/nature12385.

[55] M. Düvel, M. Merboldt, J.P. Bange, H. Strauch, M. Stellbrink, K. Pierz, H.W. Schumacher, D. Momeni, D. Steil, G.S.M. Jansen, S. Steil, D. Novko, S. Mathias, M. Reutzel, Far-from-equilibrium electron-phonon interactions in optically excited graphene, Nano Lett. 22 (2022) 4897, http://dx.doi.org/10.1021/acs.nanolett.2c01325.

[56] H. Zhang, C. Bao, M. Schüler, S. Zhou, Q. Li, L. Luo, W. Yao, Z. Wang, T.P. Devereaux, S. Zhou, Self-energy dynamics and mode-specific phonon threshold effect in Kekulé-ordered graphene, Natl. Sci. Rev. 9 (2022) 175, http://dx.doi.org/10.1093/nsr/nwab175.

[57] S. Aeschlimann, S.A. Sato, R. Krause, M. Chávez-Cervantes, U. De Giovannini, H. Hübener, S. Forti, C. Coletti, K. Hanff, K. Rossnagel, A. Rubio, I. Gierz, Survival of Floquet-Bloch states in the presence of scattering, Nano Lett. 21 (2021) 5028, http://dx.doi.org/10.1021/acs.nanolett.1c00801.

[58] D. Choi, M. Mogi, U. De Giovannini, D. Azoury, B. Lv, Y. Su, H. Hübener, A. Rubio, N. Gedik, Direct observation of Floquet-Bloch states in monolayer graphene, 2024, http://dx.doi.org/10.48550/arXiv.2404.14392, arXiv:2404.14392.

[59] M. Merboldt, M. Schüler, D. Schmitt, J.P. Bange, W. Bennecke, K. Gadge, K. Pierz, H.W. Schumacher, D. Momeni, D. Steil, S.R. Manmana, M. Sentef, M. Reutzel, S. Mathias, Observation of floquet states in graphene, 2024, http://dx.doi.org/10.48550/arXiv.2404.12791, arXiv:2404.12791.

[60] S. Ulstrup, J.C. Johannsen, F. Cilento, J.A. Miwa, A. Crepaldi, M. Zacchigna, C. Cacho, R. Chapman, E. Springate, S. Mammadov, F. Fromm, C. Raidel, T. Seyller, F. Parmigiani, M. Grioni, P.D.C. King, P. Hofmann, Ultrafast dynamics of massive Dirac Fermions in bilayer graphene, Phys. Rev. Lett. 112 (2014) 257401, http://dx.doi.org/10.1103/PhysRevLett.112.257401.

[61] S. Ulstrup, A.G. Čabo, J.A. Miwa, J.M. Riley, S.S. Grønborg, J.C. Johannsen, C. Cacho, O. Alexander, R.T. Chapman, E. Springate, M. Bianchi, M. Dendzik, J.V. Lauritsen, P.D.C. King, P. Hofmann, Ultrafast band structure control of a two-dimensional heterostructure, ACS Nano 10 (2016) 6315, http://dx.doi.org/10.1021/acsnano.6b02622.

[62] S. Aeschlimann, A. Rossi, M. Chávez-Cervantes, R. Krause, B. Arnoldi, B. Stadtmüller, M. Aeschlimann, S. Forti, F. Fabbri, C. Coletti, I. Gierz, Direct evidence for efficient ultrafast charge separation in epitaxial WS_2/graphene heterostructures, Sci. Adv. 6 (2020) 3, http://dx.doi.org/10.1126/sciadv.aay0761.

[63] K. Rossnagel, M. Bauer, Toward direct exploration of the few-femtosecond dynamics of electronic coherence and correlation in quantum materials using time- and angle-resolved photoemission spectroscopy, Crystals 14 (2024) 404, http://dx.doi.org/10.3390/cryst14050404.

[64] H. Helmholtz, Ueber einige Gesetze der Vertheilung elektrischer Ströme in körperlichen Leitern mit Anwendung auf die thierisch-elektrischen Versuche, Annu. Rev. Phys. Chem. 165 (1853) 165, http://dx.doi.org/10.1002/andp.18531650603.

[65] W. Schmickler, E. Santos, Interfacial Electrochemistry, second ed., Springer-Verlag, Berlin Heidelberg, 2010, http://dx.doi.org/10.1007/978-3-642-04937-8.

[66] O. Magnussen, A. Groß, Toward an atomic-scale understanding of electrochemical interface structure and dynamics, J. Am. Chem. Soc. 141 (2019) 4777, http://dx.doi.org/10.1021/jacs.8b13188.

[67] M. Favaro, B. Jeong, P.N. Ross, J. Yano, Z. Hussain, Z. Liu, E.J. Crumlin, Unravelling the electrochemical double layer by direct probing of the solid/liquid interface, Nature Commun. 7 (2016) 12695, http://dx.doi.org/10.1038/ncomms12695.

[68] J.B. Taylor, I. Langmuir, The evaporation of atoms, ions and electrons from caesium films on tungsten, Phys. Rev. 44 (1933) 423, http://dx.doi.org/10.1103/PhysRev.44.423.

[69] N. Fischer, S. Schuppler, T. Fauster, W. Steinmann, Coverage-dependent electronic structure of Na on Cu(111), Surf. Sci. 314 (1994) 89, http://dx.doi.org/10.1016/0039-6028(94)90215-1.

[70] Q.B. Lu, D.J. O'Connor, B.V. King, R.J. MacDonald, Local electrostatic potential determination of CsCu(111) surfaces by negative ion spectroscopy, Surf. Sci. 347 (1996) L61, http://dx.doi.org/10.1016/0039-6028(95)01039-4.

[71] J. Gauyacq, A. Borisov, M. Bauer, Excited states in the alkali noble metal surface systems: A model system for the study of charge transfer dynamics at surfaces, Prog. Surf. Sci. 82 (2007) 244, http://dx.doi.org/10.1016/j.progsurf.2007.03.006.

[72] J. Zhao, N. Pontius, A. Winkelmann, V. Sametoglu, A. Kubo, A.G. Borisov, D. Sánchez-Portal, V.M. Silkin, E.V. Chulkov, P.M. Echenique, H. Petek, Electronic potential of a chemisorption interface, Phys. Rev. B 78 (2008) 085419, http://dx.doi.org/10.1103/PhysRevB.78.085419.

[73] M. Trioni, S. Achilli, E. Chulkov, Key ingredients of the alkali atom – metal surface interaction: Chemical bonding versus spectral properties, Prog. Surf. Sci. 88 (2013) 160, http://dx.doi.org/10.1016/j.progsurf.2013.03.002.

[74] S. Ogawa, H. Nagano, H. Petek, Phase and energy relaxation in an antibonding surface state: Cs/Cu(111), Phys. Rev. Lett. 82 (1999) 1931, http://dx.doi.org/10.1103/PhysRevLett.82.1931.

[75] M. Bauer, S. Pawlik, M. Aeschlimann, Decay dynamics of photoexcited alkali chemisorbates: Real-time investigations in the femtosecond regime, Phys. Rev. B 60 (1999) 5016, http://dx.doi.org/10.1103/PhysRevB.60.5016.

[76] H. Petek, H. Nagano, M.J. Weida, S. Ogawa, Surface femtochemistry, frustrated desorption of alkali atoms from noble metals, J. Phys. Chem. B 105 (2001) 6767, http://dx.doi.org/10.1021/jp0045235.

[77] H. Petek, S. Ogawa, Femtosecond time-resolved two-photon photoemission studies of electron dynamics in metals, Prog. Surf. Sci. 56 (1997) 239, http://dx.doi.org/10.1016/S0079-6816(98)00002-1.

[78] U. Bovensiepen, M. Wolf, H. Petek (Eds.), Dynamics at Solid State Surfaces and Interfaces: Current Developments, Wiley-VCH Verlag GmbH & Co. KGaA, 2010, http://dx.doi.org/10.1002/9783520733418.

[79] C. Gahl, U. Bovensiepen, C. Frischkorn, K. Morgenstern, K.-H. Rieder, M. Wolf, Ultrafast electron solvation dynamics in D$_2$O/Cu(111): influence of coverage and structure, Surf. Sci. 532–535 (2003) 108, http://dx.doi.org/10.1016/S0039-6028(03)00186-9.

[80] J. Stähler, M. Mehlhorn, U. Bovensiepen, M. Meyer, D.O. Kusmierek, K. Morgenstern, M. Wolf, Impact of ice structure on ultrafast electron dynamics in D$_2$O clusters on Cu(111), Phys. Rev. Lett. 98 (2007) 206105, http://dx.doi.org/10.1103/PhysRevLett.98.206105.

[81] P. Auburger, I. Kemeny, C. Bertram, M. Ligges, M. Bockstedte, U. Bovensiepen, K. Morgenstern, Microscopic insight into electron-induced dissociation of aromatic molecules on ice, Phys. Rev. Lett. 121 (2018) 206001, http://dx.doi.org/10.1103/PhysRevLett.121.206001.

[82] M. Rentzepis, D.C. Douglass, Xenon as a solvent, Nature 293 (1981) 165, http://dx.doi.org/10.1038/293165a0.

[83] J. Thomas, Electron Transfer and Solvation Dynamics at Solid Cesium-Copper Interfaces in Presence of Solvents (Ph.D. thesis), 2022, http://dx.doi.org/10.17185/duepublico/77878.

[84] C. Penschke, J. Thomas, C. Bertram, A. Michaelides, K. Morgenstern, P. Saalfrank, U. Bovensiepen, Hydration at highly crowded interfaces, Phys. Rev. Lett. 130 (2023) 106202, http://dx.doi.org/10.1103/PhysRevLett.130.106202.

[85] J. Thomas, J. Patwari, I.C. Langguth, C. Penschke, P. Zhou, K. Morgenstern, U. Bovensiepen, Femtosecond electron-transfer dynamics across the D$_2$O/Cs+/Cu(111) interface: The impact of hydrogen bonding, J. Phys. Chem. C 127 (2023) 23467, http://dx.doi.org/10.1021/acs.jpcc.3c06172.

[86] J. Thomas, C. Bertram, J. Daru, J. Patwari, I. Langguth, P. Zhou, D. Marx, K. Morgenstern, U. Bovensiepen, Competition between Coulomb and van der Waals interactions in Xe-Cs$^+$ aggregates on Cu(111) surfaces, Phys. Rev. Lett. 127 (2021) 266802, http://dx.doi.org/10.1103/PhysRevLett.127.266802.

[87] H. Petek, M.J. Weida, H. Nagano, S. Ogawa, Real-time observation of adsorbate atom motion above a metal surface, Science 288 (2000) 1402, http://dx.doi.org/10.1126/science.288.5470.1402.

[88] M. Wolf, E. Knoesel, T. Hertel, Ultrafast dynamics of electrons in image-potential states on clean and Xe-covered Cu(111), Phys. Rev. B 54 (1996) R5295, http://dx.doi.org/10.1103/PhysRevB.54.R5295.

[89] J.D. McNeill, L.J. R. L., N.-H. Ge, C.M. Wong, R.E. Jordan, C.B. Harris, Dynamics and spatial distribution of electrons in quantum wells at interfaces determined by femtosecond photoemission spectroscopy, Phys. Rev. Lett. 79 (1997) 4645, http://dx.doi.org/10.1103/PhysRevLett.79.4645.

[90] W. Berthold, F. Rebentrost, P. Feulner, U. Höfer, Influence of Ar, Kr, and Xe layers on the energies and lifetimes of image-potential states on Cu(100), Appl. Phys. A 78 (2004) 131, http://dx.doi.org/10.1007/s00339-003-2310-6.

[91] K.K. Kleinherbers, E. Janssen, A. Goldmann, H. Saalfeld, Submonolayer adsorption of halogens on Ag(001) and Ag(011) studied by photoemission, Surf. Sci. 215 (1989) 394, http://dx.doi.org/10.1016/0039-6028(89)90269-0.

[92] J. Maklar, S. Dong, S. Beaulieu, T. Pincelli, M. Dendzik, Y.W. Windsor, R.P. Xian, M. Wolf, R. Ernstorfer, L. Rettig, A quantitative comparison of time-of-flight momentum microscopes and hemispherical analyzers for time- and angle-resolved photoemission spectroscopy experiments, Rev. Sci. Instrum. 91 (2020) 123112, http://dx.doi.org/10.1063/5.0024493.

[93] S.A. Kovalenko, A.L. Dobryakov, J. Ruthmann, N.P. Ernsting, Femtosecond spectroscopy of condensed phases with chirped supercontinuum probing, Phys. Rev. A 59 (3) (1999) 2369–2384, http://dx.doi.org/10.1103/PhysRevA.59.2369.

[94] J. Herbst, K. Heyne, R. Diller, Femtosecond infrared spectroscopy of bacteriorhodopsin chromophore isomerization, Science 297 (5582) (2002) 822–825, http://dx.doi.org/10.1126/science.1072144.

[95] A. Nahata, A.S. Weling, T.F. Heinz, A wideband coherent terahertz spectroscopy system using optical rectification and electro-optic sampling, Appl. Phys. Lett. 69 (16) (1996) 2321–2323, http://dx.doi.org/10.1063/1.117511.

[96] M. Weinelt, Time-resolved two-photon photoemission from metal surfaces, J. Phys.-Condens. Mat. 14 (43) (2002) R1099, http://dx.doi.org/10.1088/0953-8984/14/43/202.

[97] T. Wang, T.R. Kafle, B. Kattel, W.L. Chan, A multidimensional view of charge transfer excitons at organic donor-acceptor interfaces, J. Am. Chem. Soc. 139 (11) (2017) 4098–4106, http://dx.doi.org/10.1021/jacs.6b13312.

[98] M. Marks, S. Sachs, C.H. Schwalb, A. Schöll, U. Höfer, Electronic structure and excited state dynamics in optically excited PTCDA films investigated with two-photon photoemission, J. Chem. Phys. 139 (12) (2013) 124701, http://dx.doi.org/10.1063/1.4818541.

[99] Y. Zhang, D.T. Payne, C.L. Pang, C. Cacho, R.T. Chapman, E. Springate, H.H. Fielding, G. Thornton, State-selective dynamics of TiO$_2$ charge-carrier trapping and recombination, J. Phys. Chem. Lett. 10 (17) (2019) 5265–5270, http://dx.doi.org/10.1021/acs.jpclett.9b02153.

[100] A. Neef, S. Beaulieu, S. Hammer, S. Dong, J. Maklar, T. Pincelli, R.P. Xian, M. Wolf, L. Rettig, J. Pflaum, R. Ernstorfer, Orbital-resolved observation of singlet fission, Nature 616 (7956) (2023) 275–279, http://dx.doi.org/10.1038/s41586-023-05814-1.

[101] T. Fauster, C. Reuß, I.L. Shumay, M. Weinelt, Femtosecond two-photon photoemission studies of image-potential states, Chem. Phys. 251 (1) (2000) 111–121, http://dx.doi.org/10.1016/S0301-0104(99)00300-6.

[102] W.S. Fann, R. Storz, H.W.K. Tom, J. Bokor, Direct measurement of nonequilibrium electron-energy distributions in sub-picosecond laser-heated gold films, Phys. Rev. Lett. 68 (1992) 2834–2837, http://dx.doi.org/10.1103/PhysRevLett.68.2834.

[103] P.M. Echenique, R. Berndt, E.V. Chulkov, T. Fauster, A. Goldmann, U. Höfer, Decay of electronic excitations at metal surfaces, Surf. Sci. Rep. 52 (7–8) (2004) 219–317, http://dx.doi.org/10.1016/j.surfrep.2004.02.002.

[104] E. Knoesel, A. Hotzel, M. Wolf, Temperature dependence of surface state lifetimes, dephasing rates and binding energies on Cu(111) studied with time-resolved photoemission, J. Electron. Spectrosc. Relat. Phenomena 88–91 (1998) 577–584, http://dx.doi.org/10.1016/S0368-2048(97)00178-3.

[105] H. Petek, M.J. Weida, H. Nagano, S. Ogawa, Electronic relaxation of alkali metal atoms on the Cu(111) surface, Surf. Sci. 451 (2000) 22–30, http://dx.doi.org/10.1016/S0039-6028(00)00004-2.

[106] N.-H. Ge, C.M. Wong, R.L. Lingle, J.D. McNeill, K.J. Gaffney, C.B. Harris, Femtosecond dynamics of electron localization at interfaces, Science 279 (5348) (1998) 202–205, http://dx.doi.org/10.1126/science.279.5348.202.

[107] P. Szymanski, S. Garrett-Roe, C.B. Harris, Time- and angle-resolved two-photon photoemission studies of electron localization and solvation at interfaces, Prog. Surf. Sci. 78 (1) (2005) 1–39, http://dx.doi.org/10.1016/j.progsurf.2004.08.001.

[108] R. Naaman, Molecular controlled nano-devices, Phys. Chem. Chem. Phys. 13 (29) (2011) 13153–13161, http://dx.doi.org/10.1039/c1cp21106d.

[109] G. Mercurio, E.R. McNellis, I. Martin, S. Hagen, F. Leyssner, S. Soubatch, J. Meyer, M. Wolf, P. Tegeder, F.S. Tautz, K. Reuter, Structure and energetics of azobenzene on Ag(111): Benchmarking semiempirical dispersion correction approaches, Phys. Rev. Lett. 104 (2010) 036102, http://dx.doi.org/10.1103/PhysRevLett.104.036102.

[110] K. Onda, B. Li, J. Zhao, K.D. Jordan, J. Yang, H. Petek, Wet electrons at the H$_2$O/TiO$_2$(110) surface, Science 308 (5725) (2005) 1154–1158, http://dx.doi.org/10.1126/science.1109366.

[111] M. Weinelt, M. Kutschera, T. Fauster, M. Rohlfing, Dynamics of exciton formation at the Si(100) c(4 × 2) surface, Phys. Rev. Lett. 92 (12) (2004) 126801, http://dx.doi.org/10.1103/PhysRevLett.92.126801.

[112] S.L. Yang, J.A. Sobota, P.S. Kirchmann, Z.X. Shen, Electron propagation from a photo-excited surface: Implications for time-resolved photoemission, Appl. Phys. A 116 (1) (2014) 85–90, http://dx.doi.org/10.1007/s00339-013-8154-9.

[113] W. Widdra, D. Bröcker, T. Gieß el, I.V. Hertel, W. Krüger, A. Liero, F. Noack, V. Petrov, D. Pop, P.M. Schmidt, R. Weber, I. Will, B. Winter, Time-resolved core level photoemission: surface photovoltage dynamics of the $SiO_2/Si(100)$ interface, Surf. Sci. 543 (1–3) (2003) 87–94, http://dx.doi.org/10.1016/j.susc.2003.07.005.

[114] E. Varene, L. Bogner, C. Bronner, P. Tegeder, Ultrafast exciton population, relaxation, and decay dynamics in thin oligothiophene films, Phys. Rev. Lett. 109 (20) (2012) 207601, http://dx.doi.org/10.1103/PhysRevLett.109.207601.

[115] H. Tanimura, K. Tanimura, P.H.M. Van Loosdrecht, Dynamics of incoherent exciton formation in Cu_2O : Time- and angle-resolved photoemission spectroscopy, Phys. Rev. B 100 (2019) 115204, http://dx.doi.org/10.1103/PhysRevB.100.115204.

[116] Q. Yang, M. Muntwiler, X.Y. Zhu, Charge transfer excitons and image potential states on organic semiconductor surfaces, Phys. Rev. B 80 (11) (2009) 115214, http://dx.doi.org/10.1103/PhysRevB.80.115214.

[117] J. Liu, X. Jiang, X. Li, X. Ma, X. Sun, Q. Zheng, X. Cui, S. Tan, J. Zhao, B. Wang, Time- and momentum-resolved image-potential states of 2H-MoS_2 surface, Phys. Chem. Chem. Phys. 23 (46) (2021) 26336–26342, http://dx.doi.org/10.1039/d1cp03527d.

[118] M. Borgwardt, S.T. Omelchenko, M. Favaro, P. Plate, C. Höhn, D. Abou-Ras, K. Schwarzburg, R. van de Krol, H.A. Atwater, N.S. Lewis, R. Eichberger, D. Friedrich, Femtosecond time-resolved two-photon photoemission studies of ultrafast carrier relaxation in Cu_2O photoelectrodes, Nature Commun. 10 (1) (2019) 2106, http://dx.doi.org/10.1038/s41467-019-10143-x.

[119] R. Bertoni, C.W. Nicholson, L. Waldecker, H. Hübener, C. Monney, U. De Giovannini, M. Puppin, M. Hoesch, E. Springate, R.T. Chapman, C. Cacho, M. Wolf, A. Rubio, R. Ernstorfer, Generation and evolution of spin-, valley-, and layer-polarized excited carriers in inversion-symmetric WSe_2, Phys. Rev. Lett. 117 (27) (2016) 277201, http://dx.doi.org/10.1103/PhysRevLett.117.277201.

[120] J.A. Sobota, Y. He, Z.-X. Shen, Angle-resolved photoemission studies of quantum materials, Rev. Modern Phys. 93 (2) (2021) 025006, http://dx.doi.org/10.1103/RevModPhys.93.025006.

[121] J. Stähler, M. Meyer, U. Bovensiepen, M. Wolf, Solvation dynamics of surface-trapped electrons at NH_3 and D_2O crystallites adsorbed on metals: from femtosecond to minute timescales, Chem. Sci. 2 (5) (2011) 907–916, http://dx.doi.org/10.1039/c0sc00644k.

[122] S.B. King, D. Wegkamp, C. Richter, M. Wolf, J. Stähler, Trapped electrons at the amorphous solid water/vacuum interface as possible reactants in a water splitting reaction, J. Phys. Chem. C 121 (13) (2017) 7379–7386, http://dx.doi.org/10.1021/acs.jpcc.7b01459.

[123] S.B. King, K. Broch, A. Demling, J. Stähler, Multistep and multiscale electron transfer and localization dynamics at a model electrolyte/metal interface, J. Chem. Phys. 150 (041702) (2019) 041702, http://dx.doi.org/10.1063/1.5047033.

[124] A. Demling, S.B. King, P. Shushkov, J. Stähler, O_2 reduction at a DMSO/Cu(111) model battery interface, J. Phys. Chem. C 127 (6) (2023) 2894–2900, http://dx.doi.org/10.1021/acs.jpcc.2c07491.

[125] L. Gierster, S. Vempati, J. Stähler, Ultrafast generation and decay of a surface metal, Nature Commun. 12 (978) (2021) 978, http://dx.doi.org/10.1038/s41467-021-21203-6.

[126] L. Gierster, S. Vempati, J. Stähler, Ultrashort and metastable doping of the ZnO surface by photoexcited defects, Faraday Discuss. 237 (2022) 58–79, http://dx.doi.org/10.1039/d2fd00036a.

[127] L. Foglia, S. Vempati, B. Tanda Bonkano, L. Gierster, M. Wolf, S. Sadofev, J. Stähler, Revealing the competing contributions of charge carriers, excitons, and defects to the non-equilibrium optical properties of ZnO, Struct. Dynam. 6 (3) (2019) 034501, http://dx.doi.org/10.1063/1.5088767.

[128] L. Gierster, O. Turkina, J.-C. Deinert, S. Vempati, E. Baeta, Y. Garmshausen, S. Hecht, C. Draxl, J. Stähler, Right on time: Ultrafast charge separation before hybrid exciton formation, Adv. Sci. 2403765 (2024) http://dx.doi.org/10.1002/advs.202403765.

[129] C. Gahl, Elektronentransfer- und Solvatisierungsdynamik in Eis adsorbiert auf Metalloberflächen PhD Thesis, Freie Universität Berlin, 2004, http://dx.doi.org/10.17169/refubium-16322.

[130] C. Gahl, U. Bovensiepen, C. Frischkorn, M. Wolf, Ultrafast dynamics of electron localization and solvation in ice layers on Cu(111), Phys. Rev. Lett. 89 (2002) 107402, http://dx.doi.org/10.1103/PhysRevLett.89.107402.

[131] J. Stähler, C. Gahl, U. Bovensiepen, M. Wolf, Ultrafast electron dynamics at ice- metal interfaces: Competition between heterogeneous electron transfer and solvation, J. Phys. Chem. B 110 (19) (2006) 9637–9644, http://dx.doi.org/10.1021/jp060538c.

[132] J. Stähler, C. Gahl, M. Wolf, Dynamics and reactivity of trapped electrons on supported ice crystallites, Acc. Chem. Res. 45 (1) (2012) 131–138, http://dx.doi.org/10.1021/ar200170s.

[133] S. Lany, A. Zunger, Anion vacancies as a source of persistent photoconductivity in II-VI and chalcopyrite semiconductors, Phys. Rev. B 72 (2005) 035215, http://dx.doi.org/10.1103/PhysRevB.72.035215.

[134] N.F. Mott, Semiconductor-To-Metal Transitions, first ed., Taylor & Francis, London, 1974.

[135] S. Hellmann, M. Beye, C. Sohrt, T. Rohwer, F. Sorgenfrei, H. Redlin, M. Kalläne, M. Marczynski-Bühlow, F. Hennies, M. Bauer, A. Föhlisch, L. Kipp, W. Wurth, K. Rossnagel, Ultrafast melting of a charge-density wave in the mott insulator 1T-TaS_2, Phys. Rev. Lett. 105 (2010) 187401, http://dx.doi.org/10.1103/PhysRevLett.105.187401.

[136] S. De Jong, R. Kukreja, C. Trabant, N. Pontius, C.F. Chang, T. Kachel, M. Beye, F. Sorgenfrei, C.H. Back, B. Bräuer, W.F. Schlotter, J.J. Turner, O. Krupin, M. Doehler, D. Zhu, M.A. Hossain, A.O. Scherz, D. Fausti, F. Novelli, M. Esposito, W.S. Lee, Y.D. Chuang, D.H. Lu, R.G. Moore, M. Yi, M. Trigo, P. Kirchmann, L. Pathey, M.S. Golden, M. Buchholz, P. Metcalf, F. Parmigiani, W. Wurth, A. Föhlisch, C. Schüß ler Langeheine, H.A. Dürr, Speed limit of the insulator–metal transition in magnetite, Nature Mater. 12 (10) (2013) 882–886, http://dx.doi.org/10.1038/nmat3718.

[137] F. Schmitt, P.S. Kirchmann, U. Bovensiepen, R.G. Moore, L. Rettig, M. Krenz, J.-H. Chu, N. Ru, L. Perfetti, D.H. Lu, M. Wolf, I.R. Fisher, Z.-X. Shen, Transient electronic structure and melting of a charge density wave in $TbTe_3$, Science 321 (5896) (2008) 1649–1652, http://dx.doi.org/10.1126/science.1160778.

[138] D. Wegkamp, J. Stähler, Ultrafast dynamics during the photoinduced phase transition in VO_2, Prog. Surf. Sci. 90 (4) (2015) 464–502, http://dx.doi.org/10.1016/j.progsurf.2015.10.001.

[139] A. Jiménez-Banzo, X. Ragàs, P. Kapusta, S. Nonell, Time-resolved methods in biophysics. 7. Photon counting vs. analog time-resolved singlet oxygen phosphorescence detection, Photoch. Photobio. Sci. 7 (9) (2008) 1003–1010, http://dx.doi.org/10.1039/B804333G.

[140] S. Vempati, L. Bogner, C. Richter, J.-C. Deinert, L. Foglia, L. Gierster, J. Stähler, Photoexcited organic molecules en route to highly efficient autoionization, J. Chem. Phys. 152 (7) (2020) 074715, http://dx.doi.org/10.1063/1.5136075.

[141] L. Foglia, L. Bogner, M. Wolf, J. Stähler, Localization-dependent charge separation efficiency at an organic/inorganic hybrid interface, Chem. Phys. Lett. 646 (2016) 25–30, http://dx.doi.org/10.1016/j.cplett.2015.12.050.

[142] K.F. Mak, C. Lee, J. Hone, J. Shan, T.F. Heinz, Atomically thin MoS_2: A new direct-gap semiconductor, Phys. Rev. Lett. 105 (13) (2010) 136805, http://dx.doi.org/10.1103/PhysRevLett.105.136805.

[143] A. Splendiani, L. Sun, Y. Zhang, T. Li, J. Kim, C.-Y. Chim, G. Galli, F. Wang, Emerging photoluminescence in monolayer MoS_2, Nano Lett. 10 (4) (2010) 1271–1275, http://dx.doi.org/10.1021/nl903868w.

[144] A. Chernikov, T.C. Berkelbach, H.M. Hill, A. Rigosi, Y. Li, B. Aslan, D.R. Reichman, M.S. Hybertsen, T.F. Heinz, Exciton binding energy and nonhydrogenic Rydberg series in monolayer WS_2, Phys. Rev. Lett. 113 (7) (2014) 076802, http://dx.doi.org/10.1103/PhysRevLett.113.076802.

[145] K. He, N. Kumar, L. Zhao, Z. Wang, K.F. Mak, H. Zhao, J. Shan, Tightly bound excitons in monolayer WSe_2, Phys. Rev. Lett. 113 (2) (2014) 026803, http://dx.doi.org/10.1103/PhysRevLett.113.026803.

[146] Z. Ye, T. Cao, K. O'Brien, H. Zhu, X. Yin, Y. Wang, S.G. Louie, X. Zhang, Probing excitonic dark states in single-layer tungsten disulphide, Nature 513 (7517) (2014) 214–218, http://dx.doi.org/10.1038/nature13734.

[147] X.-X. Zhang, Y. You, S.Y.F. Zhao, T.F. Heinz, Experimental evidence for dark excitons in monolayer WSe_2, Phys. Rev. Lett. 115 (25) (2015) 257403, http://dx.doi.org/10.1103/PhysRevLett.115.257403.

[148] D. Christiansen, M. Selig, G. Berghäuser, R. Schmidt, I. Niehues, R. Schneider, A. Arora, S.M. de Vasconcellos, R. Bratschitsch, E. Malic, A. Knorr, Phonon sidebands in monolayer transition metal dichalcogenides, Phys. Rev. Lett. 119 (18) (2017) 187402, http://dx.doi.org/10.1103/PhysRevLett.119.187402.

[149] M. Selig, G. Berghäuser, A. Raja, P. Nagler, C. Schüller, T.F. Heinz, T. Korn, A. Chernikov, E. Malic, A. Knorr, Excitonic linewidth and coherence lifetime in monolayer transition metal dichalcogenides, Nature Commun. 7 (1) (2016) 13279, http://dx.doi.org/10.1038/ncomms13279.

[150] E. Malic, M. Selig, M. Feierabend, S. Brem, D. Christiansen, F. Wendler, A. Knorr, G. Berghäuser, Dark excitons in transition metal dichalcogenides, Phys. Rev. Mater. 2 (1) (2018) 014002, http://dx.doi.org/10.1103/PhysRevMaterials.2.014002.

[151] M. Selig, G. Berghäuser, M. Richter, R. Bratschitsch, A. Knorr, E. Malic, Dark and bright exciton formation, thermalization, and photoluminescence in monolayer transition metal dichalcogenides, 2D Mater. 5 (3) (2018) 035017, http://dx.doi.org/10.1088/2053-1583/aabea3.

[152] G. Wang, A. Chernikov, M.M. Glazov, T.F. Heinz, X. Marie, T. Amand, B. Urbaszek, Colloquium: Excitons in atomically thin transition metal dichalcogenides, Rev. Modern Phys. 90 (2) (2018) 021001, http://dx.doi.org/10.1103/RevModPhys.90.021001.

[153] T. Deilmann, K.S. Thygesen, Finite-momentum exciton landscape in mono-and bilayer transition metal dichalcogenides, 2D Mater. 6 (3) (2019) 035003, http://dx.doi.org/10.1088/2053-1583/ab0e1d.

[154] O. Karni, I. Esin, K.M. Dani, Through the lens of a momentum microscope: Viewing light-induced quantum phenomena in 2D materials, Adv. Mater. 35 (27) (2023) 2204120, http://dx.doi.org/10.1002/adma.202204120.

[155] M. Reutzel, G.S.M. Jansen, S. Mathias, Probing excitons with time-resolved momentum microscopy, Adv. Phys.: X 9 (1) (2024) 2378722, http://dx.doi.org/10.1080/23746149.2024.2378722.

[156] M. Bauer, A. Marienfeld, M. Aeschlimann, Hot electron lifetimes in metals probed by time-resolved two-photon photoemission, Prog. Surf. Sci. 90 (3) (2015) 319–376, http://dx.doi.org/10.1016/j.progsurf.2015.05.001.

[157] D. Kutnyakhov, R.P. Xian, M. Dendzik, M. Heber, F. Pressacco, S.Y. Agustsson, L. Wenthaus, H. Meyer, S. Gieschen, G. Mercurio, A. Benz, K. Bühlman, S. Däster, R. Gort, D. Curcio, K. Volckaert, M. Bianchi, C. Sanders, J.A. Miwa, S. Ulstrup, A. Oelsner, C. Tusche, Y.-J. Chen, D. Vasilyev, K. Medjanik, G. Brenner, S. Dziarzhytski, H. Redlin, B. Manschwetus, S. Dong, J. Hauer, L. Rettig, F. Diekmann, K. Rossnagel, J. Demsar, H.-J. Elmers, P. Hofmann, R. Ernstorfer, G. Schönhense, Y. Acremann, W. Wurth, Time- and momentum-resolved photoemission studies using time-of-flight momentum microscopy at a free-electron laser, Rev. Sci. Instrum. 91 (1) (2020) 013109, http://dx.doi.org/10.1063/1.5118777.

[158] M. Keuenecke, C. Möller, D. Schmitt, H. Nolte, G.S.M. Jansen, M. Reutzel, M. Gutberlet, G. Halasi, D. Steil, S. Steil, S. Mathias, Time-resolved momentum microscopy with a 1 MHz high-harmonic extreme ultraviolet beamline, Rev. Sci. Instrum. 91 (6) (2020) 063905, http://dx.doi.org/10.1063/5.0006531.

[159] M. Keuenecke, M. Reutzel, D. Schmitt, A. Osterkorn, T.A. Mishra, C. Möller, W. Bennecke, G.S.M. Jansen, D. Steil, S.R. Manmana, S. Steil, S. Kehrein, S. Mathias, Electromagnetic dressing of the electron energy spectrum of Au(111) at high momenta, Phys. Rev. B 102 (16) (2020) 161403, http://dx.doi.org/10.1103/PhysRevB.102.161403.

[160] J. Madéo, M.K.L. Man, C. Sahoo, M. Campbell, V. Pareek, E.L. Wong, A. Al-Mahboob, N.S. Chan, A. Karmakar, B.M.K. Mariserla, X. Li, T.F. Heinz, T. Cao, K.M. Dani, Directly visualizing the momentum-forbidden dark excitons and their dynamics in atomically thin semiconductors, Science 370 (6521) (2020) 1199–1204, http://dx.doi.org/10.1126/science.aba1029.

[161] S. Dong, M. Puppin, T. Pincelli, S. Beaulieu, D. Christiansen, H. Hübener, C.W. Nicholson, R.P. Xian, M. Dendzik, Y. Deng, Y.W. Windsor, M. Selig, E. Malic, A. Rubio, A. Knorr, M. Wolf, L. Rettig, R. Ernstorfer, Direct measurement of key exciton properties: Energy, dynamics, and spatial distribution of the wave function, Nat. Sci. 1 (1) (2021) e10010, http://dx.doi.org/10.1002/ntls.10010.

[162] R. Wallauer, R. Perea-Causin, L. Münster, S. Zajusch, S. Brem, J. Güdde, K. Tanimura, K.-Q. Lin, R. Huber, E. Malic, U. Höfer, Momentum-resolved observation of exciton formation dynamics in monolayer WS_2, Nano Lett. 21 (13) (2021) 5867–5873, http://dx.doi.org/10.1021/acs.nanolett.1c01839.

[163] A. Kunin, S. Chernov, J. Bakalis, Z. Li, S. Cheng, Z.H. Withers, M.G. White, G. Schönhense, X. Du, R.K. Kawakami, T.K. Allison, Momentum-resolved exciton coupling and valley polarization dynamics in monolayer WS_2, Phys. Rev. Lett. 130 (4) (2023) 046202, http://dx.doi.org/10.1103/PhysRevLett.130.046202.

[164] S. Beaulieu, S. Dong, V. Christiansson, P. Werner, T. Pincelli, J.D. Ziegler, T. Taniguchi, K. Watanabe, A. Chernikov, M. Wolf, L. Rettig, R. Ernstorfer, M. Schüler, Berry curvature signatures in chiroptical excitonic transitions, Sci. Adv. 10 (26) (2024) eadk3897, http://dx.doi.org/10.1126/sciadv.adk3897.

[165] S. Mathias, L. Miaja-Avila, M.M. Murnane, H. Kapteyn, M. Aeschlimann, M. Bauer, Angle-resolved photoemission spectroscopy with a femtosecond high harmonic light source using a two-dimensional imaging electron analyzer, Rev. Sci. Instrum. 78 (8) (2007) 083105, http://dx.doi.org/10.1063/1.2773783.

[166] A. Li, N.A. James, T. Wang, Z. Wang, H. Petek, M. Reutzel, Towards full surface Brillouin zone mapping by coherent multi-photon photoemission, New J. Phys. 22 (2020) 073035, http://dx.doi.org/10.1088/1367-2630/ab98d6.

[167] B. Krömker, M. Escher, D. Funnemann, D. Hartung, H. Engelhard, J. Kirschner, Development of a momentum microscope for time resolved band structure imaging, Rev. Sci. Instrum. 79 (5) (2008) 053702, http://dx.doi.org/10.1063/1.2918133.

[168] K. Medjanik, O. Fedchenko, S. Chernov, D. Kutnyakhov, M. Ellguth, A. Oelsner, B. Schönhense, T.R.F. Peixoto, P. Lutz, C.-H. Min, F. Reinert, S. Däster, Y. Acremann, J. Viefhaus, W. Wurth, H.J. Elmers, G. Schönhense, Direct 3D mapping of the Fermi surface and Fermi velocity, Nature Mater. 16 (6) (2017) 615–621, http://dx.doi.org/10.1038/nmat4875.

[169] D. Schmitt, J.P. Bange, A. AlMutairi, G. Meneghini, K. Watanabe, T. Taniguchi, D.R. Luke, R.T. Weitz, S. Steil, G.S.M. Jansen, S. Brem, E. Malic, S. Hofmann, M. Reutzel, S. Mathias, Formation of Moiré interlayer excitons in space and time, Nature 608 (2022) 499, http://dx.doi.org/10.1038/s41586-022-04977-7.

[170] D. Schmitt, J.P. Bange, W. Bennecke, G. Meneghini, A. AlMutairi, M. Merboldt, J. Pöhls, K. Watanabe, T. Taniguchi, S. Steil, D. Steil, R.T. Weitz, S. Hofmann, S. Brem, G.S.M. Jansen, E. Malic, S. Mathias, M. Reutzel, Ultrafast nano-imaging of dark excitons, 2023, http://dx.doi.org/10.48550/arXiv.2305.18908, arXiv:2305.18908.

[171] N.R. Wilson, P.V. Nguyen, K. Seyler, P. Rivera, A.J. Marsden, Z.P. Laker, G.C. Constantinescu, V. Kandyba, A. Barinov, N.D. Hine, X. Xu, D.H. Cobden, Determination of band offsets, hybridization, and exciton binding in 2D semiconductor heterostructures, Sci. Adv. 3 (2) (2017) e1601832, http://dx.doi.org/10.1126/sciadv.1601832.

[172] J.P. Bange, D. Schmitt, W. Bennecke, G. Meneghini, A. AlMutairi, K. Watanabe, T. Taniguchi, D. Steil, S. Steil, R.T. Weitz, G.S.M. Jansen, S. Hofmann, S. Brem, E. Malic, M. Reutzel, S. Mathias, Probing electron-hole Coulomb correlations in the exciton landscape of a twisted semiconductor heterostructure, Sci. Adv. 10 (6) (2024) eadi1323, http://dx.doi.org/10.1126/sciadv.adi1323.

[173] G. Meneghini, M. Reutzel, S. Mathias, S. Brem, E. Malic, Hybrid exciton signatures in ARPES spectra of van der Waals materials, ACS Photon. 10 (10) (2023) 3570–3575, http://dx.doi.org/10.1021/acsphotonics.3c00599.

[174] W. Bennecke, A. Windischbacher, D. Schmitt, J.P. Bange, R. Hemm, C.S. Kern, G. D'Avino, X. Blase, D. Steil, S. Steil, M. Aeschlimann, B. Stadtmüller, M. Reutzel, P. Puschnig, G.S.M. Jansen, S. Mathias, Disentangling the multiorbital contributions of excitons by photoemission exciton tomography, Nature Commun. 15 (1) (2024) 1804, http://dx.doi.org/10.1038/s41467-024-45973-x.

[175] J.P. Bange, P. Werner, D. Schmitt, W. Bennecke, G. Meneghini, A. AlMutairi, M. Merboldt, K. Watanabe, T. Taniguchi, S. Steil, D. Steil, R.T. Weitz, S. Hofmann, G.S.M. Jansen, S. Brem, E. Malic, M. Reutzel, S. Mathias, Ultrafast dynamics of bright and dark excitons in monolayer WSe_2 and heterobilayer WSe_2/MoS_2, 2D Mater. 10 (3) (2023) 035039, http://dx.doi.org/10.1088/2053-1583/ace067.

[176] A. Arora, M. Koperski, K. Nogajewski, J. Marcus, C. Faugeras, M. Potemski, Excitonic resonances in thin films of WSe_2: From monolayer to bulk material, Nanoscale 7 (23) (2015) 10421–10429, http://dx.doi.org/10.1039/C5NR01536G.

[177] O. Karni, E. Barré, S.C. Lau, R. Gillen, E.Y. Ma, B. Kim, K. Watanabe, T. Taniguchi, J. Maultzsch, K. Barmak, R.H. Page, T.F. Heinz, Infrared interlayer exciton emission in MoS_2/WSe_2 heterostructures, Phys. Rev. Lett. 123 (24) (2019) 247402, http://dx.doi.org/10.1103/PhysRevLett.123.247402.

[178] J. Lindlau, M. Selig, A. Neumann, L. Colombier, J. Förste, V. Funk, M. Förg, J. Kim, G. Berghäuser, T. Taniguchi, K. Watanabe, F. Wang, E. Malic, A. Högele, The role of momentum-dark excitons in the elementary optical response of bilayer WSe_2, Nature Commun. 9 (1) (2018) 2586, http://dx.doi.org/10.1038/s41467-018-04877-3.

[179] G. Berghäuser, P. Steinleitner, P. Merkl, R. Huber, A. Knorr, E. Malic, Mapping of the dark exciton landscape in transition metal dichalcogenides, Phys. Rev. B 98 (2) (2018) 020301, http://dx.doi.org/10.1103/PhysRevB.98.020301.

[180] D. Christiansen, M. Selig, E. Malic, R. Ernstorfer, A. Knorr, Theory of exciton dynamics in time-resolved ARPES: Intra- and intervalley scattering in two-dimensional semiconductors, Phys. Rev. B 100 (20) (2019) 205401, http://dx.doi.org/10.1103/PhysRevB.100.205401.

[181] C. Trovatello, F. Katsch, N.J. Borys, M. Selig, K. Yao, R. Borrego-Varillas, F. Scotognella, I. Kriegel, A. Yan, A. Zettl, P.J. Schuck, A. Knorr, G. Cerullo, S.D. Conte, The ultrafast onset of exciton formation in 2D semiconductors, Nature Commun. 11 (1) (2020) 5277, http://dx.doi.org/10.1038/s41467-020-18835-5.

[182] S. Brem, M. Selig, G. Berghaeuser, E. Malic, Exciton relaxation cascade in two-dimensional transition metal dichalcogenides, Reports 8 (1) (2018) 8238, http://dx.doi.org/10.1038/s41598-018-25906-7.

[183] J.E. Zimmermann, M. Axt, F. Mooshammer, P. Nagler, C. Schüller, T. Korn, U. Höfer, G. Mette, Ultrafast charge-transfer dynamics in twisted MoS_2/WSe_2 heterostructures, ACS Nano 15 (9) (2021) 14725–14731, http://dx.doi.org/10.1021/acsnano.1c04549.

[184] H. Zhu, J. Wang, Z. Gong, Y.D. Kim, J. Hone, X.-Y. Zhu, Interfacial charge transfer circumventing momentum mismatch at two-dimensional van der Waals heterojunctions, Nano Lett. 17 (6) (2017) 3591–3598, http://dx.doi.org/10.1021/acs.nanolett.7b00748.

[185] Q. Cui, F. Ceballos, N. Kumar, H. Zhao, Transient absorption microscopy of monolayer and bulk WSe_2, ACS Nano 8 (3) (2014) 2970–2976, http://dx.doi.org/10.1021/nn500277y.

[186] S. Brem, A. Ekman, D. Christiansen, F. Katsch, M. Selig, C. Robert, X. Marie, B. Urbaszek, A. Knorr, E. Malic, Phonon-assisted photoluminescence from indirect excitons in monolayers of transition-metal dichalcogenides, Nano Lett. 20 (4) (2020) 2849–2856, http://dx.doi.org/10.1021/acs.nanolett.0c00633.

[187] L. Yuan, B. Zheng, J. Kunstmann, T. Brumme, A.B. Kuc, C. Ma, S. Deng, D. Blach, A. Pan, L. Huang, Twist-angle-dependent interlayer exciton diffusion in $WS_2–WSe_2$ heterobilayers, Nature Mater. 19 (6) (2020) 617–623, http://dx.doi.org/10.1038/s41563-020-0670-3.

[188] C. Robert, D. Lagarde, F. Cadiz, G. Wang, B. Lassagne, T. Amand, A. Balocchi, P. Renucci, S. Tongay, B. Urbaszek, X. Marie, Exciton radiative lifetime in transition metal dichalcogenide monolayers, Phys. Rev. B 93 (20) (2016) 205423, http://dx.doi.org/10.1103/PhysRevB.93.205423.

[189] O. Karni, E. Barré, V. Pareek, J.D. Georgaras, M.K.L. Man, C. Sahoo, D.R. Bacon, X. Zhu, H.B. Ribeiro, A.L. O'Beirne, J. Hu, A. Al-Mahboob, M.M.M. Abdelrasoul, N.S. Chan, A. Karmakar, A.J. Winchester, B. Kim, K. Watanabe, T. Taniguchi, K. Barmak, J. Madéo, F.H. da Jornada, T.F. Heinz, K.M. Dani, Structure of the Moiré exciton captured by imaging its electron and hole, Nature 603 (7900) (2022) 247–252, http://dx.doi.org/10.1038/s41586-021-04360-y.

[190] K. Tran, G. Moody, F. Wu, X. Lu, J. Choi, K. Kim, A. Rai, D.A. Sanchez, J. Quan, A. Singh, J. Embley, A. Zepeda, M. Campbell, T. Autry, T. Taniguchi, K. Watanabe, N. Lu, S.K. Banerjee, K.L. Silverman, S. Kim, E. Tutuc, L. Yang, A.H. MacDonald, X. Li, Evidence for Moiré excitons in van der Waals heterostructures, Nature 567 (7746) (2019) 71–75, http://dx.doi.org/10.1038/s41586-019-0975-z.

[191] K.L. Seyler, P. Rivera, H. Yu, N.P. Wilson, E.L. Ray, D.G. Mandrus, J. Yan, W. Yao, X. Xu, Signatures of Moiré-trapped valley excitons in $MoSe_2/WSe_2$ heterobilayers, Nature 567 (7746) (2019) 66–70, http://dx.doi.org/10.1038/s41586-019-0957-1.

[192] E.M. Alexeev, D.A. Ruiz-Tijerina, M. Danovich, M.J. Hamer, D.J. Terry, P.K. Nayak, S. Ahn, S. Pak, J. Lee, J.I. Sohn, M.R. Molas, M. Koperski, K. Watanabe, T. Taniguchi, K.S. Novoselov, R.V. Gorbachev, H.S. Shin, V.I. Fal'ko, A.I. Tartakovskii, Resonantly hybridized excitons in Moiré superlattices in van der

Waals heterostructures, Nature 567 (7746) (2019) 81–86, http://dx.doi.org/10.1038/s41586-019-0986-9.

[193] C. Jin, E.C. Regan, A. Yan, M. Iqbal Bakti Utama, D. Wang, S. Zhao, Y. Qin, S. Yang, Z. Zheng, S. Shi, K. Watanabe, T. Taniguchi, S. Tongay, A. Zettl, F. Wang, Observation of Moiré excitons in WSe₂WS₂ heterostructure superlattices, Nature 567 (7746) (2019) 76–80, http://dx.doi.org/10.1038/s41586-019-0976-y.

[194] J. Kunstmann, F. Mooshammer, P. Nagler, A. Chaves, F. Stein, N. Paradiso, G. Plechinger, C. Strunk, C. Schüller, G. Seifert, D.R. Reichman, T. Korn, Momentum-space indirect interlayer excitons in transition-metal dichalcogenide van der Waals heterostructures, Nat. Phys. 14 (8) (2018) 801–805, http://dx.doi.org/10.1038/s41567-018-0123-y.

[195] Y. Wang, Z. Wang, W. Yao, G.-B. Liu, H. Yu, Interlayer coupling in commensurate and incommensurate bilayer structures of transition-metal dichalcogenides, Phys. Rev. B 95 (11) (2017) 115429, http://dx.doi.org/10.1103/PhysRevB.95.115429.

[196] C. Jin, E.Y. Ma, O. Karni, E.C. Regan, F. Wang, T.F. Heinz, Ultrafast dynamics in van der Waals heterostructures, Nat. Nanotechnol. 13 (11) (2018) 994–1003, http://dx.doi.org/10.1038/s41565-018-0298-5.

[197] S. Ovesen, S. Brem, C. Linderälv, M. Kuisma, T. Korn, P. Erhart, M. Selig, E. Malic, Interlayer exciton dynamics in van der Waals heterostructures, Commun. Phys. 2 (1) (2019) 1–8, http://dx.doi.org/10.1038/s42005-019-0122-z.

[198] P. Merkl, F. Mooshammer, P. Steinleitner, A. Girnghuber, K.-Q. Lin, P. Nagler, J. Holler, C. Schüller, J.M. Lupton, T. Korn, S. Ovesen, S. Brem, E. Malic, R. Huber, Ultrafast transition between exciton phases in van der Waals heterostructures, Nature Mater. 18 (7) (2019) 691–696, http://dx.doi.org/10.1038/s41563-019-0337-0.

[199] V.R. Policht, M. Russo, F. Liu, C. Trovatello, M. Maiuri, Y. Bai, X. Zhu, S. Dal Conte, G. Cerullo, Dissecting interlayer hole and electron transfer in transition metal dichalcogenide heterostructures via two-dimensional electronic spectroscopy, Nano Lett. 21 (11) (2021) 4738–4743, http://dx.doi.org/10.1021/acs.nanolett.1c01098.

[200] V.R. Policht, H. Mittenzwey, O. Dogadov, M. Katzer, A. Villa, Q. Li, B. Kaiser, A.M. Ross, F. Scotognella, X. Zhu, A. Knorr, M. Selig, G. Cerullo, S. Dal Conte, Time-domain observation of interlayer exciton formation and thermalization in a MoSe₂/WSe₂ heterostructure, Nature Commun. 14 (1) (2023) 7273, http://dx.doi.org/10.1038/s41467-023-42915-x.

[201] G. Meneghini, S. Brem, E. Malic, Ultrafast phonon-driven charge transfer in van der Waals heterostructures, Nat. Sci. 2 (4) (2022) e20220014, http://dx.doi.org/10.1002/ntls.20220014.

[202] Z. Jin, X. Li, J.T. Mullen, K.W. Kim, Intrinsic transport properties of electrons and holes in monolayer transition-metal dichalcogenides, Phys. Rev. B 90 (4) (2014) 045422, http://dx.doi.org/10.1103/PhysRevB.90.045422.

[203] A. Raja, M. Selig, G. Berghäuser, J. Yu, H.M. Hill, A.F. Rigosi, L.E. Brus, A. Knorr, T.F. Heinz, E. Malic, A. Chernikov, Enhancement of exciton–phonon scattering from monolayer to bilayer WS₂, Nano Lett. 18 (10) (2018) 6135–6143, http://dx.doi.org/10.1021/acs.nanolett.8b01793.

[204] L. Zhang, A. Sharma, Y. Zhang, Y. Zhang, B. Wang, M. Dong, H.T. Nguyen, Z. Wang, B. Wen, Y. Cao, B. Liu, X. Sun, J. Yang, Z. Li, A. Kar, Y. Shi, D. Macdonald, Z. Yu, X. Wang, Y. Lu, Efficient and layer-dependent exciton pumping across atomically thin organic–inorganic type-I heterostructures, Adv. Mater. 30 (40) (2018) 1803986, http://dx.doi.org/10.1002/adma.201803986.

[205] F. Mahmood, C.-K. Chan, Z. Alpichshev, D. Gardner, Y. Lee, P.A. Lee, N. Gedik, Selective scattering between Floquet–Bloch and Volkov states in a topological insulator, Nat. Phys. 12 (4) (2016) 306–310, http://dx.doi.org/10.1038/nphys3609.

[206] S. Ito, M. Schüler, M. Meierhofer, S. Schlauderer, J. Freudenstein, R. Reimann, D. Afanasiev, K.A. Kokh, O.E. Tereshchenko, J. Güdde, M.A. Sentef, U. Höfer, R. Huber, Build-up and dephasing of Floquet-Bloch bands on subcycle timescales, Nature 616 (2023) 696, http://dx.doi.org/10.1038/s41586-023-05850-x.

[207] S. Zhou, C. Bao, B. Fan, H. Zhou, Q. Gao, H. Zhong, T. Lin, H. Liu, P. Yu, P. Tang, S. Meng, W. Duan, S. Zhou, Pseudospin-selective Floquet band engineering in black phosphorus, Nature 614 (7946) (2023) 75–80, http://dx.doi.org/10.1038/s41586-022-05610-3.

[208] L. Wang, E.-M. Shih, A. Ghiotto, L. Xian, D.A. Rhodes, C. Tan, M. Claassen, D.M. Kennes, Y. Bai, B. Kim, K. Watanabe, T. Taniguchi, X. Zhu, J. Hone, A. Rubio, A.N. Pasupathy, C.R. Dean, Correlated electronic phases in twisted bilayer transition metal dichalcogenides, Nature Mater. 19 (8) (2020) 861–866, http://dx.doi.org/10.1038/s41563-020-0708-6.

[209] E.A. Arsenault, Y. Li, B. Yang, X. Wang, H. Park, E. Mosconi, E. Ronca, T. Taniguchi, K. Watanabe, D. Gamelin, A. Millis, C.R. Dean, F. De Angelis, X. Xu, X.Y. Zhu, Two-dimensional Moiré polaronic electron crystals, Phys. Rev. Lett. 132 (12) (2024) 126501, http://dx.doi.org/10.1103/PhysRevLett.132.126501.

[210] W.S. Fann, R. Storz, H.W.K. Tom, J. Bokor, Electron thermalization in gold, Phys. Rev. B 46 (1992) 13592–13595, http://dx.doi.org/10.1103/PhysRevB.46.13592.

[211] E. Bauer, Surface Microscopy with Low Energy Electrons, Springer, New York, 2014.

[212] O. Bostanjoglo, M. Weingaertner, Pulsed photoelectron microscope for imaging laser-induced nanosecond processes, Rev. Sci. Instrum. 68 (6) (1997) 2456–2460, http://dx.doi.org/10.1063/1.1148168.

[213] O. Schmidt, M. Bauer, C. Wiemann, R. Porath, M. Scharte, O. Andreyev, G. Schönhense, M. Aeschlimann, Time-resolved two photon photoemission electron microscopy, Appl. Phys. B 74 (3) (2002) 223–227, http://dx.doi.org/10.1007/s003400200803.

[214] A. Kubo, K. Onda, H. Petek, Z. Sun, Y.S. Jung, H.K. Kim, Femtosecond imaging of surface plasmon dynamics in a nanostructured silver film, Nano Lett. 5 (6) (2005) 1123–1127, http://dx.doi.org/10.1021/nl0506655.

[215] F.-J. Meyer zu Heringdorf, L. Chelaru, S. Möllenbeck, D. Thien, M. Horn-von Hoegen, Femtosecond photoemission microscopy, Surf. Sci. 601 (20) (2007) 4700–4705, http://dx.doi.org/10.1016/j.susc.2007.05.052.

[216] A. Mikkelsen, J. Schwenke, T. Fordell, G. Luo, K. Klünder, E. Hilner, N. Anttu, A.A. Zakharov, E. Lundgren, J. Mauritsson, J.N. Andersen, H.Q. Xu, A. L'Huillier, Photoemission electron microscopy using extreme ultraviolet attosecond pulse trains, Rev. Sci. Instrum. 80 (12) (2009) 123703, http://dx.doi.org/10.1063/1.3263759.

[217] M.U. Wehner, M.H. Ulm, M. Wegener, Scanning interferometer stabilized by use of Pancharatnam's phase, Opt. Lett. 22 (19) (1997) 1455–1457, http://dx.doi.org/10.1364/OL.22.001455.

[218] C. Scheider, Mapping of Surface Plasmon Polariton Fields by Time-Resolved Photoemission Electron Microscopy: Experiments, Simulations, and Applications (PhD theses), TU Kaiserslautern, 2013.

[219] M. Escher, N. Weber, M. Merkel, C. Ziethen, P. Bernhard, G. Schönhense, S. Schmidt, F. Forster, F. Reinert, B. Krömker, D. Funnemann, NanoESCA: a novel energy filter for imaging X-ray photoemission spectroscopy, J. Phys. Condens. Matter. 17 (16) (2005) S1329, http://dx.doi.org/10.1088/0953-8984/17/16/004.

[220] A. Oelsner, M. Rohmer, C. Schneider, D. Bayer, G. Schönhense, M. Aeschlimann, Time- and energy resolved photoemission electron microscopy-imaging of photoelectron time-of-flight analysis by means of pulsed excitations, J. Electron. Spectros. Relat. Phenomena 178–179 (2010) 317–330, http://dx.doi.org/10.1016/j.elspec.2009.10.008.

[221] O. Scherzer, Spherical and chromatic correction of electron lenses (Translated from German), Optik 2 (1947) 114.

[222] J. Feng, E. Forest, A.A. MacDowell, M. Marcus, H. Padmore, S. Raoux, D. Robin, A. Scholl, R. Schlueter, P. Schmid, J. Stöhr, W. Wan, D.H. Wei, Y. Wu, An X-ray photoemission electron microscope using an electron mirror aberration corrector for the study of complex materials, J. Phys. Condens. Matter. 17 (16) (2005) S1339, http://dx.doi.org/10.1088/0953-8984/17/16/005.

[223] R. Wichtendahl, R. Fink, H. Kuhlenbeck, D. Preikszas, H. Rose, R. Spehr, P. Hartel, W. Engel, R. Schlögl, H.-J. Freund, A.M. Bradshaw, G. Lilienkamp, T. Schmidt, E. Bauer, G. Benner, E. Umbach, SMART: An aberration-corrected XPEEM/LEEM with energy filter, Surf. Rev. Lett. 05 (06) (1998) 1249–1256, http://dx.doi.org/10.1142/S0218625X98001584.

[224] C. Tusche, M. Ellguth, A. Krasyuk, A. Winkelmann, D. Kutnyakhov, P. Lushchyk, K. Medjanik, G. Schönhense, J. Kirschner, Quantitative spin polarization analysis in photoelectron emission microscopy with an imaging spin filter, Ultramicroscopy 2008 (2013) 70–76, http://dx.doi.org/10.1016/j.ultramic.2013.02.022.

[225] P. Kahl, S. Wall, C. Witt, C. Schneider, D. Bayer, A. Fischer, P. Melchior, M. Horn-von Hoegen, M. Aeschlimann, F.-J. Meyer zu Heringdorf, Normal-incidence photoemission electron microscopy (NI-PEEM) for imaging surface plasmon polaritons, Plasmonics 9 (2014) 1401–1407, http://dx.doi.org/10.1007/s11468-014-9756-6.

[226] M. Dabrowski, Y. Dai, H. Petek, Ultrafast photoemission electron microscopy: Imaging plasmons in space and time, Chem. Rev. 120 (13) (2020) 6247–6287, http://dx.doi.org/10.1021/acs.chemrev.0c00146, PMID: 32530607.

[227] D. Bayer, C. Wiemann, O. Gaier, M. Bauer, M. Aeschlimann, Time-resolved 2PPEand time-resolved PEEM as a probe of LSP's in silver nanoparticles, J. Nanomater. 2008 (2008) 249514, http://dx.doi.org/10.1155/2008/249514.

[228] P. Melchior, D. Bayer, C. Schneider, A. Fischer, M. Rohmer, W. Pfeiffer, M. Aeschlimann, Optical near-field interference in the excitation of a bowtie nanoantenna, Phys. Rev. B 83 (2011) 235407, http://dx.doi.org/10.1103/PhysRevB.83.235407.

[229] P. Kahl, D. Podbiel, C. Schneider, A. Makris, S. Sindermann, C. Witt, D. Kilbane, M. Horn-von Hoegen, M. Aeschlimann, F.-J. Meyer zu Heringdorf, Direct observation of surface plasmon polariton propagation and interference by time-resolved imaging in normal-incidence two photon photoemission microscopy, Plasmonics 13 (2018) 239–246, http://dx.doi.org/10.1007/s11468-017-0504-6.

[230] C. Lemke, T.L. ner, S. Jauernik, A. Klick, J. Fiutowski, J. Kjelstrup-Hansen, H.-G. Rubahn, M. Bauer, Mapping surface plasmon polariton propagation via counter-propagating light pulses, Opt. Express 20 (12) (2012) 12877–12884, http://dx.doi.org/10.1364/OE.20.012877.

[231] E. Prinz, M. Hartelt, G. Spektor, M. Orenstein, M. Aeschlimann, Orbital angular momentum in nanoplasmonic vortices, ACS Photon. 10 (2) (2023) 340–367, http://dx.doi.org/10.1021/acsphotonics.2c01321.

[232] G. Spektor, D. Kilbane, A.K. Mahro, M. Hartelt, E. Prinz, M. Aeschlimann, M. Orenstein, Mixing the light spin with plasmon orbit by nonlinear light-matter interaction in gold, Phys. Rev. X 9 (2019) 021031, http://dx.doi.org/10.1103/PhysRevX.9.021031.

[233] S. Kosar, K.M. Deni, Time-resolved photoemission electron microscopy of semiconductor interfaces, Prog. Surf. Sci. in print (2024) http://dx.doi.org/10.1016/j.progsurf.2024.100745.

[234] K. Fukumoto, Y. Yamada, K. Onda, S.-y. Koshihara, Direct imaging of electron recombination and transport on a semiconductor surface by femtosecond time-resolved photoemission electron microscopy, Appl. Phys. Lett. 104 (5) (2014) 053117, http://dx.doi.org/10.1063/1.4864279.

[235] Z. Xue, W. Zheng, Y. Li, M. Xue, A. Hu, J. Chen, S. Jia, J. Tang, J. Chen, J. Du, P. Gao, M. Ren, S. Wang, Y. Liu, H. Yang, Z. Liao, G. Lu, Q. Gong, Ultraviolet/visible quasicylindrical waves on semimetal Cd_3As_2 nanoplates, Adv. Photon. 3 (4) (2022) 2100354, http://dx.doi.org/10.1002/adpr.202100354.

[236] M.K.L. Man, A. Margiolakis, S. Deckoff-Jones, T. Harada, E.L. Wong, M.B.M. Krishna, J. Madéo, A. Winchester, S. Lei, R. Vajtai, P.M. Ajayan, K.M. Dani, Imaging the motion of electrons across semiconductor heterojunctions, Nat. Nanotechnol. 22 (12) (2017) 36–40, http://dx.doi.org/10.1038/nnano.2016.183.

[237] L. Wang, C. Xu, M.-Y. Li, L.-J. Li, Z.-H. Loh, Unraveling spatially heterogeneous ultrafast carrier dynamics of single-layer WSe_2 by femtosecond time-resolved photoemission electron microscopy, Nano Lett. 18 (2018) 5172–5178, http://dx.doi.org/10.1021/acs.nanolett.8b02103.

[238] M. Aeschlimann, T. Brixner, D. Differt, U. Heinzmann, M. Hensen, C. Kramer, F. Lükermann, P. Melchior, W. Pfeiffer, M. Piecuch, C. Schneider, H. Stiebig, C. Strüber, P. Thielen, Perfect absorption in nanotextured thin films via Anderson-localized photon modes, Nat. Photonics 9 (2015) 663–668, http://dx.doi.org/10.1038/nphoton.2015.159.

[239] E. Beaurepaire, J.-C. Merle, A. Daunois, J.-Y. Bigot, Ultrafast spin dynamics in ferromagnetic nickel, Phys. Rev. Lett. 76 (22) (1996) 4250, http://dx.doi.org/10.1103/PhysRevLett.76.4250.

[240] A. Vaterlaus, T. Beutler, F. Meier, Spin-lattice relaxation time of ferromagnetic gadolinium determined with time-resolved spin-polarized photoemission, Phys. Rev. Lett. 67 (1991) 3314, http://dx.doi.org/10.1103/PhysRevLett.67.3314.

[241] C.D. Stanciu, F. Hansteen, A.V. Kimel, A. Kirilyuk, A. Tsukamoto, A. Itoh, T. Rasing, All-optical magnetic recording with circularly polarized light, Phys. Rev. Lett. 99 (2007) 047601.

[242] I. Radu, K. Vahaplar, C. Stamm, T. Kachel, N. Pontius, H.A. Dürr, T.A. Ostler, J. Barker, R.F.L. Evans, R.W. Chantrell, A. Tsukamoto, A. Itoh, A. Kirilyuk, T. Rasing, A.V. Kimel, Transient ferromagnetic-like state mediating ultrafast reversal of antiferromagnetically coupled spins, Nature 472 (7342) (2011) 205–208, http://dx.doi.org/10.1038/nature09901.

[243] T. Ostler, J. Barker, R. Evans, R. Chantrell, U. Atxitia, O. Chubykalo-Fesenko, S. El Moussaoui, L. Le Guyader, E. Mengotti, L. Heyderman, F. Nolting, A. Tsukamoto, A. Itoh, D. Afanasiev, B. Ivanov, A. Kalashnikova, K. Vahaplar, J. Mentink, A. Kirilyuk, T. Rasing, A. Kimel, Ultrafast heating as a sufficient stimulus for magnetization reversal in a ferrimagnet, Nature Commun. 3 (2012) 666, http://dx.doi.org/10.1038/ncomms1666.

[244] C.E. Graves, A.H. Reid, T. Wang, B. Wu, S. de Jong, K. Vahaplar, I. Radu, D.P. Bernstein, M. Messerschmidt, L. Müller, R. Coffee, M. Bionta, S.W. Epp, R. Hartmann, N. Kimmel, G. Hauser, A. Hartmann, P. Holl, H. Gorke, J.H. Mentink, A. Tsukamoto, A. Fognini, J.J. Turner, W.F. Schlotter, D. Rolles, H. Soltau, L. Strüder, Y. Acremann, A.V. Kimel, A. Kirilyuk, T. Rasing, J. Stöhr, A.O. Scherz, H.A. Dürr, Nanoscale spin reversal by non-local angular momentum transfer following ultrafast laser excitation in ferrimagnetic GdFeCo, Nature Mater. 12 (4) (2013) 293–298, http://dx.doi.org/10.1038/nmat3597.

[245] A. Kirilyuk, A.V. Kimel, T. Rasing, Laser-induced magnetization dynamics and reversal in ferrimagnetic alloys, Rep. Prog. Phys. 76 (2013) 026501, http://dx.doi.org/10.1088/0034-4885/76/2/026501.

[246] T. Seifert, S. Jaiswal, U. Martens, J. Hannegan, L. Braun, P. Maldonado, F. Freimuth, A. Kronenberg, J. Henrizi, I. Radu, E. Beaurepaire, Y. Mokrousov, P.M. Oppeneer, M. Jourdan, G. Jakob, D. Turchinovich, L.M. Hayden, M. Wolf, M. Münzenberg, M. Kläui, T. Kampfrath, Efficient metallic spintronic emitters of ultrabroadband terahertz radiation, Nat. Photonics 10 (2016) 483–488, http://dx.doi.org/10.1038/nphoton.2016.91.

[247] K. Olejník, T. Seifert, Z. Kaspar, V. Novák, P. Wadley, R. Campion, M. Baumgartner, P. Gambardella, P. Němec, J. Wunderlich, J. Sinova, P. Kužel, M. Müller, T. Kampfrath, T. Jungwirth, Terahertz electrical writing speed in an antiferromagnetic memory, Sci. Adv. 4 (2018) http://dx.doi.org/10.1126/sciadv.aar3566.

[248] A.V. Kimel, M. Li, Writing magnetic memory with ultrashort light pulses, Nat. Rev. Mater. 4 (2019) 189, http://dx.doi.org/10.1038/s41578-019-0086-3.

[249] B. Koopmans, G. Malinowski, F. Dalla Longa, D. Steiauf, M. Fähnle, T. Roth, M. Cinchetti, M. Aeschlimann, Explaining the paradoxical diversity of ultrafast laser-induced demagnetization, Nature Mater. 9 (3) (2010) 259–265, http://dx.doi.org/10.1038/nmat2593.

[250] M. Battiato, K. Carva, P.M. Oppeneer, Superdiffusive spin transport as a mechanism of ultrafast demagnetization, Phys. Rev. Lett. 105 (2010) 027203, http://dx.doi.org/10.1103/PhysRevLett.105.027203.

[251] H.C. Siegmann, Efficient metallic spintronic emitters of ultrabroadband terahertz radiation, J. Phys.: Condens. Matter. 4 (1992) 8395, http://dx.doi.org/10.1088/0953-8984/4/44/004.

[252] M. Aeschlimann, M. Bauer, S. Pawlik, W. Weber, R. Burgermeister, D. Oberli, H.C. Siegmann, Ultrafast spin-dependent electron dynamics in FCC Co, Phys. Rev. Lett. 79 (1997) 5158–5161, http://dx.doi.org/10.1103/PhysRevLett.79.5158.

[253] R. Knorren, K.H. Bennemann, R. Burgermeister, M. Aeschlimann, Dynamics of excited electrons in copper and ferromagnetic transition metals: Theory and experiment, Phys. Rev. B 61 (2000) 9427–9440, http://dx.doi.org/10.1103/PhysRevB.61.9427.

[254] A. Goris, K.M. Dobrich, I. Panzer, A.B. Schmidt, M. Donath, M. Weinelt, Role of spin-flip exchange scattering for hot-electron lifetimes in cobalt, Phys. Rev. Lett. 107 (2011) 026601, http://dx.doi.org/10.1103/PhysRevLett.107.026601.

[255] A.B. Schmidt, M. Pickel, M. Donath, P. Buczek, A. Ernst, V.P. Zhukov, P.M. Echenique, L.M. Sandratskii, E.V. Chulkov, M. Weinelt, Ultrafast magnon generation in an fe film on Cu(100), Phys. Rev. Lett. 105 (2010) 197401, http://dx.doi.org/10.1103/PhysRevLett.105.197401.

[256] U. Bovensiepen, Coherent and incoherent excitations of the Gd(0001) surface on ultrafast timescales, J. Phys.: Condens. Matter. 19 (2007) 083201, http://dx.doi.org/10.1088/1361-648X/aa6c92.

[257] H.-S. Rhie, H.A. Dürr, W. Eberhardt, Femtosecond electron and spin dynamics in Ni/W(110) films, Phys. Rev. Lett. 90 (2003) 247201, http://dx.doi.org/10.1103/PhysRevLett.90.247201.

[258] M. Lisowski, P.A. Loukakos, A. Melnikov, I. Radu, L. Ungureanu, M. Wolf, U. Bovensiepen, Femtosecond electron and spin dynamics in Gd(0001) studied by time-resolved photoemission and magneto-optics, Phys. Rev. Lett. 95 (2005) 137402, http://dx.doi.org/10.1103/PhysRevLett.95.137402.

[259] P. Tengdin, W. You, C. Chen, X. Shi, D. Zusin, Y. Zhang, C. Gentry, A. Blonsky, M. Keller, P.M. Oppeneer, H.C. Kapteyn, Z. Tao, M.M. Murnane, Critical behavior within 20 fs drives the out-of-equilibrium laser-induced magnetic phase transition in nickel, Sci. Adv. 4 (3) (2018) eaap9744, http://dx.doi.org/10.1126/sciadv.aap9744.

[260] K. Bobowski, X. Zheng, B. Frietsch, D. Lawrenz, W. Bronsch, C. Gahl, B. Andres, C. Strüber, R. Carley, M. Teichmann, A. Scherz, S. Molodtsov, C. Cacho, R.T. Chapman, E. Springate, M. Weinelt, Ultrafast spin transfer and its impact on the electronic structure, Sci. Adv. 10 (29) (2024) eadn4613, http://dx.doi.org/10.1126/sciadv.adn4613.

[261] R. Carley, K. Döbrich, B. Frietsch, C. Gahl, M. Teichmann, O. Schwarzkopf, P. Wernet, M. Weinelt, Femtosecond laser excitation drives ferromagnetic gadolinium out of magnetic equilibrium, Phys. Rev. Lett. 109 (5) (2012) 057401, http://dx.doi.org/10.1103/PhysRevLett.109.057401.

[262] B. Frietsch, A. Donges, R. Carley, M. Teichmann, J. Bowlan, K. Döbrich, K. Carva, D. Legut, P.M. Oppeneer, U. Nowak, M. Weinelt, The role of ultrafast magnon generation in the magnetization dynamics of rare-earth metals, Sci. Adv. 6 (39) (2020) eabb1601, http://dx.doi.org/10.1126/sciadv.abb1601.

[263] B. Andres, M. Christ, C. Gahl, M. Wietstruk, M. Weinelt, J. Kirschner, Separating exchange splitting from spin mixing in gadolinium by femtosecond laser excitation, Phys. Rev. Lett. 115 (2015) 207404, http://dx.doi.org/10.1103/PhysRevLett.115.207404.

[264] S. Eich, M. Plötzing, M. Rollinger, S. Emmerich, R. Adam, C. Chen, H.C. Kapteyn, M.M. Murnane, L. Plucinski, D. Steil, B. Stadtmüller, M. Cinchetti, M. Aeschlimann, C.M. Schneider, S. Mathias, Band structure evolution during the ultrafast ferromagnetic-paramagnetic phase transition in cobalt, Sci. Adv. 3 (3) (2017) e1602094, http://dx.doi.org/10.1126/sciadv.1602094.

[265] R. Gort, K. Bühlmann, S. Däster, G. Salvatella, N. Hartmann, Y. Zemp, S. Holenstein, C. Stieger, A. Fognini, T.U. Michlmayr, T. Bähler, A. Vaterlaus, Y. Acremann, Early stages of ultrafast spin dynamics in a $3d$ ferromagnet, Phys. Rev. Lett. 121 (2018) 087206, http://dx.doi.org/10.1103/PhysRevLett.121.087206.

[266] S. Suga, C. Tusche, Photoelectron spectroscopy in a wide hv region from 6 eV to 8 keV with full momentum and spin resolution, J. Electron Spectrosc. Relat. Phenom. 200 (2015) 119–142, http://dx.doi.org/10.1016/j.elspec.2015.04.019.

[267] D. Rudolf, C. La-O-Vorakiat, M. Battiato, R. Adam, J.M. Shaw, E. Turgut, P. Maldonado, S. Mathias, P. Grychtol, H.T. Nembach, T.J. Silva, M. Aeschlimann, H.C. Kapteyn, M.M. Murnane, C.M. Schneider, P.M. Oppeneer, Ultrafast magnetization enhancement in metallic multilayers driven by superdiffusive spin current, Nature Commun. 3 (2012) 1037, http://dx.doi.org/10.1038/ncomms2029.

[268] A. Eschenlohr, M. Battiato, P. Maldonado, N. Pontius, T. Kachel, K. Holldack, R. Mitzner, A. Föhlisch, P.M. Oppeneer, C. Stamm, Ultrafast spin transport as key to femtosecond demagnetization, Nature Mater. 12 (2013) 332, http://dx.doi.org/10.1038/nmat3546.

[269] A. Melnikov, I. Razdolski, T.O. Wehling, E.T. Papaioannou, V. Roddatis, P. Fumagalli, O. Aktsipetrov, A.I. Lichtenstein, U. Bovensiepen, Ultrafast transport of laser-excited spin-polarized carriers in Au/Fe/MgO(001), Phys. Rev. Lett. 107 (2011) 076601, http://dx.doi.org/10.1103/PhysRevLett.107.076601.

[270] S. Kaltenborn, H.C. Schneider, Spin-orbit coupling effects on spin-dependent inelastic electronic lifetimes in ferromagnets, Phys. Rev. B 90 (2014) http://dx.doi.org/10.1103/PhysRevB.90.201104, 201104(R).

[271] A. Goris, (Ph.D. thesis), Freie Universität Berlin, 2010, http://dx.doi.org/10.17169/refubium-6626.

[272] V.P. Zhukov, E.V. Chulkov, P.M. Echenique, Lifetimes and inelastic mean free path of low-energy excited electrons in Fe, Ni, Pt, and Au: Ab initio GW + T calculations, Phys. Rev. B 73 (2006) 125105, http://dx.doi.org/10.1103/PhysRevB.73.125105.

[273] J. Kirschner, Direct and exchange contributions in inelastic scattering of spin-polarized electrons from iron, Phys. Rev. Lett. 55 (1985) 973–976, http://dx.doi.org/10.1103/PhysRevLett.55.973.

[274] V.P. Zhukov, E.V. Chulkov, P.M. Echenique, Lifetimes of excited electrons in Fe and Ni: First-principles GW and the T-matrix theory, Phys. Rev. Lett. 94 (2005) 119902, http://dx.doi.org/10.1103/PhysRevLett.94.119902.

[275] W. Kuch, C.M. Schneider, Magnetic dichroism in valence band photoemission, Rep. Progr. Phys. 64 (2001) 147, http://dx.doi.org/10.1088/0034-4885/64/2/201.

[276] M. Pickel, A.B. Schmidt, F. Giesen, J. Braun, J. Minár, H. Ebert, M. Donath, M. Weinelt, Spin-orbit hybridization points in the face-centered-cubic cobalt band structure, Phys. Rev. Lett. 101 (2008) 066402, http://dx.doi.org/10.1103/PhysRevLett.101.066402.

[277] J. Wieczorek, A. Eschenlohr, B. Weidtmann, M. Rösner, N. Bergeard, A. Tarasevitch, T.O. Wehling, U. Bovensiepen, Separation of ultrafast spin currents and spin-flip scattering in Co/Cu(001) driven by femtosecond laser excitation employing the complex magneto-optical Kerr effect, Phys. Rev. B 92 (2015) 174410, http://dx.doi.org/10.1103/PhysRevB.92.174410.

[278] A.B. Schmidt, M. Pickel, M. Wiemhöfer, M. Donath, M. Weinelt, Spin-dependent electron dynamics in front of a ferromagnetic surface, Phys. Rev. Lett. 95 (2005) 107402, http://dx.doi.org/10.1103/PhysRevLett.95.107402.

[279] A.B. Schmidt, (Ph.D. thesis), Freie Universität Berlin, 2007, http://www.diss.fu-berlin.de/2002/251/index.html.

[280] M. Weinelt, A. Schmidt, M. Pickel, M. Donath, Spin-polarized image-potential-state electrons as ultrafast magnetic sensors in front of ferromagnetic surfaces, Prog. Surf. Sci. 82 (4) (2007) 388–406, http://dx.doi.org/10.1016/j.progsurf.2007.03.010.

[281] B. Frietsch, J. Bowlan, R. Carley, M. Teichmann, S. Wienholdt, D. Hinzke, U. Nowak, K. Carva, P.M. Oppeneer, M. Weinelt, Disparate ultrafast dynamics of itinerant and localized magnetic moments in gadolinium metal, Nature Commun. 6 (2015) 8262, http://dx.doi.org/10.1038/ncomms9262.

[282] E. Arenholz, E. Navas, K. Starke, L. Baumgarten, G. Kaindl, Magnetic circular dichroism in core-level photoemission from Gd, Tb, and Dy in ferromagnetic materials, Phys. Rev. B 51 (1995) 8211–8220, http://dx.doi.org/10.1103/PhysRevB.51.8211.

[283] B. Frietsch, R. Carley, K. Döbrich, C. Gahl, M. Teichmann, O. Schwarzkopf, P. Wernet, M. Weinelt, A high-order harmonic generation apparatus for time- and angle-resolved photoelectron spectroscopy, Rev. Sci. Instrum. 84 (2013) 075106, http://dx.doi.org/10.1063/1.4812992.

[284] A. Winkelmann, D. Hartung, H. Engelhard, C.-T. Chiang, J. Kirschner, High efficiency electron spin polarization analyzer based on exchange scattering at Fe/W(001), Rev. Sci. Instrum. 79 (8) (2008) 083303, http://dx.doi.org/10.1063/1.2949877.

[285] M. Bode, M. Getzlaff, A. Kubetzka, R. Pascal, O. Pietzsch, R. Wiesendanger, Temperature-dependent exchange splitting of a surface state on a local-moment magnet: Tb(0001), Phys. Rev. Lett. 83 (1999) 3017–3020, http://dx.doi.org/10.1103/PhysRevLett.83.3017.

[286] B. Liu, H. Xiao, M. Weinelt, Microscopic insights to spin transport–driven ultrafast magnetization dynamics in a Gd/Fe bilayer, Sci. Adv. 9 (20) (2023) eade0286, http://dx.doi.org/10.1126/sciadv.ade0286.

[287] F. Siegrist, J.A. Gessner, M. Ossiander, C. Denker, Y.-P. Chang, M.C. Schröder, A. Guggenmos, Y. Cui, J. Walowski, U. Martens, J.K. Dewhurst, U. Kleineberg, M. Münzenberg, S. Sharma, M. Schultze, Light-wave dynamic control of magnetism, Nature 571 (2019) 240, http://dx.doi.org/10.1038/s41586-019-1333-x.

[288] E.V. Chulkov, A.G. Borisov, J.P. Gauyacq, D. Sanchez-Portal, V.M. Silkin, V.P. Zhukov, P.M. Echenique, Electronic excitations in metals and at metal surfaces, Chem. Rev. 106 (2006) 4160, http://dx.doi.org/10.1021/cr050166o.

[289] M. Reutzel, A. Li, H. Petek, Coherent two-dimensional multiphoton photo-electron spectroscopy of metal surfaces, Phys. Rev. X 9 (2019) 011044, http://dx.doi.org/10.1103/PhysRevX.9.011044.

[290] M. Reutzel, A. Li, H. Petek, Above-threshold multiphoton photoemission from noble metal surfaces, Phys. Rev. B 101 (2020) 075409, http://dx.doi.org/10.1103/PhysRevB.101.075409.

[291] M. Krüger, C. Lemell, G. Wachter, J. Burgdörfer, P. Hommelhoff, Attosecond physics phenomena at nanometric tips, J. Phys. B: At. Mol. Opt. Phys. 51 (2018) 172001, http://dx.doi.org/10.1088/1361-6455/aac6ac.

[292] B. Lovász, P. Sándor, G.-Z. Kiss, B. Bánhegyi, P. Rácz, Z. Pápa, J. Budai, C. Prietl, J.R. Krenn, P. Dombi, Nonadiabatic nano-optical tunneling of photoelec-trons in plasmonic near-fields, Nano Lett. 22 (2022) 2303, http://dx.doi.org/10.1021/acs.nanolett.1c04651.

[293] H.Y. Kim, M. Garg, S. Mandal, L. Seiffert, T. Fennel, E. Goulielmakis, Attosecond field emission, Nature 613 (2023) 662, http://dx.doi.org/10.1038/s41586-022-05577-1.

[294] R. Kienberger, M. Hentschel, M. Uiberacker, C. Spielmann, M. Kitzler, A. Scrinzi, M. Wieland, T. Westerwalbesloh, U. Kleineberg, U. Heinzmann, M. Drescher, F. Krausz, Steering attosecond electron wave packets with light, Science 297 (2002) 1144, http://dx.doi.org/10.1126/science.1073866.

[295] P.B. Corkum, F. Krausz, Attosecond science, Nat. Phys. 3 (2007) 381, http://dx.doi.org/10.1038/nphys620.

[296] T. Higuchi, M.I. Stockman, P. Hommelhoff, Strong-field perspective on high-harmonic radiation from bulk solids, Phys. Rev. Lett. 113 (2014) 213901, http://dx.doi.org/10.1103/PhysRevLett.113.213901.

[297] E.N. Osika, A. Chacón, L. Ortmann, N. Suárez, J.A. Pérez-Hernández, B.o. Szafran, M.F. Ciappina, F. Sols, A.S. Landsman, M. Lewenstein, Wannier-Bloch approach to localization in high-harmonics generation in solids, Phys. Rev. X 7 (2017) 021017, http://dx.doi.org/10.1103/PhysRevX.7.021017.

[298] S. Ghimire, D.A. Reis, High-harmonic generation from solids, Nat. Phys. 15 (2019) 10, http://dx.doi.org/10.1038/s41567-018-0315-5.

[299] S. Ghimire, A.D. DiChiara, E. Sistrunk, P. Agostini, L.F. DiMauro, D.A. Reis, Observation of high-order harmonic generation in a bulk crystal, Nat. Phys. 7 (2011) 138, http://dx.doi.org/10.1038/nphys1847.

[300] R. Merlin, Perturbed periodic lattices: Sharp crossover between effective-mass-like states and Wannier-Stark-like ladders, Phys. Rev. B 108 (2023) 115128, http://dx.doi.org/10.1103/PhysRevB.108.115128.

[301] M. Schultze, M. Fieß, N. Karpowicz, J. Gagnon, M. Korbman, M. Hofstetter, S. Neppl, A.L. Cavalieri, Y. Komninos, T. Mercouris, C.A. Nicolaides, R. Pazourek, S. Nagele, J. Feist, J. Burgdörfer, A.M. Azzeer, R. Ernstorfer, R. Kienberger, U. Kleineberg, E. Goulielmakis, F. Krausz, V.S. Yakovlev, Delay in photoemission, Science 328 (2010) 1658, http://dx.doi.org/10.1126/science.1189401.

[302] F. Siek, S. Neb, P. Bartz, M. Hensen, C. Strüber, S. Fiechter, M. Torrent-Sucarrat, V.M. Silkin, E.E. Krasovskii, N.M. Kabachnik, S. Fritzsche, R.D. Muiño, P.M. Echenique, A.K. Kazansky, N. Müller, W. Pfeiffer, U. Heinzmann, Angular momentum–induced delays in solid-state photoemission enhanced by intra-atomic interactions, Science 357 (2017) 1274, http://dx.doi.org/10.1126/science.aam959.

[303] J. Freudenstein, M. Borsch, M. Meierhofer, D. Afanasiev, C.P. Schmid, F. Sandner, M. Liebich, A. Girnghuber, M. Knorr, M. Kira, R. Huber, Attosecond clocking of correlations between Bloch electrons, Nature 610 (2022) 290, http://dx.doi.org/10.1038/s41586-022-05190-2.

[304] A. Leitenstorfer, A.S. Moskalenko, T. Kampfrath, J. Kono, E. Castro-Camus, K. Peng, N. Qureshi, D. Turchinovich, K. Tanaka, A.G. Markelz, The 2023 terahertz science and technology roadmap, J. Phys. D: Appl. Phys. 56 (2023) 223001, http://dx.doi.org/10.1088/1361-6463/acbe4c.

[305] M. Borsch, M. Meierhofer, R. Huber, M. Kira, Lightwave electronics in con-densed matter, Nat. Rev. Mater. 8 (2023) 668, http://dx.doi.org/10.1038/s41578-023-00592-8.

[306] M. Rini, R. Tobey, N. Dean, J. Itatani, Y. Tomioka, Y. Tokura, R.W. Schoenlein, A. Cavalleri, Control of the electronic phase of a manganite by mode-selective vibrational excitation, Nature 449 (2007) 72, http://dx.doi.org/10.1038/nature06119.

[307] X. Li, T. Qiu, J. Zhang, E. Baldini, J. Lu, A.M. Rappe, K.A. Nelson, Terahertz field–induced ferroelectricity in quantum paraelectric $SrTiO_3$, Science 364 (2019) 1079, http://dx.doi.org/10.1126/science.aaw4913.

[308] S.V. Yalunin, M. Gulde, C. Ropers, Strong-field photoemission from surfaces: Theoretical approaches, Phys. Rev. B 84 (2011) 195426, http://dx.doi.org/10.1103/PhysRevB.84.195426.

[309] B. Piglosiewicz, S. Schmidt, D.J. Park, J. Vogelsang, P. Grosz, C. Manzoni, P. Farinello, G. Cerullo, C. Lienau, Carrier-envelope phase effects on the strong-field photoemission of electrons from metallic nanostructures, Nat. Photonics 8 (2014) 37, http://dx.doi.org/10.1038/nphoton.2013.288.

[310] P. Dienstbier, L. Seiffert, T. Paschen, A. Liehl, A. Leitenstorfer, T. Fennel, P. Hommelhoff, Tracing attosecond electron emission from a nanometric metal tip, Nature 616 (2023) 702, http://dx.doi.org/10.1038/s41586-023-05839-6.

[311] J.H. Gaida, H. Lourenço-Martins, M. Sivis, T. Rittmann, A. Feist, F.J.G. de Abajo, C. Ropers, Attosecond electron microscopy by free-electron homodyne detection, Nat. Photonics 18 (2024) 509, http://dx.doi.org/10.1038/s41566-024-01380-8.

[312] D.E. Eastman, J.K. Cashion, Photoemission energy-level measurements of chemisorbed CO and O on Ni, Phys. Rev. Lett. 27 (1971) 1520–1523, http://dx.doi.org/10.1103/PhysRevLett.27.1520.

[313] P.J. Feibelman, D.E. Eastman, Photoemission spectroscopy - correspondence between quantum theory and experimental phenomenology, Phys. Rev. B 10 (1974) 4932, http://dx.doi.org/10.1103/PhysRevB.10.4932.

[314] W. Eberhardt, E.W. Plummer, Angle-resolved photoemission determination of the band structure and multielectron excitations in Ni, Phys. Rev. B 21 (1980) 3245, http://dx.doi.org/10.1103/PhysRevB.21.3245.

[315] F.J. Himpsel, Angle-resolved measurements of the photoemission of electrons in the study of solids, Adv. Phys. 32 (1983) 1, http://dx.doi.org/10.1080/00018738300101521.

[316] M.C. Teich, J.M. Schroeer, G.J. Wolga, Double-quantum photoelectric emission from sodium metal, Phys. Rev. Lett. 13 (1964) 611, http://dx.doi.org/10.1103/PhysRevLett.13.611.

[317] W. Steinmann, Two-photon photoemission spectroscopy of electronic states at metal surfaces, Phys. Status Solidi B 192 (1995) 339, http://dx.doi.org/10.1002/pssb.2221920210.

[318] C. Chen, Z. Tao, A. Carr, P. Matyba, T. Szilvási, S. Emmerich, M. Piecuch, M. Keller, D. Zusin, S. Eich, M. Rollinger, W. You, S. Mathias, U. Thumm, M. Mavrikakis, M. Aeschlimann, P.M. Oppeneer, H. Kapteyn, M. Murnane, Distinguishing attosecond electron–electron scattering and screening in transition metals, Proc. Natl. Acad. Sci. 114 (27) (2017) E5300, http://dx.doi.org/10.1073/pnas.1706466114.

[319] H. Petek, A. Li, X. Li, S. Tan, M. Reutzel, Plasmonic decay into hot electrons in silver, Prog. Surf. Sci. 98 (2023) 100707, http://dx.doi.org/10.1016/j.progsurf.2023.100707.

[320] S. Ogawa, H. Nagano, H. Petek, A.P. Heberle, Optical dephasing in Cu(111) measured by interferometric two-photon time-resolved photoemission, Phys. Rev. Lett. 78 (1997) 1339, http://dx.doi.org/10.1103/PhysRevLett.78.1339.

[321] H. Petek, A.P. Heberle, W. Nessler, H. Nagano, S. Kubota, S. Matsunami, N. Moriya, S. Ogawa, Optical phase control of coherent electron dynamics in metals, Phys. Rev. Lett. 79 (1997) 4649, http://dx.doi.org/10.1103/PhysRevLett.79.4649.

[322] H. Petek, H. Nagano, S. Ogawa, Hole decoherence of d bands in copper, Phys. Rev. Lett. 83 (1999) 832, http://dx.doi.org/10.1103/PhysRevLett.83.832.

[323] M. Marks, C.H. Schwalb, K. Schubert, J. Güdde, U. Höfer, Quantum-beat spectroscopy of image-potential resonances, Phys. Rev. B 84 (2011) 245402, http://dx.doi.org/10.1103/PhysRevB.84.245402.

[324] M. Aeschlimann, T. Brixner, A. Fischer, C. Kramer, P. Melchior, W. Pfeiffer, C. Schneider, C. Strüber, P. Tuchscherer, D.V. Voronine, Coherent two-dimensional nanoscopy, Science 333 (2011) 1723, http://dx.doi.org/10.1126/science.1209206.

[325] A. Li, M. Reutzel, Z. Wang, D. Schmitt, M. Keunecke, W. Bennecke, G.S. Matthijs Jansen, D. Steil, S. Steil, D. Novko, B. Gumhalter, S. Mathias, H. Petek, Multidimensional multiphoton momentum microscopy of the anisotropic Ag(110) surface, Phys. Rev. B 105 (2022) 075105, http://dx.doi.org/10.1103/PhysRevB.105.075105.

[326] M. Reutzel, A. Li, Z. Wang, H. Petek, Coherent multidimensional photoelectron spectroscopy of ultrafast quasiparticle dressing by light, Nat. Commun. 11 (2020) 2230, http://dx.doi.org/10.1038/s41467-020-16064-4.

[327] V.M. Silkin, P. Lazić, N. Došlić, H. Petek, B. Gumhalter, Ultrafast electronic response of Ag(111) and Cu(111) surfaces: From early excitonic transients to saturated image potential, Phys. Rev. B 92 (2015) 155405, http://dx.doi.org/10.1103/PhysRevB.92.155405.

[328] L.V. Keldysh, Ionization in the field of a strong electromagnetic wave, Sov. Phys.—JETP 20 (1965) 1307.

[329] G.L. Yudin, M.Y. Ivanov, Nonadiabatic tunnel ionization: Looking inside a laser cycle, Phys. Rev. A 64 (2001) 013409, http://dx.doi.org/10.1103/PhysRevA.64.013409.

[330] A.M. Zheltikov, Keldysh parameter, photoionization adiabaticity, and the tunneling time, Phys. Rev. A 94 (2016) 043412, http://dx.doi.org/10.1103/PhysRevA.94.043412.

[331] O. Reshefand, E. Giese, M.Z. Alam, I.D. Leon, J. Upham, R.W. Boyd, Beyond the perturbative description of the nonlinear optical response of low-index materials, Opt. Lett. 42 (2017) 3225, http://dx.doi.org/10.1364/OL.42.003225.

[332] W.L. Schaich, N.W. Ashcroft, Theory of photoemission, Solid State Commun. 8 (1970) 1959, http://dx.doi.org/10.1016/0038-1098(70)90668-X.

[333] C. Timm, K.H. Bennemann, Response theory for time-resolved second-harmonic generation and two-photon photoemission, J. Phys.: Condens. Matter. 16 (2004) 661, http://dx.doi.org/10.1088/0953-8984/16/4/015.

[334] H. Petek, Y. Dai, A. Ghosh, A. Li, Z. Zhou, M. Reutzel, S. Yang, C.-B. Huang, Emerging Trends in Chemical Applications of Lasers, vol. 1398, American Chemical Society, 2021, http://dx.doi.org/10.1021/bk-2021-1398.ch008.

[335] T. Oka, S. Kitamura, Floquet engineering of quantum materials, Annu. Rev. Condens. Matter Phys. 10 (2019) 387, http://dx.doi.org/10.1146/annurev-conmatphys-031218-013423.

[336] A. de la Torre, D.M. Kennes, M. Claassen, S. Gerber, J.W. McIver, M.A. Sentef, Colloquium: Nonthermal pathways to ultrafast control in quantum materials, Rev. Modern Phys. 93 (2021) 041002, http://dx.doi.org/10.1103/RevModPhys.93.041002.

[337] H. Liu, H. Cao, S. Meng, Floquet engineering of topological states in realistic quantum materials via light-matter interactions, Prog. Surf. Sci. 98 (2023) 100705, http://dx.doi.org/10.1016/j.progsurf.2023.100705.

[338] Y.H. Wang, H. Steinberg, P. Jarillo-Herrero, N. Gedik, Observation of Floquet-Bloch states on the surface of a topological insulator, Science 342 (2013) 453, http://dx.doi.org/10.1126/science.1239834.

[339] M. Fleischhauer, A. Imamoglu, J.P. Marangos, Electromagnetically induced transparency: Optics in coherent media, Rev. Modern Phys. 77 (2005) 633–673, http://dx.doi.org/10.1103/RevModPhys.77.633.

[340] H.R. Reiss, Altered Maxwell equations in the length gauge, J. Phys. B: At. Mol. Opt. Phys. 46 (2013) 175601, http://dx.doi.org/10.1088/0953-4075/46/17/175601.

[341] O.D. Mücke, T. Tritschler, M. Wegener, U. Morgner, F.X. Kärtner, Role of the carrier-envelope offset phase of few-cycle pulses in nonperturbative resonant nonlinear optics, Phys. Rev. Lett. 89 (2002) 127401, http://dx.doi.org/10.1103/PhysRevLett.89.127401.

[342] B. Gumhalter, D. Novko, H. Petek, Electron emission from plasmonically induced floquet bands at metal surfaces, Phys. Rev. B 106 (2022) 035422, http://dx.doi.org/10.1103/PhysRevB.106.035422.

[343] B. Gumhalter, D. Novko, Complementary perturbative and nonperturbative pictures of plasmonically induced electron emission from flat metal surfaces, Prog. Surf. Sci. 98 (2023) 100706, http://dx.doi.org/10.1016/j.progsurf.2023.100706.

[344] R.H. Fowler, L. Nordheim, Electron emission in intense electric fields, Proc. R. Soc. Lond. Ser. A Math. Phys. Eng. Sci. 119 (1928) 173, http://dx.doi.org/10.1098/rspa.1928.0091.

[345] E.W. Plummer, J.W. Gadzuk, D.R. Penn, Vacuum tunneling spectroscopy, Phys. Today 28 (1975) 63, http://dx.doi.org/10.1063/1.3068922.

[346] J. Kröger, L. Limot, H. Jensen, R. Berndt, P. Johansson, Stark effect in Au(111) and Cu(111) surface states, Phys. Rev. B 70 (2004) 033401, http://dx.doi.org/10.1103/PhysRevB.70.033401.

[347] K. Berland, T.L. Einstein, P. Hyldgaard, Response of the shockley surface state to an external electrical field: A density-functional theory study of Cu(111), Phys. Rev. B 85 (2012) 035427, http://dx.doi.org/10.1103/PhysRevB.85.035427.

[348] K. Schubert, A. Damm, S.V. Eremeev, M. Marks, M. Shibuta, W. Berthold, J. Güdde, A.G. Borisov, S.S. Tsirkin, E.V. Chulkov, U. Höfer, Momentum-resolved electron dynamics of image-potential states on Cu and Ag surfaces, Phys. Rev. B 85 (2012) 205431, http://dx.doi.org/10.1103/PhysRevB.85.205431.

[349] M. Rocca, F. Moresco, HREELS and ELS-LEED studies of surface plasmons on Ag and Pd single crystals, Prog. Surf. Sci. 53 (1996) 331, http://dx.doi.org/10.1016/S0079-6816(96)00031-7.

[350] M.A. Cazalilla, J.S. Dolado, A. Rubio, P.M. Echenique, Plasmonic excitations in noble metals: The case of Ag, Phys. Rev. B 61 (2000) 8033, http://dx.doi.org/10.1103/PhysRevB.61.8033.

[351] M. Reutzel, A. Li, B. Gumhalter, H. Petek, Nonlinear plasmonic photoelectron response of Ag(111), Phys. Rev. Lett. 123 (2019) 017404, http://dx.doi.org/10.1103/PhysRevLett.123.017404.

[352] A. Li, M. Reutzel, Z. Wang, D. Novko, B. Gumhalter, H. Petek, Plasmonic photoemission from single-crystalline silver, ACS Photon. 8 (2021) 247, http://dx.doi.org/10.1021/acsphotonics.0c01412.

[353] D. Novko, V. Despoja, M. Reutzel, A. Li, H. Petek, B. Gumhalter, Plasmonically assisted channels of photoemission from metals, Phys. Rev. B 103 (2021) 205401, http://dx.doi.org/10.1103/PhysRevB.103.205401.

[354] N. Kinsey, C. DeVault, A. Boltasseva, V.M. Shalaev, Near-zero-index materials for photonics, Nat. Rev. Mater. 4 (2019) 742, http://dx.doi.org/10.1038/s41578-019-0133-0.

[355] T. Fauster, W. Steinmann, Two-photon photoemission spectroscopy of image states, in: Photonic Probes of Surfaces, North-Holland, Amsterdam, P. Halevi ed., 1995, http://dx.doi.org/10.1016/B978-0-444-82198-0.50015-1, 347, Chap. 8.

[356] T. Fauster, M. Weinelt, U. Höfer, Quasi-elastic scattering of electrons in image-potential states, Prog. Surf. Sci. 82 (2007) 224, http://dx.doi.org/10.1016/j.progsurf.2007.03.007.

[357] M. Marks, A. Schöll, U. Höfer, Formation of metal–organic interface states studied with 2PPE, J. Electron. Spectrosc. Relat. Phenomena 195 (2014) 263, http://dx.doi.org/10.1016/j.elspec.2014.02.009.

[358] J.M. Enoch, History of mirrors dating back 8000 years, Optom. Vis. Sci. 83 (2006) 775, http://dx.doi.org/10.1016/j.elspec.2014.02.009.

[359] M. Ludwig, G. Aguirregabiria, F. Ritzkowsky, T. Rybka, D.C. Marinica, J. Aizpurua, A.G. Borisov, A. Leitenstorfer, D. Brida, Sub-femtosecond electron transport in a nanoscale gap, Nat. Phys. 16 (2020) 341, http://dx.doi.org/10.1038/s41567-019-0745-8.

[360] M. Dąbrowski, Y. Dai, H. Petek, Ultrafast microscopy: Imaging light with photoelectrons on the nano–femto scale, J. Phys. Chem. Lett. 8 (2017) 4446, http://dx.doi.org/10.1021/acs.jpclett.7b00904.

[361] L. Bi, K. Liang, G. Czap, H. Wang, K. Yang, S. Li, Recent progress in probing atomic and molecular quantum coherence with scanning tunneling microscopy, Prog. Surf. Sci. 98 (2022) 100696, http://dx.doi.org/10.1016/j.progsurf.2022.100696.

[362] H. Petek, Spectromicroscopy at the space-time limit, Prog. Surf. Sci. 99 (2023) 100734, http://dx.doi.org/10.1016/j.progsurf.2023.100734.

[363] M. Müller, Imaging surfaces at the space–time limit: New perspectives of time-resolved scanning tunneling microscopy for ultrafast surface science, Prog. Surf. Sci. 99 (2023) 100727, http://dx.doi.org/10.1016/j.progsurf.2023.100727.

[364] S. Kosar, K.M. Dani, Time-resolved photoemission electron microscopy of semiconductor interfaces, Prog. Surf. Sci. 99 (2024) 100745, http://dx.doi.org/10.1016/j.progsurf.2024.100745.

[365] J.G. Horstmann, H. Böckmann, F. Kurtz, G. Storeck, C. Ropers, Structural dynamics in atomic indium wires on silicon: From ultrafast probing to coherent vibrational control, Prog. Surf. Sci. 99 (2024) 100743, http://dx.doi.org/10.1016/j.progsurf.2024.100743.

[366] R. Wallauer, M. Raths, K. Stallberg, L. Münster, D. Brandstetter, X. Yang, J. Güdde, P. Puschnig, S. Soubatch, C. Kumpf, F. Bocquet, F.S. Tautz, U. Höfer, Tracing orbital images on ultrafast time scales, Science 371 (2021) 1056, http://dx.doi.org/10.1126/science.abf3286.

[367] J. Güdde, U. Höfer, Ultrafast dynamics of photocurrents in surface states of three-dimensional topological insulators, Phys. Status Solidi b 258 (2021) 2000521, http://dx.doi.org/10.1002/pssb.202000521.

[368] J. Reimann, S. Schlauderer, C.P. Schmid, F. Langer, S. Baierl, K.A. Kokh, O.E. Tereshchenko, A. Kimura, C. Lange, J. Güdde, U. Höfer, R. Huber, Subcycle observation of lightwave-driven Dirac currents in a topological surface band, Nature 562 (2018) 396, http://dx.doi.org/10.1038/s41586-018-0544-x.

[369] C.W. Nicholson, A. Lücke, W.G. Schmidt, M. Puppin, L. Rettig, R. Ernstorfer, M. Wolf, Beyond the molecular movie: Dynamics of bands and bonds during a photoinduced phase transition, Science 362 (2018) 821–825, http://dx.doi.org/10.1126/science.aar4183.

[370] C.P. Schmid, L. Weigl, P. Grössing, V. Junk, C. Gorini, S. Schlauderer, S. Ito, M. Meierhofer, N. Hofmann, D. Afanasiev, J. Crewse, K.A. Kokh, O.E. Tereshchenko, J. Güdde, F. Evers, J. Wilhelm, K. Richter, U. Höfer, R. Huber, Tuneable non-integer high-harmonic generation in a topological insulator, Nature 593 (2021) 385, http://dx.doi.org/10.1038/s41586-021-03466-7.1.

[371] D.N. Basov, R.D. Averitt, D. Hsieh, Towards properties on demand in quantum materials, Nature Mater. 16 (2017) 1077–1088, http://dx.doi.org/10.1038/nmat5017.

[372] C. Tusche, A. Krasyuk, J. Kirschner, Spin resolved bandstructure imaging with a high resolution momentum microscope, Ultramicroscopy 159 (2015) 520–529, http://dx.doi.org/10.1016/j.ultramic.2015.03.020.

[373] C. Tusche, Y.-J. Chen, C.M. Schneider, Low-energy spin-polarized electrons: their role in surface physics, Front. Phys. 12 (2024) http://dx.doi.org/10.3389/fphy.2024.1349529.

[374] K. Yaji, S. Tsuda, Visualization of spin-polarized electronic states by imaging-type spin-resolved photoemission microscopy, Sci. Tech. Adv. Mater. Methods 4 (1) (2024) http://dx.doi.org/10.1080/27660400.2024.2328206.

[375] G. Schönhense, S. Babenkov, D. Vasilyev, H.-J. Elmers, K. Medjanik, Single-hemisphere photoelectron momentum microscope with time-of-flight recording, Rev. Sci. Instrum. 91 (12) (2020) 123110, http://dx.doi.org/10.1063/5.0024074.

[376] J. Tesch, F. Paschke, M. Fonin, M. Wietstruk, S. Böttcher, R.J. Koch, A. Bostwick, C. Jozwiak, E. Rotenberg, A. Makarova, B. Paulus, E. Voloshina, Y. Dedkov, The graphene/n-Ge(110) interface: structure, doping, and electronic properties, Nanoscale 10 (13) (2018) 6088–6098, http://dx.doi.org/10.1039/c8nr00053k.

[377] F. Matsui, K. Hagiwara, E. Nakamura, T. Yano, H. Matsuda, Y. Okano, S. Kera, E. Hashimoto, S. Koh, T. Ueno, T. Kobayashi, E. Iwamoto, K. Sakamoto, S.-i. Tanaka, S. Suga, Soft X-ray photoelectron momentum microscope for multimodal valence band stereography, Rev. Sci. Instrum. 94 (8) (2023) 083701, http://dx.doi.org/10.1063/5.0154156.

[378] T.-H. Chuang, C.-C. Hsu, W.-S. Chiu, J.-S. Jhuang, I.-C. Yeh, R.-S. Chen, S. Gwo, D.-H. Wei, Performance of a photoelectron momentum microscope in direct- and momentum-space imaging with ultraviolet photon sources, J. Synchrotron Radiat. 31 (1) (2024) 195–201, http://dx.doi.org/10.1107/s1600577523009761.

[379] G. Schönhense, K. Medjanik, O. Fedchenko, A. Zymaková, S. Chernov, D. Kutnyakhov, D. Vasilyev, S. Babenkov, H.J. Elmers, P. Baumgärtel, P. Goslawski, G. Öhrwall, T. Grunske, T. Kauerhof, K. von Volkmann, M. Kallmayer, M. Ellguth, A. Oelsner, Time-of-flight photoelectron momentum microscopy with 80–500 MHz photon sources: electron-optical pulse picker or bandpass pre-filter, J. Synchrotron Radiat. 28 (6) (2021) 1891–1908, http://dx.doi.org/10.1107/s1600577521010511.

[380] M. Schmitt, D. Biswas, O. Tkach, O. Fedchenko, J. Liu, H.-J. Elmers, M. Sing, R. Claessen, T.-L. Lee, G. Schönhense, Hybrid photoelectron momentum microscope at the soft X-ray beamline I09 of the diamond light source, 2024, http://dx.doi.org/10.48550/ARXIV.2406.00771, arXiv.

[381] O. Tkach, S. Chernov, S. Babenkov, Y. Lytvynenko, O. Fedchenko, K. Medjanik, D. Vasilyev, A. Gloskowskii, C. Schlueter, H.-J. Elmers, G. Schönhense, Asymmetric electrostatic dodecapole: compact bandpass filter with low aberrations for momentum microscopy, J. Synchrotron Radiat. 31 (4) (2024) 829–840, http://dx.doi.org/10.1107/s1600577524003540.

[382] E. Bauer, A brief history of PEEM, J. Electron Spectros. Relat. Phenomena 185 (10) (2012) 314–322, http://dx.doi.org/10.1016/j.elspec.2012.08.001.

[383] T. Schmidt, A. Sala, H. Marchetto, E. Umbach, H.-J. Freund, First experimental proof for aberration correction in XPEEM: Resolution, transmission enhancement, and limitation by space charge effects, Ultramicroscopy 126 (2013) 23–32, http://dx.doi.org/10.1016/j.ultramic.2012.11.004.

[384] O. Fedchenko, A. Winkelmann, K. Medjanik, S. Babenkov, D. Vasilyev, S. Chernov, C. Schlueter, A. Gloskovskii, Y. Matveyev, W. Drube, B. Schönhense, H.J. Elmers, G. Schönhense, High-resolution hard-X-ray photoelectron diffraction in a momentum microscope—the model case of graphite, New J. Phys. 21 (11) (2019) 113031, http://dx.doi.org/10.1088/1367-2630/ab51fe.

[385] O. Fedchenko, A. Winkelmann, G. Schönhense, Structure analysis using time-of-flight momentum microscopy with hard X-rays: Status and prospects, J. Phys. Soc. Japan 91 (9) (2022) http://dx.doi.org/10.7566/jpsj.91.091006.

[386] E. Brueche, Elektronenmikroskopische Abbildung mit lichtelektrischen Elektronen, Z. Phys. 86 (7–8) (1933) 448–450, http://dx.doi.org/10.1007/bf01341360.

[387] A. Recknagel, Theorie des elektrischen Elektronenmikroskops fuer Selbststrahler, Z. Phys. 117 (11–12) (1941) 689–708, http://dx.doi.org/10.1007/bf01668875.

[388] A. Recknagel, Das Aufloesungsvermoegen des Elektronenmikroskops fuer Selbststrahler, Z. Phys. 120 (5–6) (1943) 331–362, http://dx.doi.org/10.1007/bf01325849.

[389] E. Bauer, The resolution of the low energy electron reflection microscope, Ultramicroscopy 17 (1) (1985) 51–56, http://dx.doi.org/10.1016/0304-3991(85)90176-7.

[390] G.F. Rempfer, O. Griffith, The resolution of photoelectron microscopes with UV, X-ray, and synchrotron excitation sources, Ultramicroscopy 27 (3) (1989) 273–300, http://dx.doi.org/10.1016/0304-3991(89)90019-3.

[391] G.F. Rempfer, W.P. Skoczylas, O. Hayes Griffith, Design and performance of a high-resolution photoelectron microscope, Ultramicroscopy 36 (1–3) (1991) 196–221, http://dx.doi.org/10.1016/0304-3991(91)90151-u.

[392] R. Tromp, Measuring and correcting aberrations of a cathode objective lens, Ultramicroscopy 111 (4) (2011) 273–281, http://dx.doi.org/10.1016/j.ultramic.2010.11.029.

[393] R. Tromp, W. Wan, S. Schramm, Aberrations of the cathode objective lens up to fifth order, Ultramicroscopy 119 (2012) 33–39, http://dx.doi.org/10.1016/j.ultramic.2011.09.011.

[394] D.A. Dahl, T.R. McJunkin, J.R. Scott, Comparison of ion trajectories in vacuum and viscous environments using SIMION: Insights for instrument design, Int. J. Mass Spectrom. 266 (1–3) (2007) 156–165, http://dx.doi.org/10.1016/j.ijms.2007.07.008.

[395] O. Tkach, S. Fragkos, Q. Nguyen, S. Chernov, M. Scholz, N. Wind, S. Babenkov, O. Fedchenko, Y. Lytvynenko, D. Zimmer, A. Hloskovskii, D. Kutnyakhov, F. Pressacco, J. Dilling, L. Bruckmeier, M. Heber, F. Scholz, J. Sobota, J. Koralek, N. Sirica, M. Kallmayer, M. Hoesch, C. Schlueter, L.V. Odnodvorets, Y. Mairesse, K. Rossnagel, H.J. Elmers, S. Beaulieu, G. Schoenhense, Multi-mode front lens for momentum microscopy: Part II experiments, 2024, http://dx.doi.org/10.48550/ARXIV.2401.10084, arXiv, arXiv:2401.10084.

[396] Y. Hu, X. Wu, A.P. Schnyder, M. Shi, Electronic landscape of kagome superconductors AV_3Sb_5 (A=K, Rb, Cs) from angle-resolved photoemission spectroscopy, npj Quantum Mater. 8 (1) (2023) 67, http://dx.doi.org/10.1038/s41535-023-00599-y.

[397] Y. Hu, S.M. Teicher, B.R. Ortiz, Y. Luo, S. Peng, L. Huai, J. Ma, N.C. Plumb, S.D. Wilson, J. He, M. Shi, Topological surface states and flat bands in the kagome superconductor CsV_3Sb_5, Sci. Bull. 67 (5) (2022) 495–500, http://dx.doi.org/10.1016/j.scib.2021.11.026.

[398] G. Schönhense, D. Kutnyakhov, F. Pressacco, M. Heber, N. Wind, S.Y. Agustsson, S. Babenkov, D. Vasilyev, O. Fedchenko, S. Chernov, L. Rettig, B. Schönhense, L. Wenthaus, G. Brenner, S. Dziarzhytski, S. Palutke, S.K. Mahatha, N. Schirmel, H. Redlin, B. Manschwetus, I. Hartl, Y. Matveyev, A. Gloskovskii, C. Schlueter, V. Shokeen, H. Duerr, T.K. Allison, M. Beye, K. Rossnagel, H.J. Elmers, K. Medjanik, Suppression of the vacuum space-charge effect in fs-photoemission by a retarding electrostatic front lens, Rev. Sci. Instrum. 92 (5) (2021) http://dx.doi.org/10.1063/5.0046567.

[399] B. Schönhense, K. Medjanik, O. Fedchenko, S. Chernov, M. Ellguth, D. Vasilyev, A. Oelsner, J. Viefhaus, D. Kutnyakhov, W. Wurth, H.J. Elmers, G. Schönhense, Multidimensional photoemission spectroscopy—the space-charge limit, New J. Phys. 20 (3) (2018) 033004, http://dx.doi.org/10.1088/1367-2630/aaa262.

[400] F. Pressacco, D. Sangalli, V. Uhlíř, D. Kutnyakhov, J.A. Arregi, S.Y. Agustsson, G. Brenner, H. Redlin, M. Heber, D. Vasilyev, J. Demsar, G. Schönhense, M. Gatti, A. Marini, W. Wurth, F. Sirotti, Subpicosecond metamagnetic phase transition in ferh driven by non-equilibrium electron dynamics, Nature Commun. 12 (1) (2021) 5088, http://dx.doi.org/10.1038/s41467-021-25347-3.

[401] P. Hawkes, E. Kasper, Principles of Electron Optics, Vol. 2, second ed., Elsevier, 2018, http://dx.doi.org/10.1016/c2015-0-06653-9.

[402] O. Scherzer, Ueber einige Fehler von Elektronenlinsen, Z. Phys. 101 (9–10) (1936) 593–603, http://dx.doi.org/10.1007/bf01349606.

[403] H. Rose, Allgemeine Abbildungseigenschaften unrunder Elektronenlinsen mit gerader Achse, Optik 24 (1967) 36 and 108.

[404] J.O. Schunck, J. Buck, R.Y. Engel, S.R. Kruse, S. Marotzke, M. Scholz, S.K. Mahatha, M.-J. Huang, H.M. Rø nnow, G. Dakovski, M. Hoesch, M. Kalläne, K. Rossnagel, M. Beye, A compact approach to higher-resolution resonant inelastic X-ray scattering detection using photoelectrons, New J. Phys. 26 (5) (2024) 053008, http://dx.doi.org/10.1088/1367-2630/ad4206.

[405] G. Schönhense, H. Spiecker, Correction of chromatic and spherical aberration in electron microscopy utilizing the time structure of pulsed excitation sources, J. Vac. Sci. Technol. B 20 (6) (2002) 2526–2534, http://dx.doi.org/10.1116/1.1523373.

[406] W. Ackermann, G. Asova, V. Ayvazyan, A. Azima, N. Baboi, J. Bähr, V. Balandin, B. Beutner, A. Brandt, A. Bolzmann, R. Brinkmann, O.I. Brovko, M. Castellano, P. Castro, L. Catani, E. Chiadroni, S. Choroba, S. Cianchi, J.T. Costello, D. Cubaynes, J. Dardis, W. Decking, H. Delsim-Hashemi, A. Delserieys, G. Di Pirro, M. Dohlus, S. Düsterer, A. Eckhardt, H.T. Edwards, B. Faatz, J.

Feldhaus, K. Flöttmann, J. Frisch, L. Fröhlich, T. Garvey, U. Gensch, C. Gerth, M. Görler, N. Golubeva, H.-J. Grabosch, M. Grecki, O. Grimm, K. Hacker, U. Hahn, J.H. Han, K. Honkavaara, T. Hott, M. Hüning, Y. Ivanisenko, E. Jaeschke, W. Jalmuzna, T. Jezynski, R. Kammering, V. Katalev, K. Kavanagh, E.T. Kennedy, S. Khodyachykh, K. Klose, V. Kocharyan, M. Körfer, M. Kollewe, W. Koprek, S. Korepanov, D. Kostin, M. Krassilnikov, G. Kube, M. Kuhlmann, C.L.S. Lewis, L. Lilje, T. Limberg, D. Lipka, F. Löhl, H. Luna, M. Luong, M. Martins, M. Meyer, P. Michelato, V. Miltchev, W.D. Möller, L. Monaco, W.F.O. Müller, O. Napieralski, O. Napoly, P. Nicolosi, D. Nölle, T. Nuñez, A. Oppelt, C. Pagani, R. Paparella, N. Pchalek, J. Pedregosa-Gutierrez, B. Petersen, B. Petrosyan, G. Petrosyan, L. Petrosyan, J. Pflüger, E. Plönjes, L. Poletto, K. Pozniak, E. Prat, D. Proch, P. Pucyk, P. Radcliffe, H. Redlin, K. Rehlich, M. Richter, M. Roehrs, J. Roensch, R. Romaniuk, M. Ross, J. Rossbach, V. Rybnikov, M. Sachwitz, E.L. Saldin, W. Sandner, H. Schlarb, B. Schmidt, M. Schmitz, P. Schmüser, J.R. Schneider, E.A. Schneidmiller, S. Schnepp, S. Schreiber, M. Seidel, D. Sertore, A.V. Shabunov, C. Simon, S. Simrock, E. Sombrowski, A.A. Sorokin, P. Spanknebel, R. Spesyvtsev, L. Staykov, B. Steffen, F. Stephan, F. Stulle, H. Thom, K. Tiedtke, M. Tischer, S. Toleikis, R. Treusch, D. Trines, I. Tsakov, E. Vogel, T. Weiland, H. Weise, M. Wellhöfer, M. Wendt, I. Will, A. Winter, K. Wittenburg, W. Wurth, P. Yeates, M.V. Yurkov, I. Zagorodnov, K. Zapfe, Operation of a free-electron laser from the extreme ultraviolet to the water window, Nat. Photonics 1 (6) (2007) 336–342, http://dx.doi.org/10.1038/nphoton.2007.76.

[407] C. Pellegrini, A. Marinelli, S. Reiche, The physics of X-ray free-electron lasers, Rev. Modern Phys. 88 (1) (2016) 015006, http://dx.doi.org/10.1103/RevModPhys.88.015006.

[408] G. Schönhense, K. Medjanik, H.-J. Elmers, Space-, time- and spin-resolved photoemission, J. Electron Spectrosc. Relat. Phenom. 200 (2015) 94–118, http://dx.doi.org/10.1016/j.elspec.2015.05.016.

[409] R.P. Xian, Y. Acremann, S.Y. Agustsson, M. Dendzik, K. Bühlmann, D. Curcio, D. Kutnyakhov, F. Pressacco, M. Heber, S. Dong, T. Pincelli, J. Demsar, W. Wurth, P. Hofmann, M. Wolf, M. Scheidgen, L. Rettig, R. Ernstorfer, An open-source, end-to-end workflow for multidimensional photoemission spectroscopy, Sci. Data 7 (1) (2020) 442, http://dx.doi.org/10.1038/s41597-020-00769-8.

[410] A. Pietzsch, A. Föhlisch, M. Beye, M. Deppe, F. Hennies, M. Nagasono, E. Suljoti, W. Wurth, C. Gahl, K. Döbrich, A. Melnikov, Towards time resolved core level photoelectron spectroscopy with femtosecond X-ray free-electron lasers, New J. Phys. 10 (3) (2008) 033004, http://dx.doi.org/10.1088/1367-2630/10/3/033004.

[411] S. Hellmann, K. Rossnagel, M. Marczynski-Bühlow, L. Kipp, Vacuum space-charge effects in solid-state photoemission, Phys. Rev. B 79 (3) (2009) 035402, http://dx.doi.org/10.1103/PhysRevB.79.035402.

[412] S. Hellmann, C. Sohrt, M. Beye, T. Rohwer, F. Sorgenfrei, M. Marczynski-Bühlow, M. Kalläne, H. Redlin, F. Hennies, M. Bauer, A. Föhlisch, L. Kipp, W. Wurth, K. Rossnagel, Time-resolved X-ray photoelectron spectroscopy at FLASH, New J. Phys. 14 (1) (2012) 013062, http://dx.doi.org/10.1088/1367-2630/14/1/013062.

[413] M. Dell'Angela, F. Hieke, F. Sorgenfrei, N. Gerken, M. Beye, N. Gerasimova, H. Redlin, W. Wurth, Ultrafast surface dynamics probed with time resolved photoemission, Surf. Sci. 643 (2016) 197–202, http://dx.doi.org/10.1016/j.susc.2015.08.011.

[414] M. Wagstaffe, H. Noei, A. Stierle, Elucidating the defect-induced changes in the photocatalytic activity of TiO2, J. Phys. Chem. C 124 (23) (2020) 12539–12547, http://dx.doi.org/10.1021/acs.jpcc.0c02809.

[415] M. Wagstaffe, L. Wenthaus, A. Dominguez-Castro, S. Chung, G.D. Lana Semione, S. Palutke, G. Mercurio, S. Dziarzhytski, H. Redlin, N. Klemke, Y. Yang, T. Frauenheim, A. Dominguez, F. Kärtner, A. Rubio, W. Wurth, A. Stierle, H. Noei, Ultrafast real-time dynamics of CO oxidation over an oxide photocatalyst, ACS Catal. 10 (22) (2020) 13650–13658, http://dx.doi.org/10.1021/acscatal.0c04098.

[416] M. Wagstaffe, A. Dominguez-Castro, L. Wenthaus, S. Palutke, D. Kutnyakhov, M. Heber, F. Pressacco, S. Dziarzhytski, H. Gleiß ner, V.K. Gupta, H. Redlin, A. Dominguez, T. Frauenheim, A. Rubio, A. Stierle, H. Noei, Photoinduced dynamics at the water/TiO$_2$(101) interface, Phys. Rev. Lett. 130 (10) (2023) 108001, http://dx.doi.org/10.1103/PhysRevLett.130.108001.

[417] F. Roth, M. Borgwardt, L. Wenthaus, J. Mahl, S. Palutke, G. Brenner, G. Mercurio, S. Molodtsov, W. Wurth, O. Gessner, W. Eberhardt, Direct observation of charge separation in an organic light harvesting system by femtosecond time-resolved XPS, Nature Commun. 12 (1) (2021) 1196, http://dx.doi.org/10.1038/s41467-021-21454-3.

[418] K. Baumgärtner, M. Reuner, C. Metzger, D. Kutnyakhov, M. Heber, F. Pressacco, C.-H. Min, T.R.F. Peixoto, M. Reiser, C. Kim, W. Lu, R. Shayduk, M. Izquierdo, G. Brenner, F. Roth, A. Schöll, S. Molodtsov, W. Wurth, F. Reinert, A. Madsen, D. Popova-Gorelova, M. Scholz, Ultrafast orbital tomography of a pentacene film using time-resolved momentum microscopy at a FEL, Nature Commun. 13 (1) (2022) 2741, http://dx.doi.org/10.1038/s41467-022-30404-6.

[419] S. Hellmann, M. Beye, C. Sohrt, T. Rohwer, F. Sorgenfrei, H. Redlin, M. Kalläne, M. Marczynski-Bühlow, F. Hennies, M. Bauer, A. Föhlisch, L. Kipp, W. Wurth, K. Rossnagel, Ultrafast melting of a charge-density wave in the mott insulator 1t-TaS$_2$, Phys. Rev. Lett. 105 (18) (2010) 187401, http://dx.doi.org/10.1103/PhysRevLett.105.187401.

[420] M. Dendzik, R.P. Xian, E. Perfetto, D. Sangalli, D. Kutnyakhov, S. Dong, S. Beaulieu, T. Pincelli, F. Pressacco, D. Curcio, S.Y. Agustsson, M. Heber, J. Hauer, W. Wurth, G. Brenner, Y. Acremann, P. Hofmann, M. Wolf, A. Marini, G. Stefanucci, L. Rettig, R. Ernstorfer, Observation of an excitonic mott transition through ultrafast core-cum-conduction photoemission spectroscopy, Phys. Rev. Lett. 125 (9) (2020) 096401, http://dx.doi.org/10.1103/PhysRevLett.125.096401.

[421] D. Puntel, D. Kutnyakhov, L. Wenthaus, M. Scholz, N.O. Wind, M. Heber, G. Brenner, G. Gu, R.J. Cava, W. Bronsch, F. Cilento, F. Parmigiani, F. Pressacco, Out-of-equilibrium charge redistribution in a copper-oxide based superconductor by time-resolved X-ray photoelectron spectroscopy, Sci. Rep. 14 (1) (2024) 8775, http://dx.doi.org/10.1038/s41598-024-56440-4.

[422] F. Pressacco, D. Sangalli, V. Uhlíř, D. Kutnyakhov, J.A. Arregi, S.Y. Agustsson, G. Brenner, H. Redlin, M. Heber, D. Vasilyev, J. Demsar, G. Schönhense, M. Gatti, A. Marini, W. Wurth, F. Sirotti, Subpicosecond metamagnetic phase transition in FeRh driven by non-equilibrium electron dynamics, Nature Commun. 12 (1) (2021) 5088, http://dx.doi.org/10.1038/s41467-021-25347-3.

[423] V. Shokeen, M. Heber, D. Kutnyakhov, X. Wang, A. Yaroslavtsev, P. Maldonado, M. Berritta, N. Wind, L. Wenthaus, F. Pressacco, C.-H. Min, M. Nissen, S.K. Mahatha, S. Dziarzhytski, P.M. Oppeneer, K. Rossnagel, H.-J. Elmers, G. Schönhense, H.A. Dürr, Real-time observation of non-equilibrium phonon-electron energy and angular momentum flow in laser-heated nickel, Sci. Adv. 10 (5) (2024) eadj2407, http://dx.doi.org/10.1126/sciadv.adj2407.

[424] D. Curcio, S. Pakdel, K. Volckaert, J.A. Miwa, S.r. Ulstrup, N. Lanatà, M. Bianchi, D. Kutnyakhov, F. Pressacco, G. Brenner, S. Dziarzhytski, H. Redlin, S.Y. Agustsson, K. Medjanik, D. Vasilyev, H.-J. Elmers, G. Schönhense, C. Tusche, Y.-J. Chen, F. Speck, T. Seyller, K. Bühlmann, R. Gort, F. Diekmann, K. Rossnagel, Y. Acremann, J. Demsar, W. Wurth, D. Lizzit, L. Bignardi, P. Lacovig, S. Lizzit, C.E. Sanders, P. Hofmann, Ultrafast electronic linewidth broadening in the C1s core level of graphene, Phys. Rev. B 104 (16) (2021) L161104, http://dx.doi.org/10.1103/PhysRevB.104.L161104.

[425] D. Curcio, K. Volckaert, D. Kutnyakhov, S.Y. Agustsson, K. Bühlmann, F. Pressacco, M. Heber, S. Dziarzhytski, Y. Acremann, J. Demsar, W. Wurth, C.E. Sanders, P. Hofmann, Tracking the surface atomic motion in a coherent phonon oscillation, Phys. Rev. B 106 (20) (2022) L201409, http://dx.doi.org/10.1103/PhysRevB.106.L201409.

[426] X. Llopart, J. Alozy, R. Ballabriga, M. Campbell, R. Casanova, V. Gromov, E.H.M. Heijne, T. Poikela, E. Santin, V. Sriskaran, L. Tlustos, A. Vitkovskiy, Timepix4, a large area pixel detector readout chip which can be tiled on 4 sides providing sub-200 ps timestamp binning, J. Inst. 17 (1) (2022) C01044, http://dx.doi.org/10.1088/1748-0221/17/01/C01044.

[427] B. Markovic, P. Caragiulo, A. Dragone, C. Tamma, T. Osipov, C. Bostedt, M. Kwiatkowski, J. Segal, J. Hasi, G. Blaj, C. Kenney, G. Haller, Design and characterization of the tPix prototype: A spatial and time resolving front-end ASIC for electron and ion spectroscopy experiments at LCLS, in: 2016 IEEE Nuclear Science Symposium, Medical Imaging Conference and Room-Temperature Semiconductor Detector Workshop, NSS/MIC/RTSD, 2016, pp. 1–4, http://dx.doi.org/10.1109/NSSMIC.2016.8069725.